Experimental and numerical investigation of vehicle soiling processes

Dissertation

zur Erlangung des akademischen Grades

Doktoringenieur

(Dr.-Ing.)

<table>
<tr><td>von</td><td>Dipl.-Ing. Thomas Hagemeier</td></tr>
<tr><td>geb. am:</td><td>21. Juli 1981</td></tr>
<tr><td>in:</td><td>Neubrandenburg, Deutschland</td></tr>
</table>

genehmigt durch die Fakultät für Verfahrens- und Systemtechnik

der Otto-von-Guericke-Universität Magdeburg

<table>
<tr><td>Gutachter:</td><td>Prof. Dr.-Ing. Dominique Thévenin</td></tr>
<tr><td></td><td>Prof. Dr.-Ing. Rolf Radespiel</td></tr>
<tr><td></td><td>Prof. Dr.-Ing. Günter Brenn</td></tr>
</table>

<table>
<tr><td>eingereicht am:</td><td>29. Juni 2012</td></tr>
<tr><td>Promotionskolloquium am:</td><td>06. Dezember 2012</td></tr>
</table>

Disclaimer

Declaration of Authorship

Ich erkläre hiermit, dass ich die vorliegende Arbeit ohne unzulässige Hilfe Dritter und ohne Benutzung anderer als der angegebenen Hilfsmittel angefertigt habe. Die aus fremden Quellen direkt oder indirekt übernommenen Gedanken sind als solche kenntlich gemacht.

Insbesondere habe ich nicht die Hilfe einer kommerziellen Promotionsberatung in Anspruch genommen. Dritte haben von mir weder unmittelbar noch mittelbar geldwerte Leistungen für Arbeiten erhalten, die im Zusammenhang mit dem Inhalt der vorgelegten Dissertation stehen.

Die Arbeit wurde bisher weder im Inland noch im Ausland in gleicher oder ähnlicher Form als Dissertation eingereicht und ist als Ganzes auch noch nicht veröffentlicht.

Magdeburg den 29.06.2012

Thomas Hagemeier

Abstract

Recent progress in experimental and numerical methodologies for practical investigations of vehicle soiling associated with water films have been reviewed. It proved the need of improvements, especially for modeling approaches.

Knowledge concerning soiling processes and patterns is mainly achieved in real scale wind tunnel tests or on rain test tracks, using simple measurement techniques. Such tests have a broad range of possible applications, but the obtained results strongly vary in quality and accuracy. For instance, measurements of dynamic properties of liquid films, such as height, velocity and wave propagation with high spatial and temporal resolution are still difficult to realize.

Complementary to the experimental methods, computational models are used to predict liquid films generated by spray impingement on vehicle surfaces. These modeling approaches rely either on a Lagrangian or a Eulerian reference frame, resulting in advantages and shortcomings for different aspects of vehicle soiling prediction. Most of the models fail to capture all significant physical phenomena involved in vehicle soiling.

Based on this observation, which is supported by an extended literature survey, the film model of Anderson and Coughlan [8] was chosen to integrate the most important missing aspects, such as complex droplet-film interaction, wetting phenomena and breakup. Submodels have been implemented in the original code and applied to simulate film flow over generic as well as realistic vehicle geometries.

In parallel, complex optical measurements have been carried out in a two-phase wind tunnel. In this manner quantitative data of the flow field and spray properties are acquired as boundary conditions and for model validation. Film thickness measurements have been conducted out as well, using fluorescence imaging. Moreover, this configuration is used for validation of the film model.

Finally, simulation and experimental results are compared considering also experimental results from our partners at ISM Braunschweig. The quality and effectiveness of the model improvements are shown and unresolved questions are discussed. All results are gathered in a database and are therefore available as validation material for further computer simulations.

Zusammenfassung

Methoden und Verfahrensweisen zur experimentellen und numerischen Untersuchung der Fahrzeugverschmutzung machen deutlich, dass wesentliches Verbesserungspotenzial, besonders bei den verfügbaren numerischen Modellansätzen vorhanden ist.

Die Erhebung von Daten zum Verschmutzungsgrad von Fahrzeugtypen erfolgt während der späten Entwicklungsphase, am Original in Windkanalversuchen oder Regenfahrten, wobei einfache Messtechniken Verwendung finden. Die verwendeten Messtechniken sind für vielfältige Anwendungen konzipiert und unterscheiden sich aber je nach Messgröße in Qualität und Genauigkeit. So ist beispielsweise die Bestimmung von dynamischen Größen wie der Höhe, Geschwindigkeit oder Wellencharakteristik von Flüssigkeitsfilmen mit hoher räumlicher und zeitlicher Auflösung stets eine große Herausforderung.

Parallel zu den experimentellen Untersuchungen werden Simulationsmodelle genutzt, um die Bildung von Flüssigkeitsfilmen infolge von Sprayaufprall auf die Fahrzeugoberfläche zu beschreiben. Die Modellansätze beruhen entweder auf Lagranger oder Euler'scher Betrachtungsweise, was für die Verwendung bei der Verschmutzungssimulation mit verschiedenen Vor- und Nachteilen verbunden ist. Viele Modelle versagen jedoch dabei, alle verschmutzungsrelevanten physikalischen Phänomene zu erfassen.

Unter Berücksichtigung dieser Aspekte, die durch eine umfangreiche Literaturstudie gestützt werden, wird das Simulationsmodell von Anderson and Coughlan [8] erweitert, besonders im Hinblick auf eine detaillierte Beschreibung der komplexen Tropfen-Film Interaktion, des Benetzungsverhaltens und des Filmzerfalls. Hierfür werden entsprechende Modelle in den originalen Programmcode integriert und anschließend zur Simulation der Filmströmung an generischen und realistischen Fahrzeugteilgeometrien genutzt.

Gleichzeitig erfolgen experimentelle Untersuchungen am Windkanal, die entsprechende Informationen über das Strömungsfeld und die Sprayeigenschaften liefern sollen. Diese dienen zur Definition von Randbedingungen oder können zur Validierung des Filmmodells genutzt werden. Die Filmdicke wird unter Verwendung der bildgebenden Fluoreszenztechnik ermittelt und wird ebenfalls zur Validierung des Filmmodells verwendet.

Abschließend werden die Simulationsergebnisse mit den experimentellen Ergebnissen des Kooperationspartners vom ISM Braunschweig verglichen. Die Qualität und Effektivität der Filmmodellveränderungen werden zusammen mit offenen Fragen diskutiert und veranschaulicht. Alle gesammelten Daten werden in einer Datenbank für die zukünftige Nutzung, zum Beispiel zu weiteren Validierungszwecken hinterlegt.

Acknowledgements

I want to thank:

i) My doctoral adviser Prof. Dominique Thévenin.

ii) The Volkswagen AG Wolfsburg for funding my work and providing such an interesting research topic. Special thank goes to Dr. Michael Hartmann for supervising my work at Volkswagen.

iii) The other assessors for reviewing my PhD-thesis and the commission chairman.

iv) My colleagues at LSS, Dr.-Ing. Katja Zähringer, Dr.-Ing. Bernd Wunderlich, Dr.-Ing. habil. Gábor Janiga, Dr.-Ing. Róbert Bordás, Dr. Gordon Fru and many more. I want to thank you for helpful discussions and the companionship during my time as PhD-student.

v) My cooperation partners at ISM Braunschweig under the guidance of Prof. Radespiel and Dr. Möller. I especially acknowledge the support of my colleague and friend, Benjamin Faßmann.

vi) I want to thank the students Martin Kühle and Jörg Hessenkemper for supporting my work during their time at the LSS, working on case study and Bachelor's Thesis.

vii) My family and friends.

Contents

Nomenclature

Latin symbols

A	absorbance	$-$
b	width	m
C	dimensionless integration constant	$-$
c_T	constant of Voinov relation	$-$
c	concentration	mol/l
c_s	DPM film model constant	$-$
d	particle or droplet diameter	m
d_f	fringe distance	m
f_D	Doppler frequency	Hz
$\mathbf{g}$	gravity acceleration vector	m/s^2
h	film thickness	m
I	light intensity	counts
I_u	unobstructed rainfall intensity	mm/h
I_{fdr}	free driven rain intensity	mm/h
$\mathbf{i}$	tangential direction vector	$-$
$\mathbf{k}$	normal direction vector	$-$
k	surface curvature	1/m
l	length	m
$\dot{M}$	mass flow rate	kg/s

$\mathbf{n}$	unit normal vector	—
n	refraction index	—
$\dot{\mathbf{P}}$	momentum flux	kg m/s^2
p	order of error reduction	—
p_f	film impingement pressure	Pa
q	wave vector	—
r	refinement or object ratio	—
$\mathbf{S}$	momentum sources	kg m/s
$\bar{T}$	mean temperature	K
$\mathbf{t}$	unit tangent vector	—
t	characteristic time	s
U	air velocity, capillary wave velocity	m/s
$\mathbf{u},\ \mathbf{v}$	film, wall velocity	m/s
$u,\ v$	particle, droplet or fluid velocity	m/s
$\dot{V}$	volume flow rate	m^3/s
$\mathbf{x}_s$	point on wall surface	—

Greek symbols

α	inclination angle	(°)
δp_f	pressure difference across the film	Pa
δ	film thickness	m
ϵ	molar absorption of fluorescent dye	l/(mol m)
ϵ_f	film aspect ratio	—
ϵ_h	discretization error of quantity ϕ	$[\phi]$
θ	laser beam angle	(°)
$\theta_{D,\ e}$	dynamic, equilibrium contact angle	(°)
κ	Kármán constant	—

λ	characteristic wave length	m
λ	wave length of laser	nm
μ	dynamic viscosity	Pa s
π_A	cross-sectional blockage ratio	−
ρ	density	kg/m^3
σ	surface tension	N/m
τ	shear stress	Pa
τ_{imp}	characteristic impact time	s
Φ	model factor	−
$\phi_{1,2,3}$	arbitrary quantity	$[\phi]$
ϕ	burst signal phase shift	Hz
φ	refraction angle	(°)
ψ	detector angle	(°)

Indices

$0, \infty$	approach, incident, reference
$1, 2, ...$	phase, medium index
λ	at given wave length
c	capillary
cf	crater fill-up
cg	crater generation
$crit$	critical parameter
dye	fluorescent dye
e	emitted
f	film
h	horizontal
imp	impingement characteristic

l	liquid material property
lt	crater life time
s	surface
$sample$	fluid sample thickness
sl	solid-liquid
sv	solid-vapor
t	transmitted or terminal
w	wall

Abbreviations and dimensionless numbers

AMS	American Meteorological Society
Ca	Capillary number
CAE	Computer aided engineering
CFD	Computational fluid dynamics
DES	Detached eddy simulation
DPM	Discrete phase model
DSD	Droplet size distribution
ECA	Equilibrium contact angle
EWM	Exterior water management
FDRI	Free driven rain intensity
K	Splashing parameter
Ka	Kapitza number
K_f	dimensionless film number
La	Laplace number
LDV	Laser Doppler Velocimetry
LES	Large eddy simulation
LWC	Liquid water content

Oh   Ohnesorge number

PDA   Phase Doppler Anemometry

RANS   Reynolds averaged Navier-Stokes

Re   Reynolds number

Ri   Richardson number

Sr   Strouhal number

We   Weber number

rms   root mean square

Chapter 1

Introduction and Literature Review

The history of automobile industry has evolved at a remarkabl pace. It started with pioneers like Carl Benz and Gottlieb Daimler who based the manufacture of automobiles on manual work. A revolutionary change was introduced by the assembly line production of Henry Fords 'Model T'. Nowadays, almost everything in automobile industry runs with automation and each production step is assisted by robots. The development process and time have been speeded up, because new car models have to be released faster and faster. The trend goes to the so called 'frontloading' [63], where the development process runs almost everything in virtual manner and is integrated in the first engineering and production steps. Mack [93] presents interesting statements and quotes concerning the current state of the art. He explains how to further improve the development process and gain higher efficiency.

Customer decisions for a certain car are lead by convincing arguments based on small details, as Cramblitt and Gilfrin [30] accurately pointed out. Some of these details are the so called 'functional aerodynamics' [167], which affect the drivers' safety and comfort. Both issues are related to vehicle soiling processes and have been specifically considered in Zivkov [167]. If soiling predictions can be integrated in the virtual vehicle development, both, the requirements of the producer for faster development and the longing of customers, for more safety and comfort can be met. In the following a literature survey on vehicle soiling is proposed. Part of this survey has been published in the *International Journal of Multiphase Flow* [54].

1.1   Practice of Vehicle Soiling Investigation

Nowadays, the investigation of phenomena occurring during rain impact on moving cars is of increasing importance to improve driver safety and driving comfort. Although the physics governing vehicle soiling have been considered for many years, some central aspects are still unclear. As a consequence, many submodels remain completely heuristic and may potentially reduce the validity of all numerical predictions. Such issues will be analyzed in what follows.

This review considers the different steps of the practice for vehicle soiling simulation, as usually applied in the automobile industry. Since vehicle soiling is originally caused by rain and since the designation "soiling" often leads to confusion, the alternative concept of "exterior water management" (EWM) tends to be used now in order to describe the complete procedure. EWM studies should account for (Fig. 1.1):

1. the multiphase flow (rain: air plus droplets) in front and around the geometry, with all its complexity (e.g., turbulence, phase coupling, properties of the dispersed phase);

2. the impact (spray-wall-interaction);

3. the build-up of a liquid film on the surface;

4. its development along the surface, including instability considerations;

5. film break-up;

6. and finally the entrainment of separated liquid regions (secondary droplets) by the air flow, possibly leading to further impacts.

The prediction capabilities of models developed for vehicle soiling simulation are reviewed later in Chapter 3 together with the required computational effort. Soiling models can be associated with different modeling approaches for the dispersed phase, which will be discussed. Moreover, it will be considered, how the models employed to obtain the (continuous) flow field affect the soiling predictions.

Three different points of view will be used in this study. The practical aspect corresponds to a specialized engineer employed in the automobile industry and focuses on qualitative comparisons between experiments and numerical simulation results, since quantitative results are absent for real configurations. The point of view of Computational Fluid Dynamics (CFD) concentrates on the applicability, generality and remaining issues for individual numerical models, as well as their implementation to actual problems at acceptable computational cost. From the scientific point of view, identifying all necessary
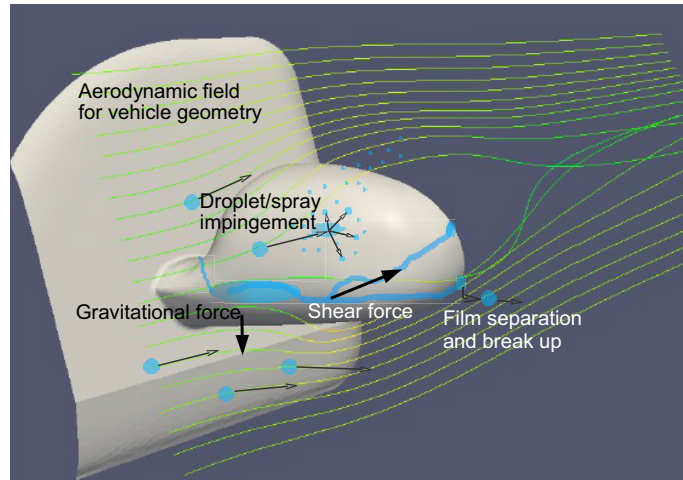
FIGURE 1.1: Main physical phenomena governing film flow in vehicle soiling

physical details as well as the associated coupling aspects is of central importance. Combining these different points of view, it becomes possible to propose recommendations for best practice guidelines as well as for urgently needed further studies, as discussed in this Thesis.

The windshield and the side window, linked by the A-pillar, as well as the rear-view mirror are most affected by soiling. Therefore, they are most relevant for driving safety [11]. Vehicle soiling can be attributed to three main origins (Fig. 1.2). In the first case, vehicle soiling occurs due to foreign contamination through (1) wind-driven rain or (2) liquid raised by other road users. Both can be distinguished by the mean droplet size, which is about one order of magnitude smaller for raised mist compared to wind-driven rain. The other reason is self-soiling due to (3) liquid mist and solid dirt particles raised for example by rotation of one's own wheels. For the latter case, the droplet size is similar to that due to foreign contamination by other road users, but the contamination regions differ, the wheel houses and the rear end of the vehicle being most affected [66].

Mist is generated during the impact of primary rain droplets on the vehicle, thus possibly reducing driver's visibility. The liquid deposited on the vehicle surface then moves either as film, rivulet or as single droplets. The displacement is governed by flow-induced shear, gravitational and adhesion forces and surface tension. The liquid motion along the surface leads to characteristic flow structures. Such liquid layers refract the light and hence decrease the visibility through the windows and mirrors. Wiper action may clear the windshield. However, it may increase the amount of liquid on the side window and on the rear view mirror, which is crucial for safety. Especially at night, the headlights of different road users may lead to blinding effects.
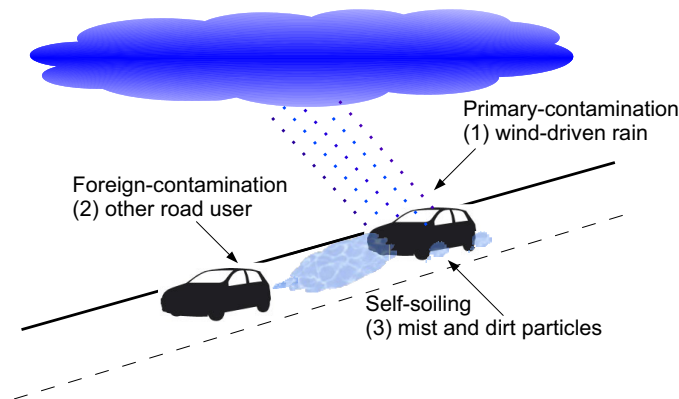
FIGURE 1.2: The three different origins for vehicle soiling (rain contamination, foreign contamination, self-soiling)

Due to safety considerations, investigating the effect of rain impinging on the surface of vehicles and thus influencing traffic behavior became essential. Note that it is not only important for the automobile industry. Indeed, there are other applications for soiling simulation, such as train and aircraft technology (possibly associated with icing problems) as well as architecture. Large buildings with complex shapes lead to difficult issues concerning rain evacuation, associated forces and surface degradation. Publications concentrating on such applications but relevant for EWM for the automobile industry will be discussed as well.

Starting their studies in the early eighties, Haines and Luers [56] and Luers and Haines [92] investigated rain water deposition on the outer surface of aircrafts and vehicles. Their motivation was to reduce the probability of accidents for aircraft landing due to heavy rainfall. More recent research work, for instance from Valentine and Decker [154] and Thompson and Marrochello [145] focused on the analysis of the performance of airfoils in rain and on the rivulet formation along the surface. The methods and modeling approaches introduced in these early publications are still used today by the automobile industry for vehicle soiling simulation. Initial publications dedicated to EWM for cars started in the nineties, see in particular Karbon and Longman [79], Piatek and Hentschel [123] and Pilkington [125]. Practical tests and validation experiments, usually carried out with full-scale vehicles placed in specialized wind tunnels were already documented in the seventies by Potthoff [127] and have been used many times since then, mostly directly using wind tunnels owned by corresponding automobile manufacturers.

For a successful prediction of vehicle soiling, many theoretical, experimental and numerical aspects must be clarified, thus leading to a large number of dedicated studies, which investigated isolated questions. For instance, Karbon and Longman [79] considered dynamic aspects associated with EWM. There, vehicle motion was considered and the focus was set on the prediction of water channeling across the windshield, side glass and

rear view mirrors of cars [79]. Bouchet et al. [17] focused on the description of realistic rain properties using meteorological studies. Vehicle soiling due to foreign contamination was considered extensively in Borg and Vevang [16]. They employed realistic drop size distributions measured behind trucks to simulate exterior contamination of vehicles. Soiling models that are able to distinguish between foreign and self-contamination due to mist raised at the rear end of a car were described by Campos et al. [24] and Kuthada et al. [84]. As already explained, reliable quantitative results are hardly available from reference experiments. Therefore, all those studies rely on qualitative comparisons obtained experimentally by wind tunnel tests, as exemplified in Fig. 1.3. In this manner, it is possible to check at least to some extent the accuracy of the obtained numerical predictions, as presented for instance in Fig. 1.4.

Recently, Gaylard and Duncan [48] provided a literature review regarding vehicle soiling simulation and Spruss et al. [142] presented a study on experimental and numerical investigation of spray generation by wheel rotation. They developed a spray simulation approach that can be directly included in soiling simulation for whole vehicle.
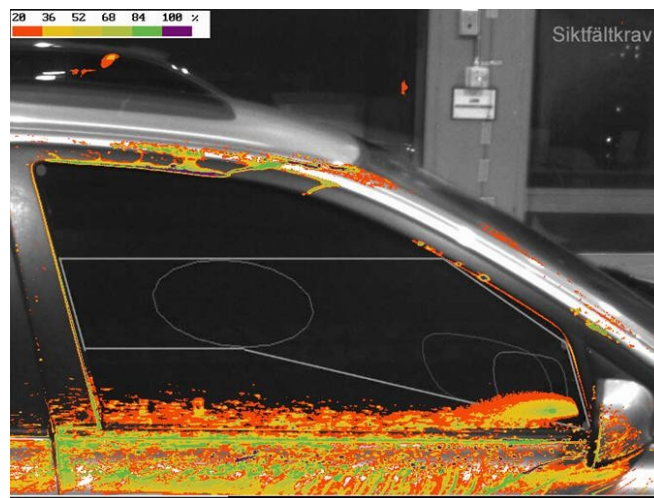
FIGURE 1.3: Vehicle soiling experiment in a wind tunnel to investigate side window contamination, as documented by Borg and Vevang [16] (Co. Volvo)

In order to obtain a refined validation of the numerical predictions, typical soiling patterns are often considered [8]. Wind tunnel hardware components are optimized to obtain a more realistic representation of real rain conditions, as documented for instance by Ghani et al. [49].

Self-contamination by solid dirt particles was considered by Zivkov [167]. Additional aspects like electrostatic adhesion of particles to each other and to the wall have been considered as well [131]. The methods employed to simulate vehicle soiling due to solid or liquid particles tend to differ and the emphasis is clearly set on the liquid case in
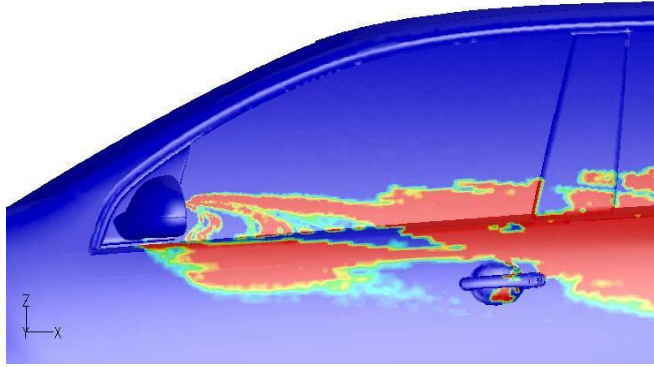
FIGURE 1.4: Numerical prediction of vehicle soiling concerning droplet deposition, as documented by Lehnhäuser [88] (Co. Volkswagen)

this Thesis. After this generic introduction, the next section considers the experimental techniques employed for EWM studies.

1.2 Experimental Soiling Simulation

During recent years, the main challenge of such studies was the improvement of the hardware to reproduce driving conditions in a more realistic manner and to be able to simulate a variety of situations. In general, rain simulation is realized in wind tunnels, often specialized for such studies or associated with other properties allowing climatic or meteorological investigations.

To be as realistic as possible, full-scale wind tunnel studies have been almost systematically considered by automobile manufacturers. Vehicle soiling obviously involves turbulent, multiphase flows. A full application of similarity theory allowing a reduction of the problem dimension is very challenging for such complex, coupled problems, and could not be found up to now in the literature concerning EWM for cars.

After wind tunnel testing, road tests are very important for practical purposes but are afflicted with known drawbacks (no reproducibility of driving conditions, no detailed knowledge of the properties of the impacting multiphase flow, concealment during the development of new car models). Indeed, it is barely possible to measure anything in detail during road tests, for instance film flow properties. Road test studies are therefore excluded from this work in the following. Measurements suitable to validate and improve numerical predictions must be obtained in dedicated wind tunnel studies under controlled working conditions. This is the only possibility for a quantitative evaluation of rain and spray properties at different locations around the vehicle. Furthermore,

global measurements are possible to obtain information concerning the liquid deposition on the surface of the vehicle.

1.2.1   Assessing Rain Properties

One important aspect for experimental soiling simulation is the correct setting of rain intensity and droplet size distribution, as demonstrated for instance by Bouchet et al. [17]. According to the American Meteorological Society (AMS) the Free Driving Rain Intensity (FDRI), written I_{fdr}, is defined as the rain quantity carried by wind, expressed in the same dimension as usual rain intensity (mm/h) associated with one square meter. In wind tunnel experiments, this formulation describes the liquid mass flow measured within a vertical surface, usually the cross section area of the wind tunnel test section. FDRI can be computed with the knowledge of unobstructed rainfall intensity I_u, terminal velocity component u_t and horizontal velocity component u_h of the rain, which is assumed to be equal to the horizontal wind speed. The rain droplet trajectories are obtained from both velocities, as dictated by gravitational and drag forces acting on the droplets.

$$I_{fdr} = \frac{u_h}{u_t} I_u \qquad (1.1)$$

For rainfall classification, the AMS gives the following intensity values and distinguishes three regimes: the light intensity type with $I_u < 2.5$ mm/h, moderate intensity is associated with $2.5 \leq I_u \leq 7.6$ mm/h and heavy rainfall intensity corresponds to $I_u > 7.6$ mm/h. The same global ranges are stated in Ghani et al. [49], but additional classes are introduced, which also cover minimal rainfall intensity regimes for fog and mist (around 0.05 mm/h) and extreme intensities for excessive rain and cloudburst with more than 100 mm/h. Natural rain simulation must also account for the liquid water content (LWC), which is the mass of liquid contained in a unit volume of air. It ranges from 0.006 to 35 g/m^3 and is always directly associated with a rain intensity class [49]. Different rainfall classes correspond to different droplet size distributions (DSD) and representative mean droplet diameters as well (Fig. 1.5). As a consequence, the DSD should also be modified in wind tunnel studies when varying FDRI, if a realistic rain representation is targeted. Ideally, the employed conditions should follow the dashed line plotted in Fig. 1.5 that represents a real meteorological correlation between droplet diameter and rain intensity.

The range in which experiments were conducted during the project presented here, is included in Fig. 1.5 with blue triangles. The employed parameters are slightly above those for realistic rain. However, the most important aspect for validation is that the

experimental conditions must be reproducible. These conditions guided the choice of our experimental conditions, together with the fact that small droplets (mean diameter below or around 1 mm) are statistically more often relevant in real practical rain events.
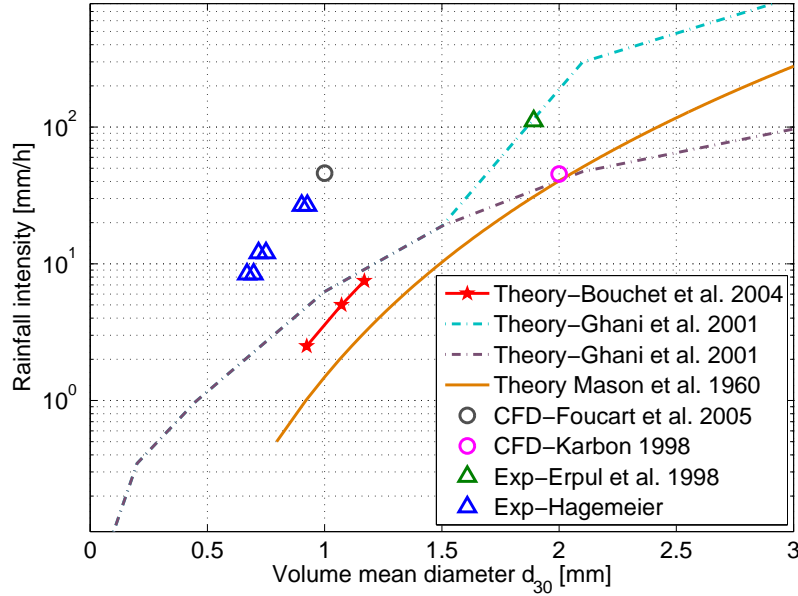
FIGURE 1.5: Rainfall intensities and associated droplet mean diameter as found in the literature

Another important aspect for vehicle soiling studies is the realistic generation of fine spray, as raised by other vehicles which also leads to foreign contamination. In those cases, the rain properties change from high diameter values to small ones comparable to secondary droplets after spray splashing, typically 80 to 300 μm large [17]. Droplet diameters are not only affected by rain intensity or water volume flow rate, but also by the wind velocity, as Erpul et al. [43] proved with experiments in the I.C.E. wind tunnel (International Center of Eremology, Ghent, Belgium).

In that case, the DSD is mainly changed due to droplet break-up and coalescence [11]. Governing parameters are the relative velocity between droplets and air flow, the primary droplet size and the material properties of the droplets [43]. These parameters can be combined into two dimensionless numbers, the aerodynamic Weber number We and the droplet Reynolds number Re_d, or alternatively into the Ohnesorge number Oh, which is commonly used to describe break-up phenomena:

$$
\begin{aligned}
\mathrm{We} &= \frac{\rho_g \, (v - u)^2 \, d}{2\sigma} \\
\mathrm{Re}_d &= \frac{\rho_g \, (v - u) \, d}{\mu_g} \\
\mathrm{Oh} &= \frac{\sqrt{\mathrm{We}}}{\mathrm{Re}_d} = \frac{\mu_g}{\sqrt{d \, \rho_g \, \sigma}}
\end{aligned}
\tag{1.2}
$$

The Weber number is the ratio between inertial forces and surface forces, based on material properties ρ_g, the density of the gas and σ, the surface tension of the liquid and kinetic properties, the relative velocity between gas v and droplet u. The Reynolds number is the ratio of the inertial forces to the viscous forces, containing the gas phase density ρ_g, its viscosity μ_g and the droplet diameter d. Notice that material properties take the index g for gas and l for liquid phase properties in multiphase flow problems. Single flow problems are written without any index. Kinetic property variables, for example liquid phase velocities are indicated with d for droplet or f for film-related velocity.

Erpul et al. [43] focused on applications in soil and tillage science, but the basic features leading to a realistic rainfall simulation are still the same. The experimentally evaluated DSD showed significant differences between wind-driven rain at 9.96 m/s and rainfall without wind. The most interesting differences are that the droplet size increases with wind and that the DSD becomes narrower. This unexpected behavior is partially explained by the atomization system used by Erpul et al. [43].

Different measurement techniques are applicable to obtain quantitative data on rain properties and to validate the spray generation process. Rain gauges used by Bouchet et al. [17] are based on working principles used in building architecture. Rain droplets are caught within the gauges and the total volume is evaluated. As mentioned above, there are also small droplets generated in the wake of a vehicle or due to spray splashing. To capture also the smallest of them, which naturally follow the air flow in an almost perfect manner, a special construction was developed in [17]. Gauges as well as patternators yield quantitative results for integral properties, rain intensity, volume flow rate or mass flow rate of the water. The temporal and spatial resolutions are very limited and there is no information concerning the individual droplet size and velocity, nor on their distributions. To obtain more accurate information, the stain method was applied by Erpul et al. [43]. Here, an absorbing paper is used, which is covered with a dried copper sulphate solution. This enables one to mark out the impinging spot in a permanent manner, allowing a later evaluation. In order to obtain some temporal resolution, the paper is exposed only for one second to the simulated rain at a specified location within the test section; whereas the spatial resolution depends on the size of the paper. Detailed information concerning spray characteristics are obtained by evaluating the number of all and the size of each individual droplet spot. Obviously, this method is only applicable for highly dispersed systems.

Further measurement techniques to evaluate spray characteristics and splash occurrence are defined in commonly accepted standards, SAE-J2245 [134] or JIS-D-0203 [73]. Two

equivalent techniques, a digitizing method and a laser method, are described in SAE-J2245 [134]. They are based on light absorption by a spray cloud which is measured either with a camera or with a laser receptor. The intensity difference between the test pattern and the control pattern (obtained from calibration) is a measure for the spray cloud size and shape. These standards are mostly applied to investigate sprays generated by wheel rotation, in particular for spray suppression devices on large trucks as described for example in Manser [96]. A recent contribution is provided by Watkins [159], who describes improvements to the usual standard digitizing method.

Note that more complex optical measurements techniques such as phase-Doppler anemometry or interferometry are used as well in research departments of automobile industry. However, they are mostly employed to evaluated spray properties associated with injection and combustion processes in the cylinder. To my knowledge, there is no published study using such methods explicitly for vehicle soiling apart from my own work [51, 53]. This will certainly change in the future, since such techniques are particularly interesting to obtain a reliable spray characterization.

Setting realistic rain properties does not mean only the specification of a suitable droplet diameter, volume flow rate or liquid water content. Associated wind velocities must also be correctly chosen. Wind tunnel experiments investigating foreign contamination were conducted at air velocities within the most usual range for passenger car speeds under heavy rain conditions, typically from 19 to 25 m/s [16, 24, 46, 82, 84]. For further studies not specifically dedicated to vehicle soiling, the air velocity range was shifted not only to lower values (for instance around 5 m/s in Erpul et al. [43]), but also to much higher values (for instance up to 36 m/s in Bouchet et al. [17]). By analyzing all these results and considering air velocity and rain intensity encountered in practice, the range of relative wind speed (corresponding to the velocity of the driving car) from 19 to 25 m/s appears indeed to be the most interesting and relevant one for vehicle soiling studies. This is also supported by tests of up to 40 m/s conducted by Karbon and Longman [79] showing almost no contamination of safety-relevant surface parts for such high velocities.

Note that CFD has been used as an additional source of information to assess the most suitable working conditions for the air and droplet flows during wind tunnel tests, as documented in particular in Ghani et al. [49]. In that case, the simulation must take into account all the physics associated with vehicle soiling, as discussed later in this work.

1.2.2   Measurements of Film Properties

Sometimes, the information concerning individual droplet properties is not required and integral facts like the water volume flow rate might be sufficient. Usually, atomization systems with known droplet size spectra are employed for practical studies of vehicle soiling in wind tunnels and corresponding DSD are considered constant (which may be questionable, as discussed previously). Then, the most important outcome of such wind tunnel experiments is the evaluation of the liquid deposition on the vehicle surface. Since safety aspects are the main motivation for these investigations, the flow conditions, spray and liquid film properties are generally analyzed only around the A-pillar, along the driver side window and around the rear-view mirror. These locations are very close and can be visualized with a single camera. As a consequence, optical techniques are almost always used for such studies. With a standard camera, only a qualitative visualization of the film flow can be realized, as documented for instance by Piatek and Hentschel [123] and Hucho and Ahmed [67]. Based on single images and on movies processed with dedicated software packages [161], some more insight can be gained on the soiling behavior, such as for instance differentiation between continuous films or break-up in separated rivulets.

A good visualization of film flow on automobile surfaces is feasible only with a proper tracer material. A cheap and common tracer material is chalk, as used in the work of Bannister [11], which produced visible characteristic lines. Furthermore, using a saltwater solution for an indirect tracking of the film flow is a known practice in wind tunnel experiments [79]. From the dried solution, the salt remains as an observable trail on the vehicle surface. This enables an estimation of the level of contamination and the shape of the film flow trails. But neither chalk nor salt can be used for a quantitative measurement of film properties, in particular film thickness or velocity. Most studies now employ fluorescent dyes solved in water. Compared to chalk or salt, which require an extensive cleaning of the full experimental facility, fluorescent solutions have a clear advantage [84]. When applying any kind of fluorescence, the working principle is that with increasing film thickness on the surface of the car, the emitted light intensity increases as well (Fig. 1.6). Hence, the level of contamination directly corresponds to the intensity of emitted light [16]. A quantitative evaluation is even possible in theory after a (complex) calibration. The illumination usually occurs at a wavelength range from 350 to 370 nm, which can be produced with a short-wave UV light lamp [24, 82].

Very recently, Aguinaga and Bouchet [3] carried out real quantitative, time-averaged film thickness measurements using UV fluorescence in full-scale experiments. The measurement principles, the validation, the calibration procedure and the highly complex film thickness measurements in a climatic wind tunnel were explained in Aguinaga et al.
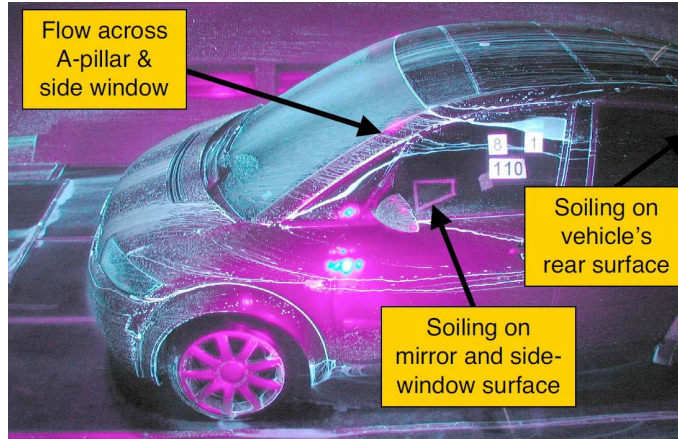
FIGURE 1.6: Wind tunnel experiments revealing soiling topology for safety relevant regions, as performed by Islam [70]

[2]. These very complex experiments were not limited to foreign contamination studies. They considered self soiling from wheel rotation and rain water entering the engine compartment under the hood.

Since most measurement techniques cannot provide detailed temporal resolution or are purely qualitative, steady flow conditions were always considered in corresponding wind tunnel studies. An often used approach is based on direct image by image comparison of wind tunnel tests and CFD. For instance, results were compared after starting rain with a wetting duration of 20 seconds in [24, 79].

Bannister [11] investigated the initial dynamics of soiling patterns on the side window of a car excluding the A-pillar during the first 60 seconds. Using side panels covered with a water-sensitive agent, particle accumulation is increased, so that measurements with a simple video technique can become fast and repeatable. This study focused on the difference between the level of liquid/dirt deposition on the side window caused by primary rain or by droplets detached from the rear-view mirror. Contrary to this study, many authors concentrated on the time independent soiling configuration obtained after a longer period. To achieve quasi-steady conditions for film height in case of foreign soiling due to rain with droplets of a diameter of 1000 μm, Foucart and Blain [46] measured after operating 130 seconds and started the comparisons with CFD at that instant. Borg and Vevang [16], investigating foreign vehicle contamination in terms of raised mist from leading cars with a mean droplet diameter smaller than 400 μm, observed fully developed soiling patterns after 5 minutes of operation. During this time span the contamination progress was regularly documented through image acquisition. In case of self contamination as investigated for instance by Kuthada et al. [84], 60 seconds were sufficient to obtain a constant soiling level in terms of contamination factor at the rear end of the car.

Clearly, most recent studies try to obtain an improved resolution in time. Tivert and Davidson [148] carried out film flow evaluation at laboratory scale, investigating the flow path of rivulets and their break-up behavior for a generic rear-view mirror, using video techniques and high speed cameras. They proposed in particular empirical break-up criteria for different flow regimes and approach velocities, based on the Weber number of the rivulet.

1.2.3 Driver Comfort

Some studies consider very specific issues associated with driver and passenger comfort. As mentioned previously, the windshield, the rear-view mirror and the side window are essential both for safety purposes and for driver comfort. Concerning comfort, the back pane and the door handles are also very important aspects. Investigations associated with a single component, in particular the rear-view mirror, are often found (for instance [11]). Extended tests with various mirror shapes were conducted, where the radii of the mirror housing were changed. Aerodynamic and aeroacoustic effects were taken into account and the influence of lift and drag of the different mirror types on the soiling behavior of the side window was investigated. Leading the deposited droplets along the mirror surface by blades or lips could reduce soiling level, but resulted in additional, unbearable noise. It was confirmed that droplets are affected by separation location and flow conditions within the mirror wake, which could be influenced by other geometrical modifications.

Foucart and Blain [46] conducted an optimization study for the A-pillar geometry combined with wiper action. Various types of water leading bands and transitions between windshield and A-pillar were evaluated and resulted in significant differences concerning soiling patterns. Such combined experimental and numerical optimization studies become more and more common procedure in car manufacturing practice. Höfer [61] considered experimentally the contamination of the side window and proposed aerodynamic modifications to reduce it and improve active driving safety.

Based on the work of Pilkington [125], the experiments of Borg and Vevang [15] have been set up at Volvo Car Corporation. Correlations between on-the-road and wind tunnel tests for the soiling behavior of the side window and of the whole vehicle side were introduced. In this manner, it becomes possible to translate results of soiling studies from wind tunnel measurement to real, on-the-road behavior.

Rain water management addresses more than the soiling of the outer surface of vehicles. There are different applications dealing with rain water penetration in air intake systems or water box from air conditioning systems. However, they are out of the focus of this

work. Nevertheless, some of these authors have developed and validated interesting film models based on experiments at laboratory scale (for instance [113, 151, 152, 153]). Such models could obviously be used as well for soiling simulations, as discussed later.

Investigations concerning emissions of contaminant particles (water mist) by heavy vehicles and trucks are also found. The reduction of spray generated by the rotation of wheels and therefore the prevention of foreign soiling due to raised mist is then the main target. Several splash and spray reduction devices, together with a cost-effectiveness analysis were in particular documented by Pilkington [125]. Paschkewitz [121] investigated spray generation due to wheel rotation and analyzed the droplet size distribution behind trucks, yielding interesting information for spray modeling purposes. Further studies are not really relevant for the issues considered in this work and are hence not listed.

Regarding vehicle wetting, surface treatment and repellent agents might be effective, and corresponding publications describing special surface properties are found, e.g. [78]. In particular, many patents are available on this subject. Surface wetting is a complex physical process describing the interaction of the solid substrate with the surrounding liquid and gas at molecular level, as described for example in [110]. Interesting theoretical considerations can be found in particular in [36]. Dedicated surface treatment options are beyond the scope of this work and are excluded from further discussion.

1.3   Research Objectives

Beside optimization of drag and lift forces and aeroacoustics, the vehicle soiling or rain water management is an important objective during the aerodynamic development of new car models. Experimental techniques and simple models have been developed to investigate soiling and have been reviewed in this chapter. Based on this analysis, the most important limitations of current soiling models can be identified, guiding us toward needed extensions and improvements.

First, series of accurate experiments in two-phase wind tunnels have to be carried out, in order to support numerical modeling relying on a truly physical background. The experimental part of this work concerns mainly the investigation and quantification of boundary conditions for the continuous gas and the dispersed droplet phase for different configurations associated with vehicle surface geometries (windshield, rear view mirror). Data sets have been acquired, processed and gathered in a large, structured data base. An experimental technique has also been developed to measure film thickness.

In a second step, the liquid film model of Anderson and Coughlan [8] was chosen together with Volkswagen AG as starting point for improvement. All improvements should be based on own and published research work. Main issues here are the model modifications for film-spray interaction, taking wetting limitation into account, as well as the implementation and evaluation of different break-up mechanisms.

Only limited experimental data are available for comparisons with simulated film thickness results. At ISM Braunschweig (our research cooperation partner) liquid film flow patterns have been recently characterized. Corresponding information is also available in my own experiments, but only for very simple geometries. This will allow first quantitative comparisons of experiments and simulations.

Chapter 2

Physics of Liquid Films

After showing the importance of vehicle soiling investigations, generic considerations concerning the physical properties of liquid films are presented in this chapter. The main focus is set on the governing physics and on associated equations of liquid film flows. Since vehicle soiling is a direct consequence of spray impingment leading to film build-up, evolution and finally break-up, it is essential to consider the physical processes associated with liquid films in order to understand vehicle soiling.

2.1 Dynamics of Liquid Film Flows

Generally, the dynamics of wall-bounded liquid films are described by the complete system of Navier-Stokes equations. Therefore, a fully three dimensional derivation of the governing equations is proposed for example by Alekseenko et al. [6]. In order to cover all physical phenomena including heat transfer and wall effects (including contact line [39]) additional equations and correlations are necessary. For a first introduction the derivation of transport equations for an isothermal film flow is considered here, since it corresponds to our practical application.

Since the complete Navier-Stokes equations are generally impractical, further simplifications are usually applied according to the 'thin film assumption' or 'long-wave theory' as described in Orno et al. [117], O'Brien and Schwartz [114] or more recently in Craster and Matar [31].

The assumptions are, that the film is thin so that the aspect ratio ϵ_f of the liquid film (height h_f to its length l) is very small $\epsilon_f = \frac{h_f}{l} << 1$, and that all gradients in tangential directions are small. Inertial effects are considered negligible and the Capillary number must be small. The dimensionless Capillary number Ca is the ratio of viscous forces to

surface tension forces, defined as:

$$\text{Ca} = \frac{\mu u}{\sigma}. \tag{2.1}$$

It involves the viscosity μ, characteristic velocity u and the surface tension σ of the liquid.

The film fluid is assumed to be continuous, without a contact line (complete wetting), so that rivulets or single droplets sliding on an otherwise dry substance are not represented. Normal stresses dominate, as in lubrication theory, which is a special formulation of the long-wave theory for small Re numbers [117]. This theory, as introduced by Reynolds, is a quasi two-dimensional approach, but is one 'corner stone of fluid mechanics' [144]. A simplification of the Navier-Stokes equation is achieved in particular by averaging over the film thickness and therewith reducing the number of relevant spatial dimensions. All the details are given next, following the notations of Kondic [81].
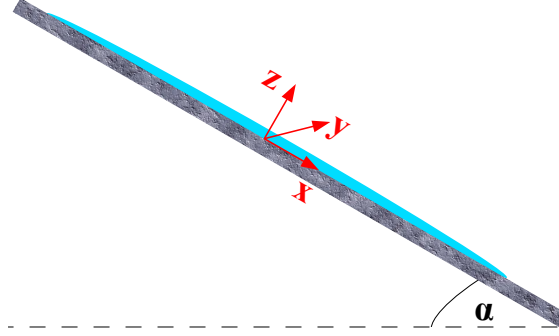

FIGURE 2.1: Film flow coordinates used for the derivation of the thin film equation (x, y-coordinates for in-plane directions and z-coordinate for normal-direction)

Starting point are the Navier-Stokes equations for an incompressible flow of a newtonian fluid, here written in vector notation for the flow over an inclined plate at angle α towards the horizontal

$$\frac{\partial \mathbf{u}}{\partial t} + (\mathbf{u} \cdot \nabla)\,\mathbf{u} = -\frac{1}{\rho}\nabla p + \frac{\mu}{\rho}\nabla^2 \mathbf{u} + g\sin(\alpha)\,\mathbf{i} - g\cos(\alpha)\,\mathbf{k}. \tag{2.2}$$

Assuming that the film velocity is constituted of two in-plane components $\mathbf{v}$ and of the normal component w enables a decomposition of the velocity $\mathbf{u}$ in:

$$\mathbf{u} = (\mathbf{v}, w). \tag{2.3}$$

For an incompressible flow $\nabla \cdot \mathbf{u}$ is zero and reduced equations for in-plane momentum component:

$$\nabla_i p = \mu \frac{\partial^2 \mathbf{v}}{\partial z^2} + \rho g \sin(\alpha)\,\mathbf{i} \tag{2.4}$$

and normal momentum component:

$$\frac{\partial p}{\partial z} = -\rho g \cos(\alpha) \tag{2.5}$$

can be derived from Eq. (2.2). Using the Laplace-Young relation as boundary condition at the interface of liquid and gas, $z = h(x, y)$

$$\Delta p = -\sigma k, \tag{2.6}$$

where k is the interface curvature, the normal momentum equation can be solved

$$p = -\rho g (z - h) \cos(\alpha) - \sigma k + const. \tag{2.7}$$

An additional approximation is necessary to solve for the curvature k of the gas-liquid interface

$$k \approx \nabla^2 h. \tag{2.8}$$

The in-plane momentum components are obtained by integrating twice the reduced equation and applying a Dirichlet-boundary condition at the liquid-solid interface (no slip condition) and a Neumann-boundary condition at the gas-liquid interface, considering stress continuity. This yields the well known parabolic velocity profile equation

$$\mathbf{v} = \frac{1}{\mu} \left[\nabla \left(\rho g h \cos(\alpha) - \sigma k \right) - \rho g \sin(\alpha) \, \mathbf{i} \right] \left[\frac{z^2}{2} - hz \right]. \tag{2.9}$$

As mentioned before, a further simplification is achieved by averaging over the film thickness. It gives the mean film velocity as

$$\langle \mathbf{v} \rangle = \frac{1}{h} \int_0^h \mathbf{v} dz. \tag{2.10}$$

Finally, using the transformed averaged mass conservation:

$$\frac{\partial h}{\partial t} + \nabla \cdot (h \langle \mathbf{v} \rangle) = 0, \tag{2.11}$$

the 'thin-film equation' can be obtained:

$$\frac{\partial h}{\partial t} = -\frac{1}{3\mu} \nabla \cdot \left[\sigma h^3 \nabla \nabla^2 h - \rho g h^3 \nabla h \cos(\alpha) + \rho g h^3 \sin(\alpha) \, \mathbf{i} \right]. \tag{2.12}$$

It is a fourth-order nonlinear partial differential equation [39].

2.1.1   Empirical Film Flow Regimes

For vehicle soiling it is possible to simplify further the governing equations, as explained next. Based on empirical observations different flow regimes were introduced as follows, according to the detailed summary of Adomeit and Renz [1] and Ausner [9]. Liquid film flows are finally discriminated into three regimes according to the Reynolds number, defined for liquid films as:

$$\text{Re} = \frac{\dot{V}}{b\nu}, \tag{2.13}$$

where b indicates the film width and $\dot{V}$ the liquid flow rate through the film. Laminar film flow can be found for very small Reynolds numbers of $\text{Re} \leq 3$. For this special case there is an analytical solution (Nusselt solution or 'Wasserhauttheorie'), based on investigations of Nusselt in 1916 [112]. Considering no-slip boundary condition at the wall $y = 0$ and assuming no momentum transfer from the ambient gas flow to the liquid film at the interface $y = h$ (Neumann boundary condition), the film velocity can be written as a function of the distance from the wall y

$$u\left(y\right) = \frac{g}{\nu}\left(yh - \frac{1}{2}y^2\right). \tag{2.14}$$

From Eq. (2.14) the maximum velocity can be derived, when calculating the velocity at the film surface $y = h$. Utilizing the liquid flow rate in the cross section of the liquid film (used for example in Zhou et al. [166]), its thickness can be approximated according to

$$h = \sqrt[3]{\frac{3\nu^2}{g}\text{Re}} = \sqrt[3]{\frac{3\dot{V}\nu}{gb}}. \tag{2.15}$$

In the range of $3 < \text{Re} \leq 400$ the transition regime from laminar to turbulent film flow is characterized as wavy film regime. Small waves develop at the surface of the film, which is completely smooth in the laminar regime. Fast changes of the velocity are a further characteristic behavior of wavy liquid films. The film setup is based on two liquid layers, consisting of a basic laminar layer, with similar properties concerning thickness and velocity profile as for the case of laminar flow and a wavy layer, which is moving on top of the laminar basic layer [18]. The velocity profile for the wavy layer differs from the Nusselt solution.

The turbulent film flow regime $\text{Re} > 400$ is characterized by an increasing cross flow mixing and increased development of surface waves.

These modifications impact industrial application, especially in process engineering, since heat and mass transfer processes are primarily governed by the flow properties.

According to Brauer [18] the development of waves can be quantified using the Kapitza number Ka:

$$\mathrm{Ka} = \frac{\sigma}{g^{\frac{1}{3}} \nu^{\frac{4}{3}} \rho}. \tag{2.16}$$

An increase of this number indicates a more stable film and reveals that wave development and growth is more difficult.

Ishigai et al. [69] propose an almost similar discrimination of film flow regimes, adding two transitional regimes:

1. The pure laminar flow regime, where no wavy motion of the liquid film occurs is linked to $\mathrm{Re} < 0.47\,\mathrm{Ka}^{0.1}$.

2. It is followed by the first transitional regime in the range of $0.47\,\mathrm{Ka}^{0.1} < \mathrm{Re} < 2.2\,\mathrm{Ka}^{0.1}$.

3. The stable wavy film flow establishes at Re-numbers of $2.2\,\mathrm{Ka}^{0.1} < \mathrm{Re} < 75$.

4. The transition to fully turbulent film flow regime follows in the range of $75 < \mathrm{Re} < 400$.

5. Fully turbulent flow regime starts, in accordance with the summary of Ausner [9] with $\mathrm{Re} > 400$. The flow becomes of shear-flow type and the law of the wall is identical with that of the turbulent boundary layer.

Interesting illustrations and another summary of the different film flow regimes can be found in Al-Sibai [4] as well. Considering this work maximum film thickness can be calculated for the different regimes and film velocities. Thus, the correlations for estimating the film thickness can be checked for various applications. Note that all curves
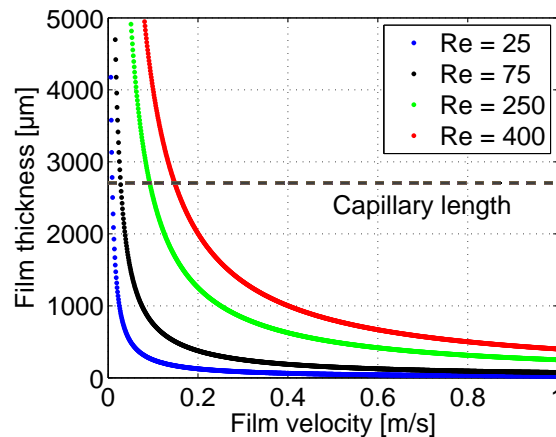

FIGURE 2.2: Maximum valid film thickness at different Re numbers following [4].

in Fig. 2.2 belong to the transitional flow regimes. Waves develop more significantly at higher Re numbers. For the case of smooth liquid films, the maximum film thickness would be very low, even for film velocities smaller than 0.1 ^{m}/s. Also shown in Fig. 2.2 is a dashed line, marking the capillary length that divides the inertia-dominated film flow regime (above the dashed line) from the surface tension dominated regime (below the dashed line). More information concerning liquid film stability, waviness and break-up of liquid films are given in the next sections.

2.2   Contact Angle, Contact Line and Wetting

The problem arising from no-slip condition at the contact line was briefly addressed during the description of hydrodynamics of free surface flows. More detailed considerations on this special topic are given here, since the wetting of solid surfaces due to liquid spreading is also of major interest in vehicle soiling situations. An example for the application of contact line forces (or contact angle forces) in film modeling was given by Meredith [103], who simulated the fire suppression by water film transport.

In the following the contact line force, the contact angle hysteresis and their effects on the flow behavior of liquid films will be discussed, mainly following the contribution of Šikalo et al. [156]. The definition of the static equilibrium contact angle θ_e, in the following also denoted as ECA, is given by Young's equation

$$\sigma \cos \theta_e = \sigma_{sv} - \sigma_{sl}, \tag{2.17}$$

where σ_{sv} and σ_{sl} are the surface tension between solid (s), vapor (v) and liquid (l). According to Šikalo et al. [156] θ_e can be considered as material property featuring a hysteresis behavior. Consequently, the static contact angle can vary between a maximum and a minimum, while the contact line stagnates at a certain position.

For static conditions and limited liquid volume, a lens-like shape is occupied by the liquid, which can be assumed to be geometrically described as calotte. Assuming this type of geometry, the static contact angle estimation for a given fluid-gas-material configuration is quite simple. Using imaging methods, the tangent to the liquid surface at the contact point with the solid has to be measured. However, this procedure depends strongly on the spatial resolution and is often inaccurate. Measuring the thickness of the calotte, which is simply a straight distance and then calculating the contact angle as illustrated in Figure 2.3, the procedure still depends on spatial resolution, but is much more accurate. Besides the geometrical assumption it is then necessary to realize an accurate measure
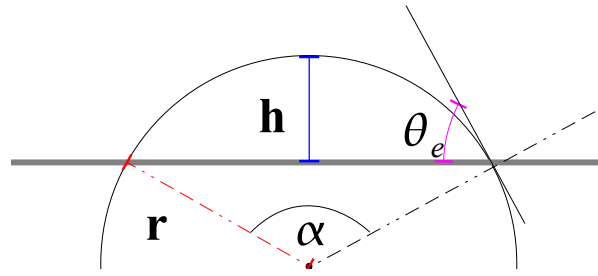
FIGURE 2.3: Contact angle estimation via predefined calotte volume

of the liquid volume, using for instance a micro-volume pipette. A detailed description of the calculation is given in Equation (2.18).

$$
\begin{aligned}
V &= h^2 \frac{\pi}{3} (3r - h) \\
h &= r (1 - \cos \theta_e) \\
\theta_e &= \arccos \left(1 - \frac{h}{r} \right)
\end{aligned}
\tag{2.18}
$$

The calculation starts with the estimation of r, which is the radius of the sphere associated to the calotte. Here, the injected volume V and the measured thickness h are required. During the next step, the equation for the calotte height can be used, to deduce an equation for the angle θ_e at the contact point, which is per definition the static contact angle. It is noteworthy, that this measurement procedure is limited by the capillary length which can be found for water to be around 2.7 mm. When h increases above that value, gravity becomes dominant and, due to hydrostatic pressure, the droplet spreads and the shape deviates from that of a calotte.

From preliminary experiments, the following results were obtained for the configuration of tap water and acrylic glass (see Figure 2.4). The single measurements vary between the correlation curves for contact angle of 60° and 70°. These values confirm those of Dhiman and Chandra [37], who found a contact value of around 71°. The high spatial resolution of 2.6 μm/pixel ensures the quality of the results, which is a difficult issue for contact angle measurement.

If the droplet moves in a certain direction, a change in contact angle values occurs, where the limits of ECA can be exceeded. The appearing contact angles are, at the front side, the advancing angle θ_a and at the back side, the receding angle θ_r, as depicted in Figure 2.5.

For moving interfaces a dynamic contact angle can be determined, where the Hoffmann-Voinov-Tanner law [62] describes the relation of the equilibrium contact angle and the
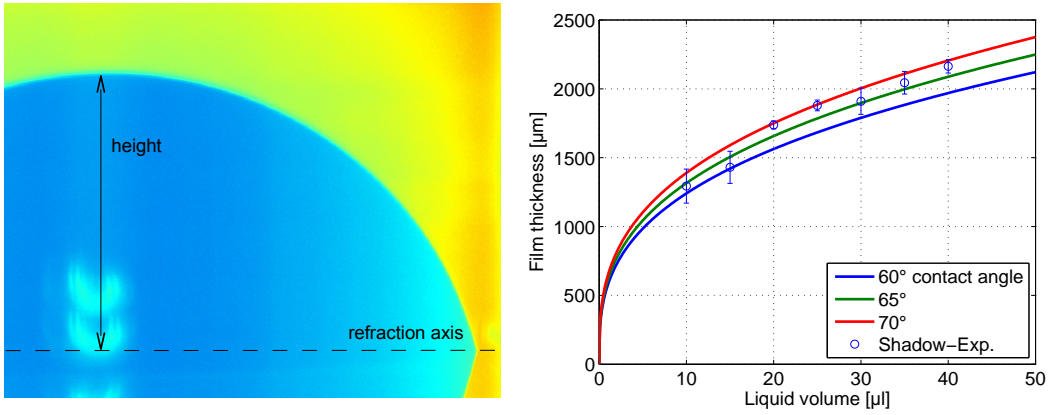
FIGURE 2.4: Own measurements for the film thickness of static calotte of tap water on acrylic glass; raw image (left), correlation (right)
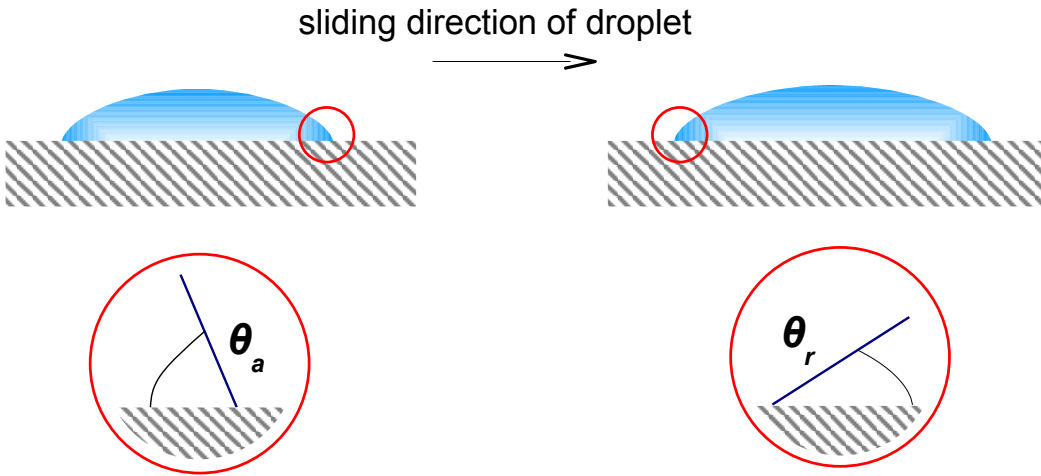

FIGURE 2.5: Advancing (left) and receding (right) contact angle

dynamic contact angle.

$$\theta_D^3 - \theta_e^3 \cong c_T \mathrm{Ca} \tag{2.19}$$

Here the Ca number is built with the velocity of the contact line in case of liquid spreading and c_T is a constant introduced by Hoffmann [62]. An explicit formulation for θ_D as function of the Ca was proposed as empirical correlation (Eq. (2.20)) by Jiang et al. [72], showing a good agreement with experimental data.

$$\frac{\cos \theta_e - \cos \theta_D}{\cos \theta_e + 1} = \tanh \left(4.96 \, \mathrm{Ca}^{0.702} \right) \tag{2.20}$$

The dynamic contact angle increases with the spreading velocity and asymptotically reaches a value of $180\,^\circ$ for Capillary number approaching unity and higher. This formalism is valid for the advancing contact or front angle of sliding droplets and rivulet. It is important to clarify this here, since the word 'spreading' indicates an expansion of

liquid mass in all directions. The receding contact angle decreases with increasing veloc-
ity, as observable at the thinning end of sliding droplets. To account for the propagation
direction of the contact line (advancing or receding) Eq. (2.19) is rewritten

$$\theta_D^3 \pm \theta_e^3 \cong c_T \text{Ca}, \tag{2.21}$$

as e.g. in [163].

2.3 Stability and Transition to Rivulets

Hydrodynamic stability is an issue of high complexity and of great importance in fluid
dynamics. The general idea is that a steady state solution of various problems can
become unstable due to small disturbances. Comparing hydrodynamic stability and the
transition of laminar to turbulent behavior of bounded flows with free a surface (such as
liquid films), one can observe that the critical Re number is three magnitudes smaller for
free surface flows. Thus, a liquid film flow is almost always associated with instabilities
leading to wave formation and break-up [6].

In the following the most important types of film instabilities and the transition of
continuous films to rivulets will be described. The latter process is often found as
characteristic form of rain water propagation along a vehicle surface.

2.3.1 Film Flow Instability

Ostrach and Koestel [120] summarized four main types of instabilities, occurring out of
interaction of inhomogeneous flows or due to processes taking place in a homogeneous
fluid. The Tollmien-Schlichting instability occurs at the transition of laminar to turbu-
lent state and can be associated with a Reynolds-number criterion, so it is an instability
of the latter type. The same holds for the Bénard-Marangoni instability, which arises
from density gradients within a fluid due to temperature gradients, associated to a crit-
ical Rayleigh-number. These two types are not considered any further, since they are of
small importance for isothermal liquid films at a fixed flow regime.

More interesting, because more significant for this study are Rayleigh-Taylor and Kelvin-
Helmholtz instabilities. They are the subject of the following brief analysis.

Rayleigh-Taylor Instability

Instabilities can be induced by external fields, in particular the gravitational field. The destabilization of a configuration where two semi-bounded fluid phases of different densities flow in layers, with the denser on top, is called Rayleigh-Taylor instability. Typical examples are wet paint on a ceiling or at the outer side of a pipe. When time goes on, the film separates into droplets, dangling from the supporting solid substrate. A noticable distance between the droplets indicates the regularity of the separation process. This type of instability is related to a density gradient between the two fluids (the color-suspension and air, when going back to the example of the painted ceiling).

An analysis of liquid film stability is based on the evaluation of the wave length of surface perturbations. Generally, the wave length is assumed to be large compared to the mean film thickness. It is defined according to de Gennes et al. [36] as:

$$\lambda = \frac{2\pi}{q},$$

(2.22)

where q is the wavevector. The wavevector has to be understood as a measure of unstable wave modes. For instability, the fastest growing mode is decisive and occurs at a critical value:

$$q^* = \frac{1}{\sqrt{2}} l_c^{-1},$$

(2.23)

where l_c is known as capillary length, defined as:

$$l_c = \sqrt{\frac{\sigma}{\rho g}}.$$

(2.24)

It is consequently a pure material parameter. As mentioned before, in the case of tap water, the capillary length takes a value of $l_c \cong 2.7$ mm. As can be seen from dimensional arguments in the capillary length, the Rayleigh-Taylor instability is a result of a competition between gravity and surface tension force.

Kelvin-Helmholtz Instability

This type of instability occurs when a relative motion of the two fluids is present and the interface is sheared. This effect is a consequence when the fluid is accelerated in parallel direction to the fluid interface. In contrast, the fluid is accelerated in perpendicular direction to the fluid interface for Rayleigh-Taylor instability. Details on hydrodynamic instability are described for instance in Chandrasekhar [26].

The Kelvin-Helmholtz instability can also be associated with a Richardson-number

$$\mathrm{Ri} = \frac{g\, l_{ch}}{u^2} \qquad (2.25)$$

criterion.

Here, the velocity of the lower medium is generally assumed lower than the upper fluid velocity or even zero, while the upper medium flows with a velocity of u_∞. This causes perturbations at the interface, which are called Kelvin-Helmholtz instabilities. In absence of gravitational perturbations, their critical length l_c takes following form [6]:

$$l_c = \frac{\sigma\left(\frac{1}{\rho_1} + \frac{1}{\rho_2}\right)}{u_\infty^2}, \qquad (2.26)$$

involving the density ρ_1 and ρ_2 of the two fluids. More detailed information are given in Ostrach and Koestel [120].

According to the Richardson criterion, Kelvin-Helmholtz instabilities are suppressed if the following condition is fulfilled [58]:

$$u_\infty^2 < 2\sqrt{g\sigma\left(\rho_1 - \rho_2\right)}\frac{\rho_1 + \rho_2}{\rho_1\rho_2} \qquad (2.27)$$

In the case of vehicle soiling due to rain both types of liquid film instability can occur and have to be taken into account.

2.3.2   Film-Rivulet Transition

The transition of a closed surface film to rivulets (i.e. small channels) was summarized in Ausner [9], where a detailed description of film separation correlations is provided. The film separation occurs, when the wetting rate decreases, such that the film flow is not continuous any more. Consequently, it separates and reveals dry patches of the solid surface. This phenomenon is expressed via the film Reynolds number, which falls below a critical value. According to Saber and El-Genk [133] and Hartley and Murgatroyd [57] the separation and break-up of a liquid film can be estimated by a force balance at the stagnation point, where the film separates. The critical Re number can be calculated from:

$$\mathrm{Re}_{crit} = 1.7\left(1 - \cos\theta\right)^{\frac{3}{5}} \mathrm{K}_f^{\frac{1}{5}}. \qquad (2.28)$$

Here, K_f is the dimensionless film number:

$$\mathrm{K}_f = \frac{\sigma^3}{g\nu^4\rho^3} \qquad (2.29)$$

and θ is the static contact angle. Note that the dimensionless film number is equivalent to the Kapitza number $\mathrm{K}_f = \mathrm{Ka}^3$. In Figure 2.6 the separation correlation and liquid-solid configurations are visualized. Here water-glass ($\theta \cong 5°$) and water-acrylic glass ($\theta \cong 60°$) were chosen exemplarily, since the contact angle values are known very well for these materials.
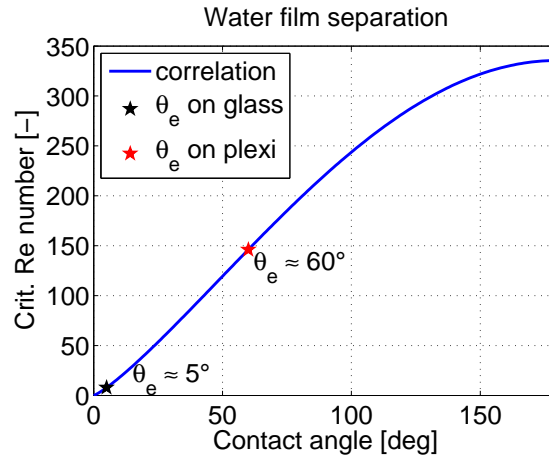

FIGURE 2.6: Separation correlation and liquid-solid configurations

Hence, it can be concluded that beside the material, the surface properties are decicive whether a film separates into rivulets or remains continuous. The most crucial factor is the contact angle, which can not be assumed constant for a given liquid-solid configuration, but underlies variations, depending on surface roughness, inclination and operating conditions. This means that one may observe different results for a given configuration, whether one approaches the point of interest in a decelerating or accelerating manner, due to hysteresis effects.

2.4   Film Interaction with Droplets and Sprays

The interaction of continuous liquid films with impinging single droplets and sprays is now analyzed, in particular concerning splashing, rebound and deposition. Decision parameters are needed, which show whether to use single drop-wall or spray-wall correlations. The idea for such a parameter is to correlate the drop-impact frequency with a characteristic film time or with the time duration of an impingement event. This parameter study should also finally support the decision in our project to use single drop-wall interaction models, although there is a spray impacting.

The interaction of droplets or sprays with walls is influenced by many aspects. The interaction type is governed primarily by droplet properties in terms of Reynolds number and Weber number, but is also a result of surface structure (rough or smooth) or surface
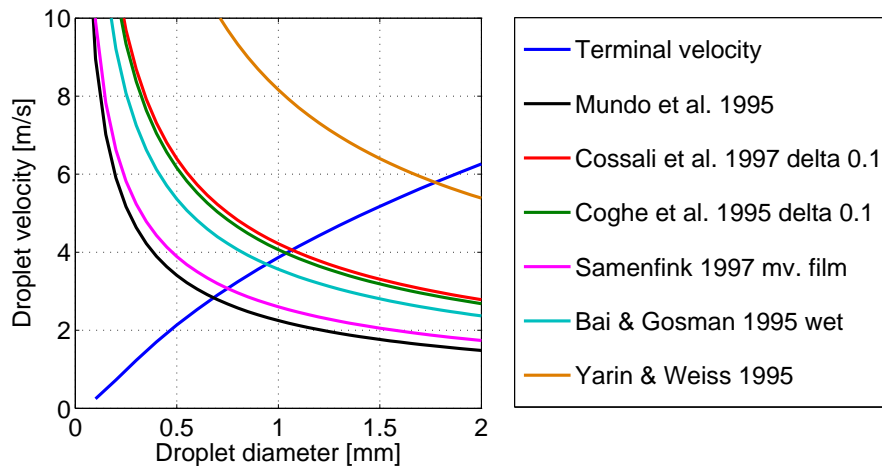
FIGURE 2.7: Terminal velocity vs. minimum velocity required to enforce splashing

temperature. The outcome of the interaction of dispersed liquid flow with walls is determind by the status of the wall (dry or wet), associated with hydrodynamics of the liquid film. Additionally, the direction of the wall (normal or inclined) compared to the incident liquid particles is of importance. As a result, the complexity of understanding and modeling these phenomena is obvious [32].

In this context the Reynolds number and the Weber number of the incident droplets are again of main interest and defined with the velocity normal to wall. Combining both dimensionless numbers, the Ohnesorge number Oh can be obtained, which is often used when dealing with sprays and spray-wall interaction.

The general spray/drop-wall interaction is extremely complex, see the contributions of Rein [130] or more recently Yarin [164]. But within these extensive review papers only few works are considering impact processes on thin liquid films, in particular on moving liquid films. A lot of research effort was spent on investigations of dry droplet impingement, e.g. by Mundo et al. [108, 109]. They defined a dimensionless splashing parameter K:

$$K = Oh \cdot Re^{1.25} \tag{2.30}$$

and observed an increase of splashed mass fraction with increasing splashing parameter.

Still, a few investigations of impingement of droplets on liquid films of various depths can be found. An early experimental contribution was made by Macklin and Metaxas [94] who investigated splashing of droplets of different aqueous solutions on shallow and deep films. Using an energy balance, the crown splashing was then characterized and deviations between experiments and theory were checked.

Also applying imaging techniques, Cossali et al. [29] analyzed the dry single drop impact. The focus of this contribution was especially on the transition of deposition to splashing. Furthermore, the morphology and dynamics of the crown in case of splashing were addressed in terms of PDF and correlations.

The contribution of Wang and Chen [157] can be interpreted as a complement to Cossali et al. [29], for splashing on even thinner liquid films, where the crown was found to be disappearing before starting to separate into single fingers. Even if the investigated films are very thin, an extrapolation of correlations for the transition from wet wall conditions to dry walls is prohibited.

A discrimination between prompt splashing and crown splashing was investigated in Vander Wal et al. [155]. These experiments showed, how the splashing threshold is shifted towards smaller values of K for wet conditions. The thickness of the preexisting film is important for onset and outcome of splashing.

Okawa et al. [115] carried out experiments using single water droplets. Another approach was presented to estimate the number and mass of secondary droplets generated by crown splashing.

A theoretical approach to predict the transition of deposition to splashing was proposed by Josserand and Zaleski [76]. The deposition criterion, previously found in experiments, was supported by their numerical simulation results.

The influence of drop impact (splashing parameter K) and film characteristics (non-dimensional film height δ) on the droplet impingement outcome was pointed out by all contributions. All publications considered impacts with moderate impact We-numbers, up to low four-digit values, at the difference of the present investigations of Brinkmann [20] with high impact We-numbers.

Particulary interesting for film flow aspects is the contribution of Samenfink et al. [135], who investigated droplet impingement on shear-driven liquid films. They found empirical correlations for secondary droplet characteristics, valid for a limited range of impact energy. Unfortunately the Laplace number:

$$\text{La} = \frac{\sigma \; \rho \; l_{ch}}{\mu^2} \tag{2.31}$$

is also limited to a valid range between $5000 < \text{La} < 20000$, implying a maximum droplet diameter of 280 μm for the material properties of water.

Extensive discussions of available models, correlations for the calculation of post-impingement characteristics and their limitations are found for instance in Horvat [64] and more recently in Mühlbauer [107]. Both authors went beyond the single droplet impact, investigating the multiple drop impact and the interaction of impingement events on each other and on the post-impingement characteristics of the droplets [77, 132, 160]. All these considerations and analyses lead to the following conclusions for drop-wall interaction:

- Empirical and semi-empirical correlations hold only for a narrow validation range.

- Most of them are limited to small droplet sizes, due to two facts:

  (i) Most applications deal with fuel injection in internal combustion engines.

  (ii) Measurements of small droplet diameters can be carried out with much higher accuracy, due to less droplet deformation.

- There is a lack of a general description and only limited correlations are available for large droplets.

- The scaling from single droplet-wall interaction to spray-wall interaction is prohibited, since the occurring phenomena differ significantly.

Many physical aspects influence the film flow and thus have to be taken into account when investigating vehicle soiling processes. The phenomena described in this chapter are considered in the different modeling approaches discussed next.

Chapter 3

Modeling Liquid Films

At the end of the present project, a validated model should be available for CFD analysis of film flows associated to vehicle soiling. For this purpose, the first step is to check the literature for existing models and to identify a promising strategy. Part of this chapter has been published in the *International Journal of Multiphase Flow* [54].

3.1 Film Modeling Approaches

Most interesting in vehicle soiling is the deposition of the spray and the motion of the liquid film on the outer surface of the car or geometry. Within the last 20 years different modeling approaches have been developed and used for predicting film flow dynamics. The approaches range from discrete Lagrangian models over continuous Eulerian film models to Volume Of Fluid (VOF) methods. The complexity and requirements of these simulation strategies therefore can be very different and are discussed in this chapter. In the beginning soiling simulation and comparisons of soiling pattern between wind tunnel or road tests and CFD were based on simple modeling approaches, like direct accumulation of droplets or dirt particles on the surface. The interaction with ambient flow fields or motion was not considered. Presently, two model approaches introduced first for the simulation of fuel injection systems, are used particularly often for vehicle soiling simulation: the discrete phase film model [118] and the continuous phase film model [10]. They will hence be considered in more details in this chapter.

3.1.1 Volume Of Fluid approach

The VOF method is particularly useful for model development, when details are studied. In this context the work of Tivert [146] has to be mentioned, where the break-up of

a rivulet is studied using VOF, with the aim to improve simpler film models. Most recently VOF was also used for liquid film simulations of vehicle soiling in Dietz [38]. Beside using the VOF method as single modeling approach, it is also considerd for hybrid film modeling approaches, which will be discussed later in the context of Eulerian film models.

The VOF method is an Eulerian method for the simulation of multiphase flows, mostly for separated fluid phases. Physics are described with one complete set of conservation equations. Additionally, a scalar transport equation for the volume fraction of each secondary phase is solved. To close the problem the volume fractions of all phases in each cell must sum to unity. Using the VOF method for the simulation of free-surface flows, in particular thin liquid films, one has to keep in mind that sharp interface capturing is only possible when coupling with front tracking methods, for example the level set method. VOF was used to predict interfaces and primary break-up of liquid jets in Ménard et al. [101]. Tivert [146] studied with VOF the break-up of rivulets, under the influence of shear stresses induced by an air flow.

There are other contributions using VOF for film flow simulations, but without capturing a sharp interface and mostly only for 2D applications. The automobile industry does not believe yet in a broad application of VOF for EWM studies, because of the high computational effort, mainly due to requirements for grid resolution. That is why two other film modeling approaches (discrete and continuous models), which are used presently for vehicle soiling simulation are reviewed in more detail in what follows.

3.1.2   Without Transport Model

The most basic method to investigate vehicle contamination is to simply let dirt particles and droplets stick to the surface of the car and then consider the following accumulation of mass sources as obtained from the Lagrangian tracking. It has been used extensively in initial studies. This basic approach, even if it neglects all transport and exchange processes along the vehicle surface, leads nevertheless to physically realistic soiling patterns, in particular when considering solid dirt deposition, as shown by Yoshida et al. [165]. Since the particles or droplets colliding with the surface are counted during the computation, a film or layer height can be estimated in a post-processing step considering the discretization area. Mass is correctly conserved in this model, while momentum of the impacting droplets or particles is completely lost, since all particles coming in contact with the wall or closer than a fixed threshold distance invariably stick onto the surface. As a consequence, this model does not account for any film velocity [165]. Recently, Gaylard and Duncan [48] investigated self soiling of various autmobile types, using the

information of deposition locality of droplets. The whole soiling simulation was part of the post-processing of an unsteady aerodynamic simulation. A Lagrangian particle tracking was carried out, based on the flow field solution of different time steps. The unsteady soiling patterns where approximated, by superimposing the calculated deposition of every time step. Hence, the dispersion effect of random turbulent fluctuations on the droplets is taken into account.

3.1.3   Discrete Phase Model

The discrete phase film model based on the wall film dynamic model of O'Rourke and Amsden [118] is often used for vehicle soiling simulation. Droplets from Lagrangian tracking impinge upon the surface and form a thin liquid film, which is still represented by discrete particles. The model accounts for mass, momentum and energy conservation and involves four physical phenomena: 1) the interaction during spray impact, 2) the subsequent tracking of wall-bound particles, 3) an estimation of chosen film variables and 4) the coupling to the gas phase. The main assumptions underlying this model will now be detailed.
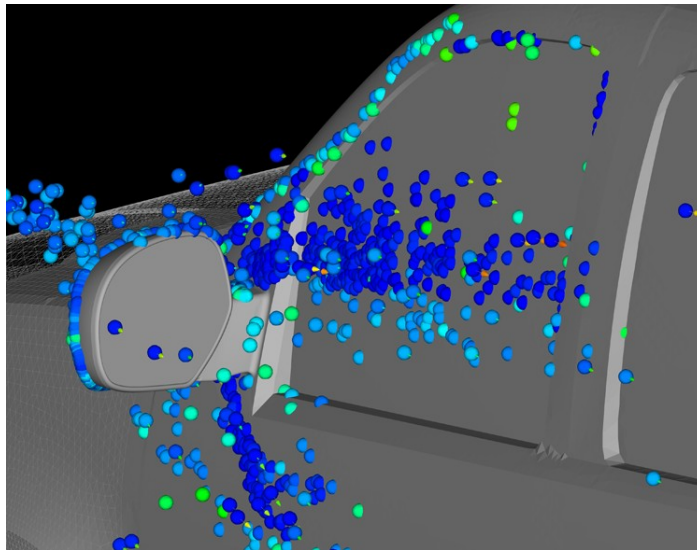

FIGURE 3.1: Free and wall-bound discrete particles in a vehicle soiling simulation using a Lagrangian frame for the dispersed phase and for the film model (by K. Karbon from Co. General Motors), reprinted with authorization from the author

For all thin film approximations, it is first assumed that the film thickness is much smaller than the characteristic geometrical size of the vehicle wall (radius of curvature). This assumption is valid for most surface areas of a car, but might break down at very sharp corners, for example at the trailing edge of the rear-view mirror. A second assumption is made by O'Rourke and Amsden [118]; that the liquid flow in the film is laminar and the velocity profile is linear. Further inertial forces and hydrostatic effects acting on the

film are assumed to be negligible and the air flow velocity above the film is assumed to be much larger than the film velocity.

For general film flow simulations, the thin film model is quite useful, but it leads to problems when film separation occurs. The original model allows film break-up only at sharp corners, where the assumption of a thin film breaks down. To account for film separation O'Rourke and Amsden [118] proposed a separation submodel based on an inertial criterion, but did not account for other destabilization mechanisms for the liquid film, e.g., unstable wave growth. Another challenge in film modeling concerns the numerical diffusion of sharp film edges, which can be reduced by dedicated modifications. One major drawback of the particle film model is the necessity of tracking all particles while keeping them attached to the wall as long as needed.

The governing equations are given next. A film mass conservation equation is not directly solved, since the particle film model automatically conserves film mass. It is only given here for the same reason as in [118], i.e., to specify useful notations for later discussion:

$$\frac{\partial (\rho_l h)}{\partial t} + \nabla_s \left[\rho_l \left(\bar{\mathbf{u}}_f - \mathbf{v}_w \right) h \right] = \dot{M} \tag{3.1}$$

The accumulation term consists of the liquid density ρ_l which is assumed as constant, the film thickness h and the time rate of change in the reference frame on the wall $\frac{\partial}{\partial t}$. The Nabla operator ∇_s is the surface gradient operator, while $\bar{\mathbf{u}}_f$ is the mean film velocity and $\mathbf{v}_w$ is the wall velocity. Mass sources $\dot{M}$ are distinguished into three different sources, due to impingement, due to re-entrainment and due to vaporization. Latter one is unimportant for soiling simulation, because the general use is isothermal flow and so heat and associated mass transfer phenomena are not accounted for. Impinging mass source per area is defined as integral mass of all spray droplets colliding with the wall, where the distribution properties of the spray is captured with f the time dependent spray droplet distribution function. In the revised description [119] this equation takes the form

$$\dot{M}_{imp} = \int \int \int \frac{4}{3} \pi r^3 \rho_l \mathbf{v} \cdot \mathbf{n} f \left(\mathbf{x}_s, \mathbf{v}, r, T_d, t \right) d\mathbf{v} dr dT_d. \tag{3.2}$$

All droplets colliding with the wall are assumed to become part of the wall film, which is shown with $\mathbf{n}$ the unit normal to the wall pointing towards the gas phase and $\mathbf{x}_s$, a point on the wall surface. Beside the mass the model conserves momentum, and O'Rourke and Amsden [118] introduce the following film momentum equation.

$$0 = \tau_g \mathbf{t} - \mu_l \left(\bar{T}_f \right) \frac{\bar{\mathbf{u}}_f - \mathbf{v}_w}{h/2} + \dot{\mathbf{P}}_{imp} - \left(\dot{\mathbf{P}}_{imp} \cdot \mathbf{n} \right) \mathbf{n} + \dot{M}_{imp} \left[\left(\mathbf{v}_w \cdot \mathbf{n} \right) \mathbf{n} - \bar{\mathbf{u}}_f \right] \tag{3.3}$$

Here τ_g represents the shear stress at the upper side of the film towards the gas and $\mathbf{t}$ is the unit tangent to the surface, thus parallel to $(\bar{\mathbf{u}}_l - \mathbf{v}_w)$. Other variables are μ_l the liquid viscosity, the mean film temperature $\bar{T}_f$ and $\dot{\mathbf{P}}_{imp}$ the momentum source due to impingement per area, which is specified as

$$\dot{\mathbf{P}}_{imp} = - \int \int \int \frac{4}{3}\pi r^3 \rho_l \mathbf{v}\mathbf{v} \cdot \mathbf{n} f\left(\mathbf{x}_s, \mathbf{v}, r, T_d, t\right) d\mathbf{v} dr dT_d \qquad (3.4)$$

Note the dyadic product $\mathbf{v}\mathbf{v}$ in Eq. (3.4), a tensor operation. The model assumptions are that the film velocity is defined by a balance of the shear stress forces on the top side of the film, viscous forces within the film arising from differences between mean film velocity and wall velocity and forces exerted by impinging droplets.

To derive Eq. (3.3) the product of the liquid film velocity $\mathbf{u}_l$ with the film mass is subtracted from the full film momentum equation and five additional assumptions have to be made. Terms for wall film inertia, pressure gradients, gravitational forces and changes in film velocity due to vaporization are neglected. Furthermore, the velocity profile within the film is assumed to vary linearly with the distance from the wall. All assumptions are valid for thin wall films, usually found in regions, where the boundary layer shear stress balances the viscous forces in the film.

For details on energy conservation, see O'Rourke and Amsden [118]. They are not given here, since the application of the discrete phase film model for soiling simulation purpose generally assumes an isothermal flow for gas and liquid phases. More important for soiling simulation is the separation of the wall film and the re-entrainment of droplets, what occurs in the case, where the film flows over sharp edges. The significance of an exact description of film separation and break-up is also discussed by Tivert [146] and Tivert et al. [147], who studied the break-up of liquid films at sharp edges experimentally and numerically. For a more detailed simulation they also applied the VOF approach together with a high resolution interface-capturing method and compared both results.

In their particle film model, O'Rourke and Amsden [118] introduce a separation criterion for sharp corners, which considers that the film stays in contact with the wall due to a pressure difference between the gas-side and the wall-side of the film. As long as the pressure at the wall-side of the film is lower than the gas-side pressure the film does not separate from the wall. The separation criterion can be written for a sharp corner geometry in the following way:

$$c_s \frac{\left[\rho_l \left(\bar{\mathbf{u}}_f - \mathbf{v}_w\right) \cdot t_1\right]^2 \sin\theta}{1 + \cos\theta} > p_g \qquad (3.5)$$

The constant c_s was found to yield best results for a value of 3, but depends on the pressure profile along the wall. O'Rourke and Amsden [118] also acknowledge that surface tension inhibits separation, but assume that it is negligible. Hence, it does not appear in the criterion equation. The film thickness and the shear stress are implicitly included in Eq. (3.5) in the mean film velocity. Consequently, they affect the criterion quadratically.

During the calculation large effort is spent to track all wall film particles. All particle properties are updated within 3 steps during each computational cycle. First, the mean film velocity is calculated by solving the film momentum equation (Eq. (3.4)). In the discretized formulation, the mean film velocity is a cell-face quantity. This means that particles in identical computational cells move with the same velocity. The calculation starts with the estimation of the impingement sources for mass, momentum and energy. Here, all spray particles are considered, which impinge upon the wall-face α. Afterwards the wall shear stress is calculated, as well as the vaporising mass (not relevant for soiling simulation) from the previous cycle. Finally, the film velocity can be calculated solving the following equation:

$$
\begin{aligned}
(\bar{\mathbf{u}}_f)_\alpha &= \left[(\tau_g)_\alpha (\mathbf{t})_\alpha + 2\frac{\mu_l (\bar{T}_\alpha)}{h_\alpha}\mathbf{v}_w + \left(\dot{\mathbf{P}}_{imp}\right)_\alpha - \left[\left(\dot{\mathbf{P}}_{imp}\right)_\alpha \cdot \mathbf{n}_\alpha\right]\mathbf{n}_\alpha \right. \\
&+ \left. \left(\dot{M}_{imp}\right)_\alpha [(\mathbf{v}_w\mathbf{n}_\alpha)\,\mathbf{n}_\alpha] \right] / \left[2\frac{\mu_l (\bar{T}_\alpha)}{h_\alpha} + \left(\dot{M}_{imp}\right)_\alpha \right]. \qquad (3.6)
\end{aligned}
$$

In the next step the film thickness can be obtained by knowing the number of particles located on one face. This allows to quantify the thickness of the liquid layer, by summing the volumes of all particles and dividing by the respective cell area.

Subsequently, the particle positions and indexes are updated. To calculate these particle properties, the mean film velocity estimated in the first step and the particle position at the previous time step are used. In the software KIVA, where the discrete phase film model was implemented first, the particle positions are defined by coordinates, allowing to localize the position within a computational cell. Information on wall-bound particles are not inevitably linked with information at the cell centers or at their edges. Logical coordinates enable the particles to reside anywhere in a computational cell. More details on this can be found in Amsden et al. [7].

The last step during a computational cycle is to calculate the particle volume and the particle temperature. Originally, an implicit formulation for the coupled heat and mass transfer approach was used. As mentioned before, film modeling in vehicle soiling simulation considers isothermal conditions for air as well as for the liquid. Hence, this step is excluded from the review.

The original particle model for wall films was proposed for application on port injection engines. O'Rourke and Amsden [119] were the first to improve the model and enable spray-wall interaction, especially splashing based on the experimental results of Mundo et al. [109]. These authors performed extensive experiments with various droplet materials and found that splashing occurs when a dimensionless parameter exceeds a critical value:

$$\text{K} = \text{Oh} \cdot \text{Re}^{1.25} \geq 57.7 \tag{3.7}$$

Regarding splashing some changes in the film momentum equation are necessary. First, there is the wall film inertia term, which is important near the impingement sites. Secondly, there is the wall film pressure gradient, which may cause the spreading of the wall film around impingement sites.

Neglecting those effects is valid for thin liquid films without spray-wall interaction. Otherwise the film momentum equation becomes:

$$\rho h \left(\frac{\partial \mathbf{u}_f}{\partial t} + \left[(\mathbf{u}_f - \mathbf{v}_w) \cdot \nabla_s \right] \mathbf{u}_f \right) + h \nabla_s p_f =$$

$$\tau_g \mathbf{t} - \mu_l \left(T_f \right) \frac{\mathbf{u}_f - \mathbf{v}_w}{h/2} + \left(\dot{\mathbf{P}}_{imp} \cdot \mathbf{n} \right) \mathbf{n}$$

$$+ \dot{M}_{imp} \left[(\mathbf{v}_w \cdot \mathbf{n}) \mathbf{n} - \mathbf{u_f} \right] + \delta p_f \mathbf{n} + \rho h \mathbf{g} \tag{3.8}$$

All variables are known from previous derivations, except p_f the film (impingement) pressure and δp_f the pressure difference across the film. O'Rourke and Amsden [119] consider p_f as mean film pressure and assume that the pressure arises completely from the impingement of the spray. Gas-side pressure as well as pressure due to surface tension are ignored in this consideration.

Owing to the changes in the film momentum equation some modifications occur in the numerical solution procedure. Contrary to the previous calculation of the film velocity, the velocity is now estimated for each individual film particle according to

$$
\begin{aligned}
\mathbf{u}_f^{n+1} &= \left[\frac{\rho h_\alpha}{\Delta t} \mathbf{u}_f^n + (\tau_g)_\alpha \, \mathbf{t}_\alpha + \frac{2\mu_l}{h_\alpha} \mathbf{v}_w + \mathbf{S}_\alpha \right. \\
&\quad - \left. \left(\frac{\rho h_\alpha}{\Delta t} \left(\mathbf{u}_f^n - \mathbf{v}_w \right) \cdot \mathbf{n}_\alpha + \mathbf{S}_\alpha \cdot \mathbf{n}_\alpha - \dot{M}_{imp,\alpha} \mathbf{v}_w \cdot \mathbf{n}_\alpha \right) \mathbf{n}_\alpha \right] \\
&\quad / \left[\frac{\rho h_\alpha}{\Delta t} + \frac{2\mu_l}{h_\alpha} + \dot{M}_{imp,\alpha} \right] .
\end{aligned} \tag{3.9}
$$

Besides shear forces from the gas side, the film flow is affected by body forces and splashing events from impinging spray. These major improvements permit more realistic modeling of liquid films for port injection engines. The resulting model becomes more

interesting for other film flow applications. Therefore, the improved particle film model was implemented in the KIVA code and in Fluent, where it is called discrete phase model (DPM) for wall films. It was used by Borg and Vevang [16] to simulate a film flow for vehicle soiling purposes. They also took into account the impingement phenomena in a simplified wall interaction model, using the same dimensionless formulation as used in Mundo et al. [109].

Another summary of the discrete phase film model in the context of vehicle soiling application was given by Björtin [12]. He shows that, if only the wall film height and its velocity are important, then the most important conservation equation is the particle momentum equation (Eq. (3.8)).

Although it is possible to apply the same model to describe injection in engines and vehicle soiling, the scales, boundary conditions and objectives differ considerably. Recognizing this fact, Kruse and Chen [82] tried to adapt the model more specifically for EWM. When redesigning the model, some elementary effects have been identified as particularly important. Therefore, the improved model should ultimately be able to:

1. distinguish between a dry and a wet surface, since different flow and impingement behavior are observed for their respective conditions;

2. lead to a mesh-independent particle representation;

3. better represent gas-liquid coupling through shear stress and dynamic pressure acting on a droplet adhering to a surface;

4. account for particle detachment from the wall, taking into account particle and wall properties;

5. account for accumulation of liquid (coalescence) in terms of a wall-particle collision model.

When including all these items, the finally obtained discrete phase film model appears to be well suited for film flow and vehicle soiling simulations, as shown by Kruse and Chen [82] after implementing the redesigned model in the WATER code at Opel AG. Most important from the effects described above and considered in many recent studies are the separation of particles from the wall (Point 4) and the wall-particle collisions (Point 1 and 5). For the first issue, three different scenarios can be identified: 1) no separation of the particle from the wall, 2) complete particle separation and 3) partial separation, where one particle separates from the wall and another one adheres to the surface. To decide whether a particle separates or sticks, the local wetting status has to be known, and the usual outcome is separation for a dry and adhesion for a wet surface.

This model is an attempt to describe resistance to liquid spread, which should depend on the hydrophobic properties of the wall surface. As further criterion for the separation, a modified Taylor Analogy Breakup (TAB) model was used, where the different forces that act on the particle are evaluated. The accelerations due to gravity, centrifugal forces and pressure jump, pointing from the surface, are compared with the acceleration due to surface force, which always points towards the wall. Depending on the dominant acceleration direction, the particles adhere or detach from the wall.

Wind tunnel experiments showed that particles are merging along the wall surface. This effect is also required for a realistic film flow model in vehicle soiling practice, and a corresponding modification was also included in the redesigned model by Kruse and Chen [82]. Even if this recent model appears particularly powerful and interesting for practical vehicle soiling simulations, some limitations remain. They are mostly inherent to the discrete approach and therefore, cannot be corrected. For instance, when liquid accumulates in puddles with a relatively high film thickness (compared to the boundary layer thickness or to the radius of curvature of the surface), all particle models fail, since the individual particles do not pile up and cannot alter the flow field boundaries. If such issues become important, it is necessary to switch toward a Eulerian representation (Fig. 3.2), as described next.

3.1.4 Continuous Phase Model

Almost simultaneously to the discrete film model described up to now, a continuous film model was proposed by Bai and Gosman [10]. It was again developed to model liquid films forming in fuel injection systems. Hence, several simplifying assumptions are similar to those described in the previous section. This model, first introduced by Bai and Gosman [10] takes full account of impinging droplet contributions to the film momentum equation, describes heat and mass transfer phenomena in the film and tracks its moving contact line and deforming interface.
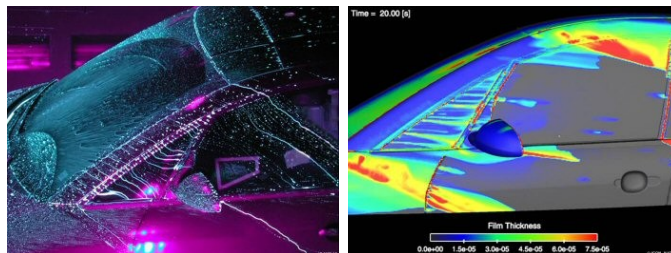

FIGURE 3.2: Soiling simulation using the Eulerian film model (right) and qualitative comparison with wind tunnel experiments (left) from Campos et al. [25]

Several assumptions have been used to derive the film transport equations. First, a laminar film is considered, possibly with waves at the surface, but thin enough to apply

a boundary layer approximation. To give some typical numbers, the maximum film thickness value found for engine applications is around 400 μm. A similar value is given by Stanton and Rutland [143], who also introduced a continuous film model. For such dimensions, the thin film assumption can be readily employed.

As a further assumption, the total pressure p_f in the film is considered as the sum of the impact pressures of the gas p_g and droplets p_d together with the capillary pressure p_σ arising from surface tension σ. Remember that the capillary pressure was neglected in the discrete particle film model. Following boundary layer assumptions, the local pressure within the film can be taken constant across the film depth and is everywhere equal to p_f. In the continuous phase film model it is further assumed that the tangential momentum source term is provided by the tangential momentum loss of the impinging droplets. The film motion is considered as driven by spatial variations of the total pressure p_f in the tangential direction, shear acting at the film interface, tangential momentum sources (as explained in the previous sentence) and additional body forces. The impinging mass flux is represented by a spatially varying function, which allows the application of conventional differential operations. Radiation and Dufour energy flux in the energy equation, as well as pressure and thermal diffusion fluxes in the species transport equations are considered negligible. The mixture of air and fuel vapor is assumed to behave as ideal gas and physical equilibrium prevails at the gas-film interface, while variations of thermodynamic properties in the liquid phase (except for latent heat) are negligible.

According to all these assumptions, the governing equations for wall films can be finally written in terms of conservation equations for mass, momentum and energy. The continuity equation in Cartesian coordinates reads simply:

$$\frac{\partial \rho}{\partial t} + \rho \nabla \cdot \mathbf{u} = Q_d, \tag{3.10}$$

with Q_d as source term due to droplet impingement. The momentum equation is given by

$$\frac{\partial \mathbf{u}}{\partial t} + \mathbf{u} \cdot \nabla \mathbf{u} = -\frac{1}{\rho} \nabla p + \mathbf{g} + \nu \nabla^2 \mathbf{u} + \frac{\mathbf{S}_d}{\rho} \tag{3.11}$$

where $\mathbf{S}_d$ are momentum sources from tangential momentum transfer of impinging droplets. To solve these equations, boundary conditions are necessary. Wall boundary conditions impose no slip condition

$$u = v = w = 0 \tag{3.12}$$

and the reduced momentum equations at the wall become in the steady case:

$$-\frac{1}{\rho}\nabla p_f + \mathbf{g} + \nu\nabla^2\mathbf{u} + \frac{\mathbf{S}_d}{\rho} = 0 \qquad (3.13)$$

Note that the contact line is excluded from these boundary conditions. Further information are necessary for the free surface, where the velocity is unknown. It is clear that other predefined conditions for the velocity have to be provided for solving these equation. In particular the velocity profile over the film depth has to be specified. Linear or parabolic profiles are commonly used in these approaches [150].

Bai and Gosman [10] validated the model against several experimental results and found good agreement. Nevertheless, they also recognized model limitations concerning for instance the influence of turbulence and droplet entrainment by the gas flow. Based on this original background, a number of derived models have been developed, in particular to apply similar ideas for vehicle soiling simulation.

The first application of the continuous film model for vehicle soiling has been reported by Karbon and Longman [79]. The original model was implemented without any specific adaptation in version 2.3 of the commercial CFD software StarCD. The authors concluded in particular that droplet splashing is a critical issue that should be implemented in future versions.

A more recent application of the continuous film model was proposed by Campos et al. [24]. The previously mentioned improvements have been implemented as default or by user-subroutines to cover phenomena occurring during the soiling process. The improved model accounts for:

- transport of droplets in the continuum including break-up and coalescence due to collision;

- spray-wall interaction in terms of droplet spreading, bouncing and splashing;

- liquid film transportation along the vehicle surface due to gravity, shear or pressure gradient effects;

- droplet re-entrainment or stripping into the continuum due to sharp edges or film instability.

Film stripping and droplet reentrainment are still the subject of present research projects. The film instability model implemented in StarCD assumes stripping of the liquid film due to waves generated by the adjacent gas flow (Kelvin-Helmholtz instability) at the gas-liquid interface. Waves can grow and become unstable, which leads to the ejection

of a cylinder of liquid into the gas phase. In its further evolution, the cylinder breaks up into spherical droplets according to a correlation based on the Rayleigh-Taylor instability. To close the model, the radii of the resulting droplets are calculated as a function of the instability wavelength. The model derived by Campos et al. [24] still considers only one-way coupling of film and gas flow. Similar to all other film modeling approaches, the gas flow remains unaffected by the presence of the film. Although models for more complex simulations can be found in the literature (e.g., two-way coupling for LES simulations), they have not been considered essential for industrial vehicle soiling applications up to now.

Another modeling approach in Eulerian reference frame was proposed by Morud [105] in 2007. It is based on two-dimensional transport equations for films on surface cells. It is coupled with an Eulerian transport equation for the droplets, comparable to the approach of Yoshida et al. [165] for solid dirt particles. The model accounts for interaction of film and droplets in the bulk gas phase. In particular, deposition and re-entrainment are captured. Kelvin-Helmholtz instabilities are the driving force for liquid film atomization, while the rate of deposition is derived from the droplet concentration near the wall. The model has been implemented in the CFD software Fluent via user defined functions (UDF) and tested for a horizontal pipe flow with small droplets. To improve the model Morud [105] suggested to use methods describing the droplet size distribution, like the quadrature method of moments (QMOM).

3.1.4.1 Hybrid Models

A special issue is the use of hybrid modeling approaches, which combine for instance common Eulerian approaches and VOF methodology for film flow situations, where the thickness of the film increases above the critical value so that the thin film assumption breaks down. Then, hydrostatic effects become important. In practice, there is a clear separation between these cases. Therefore, a switch should be defined between the Eulerian and the VOF. Since inertia and hydrostatic forces are not negligible any more, the local film velocity deviates from the prescribed velocity profile. To my knowledge vehicle soiling simulations relying on a hybrid model have not been published yet.

3.2 Improvements of Anderson's Film Model

A different approach based again on a continuous film modeling (see Section 3.1.4) was proposed by Anderson and Coughlan [8] from Fluent Europe Ltd. This was retained as the starting point for the present project. Based on the original formulation, the

model has been improved and adapted, as will be shown in the following, starting with a general presentation of the model.

The film model of Anderson and Coughlan [8] is a 2D model for 3D applications and was originally formulated for water condensation from wet air flows at cold walls. A mass source term from impinging droplets to the film was implemented together with a simple criterion for film separation. The underlying assumptions are similar to the models described previously, but the governing equations have been further simplified. The first equation consists of a transformed continuity equation, which acts as conservation equation for the film thickness h. Assuming an incompressible fluid and integrating over the film height, it is possible to reduce the mass conservation equation to a conservation equation of the film height:

$$\frac{\partial h}{\partial t} + \frac{\partial \left(h \bar{u}_i \right)}{\partial x_i} = \frac{S_{in} - S_{out}}{\rho_l A}. \tag{3.14}$$

Instead of a momentum equation, an analytical expression for the velocity is implemented based on the Nusselt approximation [112]. This equation is exact for the laminar, smooth film flow regime $\mathrm{Re} \leq 3$ described in Section 2.1.1. Consequently, Eq. (3.14) can be solved explicitly, when the mean laminar film velocity $\bar{u}_{il}$ is known.

$$\bar{u}_{il} = \frac{h}{6\mu_l} \left[2h \left(\rho_l g_{iII} - \left(\frac{\mathrm{d}p}{\mathrm{d}x_i} \right) \right)_w + 3\tau_{iw} \right] \tag{3.15}$$

On the right hand side of Eq. (3.15) the gravity force parallel to the wall g_{iII} as well as the pressure gradient at the wall $\left(\frac{\mathrm{d}p}{\mathrm{d}x_i} \right)_w$ can be found to induce parabolic velocity profiles. Also on the right hand side, the shear forces τ_{iw} induce linear velocity profiles. Assuming a superposition of both types of velocity profiles, the calculation of fluxes for the mean film velocity becomes possible.

Using such a velocity representation, the model does not account for momentum conservation, and the momentum transfer from impinging droplets to the film is also not included. Though being criticized over and over again, this is actually the only possibility to obtain an analytical solution. According to Malamataris et al. [95] it is a common method to model streamwise velocity distribution of film flows, also at high Re numbers.

Break-up Submodel

Film break-up is included in the original model. The break-up criterion is based on a film Weber number, similar to that mentioned before during the description of the discrete particle film model. Droplets are released from the film when the film Weber

number

$$\text{We}_f = \frac{\rho_l h u_s^2}{\sigma}, \tag{3.16}$$

composed of liquid density ρ_l, film surface tension of the liquid towards the gas σ, surface velocity of the film u_s and the film thickness h exceeds the critical value. A value of $\text{We}_{crit} \approx 10$ was proposed by Anderson and Coughlan [8] to yield qualitatively good results. The separated droplets take diameter values equal to the film depth present at their respective location of release. Their mass is modeled by solving

$$\dot{m} = \frac{K \rho_l h \left(\text{We}_f - \text{We}_{crit}\right)}{\text{We}_{crit}}, \tag{3.17}$$

where K is a model constant with a unit of squared meters per second and a value of unity. Due to this criterion for released mass, the film thickness is limited automatically. Therefore, a numerical limitation is unnecessary.

A recent contribution to continuous film modeling is given in Björtin [12], where an identical film model formulation is used. The main difference between both approaches appears when handling the film separation and break-up. As in other applications a Weber number criterion for the liquid film was implemented, considering separation, when a critical value is exceeded. Here, a value of $\text{We}_{c,sep} = 928$ was used, which was experimentally found by Lafuente [85]. It is the average value of experimental results at free stream velocities of 11 and 25 m/s, where for increasing free stream velocities, the critical separation Weber number tends to increase as well. The separation Weber number is defined as

$$\text{We}_{sep} = \frac{\rho_l D_{sep}^3 \tau_w^2}{\sigma \mu^2}, \tag{3.18}$$

with

$$D_{sep} = 2 \left(\frac{3}{4\pi} h A\right)^{\frac{1}{3}}. \tag{3.19}$$

Using this criterion the location within the film is known, where liquid detaches from the wall. However, no information concerning the diameter of the respective droplets is available. A break-up criterion is used to specify the droplet diameter after separation, based on the common formulation of the Weber number, denoted as We_{break}

$$\text{We}_{break} = \frac{\rho_g D_{sep} \left(v_g - u_f\right)^2}{\sigma}. \tag{3.20}$$

A critical mean value for break-up of $\text{We}_{c,break} = 18$ was also found by Lafuente [85]. After determining the separation and size of the released droplet, the release point was set to half of its diameter normal to the cell.

Overall, recent research projects investigating separation criteria or splashing parameters

demonstrate that existing models fail to predict real physics. It shows the need for further research activity, as concluded in many publications dealing with vehicle soiling simulation [16, 24, 46, 82].

3.2.1 Discretization and Model Algorithm

The transformed mass conservation equation was defined in Eq. (3.14) and is already given in an integral form. To deduce this equation, the continuity equation was first integrated over the film thickness and then divided by the density, which is possible for incompressible fluids. Finally one has to divide by the face area, to obtain Eq. (3.14) in the presented form. Foucart et al. [47] described the process of model reformulation and discretization in more details. They considered full conservation of mass, momentum and energy. On the contrary, the model of Anderson and Coughlan [8] uses an analytical solution for the mean film velocity, based on the solution of Nusselt [112].

For the present case, the convective term is solved explicitly without any iteration. Therefore, the convective term is discretized in terms of flux calculation over the edges of each surface cell. The computed flux value together with values from droplet impingement and film break-up are added to the source term. The explicit solution for the film thickness calculation is described in the following, using the schematic of Fig. 3.3.

Initially, the film thickness is zero everywhere on the surface, which means that all convective terms (corresponding fluxes) are equal to zero in each surface cell. Other source terms are calculated before the first film simulation step.

The source terms from droplet impingement are linked locally to impingement spots, which are the results of the discrete phase simulation. When a droplet track contacts the wall, an impingement source term is defined according to the spray-wall interaction model.

The film break-up source terms depend on the fulfillment of the break-up criterion. Film break-up means reduction of liquid volume in a certain surface cell, hence a negative source term is set to a respective value.

In the following the single steps of the model algorithm and calculation of source and sink terms are explained in every detail.

1. At first the Lagrangian particle tracking is performed for all injected or ejected particles. It can run by one-way or two-way coupling between the flow field and the particles. A **deposition source term** is specified in a certain surface cell from droplet-wall interaction data, in particular the impingement location and
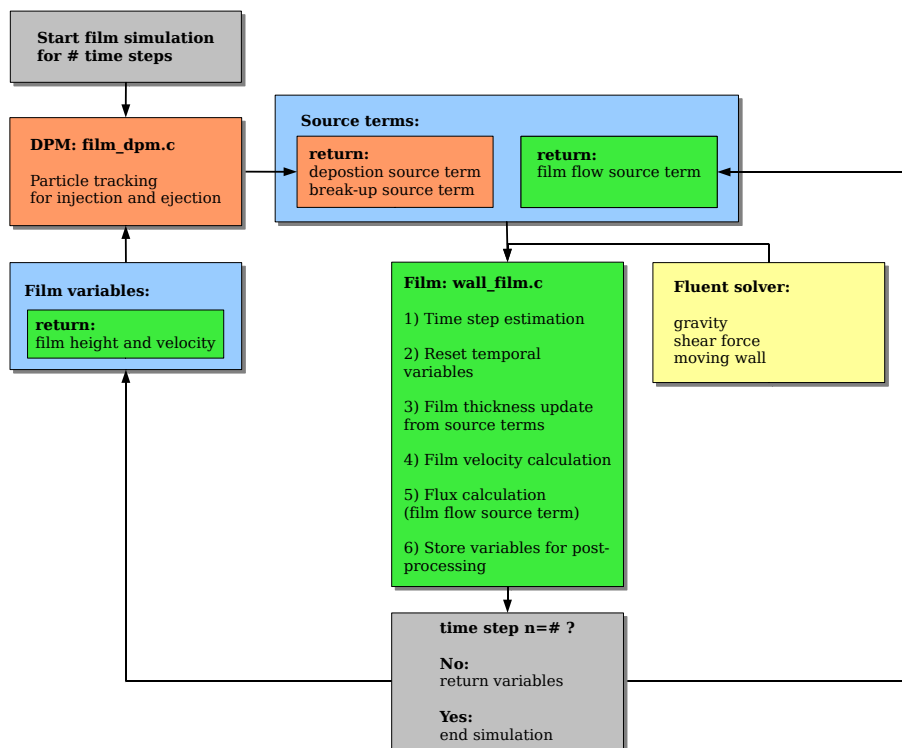
FIGURE 3.3: Film model algorithm as block diagram

mass transfer rate. The estimation of the impingement sources runs in loop over all impinging particles and surface cells. Thus, the overall liquid volume is known and the film thickness can be analyzed.

2. Subsequently, the algorithm verifies, if there is any film instability leading to break-up. If the break-up criterion is fulfilled the local film thickness value is reduced by the corresponding amount of liquid as **break-up sink term**. Meanwhile it is stored and then ejected as newly generated particle in the next particle tracking step. Both algorithm steps are implemented via the *film_dpm.c* and called by the DPM multiphase model of Fluent. The following steps are implemented via the *wall_film.c*. The complete implementation structure is described in Section 3.2.2.

3. The **film time step** is calculated during an intermediate step, based on Courant criterion with respect to the film velocity of the previous time step and the smallest cell edge length. This is the last usage of all temporal film variables, which are then reset for the actual modeling step.

4. Next step is to update the film thickness value in all cells. The new film thickness is calculated from previously calculated **film flow source term**, **deposition source term** and **break-up sink term**. It is also checked, whether any user defined thickness limitation is violated. In that case, the amount of liquid mass exceeding the limit is numerically removed from the calculation. This step was implemented

to control unrealistic film thickness values. To be completely accurate, assumptions for film velocity profiles are only valid for the laminar film flow regime. This special topic is addressed in Section 3.2.4 later on. For the present case the film thickness limit was set to a value of 3 mm which seems unnaturally high for liquid films. Here, one has to keep in mind, that the simulation, as well as real rain processes never yield continuous mass sources to feed a homogeneous film. Expecting sliding droplets and rivulets to form, this value is well suited for the actual problem of vehicle soiling simulation.

5. The film flow velocity is calculated based on the film thickness values from the previous step. Here the algebraic equation for film velocity is solved, accounting for driving forces from gravity and shear stress. At first the film surface velocity is calculated. Then, specific velocity profiles are assumed across the film depth. These provide mean velocity values when averaging over the film thickness. As known from Nusselt solution, gravity yields a parabolic profile, while shear stress gives a linear velocity profile. All velocity contributions are combined by superposition to **obtain the final film velocity in every cell**. Since the film model is coupled to a specific surface domain, the film motion is always tangential to the surface and the velocity is splitted into normal components to the cell edges.

6. A simple flux estimation is possible from the mean film velocity normal to a cell edge and the local film thickness. It gives the **film flow source term** over an edge from one cell to another. A loop over all cells is necessary to account for the complete film motion. These values are stored for the film thickness calculation in the next time step.

The algorithm is visualized as block diagram in Figure 3.3 and a typical protocol is given in Appendix A, where all dumps can be followed chronologically.

3.2.2   Implementation

The film model described before, was implemented in the commercial CFD software Fluent via UDF. Information about how to set up and compile UDF in general can be found in Fluent UDF manual. For this special UDF several h-files

- edges.h

- film_dpm.h

- h2o_props.h

- list.h

- rp_defined.h

- surface_facet.h

- wall_film.h

and c-files

- edges.c

- film_dpm.c

- list.c

- surface_facet.c

- wall_film.c

are necessary for constitution. They define functions, variables, boundary conditions for the film model and specify the calculation procedure of the film physics. Most relevant for the film physics and core of the UDF are the film_dpm.c and the wall_film.c, where all equations were implemented in discretized form. In addition to these 12 files a scheme file exists, which is used to generate a graphical user interface. In that manner the user can specify model parameters from the command tree. In the wall film panel the user can change model and solution parameters, such as critical Weber number, limit for film depth and surface tension but also the under relaxation for the film depth or the Courant number for time step estimation.

3.2.3   Improvements

After reviewing the modeling details of the original model formulation, aspects for possible improvements are quite obvious. The main goal is to improve model details, for example to include momentum transfer and droplet-film interaction dynamics. Besides, it would also be useful, to keep the model as simple and the simulation effort as low as possible. With both aspects in mind, the model was extended and adapted at selected points, most valuable for film flow physics. In particular, there are four objectives which have been taken into account:

- The interaction of the dispersed droplet phase with the wall and the wall-bound film has to be improved in the model. Especially the momentum transfer from

impinging droplets to the film is essential when computing film velocity. Also important in this context is the ratio of deposited and splashed liquid mass, so that the generation of secondary droplets has to be considered to ensure of mass conservation. In the following it will be addressed as droplet-wall interaction, where the wall may be both, dry or wet.

- Liquid film flows are known to be affected very much by surface forces. This becomes even more dominating, if the film only partially covers the substrate. It is desireable to account for liquid compression due to surface tension force and to limit the wetting behavior of the film.

- Although the thin-film-assumption considers hydrostatic effects to be negligible, it might be of interest in this work. Liquid films occurring in vehicle soiling may accumulate to larger thicknesses (several mm). Due to differing film heights in neighboring surface cells pressure gradients may occur. These gradients act like driving forces on the liquid film and may influence the film expansion. Moreover, this driving force depends on the surface orientation. Film separation can be better captured when including pressure gradient effects, as will be shown later.

- The film break-up is an unresolved issue often mentioned in film modeling. Although there is a break-up model implemented in Andersons film model, a physically reasonable approach is needed to replace this. Based on stability analysis the new model accounts for Kelvin-Helmholtz and Rayleigh-Taylor instabilities.

All details of the new submodels are described in the following including physical background of related publications and implementation procedure, as well as working principles in the model.

Complex Droplet-Wall Interaction

The droplet-wall interaction calculation is based on empirical correlations valid for single droplet impact. Although the process is considered as spray-wall interaction, where impact events influence each other, this assumption is justified as is shown in the following.

The idea behind the following consideration is, that the complex process of multiple droplet impingement can be simplified as single droplet-wall interaction. This is possible when the droplet impacts are temporally or spatially separated. It is a reasonable assumption, when there is enough time for the liquid film to relax after an impact to undisturbed, 'initial' conditions. Two principles exist that can be used to describe this time estimation. The first one is based on the characteristic impact time which is defined

according to [94, 164] as:

$$\tau = \frac{d}{v},$$
(3.21)

where d is the droplet dimension and v represents the impact velocity normal to the solid surface. The time value defined here, yields the required time for a droplet to pass a distance equal to its diameter or in other words it completely merges with the liquid film existing on the surface. On the other hand there is an impingement frequency f which specifies the rate of droplet impact events per unit time (#/s). Obviously it is directly linked to the concentration of droplets in the vicinity of the wall and the direction towards which they are moving.

When spray impinges onto a wall it can be considered as single droplet impingement as long as, the impingement frequency is lower than the inverse of the characteristic impact time.

$$f \leq \frac{1}{\tau}$$
(3.22)

This first principle is an approved, but rough time estimate. The film and its variations are excluded from the consideration.

It would be more precise, to base the estimation upon a different characteristic time. This can be for example the value for the impingement life time or the duration of a process that flattens the film surface after an impact in a narrow area.

Based on Sivakumar and Tropea [140] and Kuhlman et al. [83] an estimate for the life time of a crater, generated by one impinging droplet can be given as follows.

The generation of a crater to its maximum extent takes a time t_{cg}. Experimental results of Sivakumar and Tropea [140] confirmed that the crater-generation time t_{cg} correlates with the characteristic impact time τ in the way of

$$t_{cg} = 12.5\tau.$$
(3.23)

After extending to a maximum crater diameter, which is assumed to be equal to five times the droplet diameter the crater starts to shrink [83, 140]. Capillary waves are assumed to fill existing craters if body forces are negligible. The characteristic velocity of a capillary wave U is calculated from:

$$U = \sqrt{\frac{\sigma}{\rho \bar{h}_f}}.$$
(3.24)

The time to fill the crater and therefore, rebuild a flat film surface is derived from the wave velocity and the size of the crater d_c

$$t_{cf} = \frac{d_c}{U}.$$ (3.25)

Finally the total life time is the sum of the times needed for generating the crater and closing the crater

$$t_{lt} = t_{cg} + t_{cf}.$$ (3.26)

Comparing the inverse life time of a single crater with the local impingement frequency is a more precise estimate for the type of impingement process.

In the present case the outcome of droplet-wall interaction was modeled, using the empirical correlations of Mundo et al. [109] for dry and of O'Rourke and Amsden [119] for wet wall conditions, as specified in Table 3.1. The droplet-wall interaction regime is dictated by the impact energy. In case of splashing it can be described as a partial mass transfer from primary droplets to the film. The modification compared to the original model is rather simple, since a trap boundary condition is already implemented. Associated with a threshold value (Table 3.1) the extended model switches the boundary condition from 'trap' to 'reflect' when splashing occurs. The reflection conditions are now suitably adapted. Discrimination between dry and wet impact is possible by considering the local instantaneous film thickness h_f on the impacted surface cell.

TABLE 3.1: Correlations for post-impingement characteristics.

Quantity	Mundo et al. [109]	O'Rourke and Amsden [119]
Wall condition	dry, $h_f = 0$	wet, $h_f > 0$
Splashing parameter	$K = Oh\,Re^{1.25}$	$K^2 = \frac{u^2 \cdot d\rho}{\sigma}\left(\min(\delta,1) + \frac{1}{\sqrt{Re}}\right)^{-1}$
Limitation	$57.7 < K < 180$	$3329 < K^2 < 32400$
Mass fraction	$\frac{m_a}{m_b} = 1 - \frac{n_a}{n_b}\left(\frac{d_a}{d_b}\right)^3$	$\frac{m_a}{m_b} = 1.8 \cdot 10^{-4} \cdot (K^2 - K_{crit}^2)$, for $K_{crit}^2 < K^2 < 7500$ $\frac{m_a}{m_b} = 0.75$ for $K^2 > 7500$
Secondary droplet size	$\frac{d_a}{d_b} = \min(8.72\exp(-0.0281 \cdot K), 1)$ d_a, mean diameter	$\frac{d_{max}}{d_b} = \max\left(\frac{K_{crit}^2}{K^2}, \frac{6.4}{We}, 0.06\right)$ d_{max}, maximum diameter of Nukiyama distribution
Number of secondary droplets	$\frac{n_a}{n_b} = 1.676 \cdot 10^{-5} \cdot K^{2.539}$	$n_a = \frac{m_a}{\left(\frac{16}{3}\sqrt{\pi}\cdot\rho\cdot\left(\frac{d_{max}}{2}\right)^2\right)}$

As pointed out in Table 3.1, the kinetic properties of the secondary droplets are derived in a different way. Simplifying assumptions are made for the calculation of secondary droplet velocity, based on several considerations. First, it is complex to measure secondary droplet velocity with high accuracy, as mentioned for instance by Matysiak [100]. Furthermore, small secondary droplets respond very fast to the ambient air flow. The decision to simply apply a reflection condition for the velocity (inverted normal velocity and unchanged tangential impact velocity component) seems reasonable. Assuming this in general is questionable, for instance for ambient air at rest, as shown by Mühlbauer [107]. However, it is in physical agreement with averaged results for kinetic properties of secondary droplets in the case of normal and oblique impacts. It is known from experimental investigations that impact without tangential velocity component (normal impact) results in symmetrical crown formation. Therefore, the averaged tangential velocity of all splashed droplets is zero. The center of the liquid mass is simply reflected from the wall. Oblique impact also results in crown formation, but the leading rim rises much higher and so the droplets splashed to this side have much higher velocities. In this case the center of mass moves with a tangential velocity directed towards the leading side of the crown.
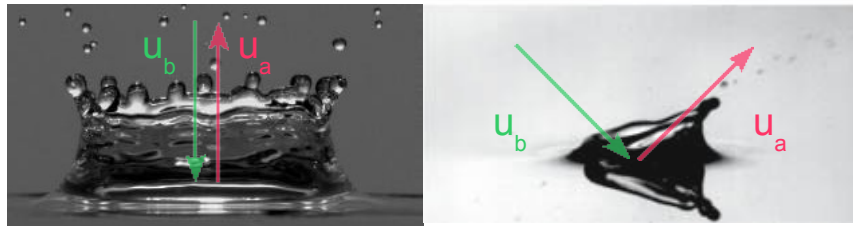
FIGURE 3.4: Velocity vectors prior and after splashing for normal [28] and oblique droplet impact [116]

In order to include momentum transfer from the dispersed liquid phase to the continuous liquid phase, a simple momentum balance is used. Summing up the momentum of secondary droplets and the film must equal the momentum of an impinging droplet. The momentum of the impinging droplet is obtained from the tangential velocity and the incoming flow rate of the impinging parcel. Secondary droplet momentum is computed as the outgoing flow rate multiplied by the tangential velocity. These properties are based on the correlations described previously. The tangential velocity u_{t0} of primary and secondary droplets is equal for 'reflect' boundary conditions. Hence, the transferred momentum is proportional to the deposited mass and the relative velocity between the impinging droplet and the film (u_{f0} initial film velocity).

$$u_f = \frac{m_{dep}}{m_f} \left(u_{t0} - u_{f0} \right) \tag{3.27}$$

The induced film velocity is superimposed with the mean film velocity from gravity and shear stress (see Eq. (3.15)), leading to the film mean velocity.

All changes have been implemented at selected locations of the film_dpm and wall_film c-files. All modifications of the model are reported already in Hagemeier and Thévenin [55].

Wetting Phenomenon and Contact Line Motion

Further improvement of the model have to be made, when considering the flow dynamics of isolated droplets and rivulets that definitely occur in vehicle soiling. For these situations a three-phase line appears between the wall area covered with liquid and dry substrate. This phenomenon is crucial also when solving complete Navier-Stokes equations for the film, since the no-slip condition at the wall enforces a non integrable singularity as stated for example by O'Brien and Schwartz [114]. Different approaches are available for models involving all details of surface flows. This is different for models as simple as the present one. Obviously, deriving an improvement is very challenging.

The idea is to specify a minimum velocity, for liquid mass transport from a wetted to dry surface cell. This formulation is similar to the transition of meniscus regime to film regime, as described by de Gennes et al. [36]. It is assumed that no meniscus or contact line can exist, if the local film velocity is higher than 0.2 mm/s for water. This last value depends on material and surface properties.

From the correlation discussed in Section 2.3 a criterion for the wetting of dry surface areas by the liquid film may be obtained, which can be utilized in the film model of Anderson and Coughlan [8]. The decision whether the neighboring surface cells will be wetted or remain dry is based on a force balance along the contact line of liquid, solid and gas.

The contribution of Penn et al. [122] illustrates how a force balance works at a stagnation point of a liquid film, where a dry patch is initiated. They consider four forces (liquid inertia, gravity, surface tension and shear force) for their dry patch model, which describes whether a dry patch within a film area stays dry or becomes wet. Without showing details of the derivation, the force balance equation takes the following form for a vertically flowing liquid film:

$$\frac{1}{6}\rho_l \delta u_i^2 + \frac{1}{2} l_\lambda \tau_{gl} = \rho_l g \delta l_\lambda + \sigma(1 - \cos\theta). \tag{3.28}$$

Except for l_λ all variables are known. The l_λ represents the characteristic length over which force imbalances occur. Quantifying this value is usually the crucial point in balancing the forces. Murgatroyd [111] determined this value from an empirical correlation, to fit his experimental data. An averaged value for l_λ is given in Penn et al. [122], depending on the film thickness:

$$l_\lambda = 168 \ h_f. \tag{3.29}$$

Assuming this value for the film model improvement is not meant as a statement for the universal applicability of l_λ. Instead, it is an attempt to capture realistic magnitude for associated forces.

The two terms on the left hand side of Eq. (3.28) are the contributions of inertia and shear force and represent the wetting driving forces. On the right hand side of this equation are the terms of gravitational and surface tension force. They are stabilizing the stagnation point and consequently the dry patch. The gravitational force contribute to the wetting driving forces as well, which depends on the orientation of the face tangent vector compared to the gravitational vector. If the left hand side is dominant the dry neighboring surface cell becomes wet. A stable configuration is present in case of equality of both sides. If the right hand side of Eq. (3.28) outbalances, the dry area should grow.

To improve the film model of Anderson and Coughlan [8] toward a more realistic wetting behavior, an extension of the dry patch model formulation of Penn et al. [122] seems appropriate. It has to be ensured, that the extended formulation accounts for gravity, since in some cases it becomes dominant compared to or at least equal to the shear forces. In the following the modifications are explained in more details.

The wetting model works along the contact line, where a force balance is set according to Penn et al. [122]. A first request is made in the implemented submodel to obtain the film height of each cell, in order to identify the contact line. It is defined as edge between a pair of cells, where one is already wet and one is still dry. The flow field solution yields the information for driving forces. Liquid volume fluxes can be calculated from the edge normal components of the driving forces (see Fig. 3.5). In the original formulation the source terms of the film height were updated after this step. A new film height value was calculated and the next film time step was started.

A new contribution at this point is the evaluation of the force balance (Eq. (3.28)) for wetted cells along the contact line. The driving forces are checked, in order to know whether they dominate the surface tension forces, which work as resistance and wetting limit (Fig. 3.5).

An *if* condition is applied to set the liquid volume flux to zero if the surface tension forces are dominating. The source terms from the transformed mass conservation are
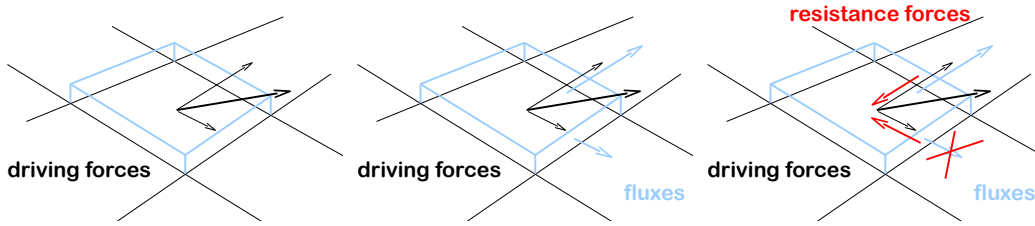
FIGURE 3.5: Schematic principles of wetting model

updated according to the information from the fluxes afterwards. After this procedure, the next film time step may occur without changes in film height, if the film propagation is prevented by the wetting limitation.

It is necessary to mention that this model works only in one direction. It estimates whether dry surface areas are stable or become wet. The receding behavior of distorted droplets or liquid fragments and associated dewetting, is not captured with this condition. Nevertheless, an enormous model improvement is already achieved with the implementation of the wetting limitation.

Pressure gradient representation

To further improve the reliability of the the simulation results, the film model should also account for hydrostatic effects. Those appear as pressure gradients within the film which become significant, if the film thickness is equal or even higher than the capillary length. For the material properties of water the capillary length is $k \approx 2.7$ mm, as mentioned before. The pressure gradients are generated by film thickness variations. They induce a flattening of the film profile or an increase of the local film thickness, depending on the orientation of the surface. The latter case is also interesting for film instabilities, as described by the Rayleigh-Taylor instability (see Section 2.3.1). Therefore, it is possible to capture both, driving forces for film flow and destabilizing forces.

$$p_{hs,i} \quad = \quad p_i - \mathbf{n}_i \cdot \mathbf{g} \, \rho \, h_{f,i} \tag{3.30}$$

The hydrostatic pressure is calculated in every single cell, based on the local film height (see Eq. (3.30)). It is stored as user defined scalar (UDS) in Fluent. Afterwards one can easily estimate the gradient of this scalar, which gives the pressure gradient vector for each surface cell. A further contribution to the film velocity can be obtained from wall tangential component of the pressure gradient vector. Finally, the pressure gradient film velocity component is superimposed with the other velocity components, to give the mean film velocity, as described in Eq. (3.15).

Usually, the effect of the pressure gradient is expected to be rather small. It may only become significant, whenever liquid accumulates without exceeding the threshold for film break-up.

Modifying the Break-up Criterion

The investigation of film break-up in terms of liquid ejection from the film volume was declared as one main research objective. Clearly, the complexity of this task is very high. An attempt to include an improved break-up model in the film simulation is explained in what follows. A break-up criterion is defined by Foucart and Blain [46], which accounts for Kelvin-Helmholtz and Rayleigh-Taylor instabilities. The model evaluates the amount of liquid h_e that is ejected,

$$h_e = 0.03877 \cdot \lambda \tag{3.31}$$

when the local film thickness h_f exceeds the critical film height

$$h_c = \frac{\lambda}{2\pi}. \tag{3.32}$$

The most unstable wave length λ, which is a measure for the stability of liquid films, is defined as

$$\lambda = \frac{2\pi}{\rho_l \vec{g} \cdot \vec{n}} \left(\sqrt{\frac{1}{9} \rho_a^2 U^4 + \rho_l \sigma \vec{g} \cdot \vec{n}} - \frac{1}{3} \rho_a U^2 \right), \tag{3.33}$$

with U the relative velocity between the gas and the film.
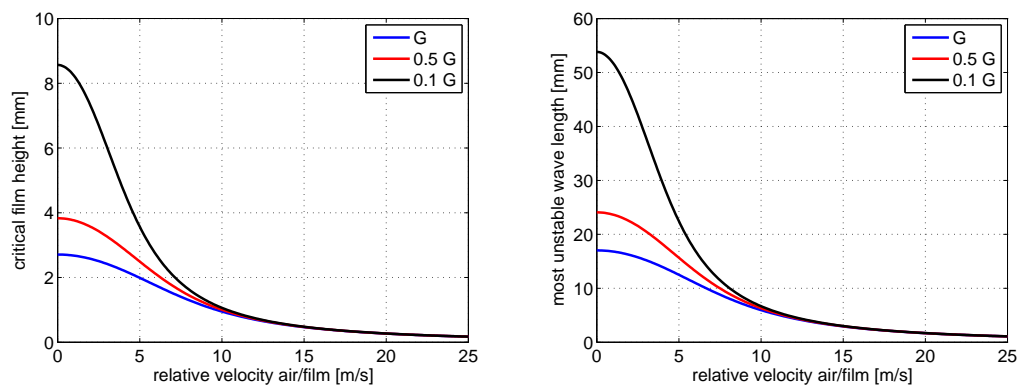
FIGURE 3.6: Critical film height and most unstable wave length [46]

Figure 3.6 yields the evolution of the critical film height and the most unstable wave length according to the formulation of Foucart and Blain [46], for common conditions in vehicle soiling processes and geometries. The effect of gravity becomes insignificant with increasing relative velocity between the surrounding air flow and the film flow.

Furthermore, the critical film height reaches a maximum value at film stagnation points. To evaluate different surface orientations, different G-force strengths are defined.

The implementation as submodel in the film model of Anderson and Coughlan [8] is based on a modification of the standard break-up model. The criterion has to be adapted to account for Kelvin-Helmholtz and Rayleigh-Taylor instabilities. Therefore, the gas-liquid relative velocity is assumed to be equal to the film surface velocity induced by the gas shear. All other quantities used in Eq. (3.33) are available. Thus, further calculations are unnecessary.

The Weber number criterion is simply replaced by the critical film height that results from the most unstable wave length. Film break-up occurs for cells where the local film height exceeds the critical film height, which is checked by an *if* request ones again. Subsequently, the droplet release is computed the same way as before. This means that routines for initialization of droplet parcel properties (diameter, velocity, etc.) are used as before, with the droplet diameter set equal to the local film thickness value.

In comparison with the original break-up model, there is no need for a user defined threshold value for critical film height, which is a significant improvement. The critical film height is calculated automatically by means of a stability analysis. Hence, the film simulation shows a more realistic film break-up behavior.

It turned out that the prediction of realistic film break-up is primarily linked to accurate film flow prediction. The different break-up models play a minor role in determining the break-up location. They may improve the film model for more realistic release rates. But until now they are almost impossible to validate quantitatively due to missing experimental data.

3.2.4 Model Validation

Many efforts were spent to introduce the submodels and describe model improvement in the previous section. A first validation of the model will be described in the following part. It is a most important part of model development. In order to validate the film model, simulation results have been compared with experimental and theoretical values for an open channel flow configuration. A detailed description of the experimental setup and measurement technique applied for film thickness measurements, is given later in Section 4.5. The focus is here set on the numerical validation, giving all details of the simulation setup.

Generally, open channel flows are known to yield reproduceable flow properties, which can be described with an analytical solution of the Navier-Stokes equations for simpler

cases. Therefore, this kind of configuration was chosen as appropriate test case. An existing laboratory scale model was used to design a geometry for the CFD investigation (see Fig. 3.7).
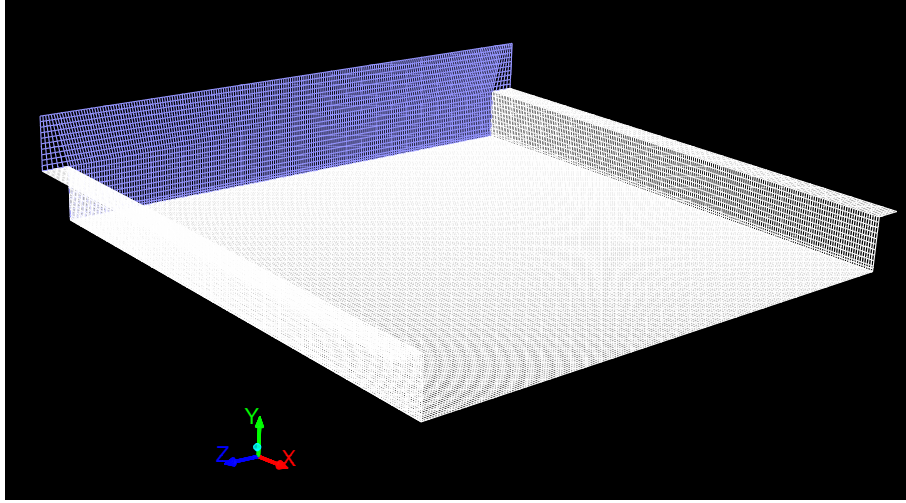

FIGURE 3.7: Open channel flow geometry

The computational grid is completely structured and has a minimum cell size of 1 x 1 mm^2 at the bottom of the side walls. The flow field is calculated using a RANS approach, with specified ambient pressure at the inlet and the outlet. Actually, no air flow occurs along the plate, which means that no shear stress acts on the film.

Since all computational algorithms have been described previously, only the specific model settings are given here. Bottom and side walls of the open channel geometry are specified as wall-film surfaces. Therefore, the film is calculated only for these surface cells. Liquid mass is injected at discrete points of an injection surface. It is defined as line with 200 injection points, located at the upper end of the inclined plate of the open channel. Further settings are listed in Table 3.2, with case-specific values for each flow rate (FR). These values have been adapted for different flow rates. The droplets are injected with the x-velocity, diameter and flow rate corresponding to that of the open channel film flow.

The settings for the injection surface dimensions are also given in Table 3.2. Three points are used to geometrically define a plane. Additionally, the number of injection points is given for the plane edges (e1 and e2).

To conserve mass, the film depth limitation is set to a high value of 3 mm such that no mass may be lost due to numerical effects.

Finally, the results of the simulation are compared with experimental and theoretical data. An excellent agreement can be observed for the predicted film thickness values

TABLE 3.2: Injection and surface settings for validation

Injection setting	FR 1	FR2	FR3	FR4	FR5
injection type	surface	surface	surface	surface	surface
injection name	random	random	random	random	random
x-vel [m/s]	0.171	0.175	0.179	0.2838	1.1377
y-vel [m/s]	-0.2	-0.2	-0.2	-0.3	-1
z-vel [m/s]	0	0	0	0	0
diameter [mm]	0.774	0.784	0.792	1	2
total mass flow rate [kg/s]	0.0265	0.0274	0.0284	0.0567	0.4537
Surface setting	**FR 1**	**FR2**	**FR3**	**FR4**	**FR5**
bounded	-	-	-	-	-
sample points	e1 200	e1 200	e1 200	e1 200	e1 200
sample points	e2 1	e2 1	e2 1	e2 1	e2 1
P0(x,y,z)	(0.001,	0.005,	-0.1)		
P1(x,y,z)	(0.001,	0.005,	0.1)		
P2(x,y,z)	(0.001,	0.01,	0.1)		

(see Fig. 3.8). The values shown here have been averaged for the whole plate. A small part was excluded from the analysis, because it is located upstream of the injection surface. The computed film thickness values are very slightly below the theoretically predicted curve. Futhermore, they are below the experimentally measured points for all cases as well. It has to be concluded that the model under predicts systematically the film thickness for this configuration. However, the deviation between experiment and simulation is below 3 % in the worst case (FR1), demonstrating the accuracy of the employed model.
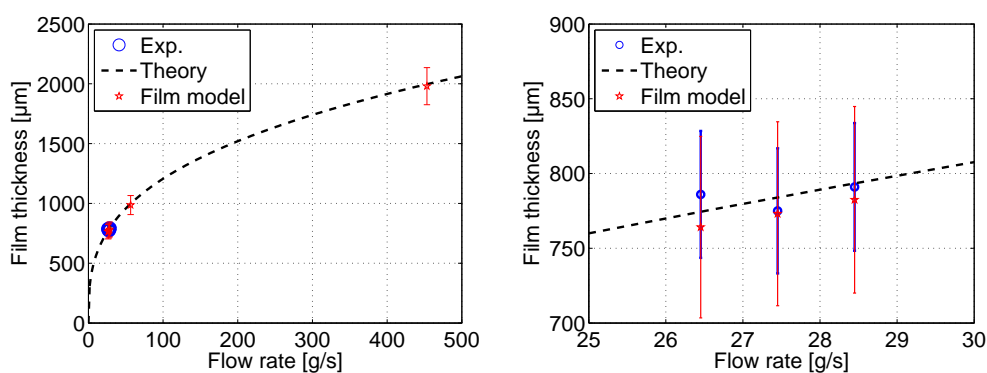
FIGURE 3.8: Film model validation: comparison of simulation results with experimental and theoretical data (left), details for experiments (right)

The error bars shown in Fig. 3.8 are equal to the standard deviation of the measurements and the simulations, respectively. Both are in the same order of magnitude and always

meet the corresponding experimental or simulation result as well as the theoretical prediction.

Conclusions

The following conclusions can be drawn from the model improvements and the validation:

1. The film model is now applicable for film flow simulations including complex and coupled physical phenomena. Especially the interaction of the liquid film with impinging droplets and the limitation of surface wetting are essential for the simulation of vehicle soiling processes. Although the model accounts for more physical details, the computational requirements could be kept almost constant. All new submodel equations can be solved analytically or rely on internal computational routines, as for example the pressure gradient calculation. As a consequence, the model stays almost as simple as before, but delivers more realistic simulation results.

2. The validation of the film model proved that it is appropriate to simulate a film flow of water. For continuous liquid films (open channel flows) it almost exactly predicts film height values.

3. An application of this model to wavy films should be possible in case of parabolic film velocity profiles, since these profiles generally result from gravitational acceleration.

3.3 Aerodynamic and Dispersed Phase

In the following some basic ideas are discussed concerning the ambient properties of the film. Of major importance are the surrounding flow field and information about the dispersed phase (water droplets).

3.3.1 Modeling External Vehicle Aerodynamics

An accurate solution of the flow field around the geometry is required as first step for a realistic soiling simulation. The wall shear stresses, entering later the film model, are particularly important. Moreover, the air flow velocity and pressure are needed to compute the droplet trajectories. These computations have been usually carried out using a Eulerian approach. However, alternative techniques like the Lattice-Boltzmann method have also been employed [167]. This first step is highly classical for the development of new car concepts, since extensive aerodynamic studies are always included. A variety of in-house codes, open source or commercial CFD software is available to serve this purpose. Steady-state RANS simulations are clearly favored in most publications, in order to keep reasonable computing times for such complex geometries, which are usually meshed with millions of volume cells. The governing equations for the simulation of the incompressible flows are deduced from the conservation equations of mass and momentum by employing the Reynolds decomposition between time-averaged variable $(\bar{\ })$ and fluctuation $()'$. Mass conservation equation simply becomes:

$$\frac{\partial \bar{v}_j}{\partial x_j} = 0, \tag{3.34}$$

employing the summation convention of Einstein. The momentum conservation equation for steady flows is given by $(i = 1, 2, 3)$:

$$\rho \frac{\partial (\bar{v}_i \bar{v}_j)}{\partial x_j} = \bar{f}_i - \frac{\partial \bar{p}}{\partial x_i} + \mu \frac{\partial}{\partial x_j} \left(\frac{\partial \bar{v}_i}{\partial x_j} + \frac{\partial \bar{v}_j}{\partial x_i} \right) - \left(\frac{\partial}{\partial x_j} \rho \overline{v_i' v_j'} \right) \tag{3.35}$$

It features an additional tensor, the Reynolds stress tensor $-\rho \overline{v_i' v_j'}$ on the right-hand side, which describes the momentum transport associated to turbulent fluctuations. The equation system is not closed and requires a model for the Reynolds stress tensor, since the fluctuations are not known. In most publications, the standard k-ϵ turbulence model or slightly modified versions have been used to model turbulent flows. Ghani et al. [49] and Nylander [113] discuss the application for wind tunnels and for simple aerodynamic simulations. A different suggestion is made by Langrish and Kota [86]. They successfully applied the SST k-ω turbulence model, which was introduced by Menter [102], for the

purpose of droplet deposition. A special near-wall treatment is the advantage of the SST k-ω turbulence model compared to other models. The highly complex issue of turbulence modeling is beyond the scope of this work. For more information it is referred to reference textbooks, for instance Ferziger and Perić [45] and Pope [126].

Often, it is unnecessary to retain a detailed flow field solution for the whole vehicle. Therefore, the focus is now on the most relevant components for vehicle soiling (windshield, A-pillar with rear-view mirror and side window). This leads to a second substep when computing the aerodynamic field, the so-called flow field mapping. The converged aerodynamic solution is used for initial and boundary conditions in further computations. These are carried out on a considerably finer grid, which is centered around the interesting part of the geometry [46, 79]. In a similar manner Campos et al. [24] derived a time-averaged flow field solution from LES calculation. They used a RANS solution for boundary conditions.

A refined grid increases the accuracy of the obtained solution. Since the aerodynamics control the second step (droplet tracking), it is obviously of fundamental importance to obtain realistic flow conditions. It appears impossible to receive a proper estimation of vehicle soiling starting from a wrong aerodynamic field. The second step of the algorithm is considered now, assuming a correct flow field solution (air flow around the geometry) has been obtained.

3.3.2   Phase Coupling

The issue of phase coupling should be addressed, before describing the tracking step. Generally, the coupling of the continuous and the dispersed phases is based on key integral quantities, which characterize multiphase flows (Fig. 3.9). Studies of multiphase flows and overviews of modeling methodologies are provided for instance in Crowe et al. [33] and Prosperetti and Tryggvason [128]. One distinguishes between dilute and dense dispersed flows. A threshold value for volume fraction of the dispersed phase is typically set to 10^{-3} [141], for a two-phase flow (water-spray in air). One may omit four-way coupling, if this condition is fulfilled. Then, particle interactions such as collisions can be neglected. Coupling approaches are rarely discussed in vehicle soiling simulation studies. All listed references considere only one-way coupling. This is theoretically justified, if the volume fraction of the dispersed phase remains below a value of $\approx 10^{-6}$ (see Fig. 3.9). The gas phase stays completely unaffected by the presence of the droplets for such extremely dilute cases, as found for instance by Borg and Vevang [16].

Also included in Fig. 3.9 is the range of liquid volume fraction in which experiments have been conducted in the LSS wind tunnel. The injected liquid flow rate is divided
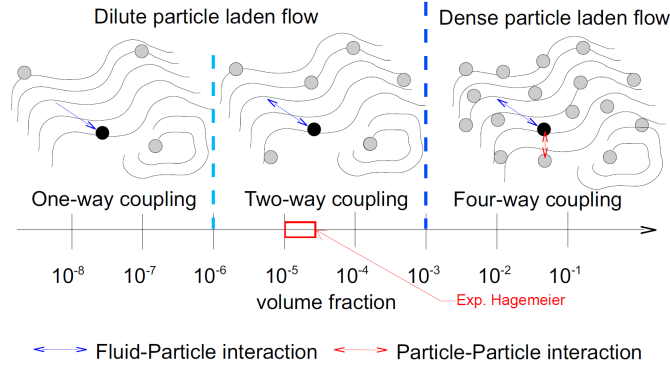
FIGURE 3.9: Regimes of dispersed two-phase flows

by the air flow rate to give the volume fraction. For the present case, volume fractions in the range of $1.1 \cdot 10^{-5}$ to $1.85 \cdot 10^{-5}$ are derived, if considering three air velocities (15, 20 and 25 m/s) and a constant liquid flow rate of 5 l/min. Certainly, this is a rough approximation of the volume fraction. More realistic values can be obtained from details of PDA measurements, as will be discussed in the next chapter.

Most important conclusion is that pure one-way coupling is unlikely to apply, even for 'designed' test cases in laboratory scale, where nearly everything can be controlled. Note, however, that the thresholds given in Fig 3.9 are very severe compared to current practice.

In order to assess the importance of two-way coupling for vehicle soiling, Paschkewitz [121] used a momentum coupling parameter. It is based on the ratio of particle drag to the momentum flux of the carrier fluid:

$$\Pi \approx \frac{C}{1 + \text{St}} \tag{3.36}$$

In this formulation, C is the ratio of the mass flow rates of the two phases. The Stokes number St is defined as ratio of the response time of disperse and continuous phases. It reads

$$\text{St} = \frac{\rho_l d^2 U}{18 \mu_g H}, \tag{3.37}$$

when considering Stokes' flow regime. U/H represents the characteristic flow time scale, while μ_g is the dynamic viscosity of the gas phase. A detailed derivation can be found for instance in Crowe et al. [33].

If the momentum parameter Π exceeds unity, two-way coupling is important and should be taken into account. Paschkewitz [121] found high mass loading of water and low droplet diameter, for the multiphase flow near and around the tires of heavy vehicles. Therefore, $\Pi > 1$ is obtained and two-way coupling should be considered. On the

contrary, the air flow is unaffected by the presence of the droplets farther from to the tires. Consequently, one-way coupling appears to be sufficient for the case of foreign contamination and should deliver sufficiently accurate results.

3.3.3   Dispersed Phase Modeling

Discussing vehicle soiling due to self- or foreign contamination with rain water, one automatically considers a multiphase flow problem. The primary (continuous) phase, as discussed above, is usually calculated in a Eulerian reference frame. In contrast, it is not obvious to choose the most appropriate description for the secondary phase (spray or disperse droplets). Dispersed phase modeling approaches may either use the Lagrangian or Eulerian reference frame, depending on global modeling assumptions and flow conditions. A more detailed description of simulation approaches for dispersed multiphase flows is given for instance by Sommerfeld et al. [141]. When the Eulerian frame is suitable, both phases are calculated as interpenetrating continua, whereas the Lagrangian approach transports the disperse phase as discrete particles.

Even heavy rain properties (i.e. droplet concentration and volume fraction), as listed before, are far below the upper limit accessible to Lagrangian models. For instance, a volume fraction of 10 % is given as maximum value for Lagrangian description by Elghobashi [42]. Borg and Vevang [16] mentioned a droplet phase volume fraction of only $\approx 10^{-6}$ for their study concerning foreign contamination. For such highly dispersed systems, the application of the Lagrangian approach is fully justified. Consequently, most studies have indeed employed such a Lagrangian methodology. However, some references can be found, which compute the evolution of the dispersed phase in a Eulerian frame.

For example, Yoshida et al. [165] considered the contamination due to solid dirt particles using a Eulerian method. More recently, Morud [105] solved droplet dynamics in a pipe flow with a Eulerian approach. The work described by Morud [105] is relevant, since it presents a coupled approach of Eulerian droplet and film modeling. The droplet or particle concentration is a scalar, which is transported through convective and diffusive motion, in both publications. Accordingly, a diffusion equation is solved in a Eulerian reference frame, assuming Stokes' flow regime. These are the only documented references comparing directly Eulerian and Lagrangian approaches for issues related to vehicle soiling processes, to the best of my knowledge.

Yoshida et al. [165] concluded that it is possible to reduce the computing time when using a continuous dirt concentration instead of the common Lagrangian tracking method. They acknowledged that the Eulerian approach is not applicable to large dirt particles,

which are excluded from the Stokes' regime (requiring particle diameters < 0.1 mm). Considering all published studies, the simulation of foreign contamination seems a typical Lagrangian task. Therefore, the spray computation is now described for a Lagrangian particle tracking.

The droplet motion in gas flows is governed by several physical phenomena, which are combined in the equation of motion. This equation is simply a force balance equation deduced from Newton's second law. It can be written as follows

$$m_l \frac{\mathrm{d}\mathbf{u}}{\mathrm{d}t} = \mathbf{F}_D + \mathbf{g}\left(m_l - m_g\right) + \mathbf{F}_x. \tag{3.38}$$

Eq. (3.38) includes the droplet velocity, written as $\mathbf{u}$. It further contains directly the effect of the drag force $\mathbf{F}_D$, of the gravitational acceleration $\mathbf{g}$, and additional forces, gathered into $\mathbf{F}_x$. Particle rotation as well as heat and mass transfer are not considered in this simplified approach. The drag force $\mathbf{F}_D$, first term on the right side of Eq. (3.38), can be expressed for spherical particles as:

$$\mathbf{F}_D = \frac{3}{4} \frac{\rho_g\, m_d}{\rho_l\, d} C_D \left(\mathbf{v} - \mathbf{u}\right) \left|\mathbf{v} - \mathbf{u}\right|, \tag{3.39}$$

according to the formulation used by Sommerfeld et al. [141]. Here, the gas phase velocity is given as $\mathbf{v}$. Moreover, droplets are assumed as ideal spheres and non-deforming particles, for all cases relevant for vehicle soiling simulation. An additional factor has to be included in Eq. (3.39) for shape correction, if droplet deformation is considered. The drag coefficient C_D can be calculated according to the correlation of Schiller and Naumann [136]:

$$C_D = \frac{24}{\mathrm{Re}_d} \qquad \text{for } \mathrm{Re}_d \leq 1$$

$$C_D = \frac{24}{\mathrm{Re}_d}\left(1 + 0.15\,\mathrm{Re}_d^{0.687}\right) \qquad \text{for } 1 < \mathrm{Re}_d < 1000$$

$$C_D = 0.44 \qquad \text{for } \mathrm{Re}_d \geq 1000 \tag{3.40}$$

which is frequently used. Here Re_d is the particle or droplet Reynolds number, defined in Eq. (1.3). Beside the drag force, gravity (second term on the right side of the equation of motion) affects the droplet motion. This becomes significant, especially for droplets of a large volume (diameter of 1 to 2 mm), which are typically found in heavy rain. Additional forces are summarized in the last term on the right-hand side of Eq. (3.38). They account in particular for lift force, virtual mass force or history force. They are considered of negligible importance to describe the motion of large water droplets in air (with density ratio $\rho_g/\rho_l \approx 0.001$), in comparison with the other forces [141]. They have been systematically neglected in all Lagrangian simulations dealing with vehicle soiling.

Nevertheless, studies on particle deposition showed that the relative influence of the lift force on the deposition rate could be noticeable for large spherical particles. Therefore, the effect of lift could be important for some configurations. It is recommended to check this issue by an order of magnitude estimation before neglecting its contribution. More details on this topic can be found in Wang et al. [158] or Marchioli et al. [97].

Addtionally, one should account for the turbulent dispersion of the particles, since the aerodynamic gas flow is turbulent. Usually, this is realized with a stochastic method, like an eddy lifetime model or a random walk model. Borg and Vevang [16] concluded that a minimum number of droplets (also labeled as tries) has to be tracked through the domain, to account for turbulent dispersion of the droplets. This has to be realized for each injection point, in case of steady computations. Each track is subject to random turbulent fluctuations impacting the trajectory. Borg and Vevang [16] found that the statistical spread of the particle stream remains almost constant, if more than 10 repetitions are considered. For transient calculations, the particles are tracked only once per time step, using instantaneous fluctuation values.

Another issue of high complexity concerns the interaction between individual droplets and the definition of appropriate boundary conditions. Often, droplet-droplet collisions and aerodynamic droplet break-up are excluded from vehicle soiling studies [12, 165]. Particle interactions, in particular droplet-droplet collisions, can be neglected for very low volume fractions of droplets within the surrounding gas phase. A droplet volume fraction of 10^{-6}, as considered by Borg and Vevang [16], fully justifies this assumption [141]. However, the aerodynamic break-up of droplets is based on individual droplet properties as the diameter and the relative velocity between droplets and gas phase. The break-up criterion is quantified by the Weber number, comparing the material properties of the liquid and the ambient gas. Pilch and Erdman [124] stated that droplets retain a stable shape for We values up to 12. A maximum stable droplet diameter of 1.1 mm is reported by Borg and Vevang [16], for a high relative velocity of 25 $^\text{m}/_\text{s}$. In case of lower relative velocities, the maximum stable droplet diameter becomes even larger. Many publications associated with vehicle soiling simply neglect droplet-droplet interactions and aerodynamic break-up. Hsiang and Faeth [65] and Faeth et al. [44] provide further information concerning secondary break-up of droplets and sprays.

Boundary conditions are needed for the inlet, the outlet as well as the walls. Most important is the choice of velocity, diameter and mass flow rate of the droplets. The inlet values, also called injection for tracking simulations, are either obtained from real measurement data or from the literature. A mean droplet diameter between 1 and 2 mm is often applied, in the absence of suitable information concerning the exact DSD. These values are reasonable for most cases involving direct contamination by heavy rain

[46, 79]. Occasionally, droplets only have to be provided as a mass source to initiate a liquid film, if studies concentrate on the development of film models [8]. A correct representation of droplet properties is not essential for these initial tests.

A different situation is, if foreign contamination processes are considered. To this end, it is necessary to specify accurate probability density functions (PDF) for the DSD of the injected droplets [16, 24]. Wind tunnel experiments and road tests yield the required information.

In contrast, it is simple to specify velocity boundary conditions for the injection, even without knowing the exact velocity distribution. There is one main velocity component which is equal to the driving speed of the car. It is directed horizontally, parallel to the free gas flow. Additionally, the vertical velocity component is specified as the terminal velocity of the droplet. These simplified initial spray velocities are useful for the comparison of simulation results and experiments as well [46]. Usually, CFD packages provide user sub-routines to specify all these parameters and link them to the computation [24]. In more complex cases, preprocessing may be necessary, applying special software tools [113].

All details concerning liquid film modeling have been presented in this chapter. It started with the description of available approaches. The approach of Anderson and Coughlan [8] was introduced and chosen for further investigations and improvements, because of its simplicity and low computational costs. It was improved using four significant submodels, but its simplicity was retained. At first, a spray-film interaction submodel has been implemented. Subsequently, a wetting limitation and the effect of the pressure gradient have been included in the film simulation. Finally, an alternative film break-up model has been specified. The computational requirements remain almost constant. The effectiveness of some improvements was discussed in Hagemeier et al. [53] and Hagemeier and Thévenin [55].

In the following, numerical investigations have to be validated and improved thanks to further experimental results. The experimental configurations are explained in the next chapter, together with a description of the facility and of the corresponding measurement techniques.

Chapter 4

Experimental Investigations

4.1   Wind Tunnel Experiments

Wind tunnel experiments, whether in laboratory or full scale, are one important component of vehicle soiling investigation, as mentioned previously in the introduction. Full scale experiments and qualitative measurements are often carried out, for a general evaluation of soiling behavior. Experiments in laboratory scale are favored, if special soiling processes are of interest, as in the present case. The flow properties of the primary phase around the geometry are first considered. The behavior of the secondary phase is also important, which includes the interaction with the solid geometry.

Measurement results are needed for numerical soiling simulation. They are used both, for setting the initial and boundary conditions as well as for improvement and validation of the models. Consequently, the measurements have to satisfy high quality requirements.

FIGURE 4.1: Experimental configurations: K0 empty test section (left), K1 generic windshield geometry (middle), K2 rear view mirror geometry (right); pictures of windshield and rear view mirror by B. Faßmann

The experiments carried out within this research project are structured according to the following aims. At first, experimental configuration K0 is used to evaluate and improve

TABLE 4.1: Operation parameter for experiments.

Variable	Value	Units
Wind tunnel velocity	15, 20, 25	m/s
Atomization pressure (atomizer type Delavan CJM)	0.3	bar
Water flow rate	5.5	l/min

the measurement techniques and to evaluate resulting accuracy. In addition, facility parameters and operation settings have to be specified. All results are directly included in subsequent experiments. Therefore, no separate presentation is given for the results of configuration K0. Instead, explanatory comments are made within the text, in order to clarify certain details.

The second configuration K1 is directly linked to vehicle soiling and concerns the aerodynamic investigation of a generic windshield geometry. Several measurement techniques are applied to quantify the primary and secondary droplet size around this geometry. Finally, the third configuration K2 is dedicated to aerodynamic investigations of a more complex geometry, a rear view mirror. Pre- and post-impingement characteristics of the dispersed phase are quantified, similar to configuration K1. All three configurations are investigated for three approach velocities of 15, 20 and 25 m/s, as discussed on Page 10.

4.1.1   Wind Tunnel Facility

All experimental investigations of soiling processes are carried out in a two-phase wind tunnel, which operates with a closed test section. The wind tunnel is a Göttingen type wind tunnel, featuring a recirculation of the air flow. Flow velocities can be selected in the range of 0.3 to 55 m/s, while the nominal turbulence intensity in the pure gas phase is around 0.1 %.

An atomization system is installed to generate a two-phase flow, involving gaseous primary phase and liquid secondary phase. It consists of a radial pump, a fixed pipe system, flow rate and pressure control devices and a pressure atomizer. The atomizer generates a fan spray, which is adjusted vertically and aligned with the center line of the wind tunnel test section. It is mounted in front of the test section and directed co-current to the air flow. The dimensions of the test section are 600 mm in width, 500 mm in height and 1200 mm in length.

Hence, only laboratory scale experiments can be conducted. The focus is set, in particular on the soiling behavior of a simplified windshield and a rear view mirror geometry. Further operation variables are listed in Table 4.1.

The test section is accessible for measurement techniques through three windows (at the top and on both sides), which are covered with float glass. Accordingly, non invasive measurements are possible, with low light intensity absorption. Several optical measurement techniques are suitable for the purpose of primary and secondary phase characterization. In particular, Laser-Doppler Velocimetry (LDV) and Phase-Doppler Anemometry (PDA) are employed, but also imaging techniques, such as Particle-Image Velocimetry (PIV) and Shadowgraphy. Their individual principles and application are briefly explained in the following section.
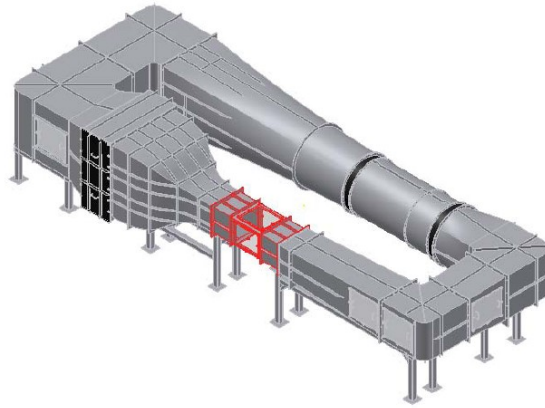
FIGURE 4.2: LSS two-phase wind tunnel, test section highlighted in red

4.2 Applied Measurement Techniques

4.2.1 LDV

The LDV technique is a point measurement technique, which acquires the velocity information from light scattering particles. Tracer particles are used for the characterization of the primary phase. Therefore, they have to perfectly follow the gas flow. Properties and requirements of the LDV technique can be summarized as follows:

- Monochromatic, non-divergent laser light source

- Configuration optics to split main beam into two beams of equal light intensity and shift one (commonly by 40 MHz)

- Sending optics to focus the beams to build measuring volume at intersection point

- Optically accessible facility

• Seeding with tracer particles with ideal response properties and in proper concentration

The measurement principle is based on the evaluation of the Doppler-frequency of scattered light signals. These signals are generated by particles crossing the measuring volume. It can be imagined as an ellipsoid containing interference planes seperated by a constant distance. That distance is fixed by optical parameters of the LDV system, such as λ the wave length of the laser and θ the inclination angle of the two laser beams. It can be calculated according to Eq. (4.1).

$$d_f = \frac{\lambda}{2 \sin\left(\frac{\theta}{2}\right)} \tag{4.1}$$

Measuring the Doppler-frequency f_D, the particle velocity u can be obtained from Eq. (4.2), if the distance between the fringes d_f is known:

$$u = d_f \cdot f_D \tag{4.2}$$

Velocity fluctuations within the primary phase can be resolved due to the high temporal resolution of LDV (typically several kHz). Consequently, LDV is mainly applied to characterize flow velocities and turbulence properties. Further details are not discussed here, since it is a well known and widely used techniques. More information can be found in standard literature for example Durst et al. [40] or Tropea et al. [149].

All LDV parameters, employed for the experimental investigations, are summarized in Table B.1 in Appendix B. They are listed as settings, specified within the BSA measurement software. Column entries marked with channel 2 and 3 are related to the PDA configuration, working with 3 photomultipliers.

Three wind tunnel velocities are applied (Table 4.1), which require additional adaption of the measurement technique. Therefore, the settings for center velocity and velocity span are exemplary values for the case of 15 ᵐ/s. They may change for other cases.

4.2.2   PDA

As second measurement technique, the PDA technique is applied, which has been directly invented for simultaneous characterization of particle size and particle velocity [41]. It is based on identical principles as LDV, but extended with a separate receiving optics. The receiving optic is adjusted to the measuring volume, but located in a certain inclination compared to the sending axes. A scattering angle is defined between sending axis and

receiver axis. Three diodes are implemented within the PDA receiver, in contrast to the LDV receiver, where only one photodiode is used. The signal from the scattered light is received by each photodiode with a signal shift. The signal shift correlates with the diameter for a given scattering mode, refraction (1st or 2nd order) or reflection and certain material properties. The PDA principles and processing steps can be seen in Figure 4.3.
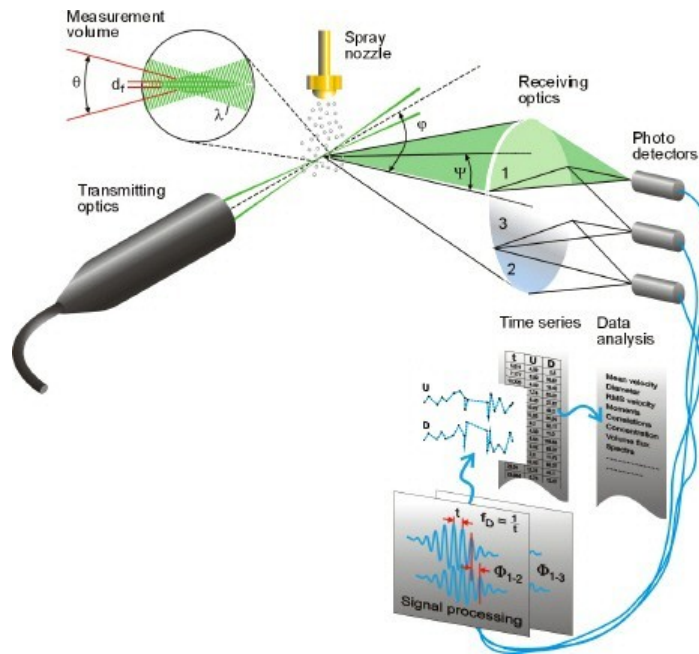
FIGURE 4.3: Schematic of PDA System [35]

An 1D-PDA system is employed for spray investigation, which means that the droplet diameter and the droplet x-velocity are acquired at the same time. All parameters applied for the experimental investigation in the wind tunnel are specified in Table B.2 in Appendix B. The sending optic parameters (Table B.1) are identical for both, LDV and PDA. A significant difference is the number of samples, which is set to 10 000 in case of PDA. The operational parameters have been evaluated in order to ensure reasonable measurement results. Hagemeier et al. [51] show a meaningful comparison of results from PDA working in backscatter configuration and other measurement techniques. Consequently, the PDA results are validated for this particular configuration.

4.2.3 PIV

Particle Image Velocimetry is a common imaging technique to acquire fluid flow velocity in 2D. A laser light sheet illuminates the scene of interest and a CCD-camera, adjusted

orthogonally to the light sheet, acquires double-frame images of the flow, which is seeded with tracer particles, similar to those used in LDV.

Post-processing of the images is necessary to obtain the objective quantities, for example velocity or turbulence properties. Basically, the image is divided into interrogation areas, for which the process steps are carried out, usually starting with a cross or adaptive-correlation. The displacement of particles between the two frames is evaluated and velocity vectors are computed. Subsequently, validation and filtering processes improve the results. Averaging over a certain number of images leads to the final result, depending on the flow conditions (steady, unsteady or periodical). Raffel et al. [129] and Tropea et al. [149] provide further information on the PIV measurement technique.

System parameters and setup variables used for the measurements are summarized in Table 4.2.

TABLE 4.2: PIV system parameter.

Parameter	Setting
Laser	Litron double Nd:YAG
Power/Shot (mJ)	300
Repetition rate (Hz)	15
Double frame CCD camera	Flow Sense (Dantec Dynamics) 1600×1200 pix^2
Objective	Nikon Micro Nikkor $f = 60$ mm

4.2.4 Shadowgraphy

Shadowgraphy is an imaging technique, offering also a 2D insight of the flow. Contrary to PIV, the illumination occurs as backlight. The motion of fluid or solid structures is visualized. Their minimum size is limited here to 5 μm, because of requirements for the optical resolution. A particle has to be resolved by a minimum number of pixel, for example 5 pixels in each direction. Fluid or particle structures are observed by means of image segmentation, which is an intensity analysis. Shadow regions feature low light intensity and thus are related to a fluid or solid structure. Several threshold conditions are defined, which allow to delineate the structures for further evaluation. First the particle size is analyzed. Particle velocity can be estimated as well, if double-images are acquired. Recently, the collision rate of droplets within turbulent two-phase flows was measured by Bordás et al. [13], using also shadowgraphy.

The aim of all these experiments is to quantify the multiphase flow conditions around the geometries (windshield and rear view mirror). All measurement techniques described previously, are applied to gather information. Experimental data obtained at the front

side of the geometry are employed primarily as inlet conditions for numerical studies. In contrast, data obtained downstream are used for comparisons and validation.

4.3   Configuration K1 (Windshield)

Some preliminary studies have been conducted, in preparation for the experimental investigation of soiling processes for the K1 configuration. Essential parameters have been specified, such as the location in the wind tunnel test section or the inclination of the windshield, as summarized in Brinkmann and Hagemeier [22]. Accordingly, a model geometry (see Fig. 4.4) was finally produced at ISM Braunschweig. The geometry is made of aluminum side walls, supporting a glass plate in the center. It is inclined by 28° towards the horizontal, which is a typical value for automobile windshield inclination. Furthermore, the radius of the side wall is adapted to a realistic automobile shape. Its curvature is set to mimic that of the A-pillar of a vehicle, which reduces the generation of vortex structures. Otherwise, those vortices may influence the liquid film on the plate. A horizontal plate is installed toward the front (upstream) and the trailing edge (downstream) of the windshield. Consequently, two corner points are defined, a concave one (upstream) and a convex one (downstream). Both show a specific behavior, as will be discussed later on.
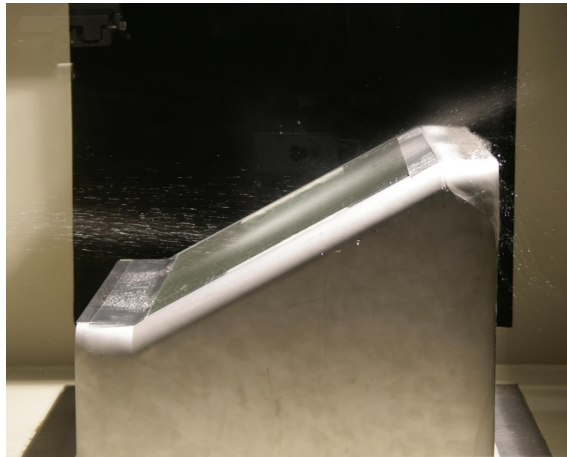
FIGURE 4.4: Generic windshield geometry mounted in the wind tunnel test section, with water spray impinging upon the geometry.

A part of the cross sectional area is blocked, when installing the windshield geometry in the test section of the wind tunnel. The wind tunnel blockage ratio describes the ratio of projected area of objects within the test section in streamwise direction to the cross sectional area. A very high blockage ratio of $\pi_A = 23$ % is obtained for the projected area of $A_x = 0.0694$ m^2 and the cross sectional area of $A_{cs} = 0.3$ m^2. Continuity and Bernoulli equation for low Mach number flows, describe an increase of flow velocity, with

decreasing cross sectional area. Accordingly, the wind tunnel blockage increases the free stream velocity around the solid body. Additionally, turbulent structures are induced in the wake of the body [99].

The LDV technique is employed to measure the inlet boundary conditions for the air flow in front of the geometry. This location is the so called x=0 mm plane, which is located 620 mm downstream of the spray injection orifice (Fig. 4.5). A measurement grid is specified, consisting of 1 702 points with 10 mm spacing in y and z direction. Averaged values from 2 000 samples are obtained for velocity and turbulence quantities, in particular x-velocity component and turbulence intensity, to achieve converged results.

LDV measurements are also conducted behind the windshield geometry (x=410 mm plane) for validating the simulation results. The number of samples was increased to 5 000 at this measurement location, because of the strong temporal fluctuations. Back-flow pattern may lead to mean velocity values close to zero with large rms values, when averaging the results there. Of course, an increased number of samples implies an increased measurement time.
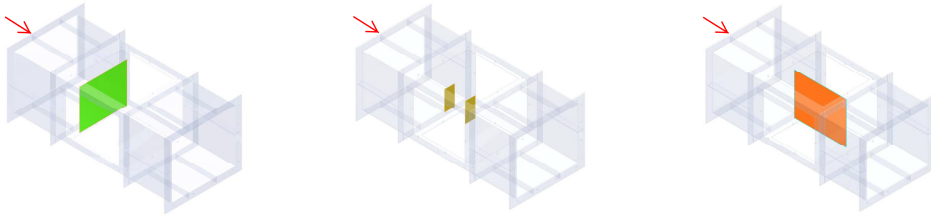
FIGURE 4.5: Inlet measurement plane ($x = 0$ mm) for LDV (left), PDA measurement planes at $x = 0$ mm and $x = 200$ mm (middle), PIV measurement plane (right), red arrows show the flow direction

A smaller measurement grid containing only 35 points is used as a subset of the LDV grid, to quantify the droplet characteristics for the inlet conditions ($x = 0$). Another measurement plane is specified, 200 mm downstream (see Fig. 4.5). Secondary droplets are included within the second measurement plane, due to previous impingement events. Further PDA measurements are carried out along 3 lines containing 7 points, in the center plane of the test section in flow direction. The three profiles are defined parallel to the windshield surface, 10, 20 and 30 mm from the plate surface. At least 10 000 samples have been acquired at each point to ensure high quality measurements. That value is well above the threshold of 5 500, which was suggested by Lefebvre [87] for an accuracy of ± 5 %.

Although the measurement grid is limited to a small area around the spray core, it is very challenging to reach a high accuracy for very dilute sprays.

Velocities are obtained by PIV measurements, which are carried out in the center plane. A laser light sheet illuminates the scene from the top such that the flow structures around the windshield can be observed. The PIV-camera field of view is set equal to the window size of the test section, for a global observation. Accordingly, the complete geometry is captured within one experimental picture. On the other hand, the resulting resolution is low. The boundary layer is not resolved in these PIV measurements. Further details are reported in Brinkmann and Hagemeier [21].

A systematic overview is given in Table 4.4 for all experiments carried out for configuration K1.

4.4 Configuration K2 (Rear View Mirror)

The simplified rear view mirror geometry (wing mirror) is the second configuration with a practical background. It is investigated in a similar manner as the windshield. A picture of the mirror installed in the wind tunnel test section can be seen in Fig. 4.6. Similar to the windshield geometry, the mirror was produced at ISM Braunschweig.

FIGURE 4.6: Wing mirror model mounted in the test section of the wind tunnel; side view (left) and view in upstream direction (right)

A part of the cross sectional area is blocked due to the installation of the mirror geometry. The projected area of the mirror housing is $A_x = 0.0291$ m^2 which leads to a blockage of $\pi_A = 9.7$ % for the mirror geometry within the wind tunnel.

The same measurement techniques are employed as in configuration K1. LDV is used to measure the inlet boundary conditions for the air flow in front of the geometry. The $x=0$ plane grid size and spacing are set to identical values as for K1 both for hardware and software parameters. In addition LDV measurements are carried out at the position $x = 325$ mm, which is well behind the mirror geometry. Therefore, these LDV data may

TABLE 4.3: Location in K2 without PDA data

y-plane	points without acquired data
-25	-
0	3, 4, 19
25	2, 3, 4, 5, 9, 19

serve for validating the simulation results once more. An increased number of samples is required, due to high temporal fluctuations at this point, as discussed before.

Single point measurements have been additionally conducted along the x-axis, to obtain information concerning vortex shedding and its frequency.

The PDA technique is applied to characterize the dispersed liquid phase, using an identical inlet grid as for configuration K1. A $x = 400$ mm plane is introduced as substitute for the plane $x = 200$ mm, because the mirror body covers the area all around $x = 200$ mm. Primary and secondary droplets are captured within the samples of the validation plane $x = 400$ mm, behind the mirror. The secondary droplets may originate from splashing as well as from film break-up.

Futhermore, three arrays of 7×3 points are investigated. The first one is located in the center plane of the test section at $y = 0$, while the other two are defined 25 mm in and out of the center plane, respectively toward positive and negative y-directions. The grid points are radially arranged, in a near quarter circle following the outer surface of the mirror (see Fig. 4.7).
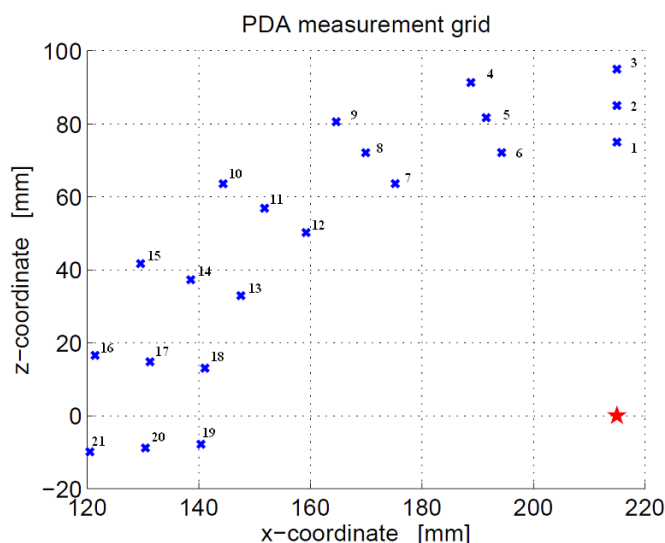
FIGURE 4.7: PDA measurement grid around the mirror outer surface with labeled grid points. The red star represents the center of the circle.

The grid shape deviates slighty from that of the mirror surface curvature. Therefore, an overlap of grid and object occurs at certain grid points. Additionally, some points are out of receiving range of the PDA receiver. Consequently, the PDA does not acquire data at these points. Table 4.3 yields an overview of measurement locations without PDA results.

A systematic overview is given in Table 4.5 for all experiments carried out for the configuration K2. Hessenkemper [59] reports more information concerning the applied measurement techniques and specific experimental parameters.

TABLE 4.4: Configuration K1 (windshield).

Measurement technique	Location	Grid size	Quantity
LDV	$y-z$ plane at $x = 0$ mm, $x = 410$ mm	1702 points	gas velocity and turbulence (1D)
PDA	$y-z$ plane at $x = 0$ mm, $x = 200$ mm	35 points	droplet velocity and size (1D)
PDA profile	$x-z$ plane at $y = 0$ mm	3×21 points	droplet velocity and size (1D)
PIV	$x-z$ plane at $y = 0$ mm	-	gas velocity (2D)
Shadowgraphy	test measurements	-	droplet velocity, size and shape (2D)

TABLE 4.5: Configuration K2 (rear view mirror).

Technique	Position	Mesh size	Quantities
LDV	$y-z$ plane at $x = 0$ mm, $x = 325$ mm	1702 points	gas velocity and turbulence (1D)
LDV profile	$y-z$ plane at $x = [225, 250, 275, 300, 325, 350, 375, 400]$ mm	single points	gas velocity and turbulence (1D)
PDA	$y-z$ plane at $x = 0$ mm, $x = 400$ mm	35 points	droplet velocity and size (1D)
PDA profile	$x-z$ plane at $y = 0$ $[-25, 0, 25]$ mm	3×21 points	droplet velocity and size (1D)

4.5   Film Thickness Measurements

Laboratory-scaled film thickness measurements are carried out in addition to the practical measurements explained before. The main aim of these measurements is to acquire validation data for model improvement. Another objective is to assess and validate this simple measurement technique. A short description of the measurement technique methodology, setup and system parameters is provided in the following. More information have been published in Hagemeier et al. [52]. The publication features additional online material (videos), visualizing the investigated film flow.

4.5.1   Laser-Induced Fluorescence Measurements

The determination of important film quantities such as thickness, velocity or wave structure is of major importance for various engineering applications, for instance when considering vehicle soiling [54]. It is also needed to predict heat and mass transfer processes within film flows. Existing film modeling approaches rely mostly on approximated, empirical models and must always be validated by comparison with experimental results, as discussed in Chapter 3. In order to develop, validate and improve further film models, reliable measurement data are needed. To measure for instance the film thickness, a number of methods have been developed and applied in the past, as described in Alekseenko et al. [6]. However, all these techniques are intrusive and may modify the quantity that should be determined.

Non-intrusive measurement techniques, mostly based on an optical information obtained from fluorescence, have been later developed as described e.g. in Brinkmann and Möller [23], Hidrovo and Hart [60], Lel et al. [90] or recently in Greszik et al. [50]. One main advantage, beside the non-intrusiveness, is the resulting, high spatial and temporal resolution. However, a good measurement accuracy can only be obtained for single point measurements [166] or at most for one-dimensional profiles [138, 139].

Particularly interesting for the present work is the fluorescence imaging method used in the past to measure laminar film thickness and velocity of traveling waves, described first in Liu et al. [91] and later on used in Adomeit and Renz [1], Alekseenko et al. [5] and Moran et al. [104]. In a derived version, this technique has also been used to investigate contact line motion and contact angles [74, 75]. Furthermore, it has been used for experimental investigations of two-phase flows, see e.g. Aguinaga and Bouchet [3], Ausner [9] and Chinnov et al. [27].

As presented in Hagemeier et al. [52], an extended version of this fluorescence imaging method is applied now to characterize two-dimensional films, single droplets and rivulets,

in order to determine simultaneously the associated film thickness, velocity and contact angles. In order to be relevant for practical applications, this technique must be able to deliver two-dimensional information with single-shot measurements.

The measurements described in the following, are based on the principles of laser-induced fluorescence (LIF) and rely on a fluorescent dye tracer. A general description of LIF is given for example in Kohse-Höinghaus and Jeffries [80] and Tropea et al. [149]. The physical background for the thickness measurements is given by the Beer-Lambert law, often employed for absorption measurements [106]. It relates the decrease of light intensity passing through a fluid to the absorption strength:

$$A_\lambda = \ln \frac{I_0}{I_t}. \tag{4.3}$$

The absorbance A_λ is determined from the incident light intensity I_0 and the transmitted light intensity I_t. Another expression for the absorbance yields the connection to the thickness of the fluid film, l_{sample} (in m), the key quantity for film characterization:

$$A_\lambda = c_{dye} \cdot l_{sample} \cdot \epsilon_\lambda, \tag{4.4}$$

where c_{dye} is the (constant and spatially homogeneous) dye concentration in the solution (in $^{mol}/_l$) and ϵ_λ is the molar absorptivity of the fluorescent dye (in $^l/_{mol\ m}$) at a given wavelength λ (in nm). Combining both equations, one obtains:

$$I_t = I_0 \exp(-c_{dye} \cdot l_{sample} \cdot \epsilon_\lambda). \tag{4.5}$$

When working on a top view configuration, the essential property for film thickness measurement is the emitted light intensity in the backward direction, not the transmitted light. Therefore, a simple linear model can be applied ($I_e = \Phi\, I_t$) to deduce the emitted light intensity I_e from the transmitted light intensity [3]. As a result, the emitted light intensity can be finally expressed theoretically as:

$$I_e = \Phi\, I_0 \exp\left(-c_{dye} \cdot l_{sample} \cdot \epsilon_\lambda\right). \tag{4.6}$$

Considering a constant fluorescent dye tracer concentration in the liquid, Eq. (4.6) is an appropriate theoretical description for the emitted light intensity as a function of the film thickness.

4.5.2   Measurement Setup and Calibration

In order to carry out quantitative film thickness measurements, a stable orthogonal arrangement is needed, where all components are fixed at defined positions. Hence, everything is arranged such that no mounting operation is necessary between calibration and measurements, avoiding any artifact induced by modified positions. A detailed description of all components is given in the following and a sketch of the setup is presented in Fig. 4.8.
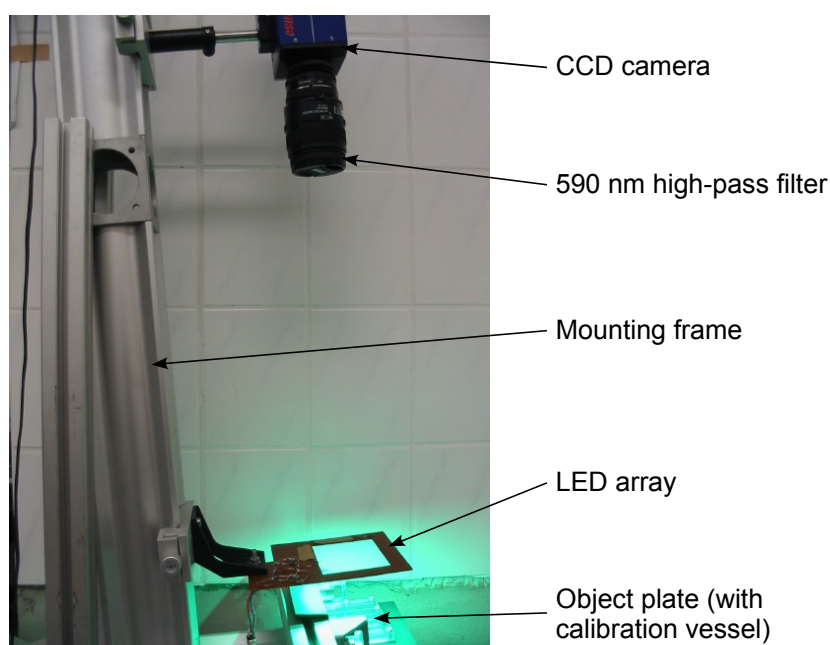
FIGURE 4.8: Setup employed for film thickness measurements

A CCD camera (PCO Sensicam) and the associated software DaVis (from Co. LaVision) are the main components of the measurement system. The 12-bit camera, featuring 4096 gray levels, relies on a chip with 1376×1040 pixels. A 60-mm Nikon objective lens is mounted in combination with a 590-nm high-pass filter. The f-number is set to 2.8 in order to capture as much light as possible, since the illumination with LED is still at low intensity. The exposure time during calibration and measurements has been set to either 30 or 50 ms, depending on the employed fluorescent dye. The imaging rate has been varied between 4.95 and 6.72 Hz, which is suitable for slow, gravity-driven film flow.

An array of 10 green LEDs (from Nichia Corporation) has been employed for the illumination of the imaging scene. Each LED has an electrical power of 1.8 W and a luminous flux of 52 lm. The key properties of the LEDs, in particular the spectrum and temperature emission wavelength are shown in Fig. 4.9. The emission of the LEDs is centered

around 520 nm with an FWHM of 35 nm. They have been operated in continuous mode, which usually requires power correction for long-time measurements, due to a decrease of light intensity associated with increasing temperature. Instead, the employed LEDs have been found to be very stable, even for long operation times for the measurements carried out.
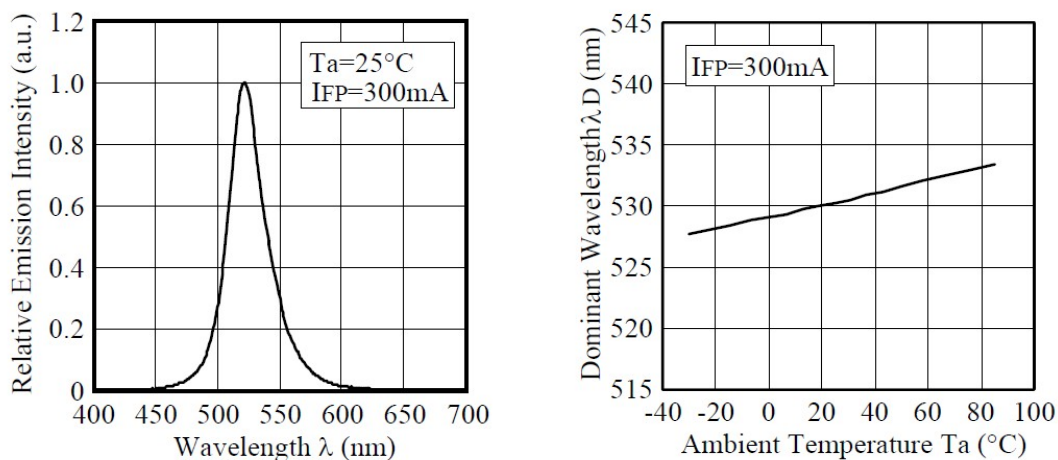
FIGURE 4.9: LED spectrum and emission wavelength as function of ambient temperature (Co. Nichia Corporation)

In any case, the illumination wavelength has to fit the fluorescence dye for LIF application. For illumination wavelengths around 520 nm, Rhodamin B and Rhodamin 101 are suitable and have been employed for the experiments. Information concerning the absorption spectrum compared to other fluorescent dyes can be found in Lehwald et al. [89].

The calibration procedure consists of two separate steps, 1) the geometrical and 2) the intensity calibration. Both are rather simple in principle, but have to be carried out with great care in order to obtain a good accuracy. For the geometrical calibration, a regular dot pattern is used, provided together with the DaVis software. It is automatically recognized when applying the corresponding calibration function. A spatial resolution of 17 $\mathrm{pixel}/\mathrm{mm}$ has been achieved in this manner for the given experimental parameter. The resulting image size (field of view, FOV) is 81×61 mm^2.

As second step, the intensity calibration is carried out. Each of the $4\,096$ gray levels of the camera chip is allocated to a film thickness value. A calibration vessel (Fig. 4.10), made of acrylic glass, is employed with 6 channels of controlled depth: $2, 1, 0.7, 0.5, 0.2$ and 0.1 mm (in Fig. 4.10 from left to right). Every channel is filled with the fluorescent liquid and exposed for excitation. This calibration method can be employed for even thinner films, as shown by Inagaki et al. [68].

TABLE 4.6: Accuracy of calibration vessel

Channel depth [μm]	Standard deviation [μm]	Relative deviation [%]
100	19.97	19.97
200	21.84	10.92
500	25.32	5.06
700	27.75	3.96
1000	44.23	4.42
2000	59.47	2.97
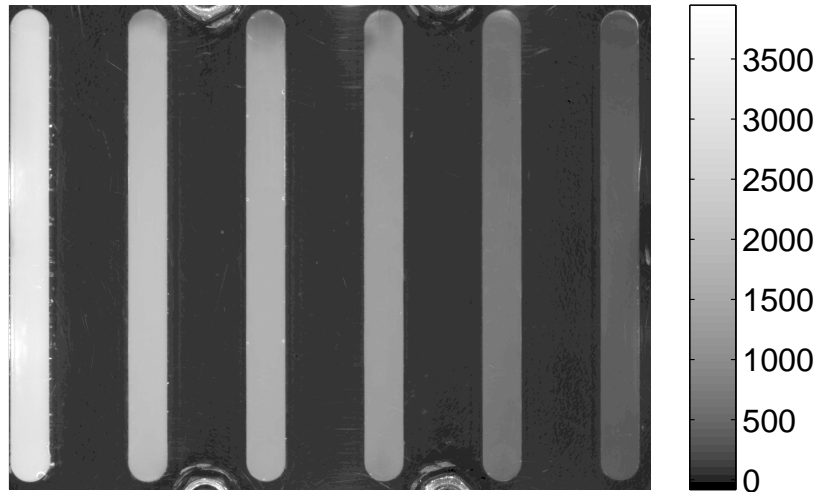
FIGURE 4.10: LIF calibration vessel, showing calibrated channels filled with the corresponding fluorescent solution; colorbar shows gray level intensity (in counts)

The resulting accuracy associated with the manufacture of the calibration vessel (see Table 4.6), is smaller than that of the statistical repetition error obtained during calibration (see Table 4.7 and Fig. 4.11). In addition to the six film thickness values listed above, the intensity value between the channels (i.e., the zero film thickness) can be used as a seventh value for obtaining a calibration function. Finally, the calibration is carried out for two fluorescent dyes solved in water, Rhodamin B at a concentration of 10 $\mathrm{mg/l}$ with an exposure time of 50 ms and Rhodamin 101 at a concentration of 10 $\mathrm{mg/l}$ with an exposure time of 30 ms.

TABLE 4.7: Averaged results of film thickness calibration (in gray level counts).

Film thickness [μm]	Rhodamin B	max(RMS)	Rhodamin 101	max(RMS)
0	128.2	33.9	70.3	16.8
100	604.5	153.7	423.4	108.3
200	805.2	58.4	647.4	60.4
500	1418.1	90.9	1251.4	87.4
700	1786.7	75.7	1636.3	79.6
1000	2156.4	102.8	2060.8	112.2
2000	3243.8	158.9	3225.4	136.4
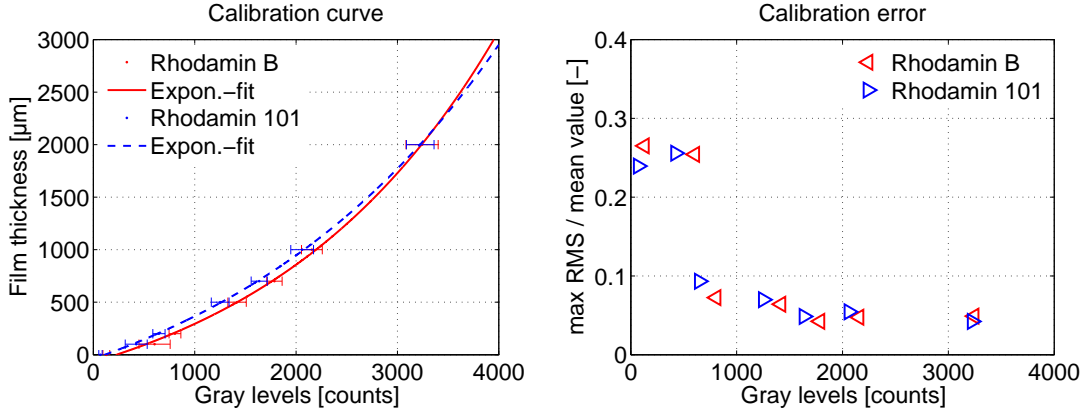
FIGURE 4.11: Calibration curve (left) and normalized calibration error (right)

The post-processing of the calibration images is realized in several steps. First, the background image is subtracted to eliminate illumination inhomogeneities. This background image is an average of 100 images taken from a dark paperboard, without the calibration vessel. Afterwards, a pixel array of 20×700 pixels, associated with a defined area within each channel of the calibration vessel, is used to obtain mean value and standard deviation of the gray level in each channel. One calibration set consists of 100 single images, such that an average value is obtained from 1.4 million samples during this procedure.

The complete calibration process is repeated three times separately for each fluorescent dye tracer, in order to check repeatability. An overall intensity count is derived by averaging over the three runs. Since the average for the standard deviation should smooth out any measurement error, only the maximum deviation values are considered to quantify the quality of the calibration. All relevant data are summarized in Table 4.7, where all values have been rounded up to the first decimal. Of course, all computations are carried out with double-precision quantities.

Finally, the averaged values have been used to fit a function to the experimental data (see Fig. 4.11). The curve is fitted, employing an exponential function, which is estimated as best fit from the correlation coefficients. It takes the form:

$$h_f = y_0 + A_1 \exp\left[\frac{I_g - x_0}{t_1}\right], \tag{4.7}$$

where I_g is the measured gray level intensity. The function parameters are provided in Table 4.8. Be aware that the validity of the calibration function has been checked only for the calibration range up to a gray level of $3\,250$ counts. It is assumed to be valid also for higher count values and corresponding, higher film thickness values. This assumption is only needed, if measuring rivulets or droplets thicker than 2 mm.

TABLE 4.8: Exponential function parameters for both calibration cases.

function parameter	Rhodamin B	Rhodamin 101
y_0 [μm]	-729.5	-991.0
x_0 [counts]	-1796.7	-2476.4
A_1 [μm]	300.5	394.7
t_1 [counts]	2282.1	2814.2
Correlation coefficient	$999.4 \cdot 10^{-3}$	$999.9 \cdot 10^{-3}$

Due to the employed, non-linear calibration function, the resolution of the method differs with the measurement range. For Rhodamin B, the resulting minimum and maximum resolution values are 0.14 and 1.29 μm, respectively; while they are 0.13 and 1.03 μm for Rhodamin 101, respectively.

As stated previously, the light power output of the LEDs may decrease due to heating up with time. In order to evaluate the associated power loss of the LEDs, the overall intensity value of the illuminated image is calculated by summing up the individual pixel counts. To this end, 2 500 images are taken with an acquisition rate of 6.72 Hz which means a total time of 6.2 minutes. The results (see Fig. 4.12) indicate that the LEDs are working at constant power for this time. However, a start-up time of about 40 seconds is required to reach a power output ratio of 0.99, as shown in the zoom in the embedded figure.
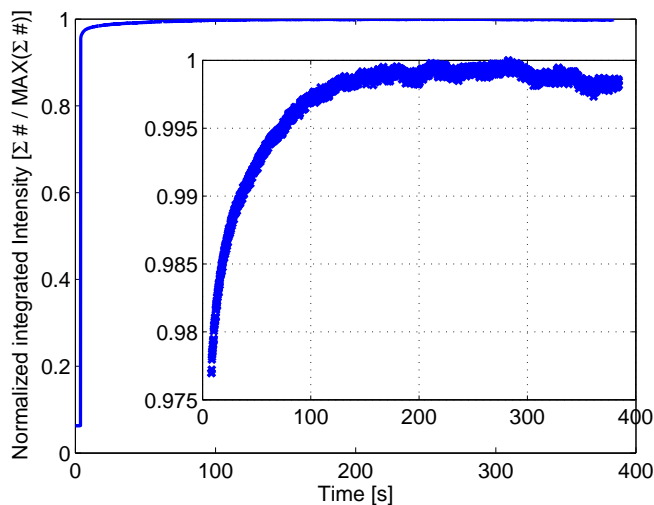
FIGURE 4.12: LED light power output during the experiments; the embedded graph is a zoom on the upper left part of the curve

4.5.3 Experimental Film Configurations

Two main configurations have been investigated. The first is an open-channel flow and the second a rivulet generated by single droplet deposition. Both experiments have been conducted using Rhodamin 101 as dye tracer, which is chosen because of the better calibration results. Using Rhodamin 101, higher film thickness values can be resolved with more gray levels and less deviation (see Table 4.7).

Open-channel flow

A standard open-channel configuration is used as a first validation experiment. At a fixed inclination angle of 5°, a continuous film flow is generated on a glass plate (width: 200 mm; length: 200 mm).
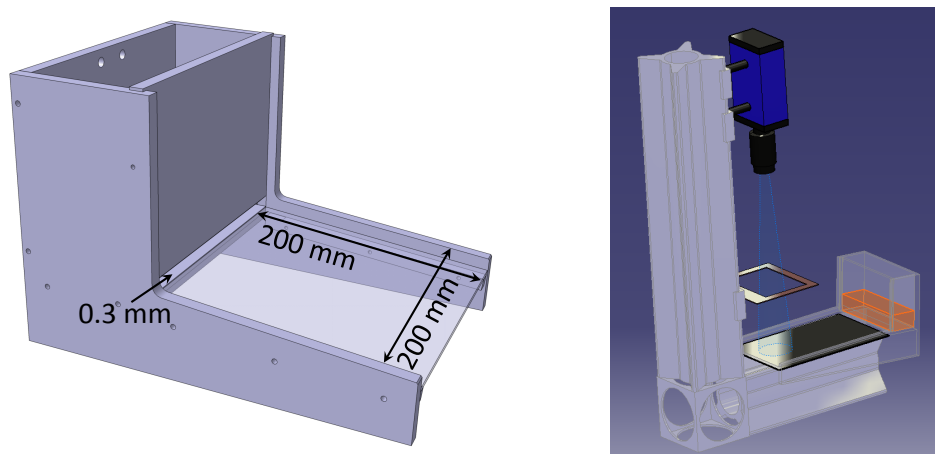
FIGURE 4.13: Schematic drawing of the open-channel flow setup (right), details of the open-channel vessel (left)

The ratio of plate width to image width is $r_w = 2.44$ and the length ratio is $r_l = 3.22$, which are important for later interpretation of the results.

Three different volume flow rates have been considered: 1.59, 1.65 and 1.71 ^{l}/min. According to the definition used for instance in Zhou et al. [166]:

$$\mathrm{Re} = \frac{4\,\dot{m}}{b\,\mu},\tag{4.8}$$

they are associated with Reynolds numbers Re=525, 545 and 565, respectively. In Eq. (4.8), b is the plate width (in m), μ is the dynamic viscosity (in ^{kg}/m s) and $\dot{m}$ is the liquid mass flow rate (in ^{kg}/s). The film thickness can be calculated, based on the simplified Navier-Stokes equations. An analytical expression for the film thickness can

be derived, when the volume flow rate is known:

$$h_f = \left(\frac{3 \, \dot{V} \, \mu}{b \, \rho \, g \sin(\alpha)} \right)^{\frac{1}{3}},$$

$$(4.9)$$

as was shown by Nusselt [112]. Subsequently, the mean film velocity can be obtained by using the continuity equation. The corresponding film thickness and mean film velocity values are listed in Table 4.9. The reservoir opening affixed to the upper end of the glass

TABLE 4.9: Open channel flow configuration.

Reynolds number	Film thickness [µm]	Mean film velocity [m/s]
525	774	0.171
545	784	0.175
565	792	0.179

plate has a fixed slit width of 0.3 mm.

In order to increase the complexity of this simple configuration, a cylindrical obstacle (diameter 9.9 mm) has later been placed in the middle of the flow. As a consequence, the flat film becomes wavy and associated disturbances can be measured.

Rivulets

First experiments are performed with single droplets impacting onto the inclined surface, made of acrylic glass. The inclination angle towards the horizontal direction has been varied, considering in particular angles of 5, 15 and 19.5°. The distance between plate, camera and LED is always kept identical during calibration and later measurements.

Droplets are generated using a medical cannula. The cannula properties and the resulting droplet diameters are known: 2.16, 2.86 and 3.3 mm, from previous measurements [14]. The droplet rate is controlled using a hose clip, set to a constant value of 1 Hz. A bottle with a volume of one liter is used as a reservoir for the fluorescent dye solution. The tip of the cannula is located 8 cm above the surface, such that the interaction regime for droplet impingment is simple deposition. It is associated to low Weber numbers, ranging from 40 to 62 for normal impingement.

Camera and LED settings are kept identical to those employed during the calibration procedure. The software settings were modified, in particular the acquisition rate which is reduced to 4.95 Hz while the number of acquired images is increased to 1 000.

Generally, it is observed that several primary droplets impact the surface and accumulate into a larger puddle. When reaching a certain volume, this puddle starts to flow down

the inclined plate. In Table 4.10, the corresponding number of accumulated droplets has been summarized (rounded values).

At small inclination angles, this value could not be obtained, since the puddle moves stepwise with each impingement event. This is a well-known problem with single droplet and rivulet flows at small inclination angles as stated by Johnson et al. [75]. Accordingly, configurations with small angles have been excluded from the velocity estimation process described later.

TABLE 4.10: Number of accumulated droplets associated with the onset of a continuous sliding movement downwards in the experimental configurations. A special indication is applied for the case of 5° inclination, where no values (n.v.) can be defined.

Inclination angle [deg]	cannula I 2.16 mm	cannula II 2.86 mm	cannula III 3.3 mm
5	n.v.	n.v.	n.v.
15	14	8	6
19.5	10	7	5

Besides the film thickness values, the velocity of the sliding droplets is very interesting and can be obtained with the presented method. Hence, a time series of images has to be analyzed. The film thickness gradient along the profile in flow direction can be obtained during the post-processing.
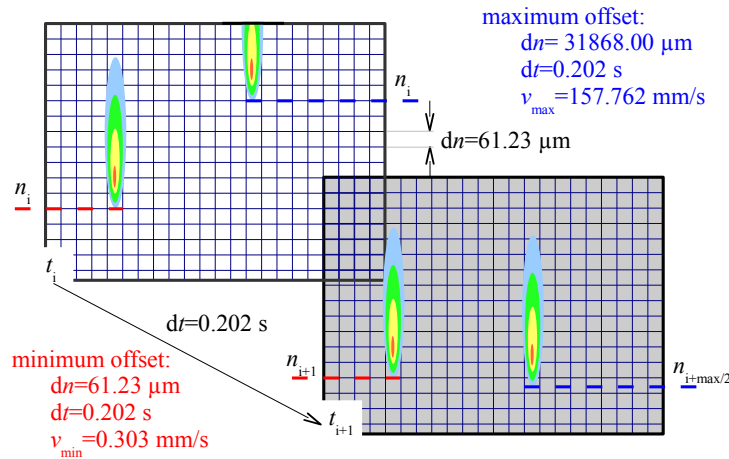
FIGURE 4.14: Schematic description of image processing to estimate minimum and maximum velocity limits which can be measured with the developed technique.

The quantitative information for sliding droplet velocity have been obtained from image processing. The velocity limit and resolution are related to the temporal and spatial resolution as well as the FOV (Fig. 4.14). The temporal resolution is given by the image acquisition rate ($f_r = 4.95$ Hz), while the spatial resolution corresponds to the scale

factor ($s_f = 16.97$ pixel/mm). A value of $v = 0.30$ mm/s can be obtained as minimum velocity (apart from zero). Furthermore, it is the velocity resolution (minimum class size). The theoretical, maximum velocity is $v = 157.76$ mm/s. It can be derived from the half image length in flow direction divided by the repetition rate. This corresponds to the condition, such that a droplet must be seen at least twice when passing through the image. Nevertheless, the real peak velocity that can be measured is even lower, considering that the droplet path starts at a location within the image.

The image processing algorithm runs in the following steps:

1. Identify characteristic flow path (pixel column with thickness values) for considered data set.

2. Loop over all images, to account for each time step and store pixel columns to assemble a matrix of the size $m \times n$. The variable m is the number of pixels in flow direction and n is the number of time steps (see left image in Figs. 6.29 and 6.30).

3. Calculate gradients (in x, y-direction) of the image quantity (film thickness).

4. Convert pixel gradients into gradients in time and space using values of temporal and spatial resolution. The following equations yield the film thickness gradient in space:

$$\frac{\mathrm{d}h_f}{\mathrm{d}y} = \frac{\mathrm{d}h_f}{\mathrm{d}pix} \cdot \frac{\mathrm{d}pix}{\mathrm{d}y} \tag{4.10}$$

and time

$$\frac{\mathrm{d}h_f}{\mathrm{d}t} = \frac{\mathrm{d}h_f}{\mathrm{d}pix} \cdot \frac{\mathrm{d}pix}{\mathrm{d}t}. \tag{4.11}$$

The variables in these equations are the film thickness h_f and its variation in time $\frac{\mathrm{d}h_f}{\mathrm{d}t}$ and in space $\frac{\mathrm{d}h_f}{\mathrm{d}y}$. Accordingly, the latter two are obtained from the image gradient, which yields the film thickness variation along the image pixel $\frac{\mathrm{d}h_f}{\mathrm{d}pix}$. The gradients $\frac{\mathrm{d}pix}{\mathrm{d}y}$ and $\frac{\mathrm{d}pix}{\mathrm{d}t}$ represent the spatial and temporal resolution of the measurement technique. Therefore, they are fixed values, as described in the previous section.

5. Divide gradient matrices elementwise to obtain velocity matrix:

$$v_y = \frac{\mathrm{d}y}{\mathrm{d}t} = \frac{\frac{\mathrm{d}h_f}{\mathrm{d}t}}{\frac{\mathrm{d}h_f}{\mathrm{d}y}} \tag{4.12}$$

6. Evaluate matrix elements in terms of a velocity histogram.

This conversion process leads to velocity information for all droplets within one data set.

Conclusions

The two main experimental configurations (windshield and rear view mirror) have been presented in this chapter, including all important details concerning the measurement techniques and specifications. In addition, information concerning the expected accuracy have been given.

Then, an innovative film thickness measurement technique, based on induced fluorescence was presented. To my knowledge, this is the first time that fluorescence was induced by LEDs, using Rhodamin 101 as fluorescence tracer.

Further tests showed the even higher potential of LEDs, in comparison with lasers, when using the LEDs in pulsating mode. While increasing considerably light intensity, the stability is improved due to short-term operation. Future application may focus on high-speed fluorescence imaging using LEDs.

In the following chapter the film flow simulations are presented. There, the necessity of correct boundary conditions and values for validation is quite obvious. Finally, experimental and numerical results are compared in Chapter 6.

Chapter 5

Numerical Simulations

5.1 Simulation Procedure

As a complement to experimental investigations of vehicle soiling processes, there are efficient tools for development and optimization based on Computer Aided Engineering (CAE), especially in CFD. Numerical models are available, as described in Chapter 3. Thanks to the fast progress in computing power, the importance of numerical contributions are rapidly increasing in the area of rain water management research. Earlier CFD investigations were limited to steady computations or poor grid resolution in order to keep everything tractable. Nowadays, parallel computing has enabled not only complex, but also improved numerical simulations of vehicle soiling processes. The approaches proposed in the literature range from simple Reynolds-Averaged Navier-Stokes (RANS) approaches [16] over more detailed hybrid methods like the Detached-Eddy Simulations (DES) [71], to computationally expensive Large-Eddy Simulations (LES) [24] or Lattice-Boltzmann approaches [46, 167].

The modeling approaches used in practice, including all assumptions, employed sub-models and limitations are reviewed here in detail. Since vehicle soiling simulation is a complex procedure involving many computational steps, a multi-step algorithm has emerged as most promising solution from the beginning of numerical soiling simulations. Karbon and Longman [79] were the first to propose a 3-step algorithm, which was later described by Foucart and Blain [46]. Using this kind of algorithm, the computation of the aerodynamic field, the droplet tracking and the film modeling are successively included for vehicle soiling simulation. Each step requires its own modeling approach. Campos et al. [24] combined the two last steps (droplet tracking and film flow) into one simultaneous step, since an instationary modeling approach was used. Obviously, the coupling between the different steps must always be considered. To go into more detail,

the first modeling step in the simulation sequence is the simulation of the aerodynamic field around the car or the obstacle of interest.

As mentioned before, different approaches are available for the flow field simulation, impacting all results that are derived from the flow field. Different solution strategies for the aerodynamic flow field may lead to different soiling patterns. Preliminary studies showed that particle tracking performed in a RANS flow field compared to a time averaged solution from URANS, SAS or DES/LES leads to different tracks and deposition location for an identical configuration. This is clearly an interesting aspect for numerical investigations, but goes beyond the scope of this study. Those questions have to be considered in the future.

All simulations carried out during this study are based on simple RANS solutions for the flow field around a rear view mirror. The film flow is computed using the original film model by Anderson and Coughlan [8] together with an improved version of the film model. The improved version of the film model includes all aspects discussed in Section 3.2.

The results obtained from the improved film model are compared with those from the original formulation. Similarities and differences are discussed in Chapter 6. Details concerning the pre-processing and simulation setups are presented in what follows.

5.2   Configuration K2 (Rear View Mirror)

The rear view mirror configuration has a highly complex geometry. This is due to the curved surface and the asymmetric shape. The mirror shape is most interesting for soiling investigations because of several reasons:

1. The aerodynamic behavior of the mirror is important for further aspects like aero-acoustics and drag reduction. This is because the mirror is completely exposed to the approaching air flow.

2. There is no cleaning system and no wiper blade to keep the mirror housing free from liquid films.

3. The complete liquid volume that is deposited on the mirror surface is subject to aerodynamic forces that dictate the film motion and break-up.

4. Droplets, that are released from the film often re-impact the side window.

Consequently, the investigation of the mirror geometry is highly relevant for understanding the vehicle soiling process. In the following, the numerical approaches for aerodynamics, dispersed phase and film simulations are described. The preliminary steps, which include grid independence study, the choice of an appropriate turbulence model and of the boundary layer refinement are also outlined.

5.2.1 Numerical Approach

The basis for any soiling simulation is the exact flow field around the vehicle. Once again, the flow field can be obtained from different approaches available for flow field simulation. More details in terms of resolved turbulent structures can be obtained if DES or SAS approaches are employed. Due to the transient nature of these approaches, a special treatment is needed if one-way coupling is considered for the subsequent Lagrangian droplet tracking and film simulation. The flow field decides in which direction droplets move and where they impinge upon the surface.

For preparing the numerical investigations, some preliminary studies have been conducted to define the correct model parameters. One meaningful non-dimensional number is the Reynolds number, which is built from the characteristic length of the geometry, the mirror diameter (15 cm) and flow properties (velocity and viscosity). For the present case, three Re numbers, $1.46 \ 10^5$, $1.95 \ 10^5$ and $2.44 \ 10^5$ have been obtained for three approach velocities, 15, 20 and 25 $\mathrm{m/s}$. Simplifying assumptions have been made for the shape of the mirror, assumed to be a symmetrical half cylinder.

The Mach number, which is found to be 0.043, 0.058 and 0.072 for the three cases, justifies the assumption of incompressible flow conditions.

Beside the parameters discussed before, one can have an idea of the unsteady behavior of the flow in the wake of the geometry. In particular, the vortex detachment frequency can be estimated according to the Strouhal number (Sr), which is defined as

$$\mathrm{Sr} = \frac{f \cdot d}{v_\infty}, \tag{5.1}$$

where f, d and v_∞ are the detachment frequency, the diameter and the approaching velocity. For higher Re ($150 < \mathrm{Re} < 1.3 \ 10^5$) also known as sub critical regime [137], the Sr number takes a constant value of $\mathrm{Sr} = 0.21$, such that the frequency f can be derived. Since the Re numbers calculated for the rear view mirror deviate insignificantly from the upper limit, an a priori guess of the frequency values yields 21, 28 and 35 Hz for the three approaching velocities. The order of magnitude is now clear, but of course this deviation has to be kept in mind when analyzing any results.

5.2.2   Simulation preparation

The mesh generation is important as well, especially for more complex simulations using DES or SAS. Here, the grid must fulfill requirements arising from RANS and LES approaches in different regions of the computational domain. Most important during mesh generation is to resolve the boundary layer of the geometry. The dimensionless wall distance y^+ can be derived according to Schlichting [137] from:

$$y^+ = \frac{y}{\nu}\sqrt{\frac{\tau_w}{\rho}}, \tag{5.2}$$

where τ_w is the wall shear stress, ν and ρ are the fluids kinematic viscosity and density and y is the distance to the wall. Since an a priori estimation of the boundary layer thickness is hard, especially for complex geometries, a block-structured mesh is generated, using ICEM-CFD from Co. ANSYS. That way, a grid refinement is possible, when it proves necessary during the numerical studies.

5.2.2.1   Grid independence study

The mesh generation is directly linked to the computation itself, since a mesh independent solution is desired. Hence, three meshes have been generated, each with a successively refined grid. The number of vertices along the edges of the mesh was increased by a constant factor of 1.25, resulting in three meshes with 2.08, 4.53 and 8.54 million cells.

The criterion used to estimate the independence of the solution is directly linked to the objectives of the computation. For vehicle soiling simulations, the exact prediction of the film flow is most important. Based on this fact, it is straightforward to use a variable that is decisive for film transportation, which is the wall shear stress.

Since there are other aspects to be taken into account, such as the tracking of the droplets that form the film by impinging on the surface, additional parameters have to be checked.

Finally, the face-averaged wall shear stress around the mirror geometry, the pressure drop between inlet and outlet, and the pressure and friction coefficients have been used to estimate the grid independence. As can be seen from Fig. 5.1, all parameters show an asymptotic convergence behavior for refined computational meshes, with more than 4 million grid cells. Therefore, all computational results obtained with the finest mesh, with approximately 8.5 million grid cells are mesh independent solutions.
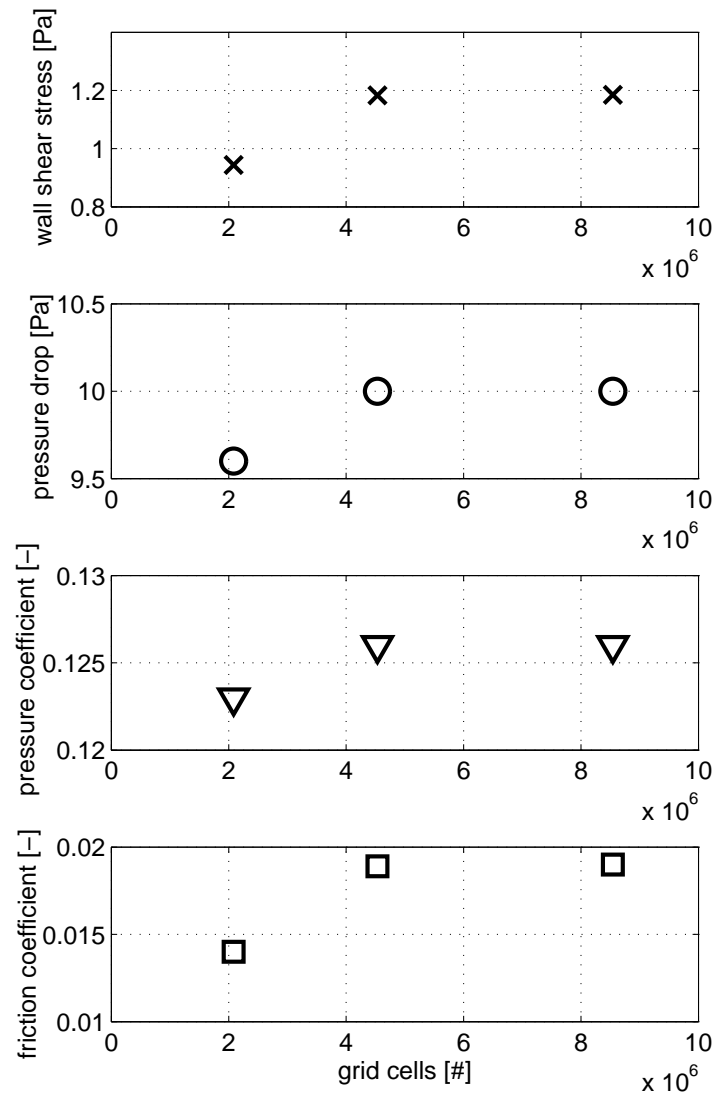
FIGURE 5.1: Wall shear stress, pressure drop, pressure coefficient and friction coefficient obtained during grid independence study

This result has been obtained with the $k-\omega$ SST model. To evaluate the best turbulence model, further considerations are made in Section 5.2.2.2, where a comparison of the results obtained with different turbulence models is presented.

5.2.2.2   Turbulence modeling

The computational mesh with 8.5 million grid cells, which is considered to deliver grid independent simulation results is then used to investigate the performance of different turbulence models.

Turbulence modeling is an important aspect for the whole simulation process, since particles interact with turbulent structures. Thus, the impingement locations are directly coupled to the turbulence representation.

As mentioned before, different studies showed an advantage of the k-ω turbulence model, when dealing with wall-bounded flows or flows considering particle deposition [86]. In principle, there are several types of k-ω models each having parameters and submodels. To identify the most appropriate model for the simulation of vehicle soiling, test calculations have been carried out with the standard k-ω, the k-ω SST and the transitional SST turbulence models. The first two models are 2-equation models, while the last one is a 4-equation model that describes the laminar-turbulent transition.

All three turbulence models have been employed each for three different approach velocities, 15, 20 and 25 ^{m}/s, used before in the windshield configuration. Combining the approach velocities with the mirror diameter (vertical extension of the mirror) and the kinematic viscosity of air at 20°C, the associated Re numbers are 1.47 10^5, 1.96 10^5 and 2.45 10^5.

Figure 5.2 shows the face-average wall shear stress on the mirror housing, as well as the pressure and friction coefficient obtained as a function of Re, for the three different turbulence models. It can be seen that differences exist between all of them. Most similar results have been observed for the k-ω SST and the transitional SST turbulence models. The deviation of the standard k-ω model to the other turbulence model is not only quantitative, but also qualitative (see pressure coefficient in Fig. 5.3).

Investigating local values of pressure coefficients along the profile around the mirror contour (Fig. 5.4), it becomes increasingly obvious that the largest deviation exist with the use of the standard k-ω model. The profiles from the k-ω SST and the transitional SST turbulence models are almost identical. From these findings, the application of the k-ω SST or the transitional SST turbulence model seems to be appropriate for calculating the turbulence flow field around the mirror geometry. The transitional SST turbulence model was finally chosen for further simulations, since the transitional behavior of the boundary layer has to be accounted for.

5.2.2.3   Boundary layer resolution

After checking the grid independence and identifying the most appropriate turbulence model, the needed resolution of the boundary layer was checked. A refinement is necessary to improve the resolution near the walls, especially around the mirror housing. In two steps, the boundary layer resolution was improved by refining the cells in the first
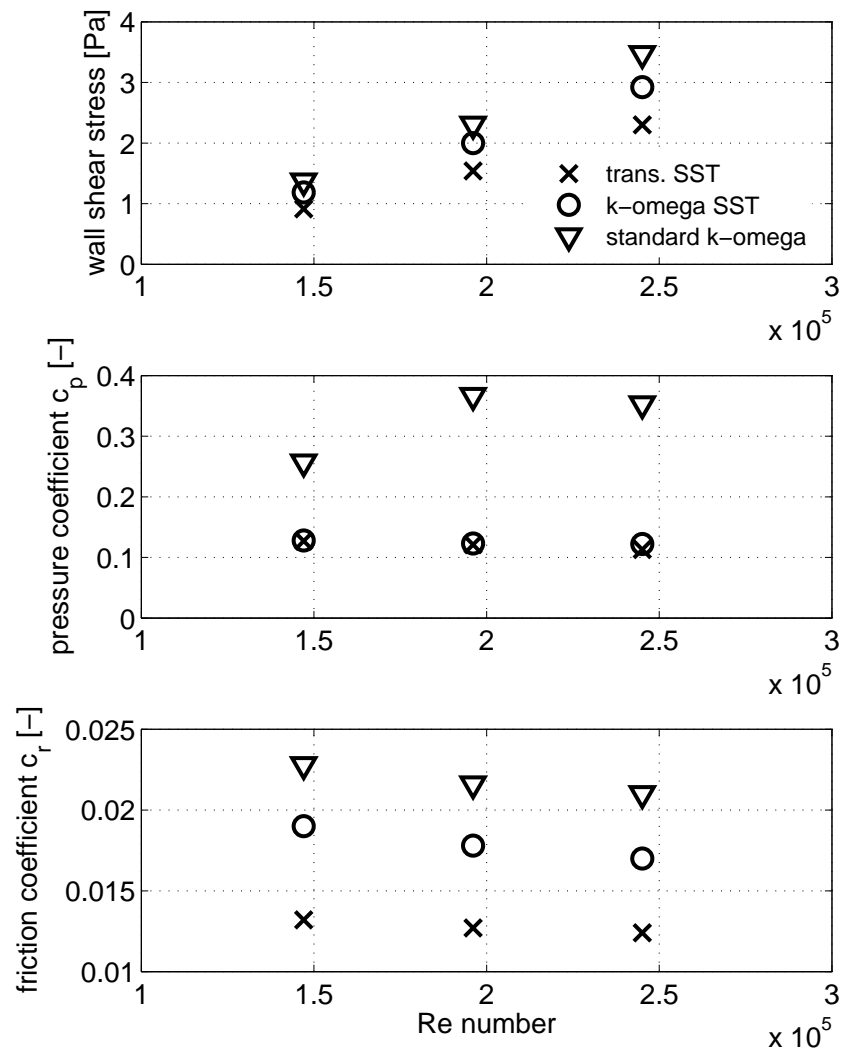
FIGURE 5.2: Comparison of simulated wall shear stress (top), pressure coefficient c_p (middle) and friction coefficient c_r (bottom) obtained with different turbulence models

blocks around the mirror. The adapt-function for y^+ included in Fluent CFD software was used.

The comparison of the solutions with the adapted grids are shown on Table 5.1, where the number of cells and further important values for the different grids are given. Note that all simulations have been performed with the transitional SST turbulence model, because of the aforementioned turbulence model investigations. As can be seen, the pressure and friction coefficients are almost unaffected by the improved boundary layer resolution. On the other hand, the wall shear stress does change after the grid adaptation. Further effects of the boundary layer adaptation are described using profile plots along one contour of the mirror, as shown in Fig. 5.4. Several profiles at different locations around
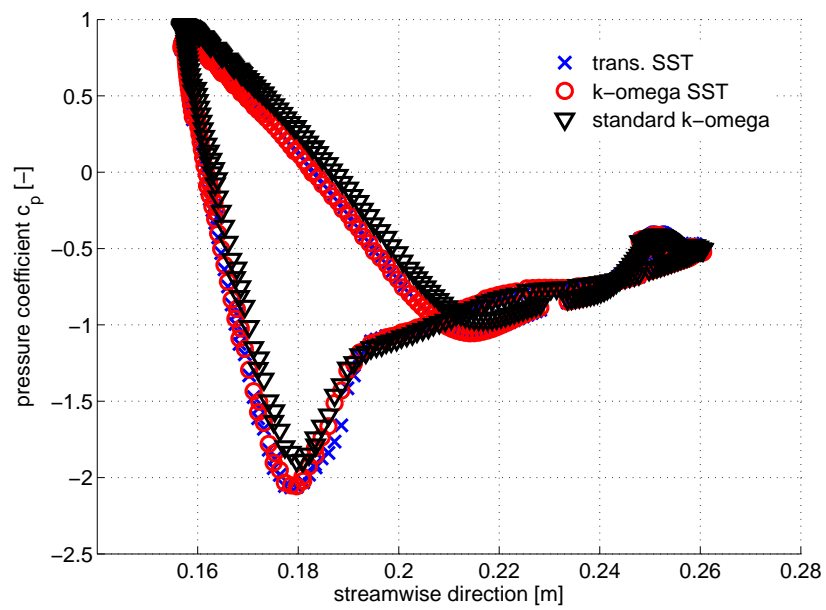
FIGURE 5.3: Comparison of pressure coefficient profiles
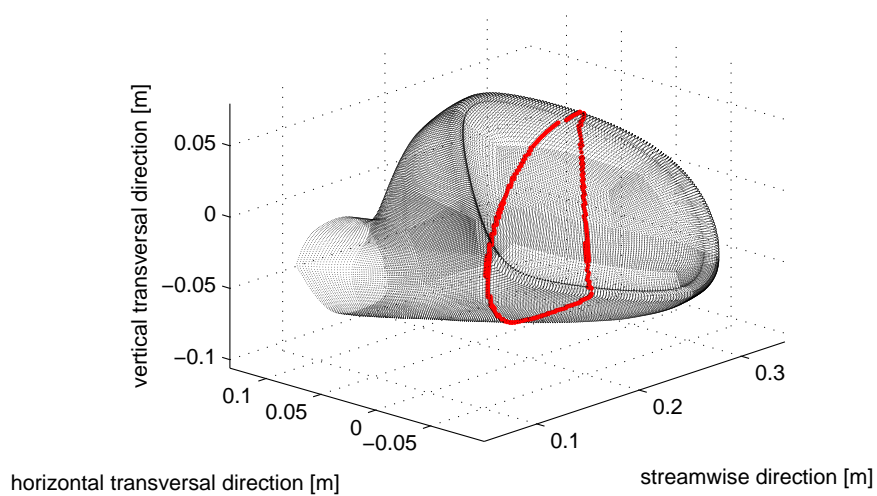
FIGURE 5.4: Mirror contour for boundary layer examination

TABLE 5.1: Boundary layer adaption.

# grid cells	wall shear stress [Pa]	face-averaged y^+	c_p	c_r
8.544 10^6	0.913	3.587	1.27 10^{-1}	1.32 10^{-2}
9.216 10^6	0.958	1.186	1.14 10^{-1}	1.34 10^{-2}
11.227 10^6	0.975	0.003	1.14 10^{-1}	1.34 10^{-2}

the mirror have been used to investigate the evolution of the dimensionless velocity u^+ over the dimensionless wall distance y^+. The dimensionless velocity u^+ is defined as:

$$u^+ = \frac{u}{u^*} = \frac{u}{\sqrt{\frac{\tau_w}{\rho}}}, \tag{5.3}$$

where u is flow velocity tangential to the surface. The other variables have been introduced earlier and therefore are known by now.

The profiles are defined similar to the profiles used for the experiments, where the spray was analyzed close to the mirror surface using the PDA technique (see Section 4.4). Seven profiles are prescribed in accordance to the experiments at three different horizontal positions that are perpendicular to the flow direction. There, simulation data are extracted for local flow velocity, wall distance and wall shear stress. The velocity profiles obtained from the simulation follow closely the theoretical velocity profiles for the sub-layer and log-region. According to Wilcox [162], the velocity in these regions is given by

$$u^+ = y^+, \tag{5.4}$$

for the sub-layer and

$$u^+ = \frac{1}{\kappa} \ln y^+ + C \tag{5.5}$$

for the log-region. The second correlation is also know as the law of the wall, featuring $C \approx 5$, a dimensionless integration constant and $\kappa \approx 0.41$, the Kármán constant. Both values are valid for smooth surfaces [162], as considered for all investigations in this work.

The transition from one boundary layer region to another occurs around the point y^+, which can be identified by equalizing Equations (5.4) and (5.5). With the considered values of C and κ, the transition occurs at $y^+ \approx 10.8$.

From Figure 5.5, it can be seen that there is only a small deviation from the theoretical boundary layer within the sublayer region. All plots show the same trends for the log-layer, deviating from the progress of the theoretical curve. This could be expected, because of the complex geometry of the mirror. Moreover, the stagnation point at the front is included within the profiles that have been defined along the upper curvature
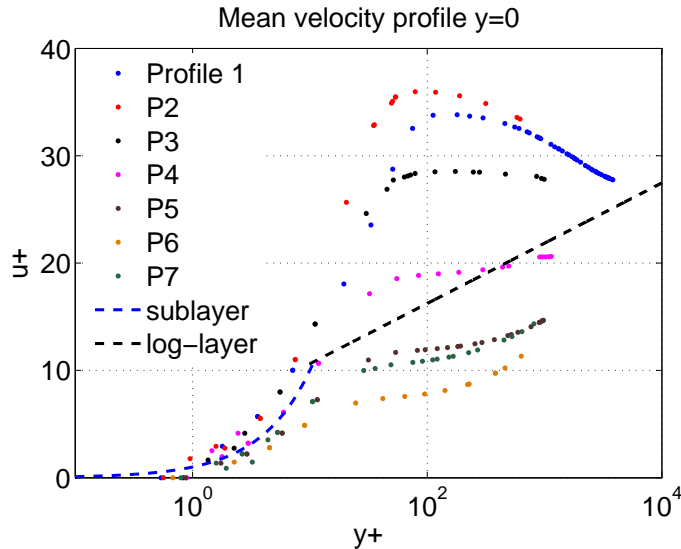
FIGURE 5.5: Mean velocity profile as a function of wall distance from the mirror at the vertical center plane of the wind tunnel test section, at an approach velocity of 25 $^m/_s$. The correlations for sub-layer and log-region are plotted as dot or dash-dot lines. The profiles correspond to the experimentally investigated points shown in Fig. 4.7. Profile 1 extends along the direction through the points 1, 2 and 3, profile 7 extends along the direction through the points 19, 20 and 21. All other profiles are located in between in the respective direction.

of the mirror surface. Especially here, a fully developed boundary layer can not be expected.

In conclusion, if a fully resolved boundary layer is required, the total number of grid cells has to be increased by 2.7 million cells, in addition to the solution of the grid independence study ($\approx$ 8.5 million cells). The final simulations have to run with less grid cells, since film simulations are not affordable for grids with 11.2 million cells. However, interesting information have been obtained from the boundary layer analysis. The dimensionless air velocity profiles give an insight of the flow field around the mirror. They are useful for further interpretation of experimental results, as will be discussed in the next section.

5.2.3 Lagrangian particle tracking

The steady flow field solution is used as a basis for the film simulation, where a simple one-way coupling is considered. In the same manner, the Lagrangian droplet tracking is carried out. Furthermore, the tracking is kept as simple as possible without particle-particle interaction, evaporation or breakage. These simplification are based on reasonable considerations. Droplet interaction is neglected because of the dilute spray. As shown in Fig. 3.9 of Section 3.3.2, the volume fraction ranges well below that which necessitates a four-way coupling. Evaporation can be neglected in the simulation when
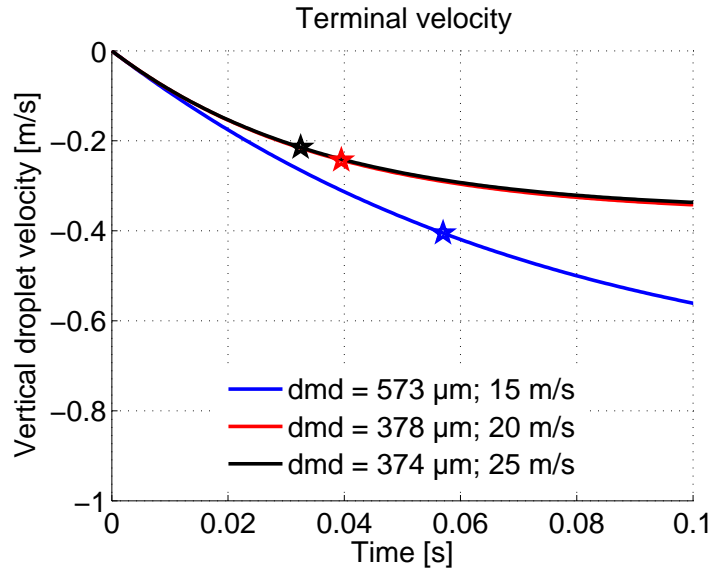
FIGURE 5.6: Accelerating vertical droplet velocity

assuming isothermal conditions. Droplet break-up is unlikely to occur as proved by the analysis of the aerodynamic We number (see Section 3.3.3).

All injected particles are initialized as parcels with representative properties that have been measured with the PDA on a 7×5 points grid. Initial positions are altered randomly in a specified range around respective pre-defined mean values for x, y and z-coordinates. The most important injection properties are summarized in Table 5.2 for the three investigated velocities. It is noteworthy that the y-velocity component is

TABLE 5.2: Injection properties for the dispersed phase simulation.

Property	15 m/s	20 m/s	25 m/s
mean diameter [m]	$5.73 \cdot 10^{-4}$	$3.78 \cdot 10^{-4}$	$3.74 \cdot 10^{-4}$
x-velocity [m/s]	10.9	15.58	19.16
y-velocity [m/s]	-0.4051	-0.2428	-0.2147
mass flow rate [kg/s]	$8.32 \cdot 10^{-2}$	$8.32 \cdot 10^{-2}$	$8.32 \cdot 10^{-2}$

not measured, but computed by solving the equation of motion in vertical direction. Assuming spherical particles and accounting for gravitational and drag forces only, the terminal velocity (y-velocity) was obtained for the different mean diameters. Respective time intervals are related to the traveling distance of 620 mm from the orifice to the $x = 0$ plane. The traveling velocity is assumed to be equal to the measured x-velocity component. Thus, the time intervals of 32.4 ms, 39.8 ms and 56.9 ms can be deduced. These values have been marked as stars on the droplet acceleration curves in Fig. 5.6.

5.2.4 Film flow modeling

The film simulations have been carried out with the modified version of the film model as well as with the original model [8]. The modified model accounts for complex droplet-wall/film interactions and wetting limitation as explained in Section 3.2.3. The improved break-up model has been implemented, but remains inactive. Still, the difference in the break-up behavior is considerably due to the film expanding in a different way.

The film simulations for the rear view mirror configuration are performed with a reduced computational grid compared to that described for the refined boundary layer. The reason is that limited computational resources enable a computation only up to a few million cells. They prohibit simulations with a grid of more than eleven million cells. As main difference, deviating shear stress values are found along the mirror surface when using the coarser grid. Additionally, less particles will be released during the film break-up computation, but they feature higher mass flow rates, which compensate the difference at this point.

The film flow has been simulated for three different air flow velocities (15, 20 and 25 $\mathrm{m/s}$). The flow field remains the same during the film computation, such that there is no back coupling of the injected droplets or of the film on the aerodynamic solution.

The droplet injection occurs from an injection grid with randomly moving starting points. Initial properties of the injected droplets (velocity, diameter, mass flow rate) have been set according to experimental parameters and results from PDA measurements.

Table 5.3 summarizes the film simulation configurations. The simulations carried out with the original model have been label with 'o', while the simulations where the improved film model was employed, are label with 'i'.

TABLE 5.3: Film simulation configurations.

Geometry	15 $\mathrm{m/s}$	20 $\mathrm{m/s}$	25 $\mathrm{m/s}$
rear view mirror	o/i	i	i

The film flow has been simulated for the duration of 1.5 s flow time, which yields a quasi-steady film behavior. Figure 5.7 shows the progression of the face-averaged film thickness. The mean film thickness and the standard deviation are given as numbers at steady state. It is assumed that steady state is reached after 40000 iterations (curve red enclosed until this point), which corresponds to 1.5 s.
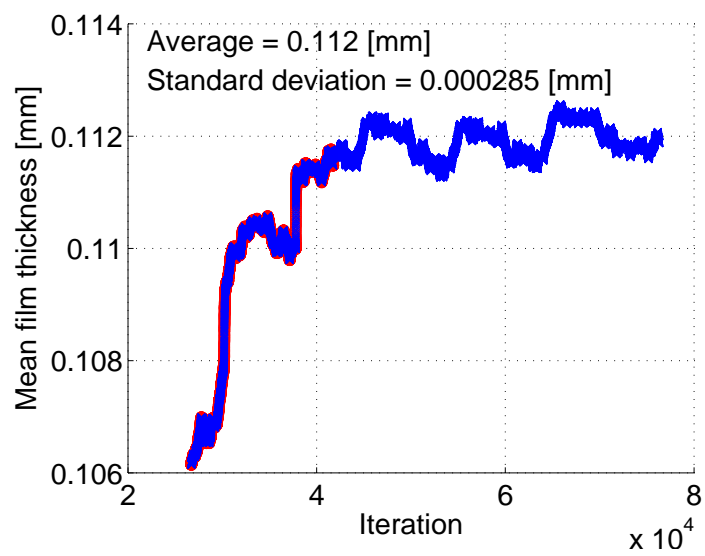
FIGURE 5.7: Face-averaged film thickness approaching steady state for the mirror configuration at 15 ᵐ/ₛ

The results of the film simulations are presented in the following chapter, together with the experimental results obtained by Brinkmann [20].

Chapter 6

Results and Comparisons

The experimental and numerical results are presented in this chapter. Its structure is briefly outlined here. At first the experimental results for the wind tunnel experiments (windshield and rear view mirror configuration) are discussed. Subsequently, the results from the film thickness measurements are analyzed, including detailed information concerning the post-processing. The numerical results (film simulation) are presented in the last part of this chapter. They are compared with the experimental results obtained at ISM Braunschweig. The comparisons of experimental and numerical results confirm the positive aspects of the model improvements. Nevertheless, they also show remaining drawbacks and uncertainties of the current model version. Therefore, further, more detailed and accurate experiments are needed in the near future.

6.1   Experimental Results: Configuration K1 (Windshield)

The experimental results are presented for the two different experimental configurations in the following, starting with results for air and droplet phases around the windshield geometry configuration(K1).

Characteristics of the continuous gas phase

The air flow is analyzed for all three nominal wind tunnel velocities (15, 20 and 25 $\mathrm{m/s}$) in front (inlet conditions) and behind (validation based on outflow conditions) the geometry. Generally, the orientation of all y-z-plots is such that the view of the observer is in counter flow direction. Therefore, the LDV optics would be located to the left hand side of each plot. The results for 15 $\mathrm{m/s}$ are presented here exemplarily as an interpolated

pcolor-plot of the 46×37 data points. A visualization of the other velocity configurations is given in Appendix C.
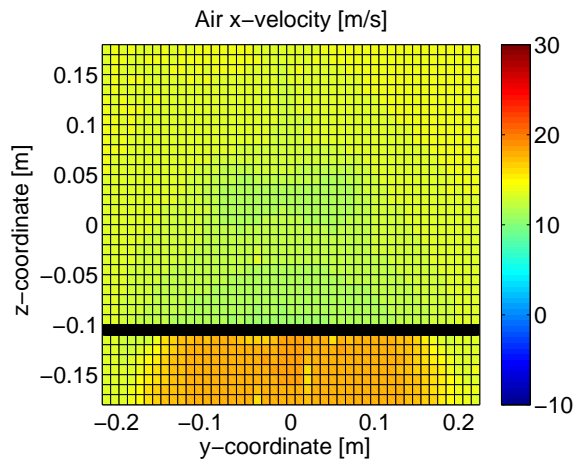
FIGURE 6.1: Cross-sectional x-velocity distribution measured by means of LDV; exemplarily for 15 $^{m}/_{s}$ at the $x = 0$ m-plane. The black line represents the front plate which separates the cross-sectional area in two regions and prohibits measurements along the $z = -0.1$ m-plane.
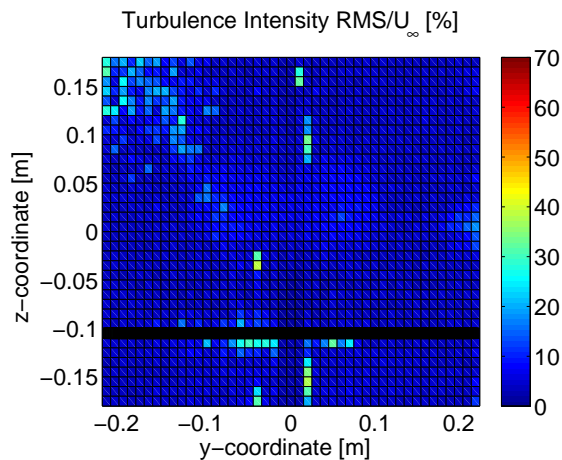
FIGURE 6.2: Cross-sectional turbulence intensity distribution measured by means of LDV; exemplarily for 15 $^{m}/_{s}$ at the $x = 0$ m-plane. The black line represents the front plate which separates the cross-sectional area in two regions and prohibits measurements along the $z = -0.1$ m-plane.

The cross-sectional inlet ($x = 0$ m) x-velocity distribution (Fig. 6.1) shows the same characteristics for all wind tunnel velocities. Quantitatively, the air flow mean velocities are almost identical to the approach velocity specified in the wind tunnel settings. Small disturbances can be observed in the wake of the injection system, in the center of the channel (around $y = 0$ m and z between 0 and 0.05 m). It should be recalled once more that the injection system is installed but inactive during the air velocity measurements. The air velocity is slightly increased in the lower part of the channel. It is a consequence of flow acceleration due to a decrease in cross-sectional area, which is in agreement with theory. The lower area is separated from the rest by a sharp line at $z = -0.1$ m, where

the horizontal front plate is located. Measurements are not possible along this line. It has thus been masked and is excluded from the results.

In Fig. 6.2 the turbulence intensity is shown. Highest turbulence intensity is found again in two regions. The first one is located in the wake of the injection system. As expected only slightly increased values are observed here compared to the bulk flow, thank to the profiling of the injection pipe. The second region with enhanced turbulence is found around the horizontal front plate.

As expected, the cross-sectional outflow ($x = 0.41$ m) x-velocity distribution shows the contour of the windshield geometry.
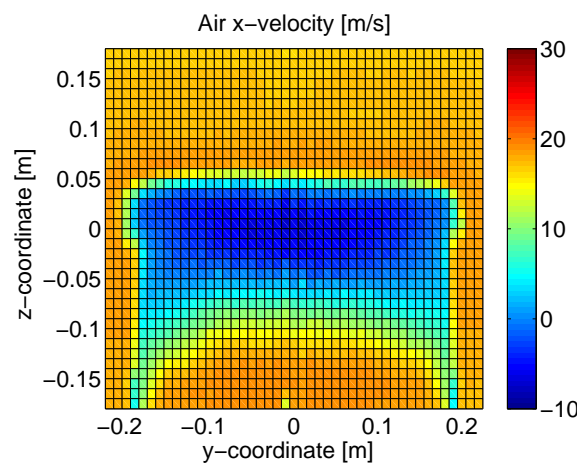
FIGURE 6.3: Cross-sectional x-velocity distribution measured by means of LDV; exemplarily for 15 $^m/_s$ at the $x = 0.41$ m-plane
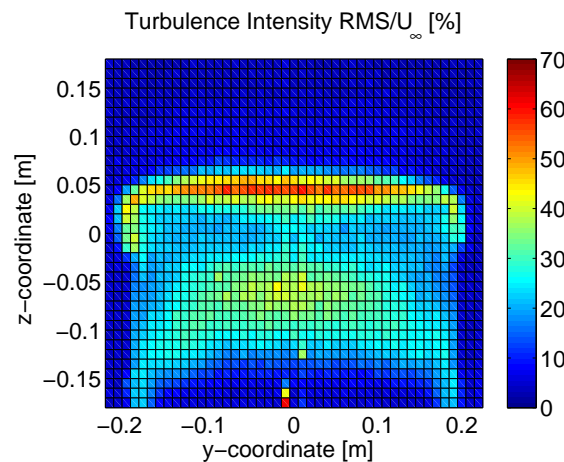
FIGURE 6.4: Cross-sectional turbulence intensity distribution measured by means of LDV; exemplarily for 15 $^m/_s$ at the $x = 0.41$ m-plane

Due to the wind tunnel blockage, the air flow velocity increases by approximately 5 $^m/_s$ all around the geometry for all three cases.

A strong back flow occurs in the wake of the geometry with mean x-velocities up to $\bar{u}_x = -10$ m/s. It is a consequence of flow detaching from the model surface and swirling around. PIV measurement provide a better view on the flow detachment, as will be shown later on.

Information concerning the turbulence properties are captured as well. They are presented in Fig. 6.4. The turbulence intensity is quite low far from the model surface for all three cases. It increases to large values near 70 % in the wake of the model, especially at the rear edge. This high turbulence level is directly connected to the vortices behind the model. A second area with increased turbulence intensity is located below the plate, ranging from the coordinates $y = -0.1$ m to $y = 0.1$ m and $z = -0.1$ m to $z = -0.025$ m. It appears to be a consequence of the flow detaching from the horizontal leading plate and streaming below the model.

In addition to the local investigation of the air flow velocities using LDV, those have been analyzed globally, employing the PIV measurement technique. These measurements yield an average, two dimensional vector plot of the air velocity in the wind tunnel center plane. They are shown in Fig. 6.5 and in Appendix C, where the colorbar gives the corresponding velocity magnitude. Obviously, the flow velocity increases with increasing
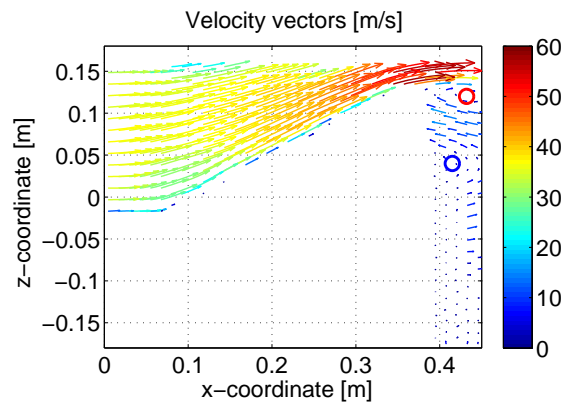
FIGURE 6.5: Averaged air velocity field measured by means of PIV; exemplarily for 15 m/s at the $y = 0$ m-plane

wind tunnel velocity. More interesting is the flow behavior at the upper corner (convex point of the geometry). The flow detaches at the upper corner of the inclined plate and hardly manages to reattach again, even at the lowest wind tunnel velocity. In case of higher wind tunnel velocities, the flow does not reattach to the surface at all.

Large vortices are generated behind the rear edge. After averaging, a vortex pair with opposite circulation is visible in the upper right corner of Fig. 6.5 for the configuration

with 15 m/s wind tunnel velocity. The red circle marks the clock-wise rotating vortex, while the blue circle represents the vortex rotating counter-clock-wise.

The boundary layer is not resolved accurately due to the large field of view. Nevertheless, the flow velocities are observed to decrease with decreasing distance to the wall, as expected.

Characteristics of the dispersed liquid phase

Besides the air flow properties, the dispersed water phase has been investigated. Using the PDA measurement technique, information concerning the droplet size and velocity are obtained simultaneously. The measurements are limited to a certain number of measurement points, as explained before. Droplet size and velocity distributions are acquired at each point.
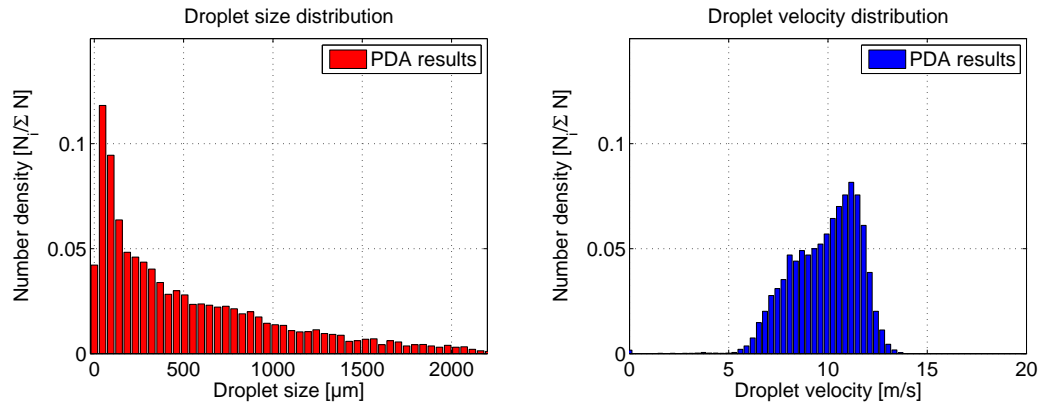
FIGURE 6.6: Droplet size and velocity distribution measured by means of PDA; exemplarily for 15 m/s at measurement point $x = 0$, $y = 0$, $z = 0.005$ m

The distributed spray properties presented in Fig. 6.6 indicate that the spray is very coarse. Droplet diameters are detected up to and probably above 2.2 mm, which is the upper limit of the measurement range (see Section 4.2.2).

Globally, the size distribution has nearly the shape of a log-normal distribution. However, it seems to be inappropriate to evaluate the size distribution at each measurement point with the same type of fitting function. Especially in the wake of an object, the size distribution of the spray is rather complex. Consequently, a log-normal distribution is not able to capture this complexity. Using the moments of the distribution, computed from the acquired data yields a more accurate description and a better comparability for the size distribution at different locations. The first 4 moments are most important in order to describe the size distribution and statistical values of a spray. Generally, the

k^{th}-moment of a number density distribution is computed by:

$$m_k = \int_0^\infty x^k n\,(x)\mathrm{d}x. \tag{6.1}$$

The resulting first 4 moments are $m_0 = 10000$, $m_1 = 5.2382 \cdot 10^6$ μm, $m_2 = 5.2916 \cdot 10^9$ μm^2, $m_3 = 6.9602 \cdot 10^{12}$ μm^3 at this location. They have the following meaning: m_0 gives the total number of samples, while m_1 describes the total length of all droplets. Consequently, both can be combined

$$\bar{x} = \frac{\int_0^\infty xn(x)\mathrm{d}x}{\int_0^\infty n(x)\mathrm{d}x} = \frac{\mu_1}{\mu_0} = d_{10} \tag{6.2}$$

to obtain the mean diamter $d_{10} = 523.8$ μm. The Sauter mean diamter $d_{32} = 1315.3$ μm can be computed from m_2 (the total surface area) and m_3 (the total volume). This statistical value is widely used to describe spray processes including heat and mass transfer.

The velocity distribution can be evaluated in a similar way. However, there is no obvious meaning in combinations of higher order moments. The first two moments capture the most significant statistics. They are given by $m_0 = 10000$, $m_1 = 9.8452 \cdot 10^4$ m/s and the mean velocity $v_{10} = 9.84$ m/s at this location. Additionally, the moments $m_2 = 9.9891 \cdot 10^5$ m^2/s^2 and $m_3 = 1.0380 \cdot 10^7$ m^3/s^3 can be used to further distinguish between the velocity distributions at different locations.
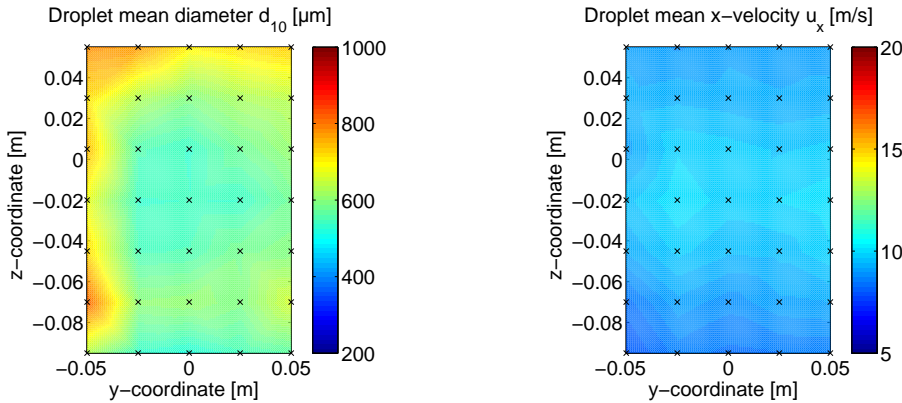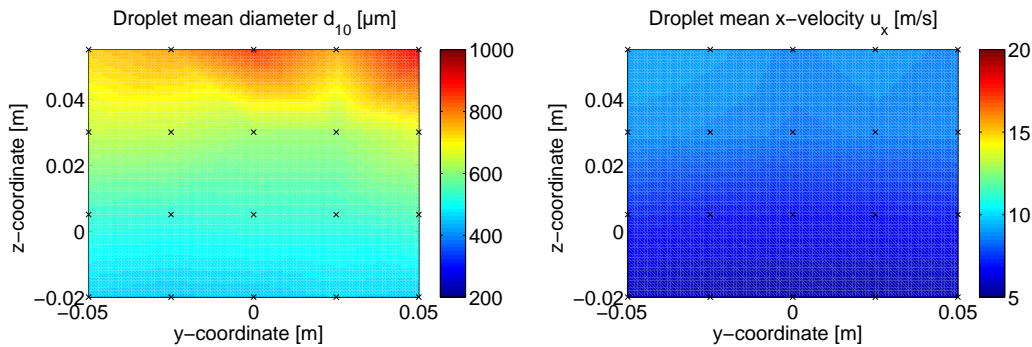

FIGURE 6.7: Spatial mean droplet diameter and velocity distribution measured by means of PDA; exemplarily for 15 m/s at the $x = 0$ m-plane

The spatial measured PDA results deliver the mean values of the size and velocity distribution. Therefore, the inlet ($x = 0$ m) spray parameters can be presented in Fig. 6.7 in terms of spatially distributed droplet mean diameter and mean velocity. The limited information obtained in reality only at the marked positions (black crosses) can be interpolated using a bilinear interpolation scheme, to generate the contour plots. A distribution typical for spray cones can be observed. The highest velocities are located

in the core of the spray cone, decreasing towards the boundaries. On the contrary, the diameter values in the center are low and increase towards the boundaries. Additionally, the number of droplets decreases from the core region of the spray cone towards the side area. The diameter distribution strongly deviates from an ideal spray cone shape, what can be seen in the limited field of view in Fig. 6.7. This appears due to the fact that the leading plate of the windshield geometry impacts the $x = 0$ m-plane. Similar results are found for other configurations as shown in Appendix C.

As the spray approaches the windshield, its properties change. Hence, clear differences can be observed, when comparing the size and velocity distributions of the measurement points at the inlet (Fig. 6.6) with further downstream positions (Fig. 6.8).

Obviously, the number of very small droplets is reduced compared to the size distribution at the inlet. They quickly respond to the flow. Therefore, they easily turn around the geometry and stay at a certain distance from the windshield. The moments at this point read: $m_0 = 10000$, $m_1 = 5.1714 \cdot 10^6$ µm, $m_2 = 4.1720 \cdot 10^9$ µm^2 and $m_3 = 4.5900 \cdot 10^{12}$ µm^3. The associated statistical values $d_{10} = 517.1$ µm and $d_{32} = 1100.2$ µm do not represent the distribution behavior shown in the histogram. The mean diameter is smaller here in comparison with the inlet position. At the same time, the peak position is shifted to a higher diameter value.

Concerning the velocity distribution, a block-like shape including all velocities between 3 and 12 m/s can be observed for the histogram. This is caused by the deceleration of the droplets, when they come closer to the windshield surface. The corresponding moments are $m_0 = 10000$, $m_1 = 6.7423 \cdot 10^4$ m/s, $m_2 = 5.0908 \cdot 10^5$ m^2/s^2 and $m_3 = 4.2077 \cdot 10^6$ m^3/s^3. These moments result in a mean velocity of $v_{10} = 6.74$ m/s.
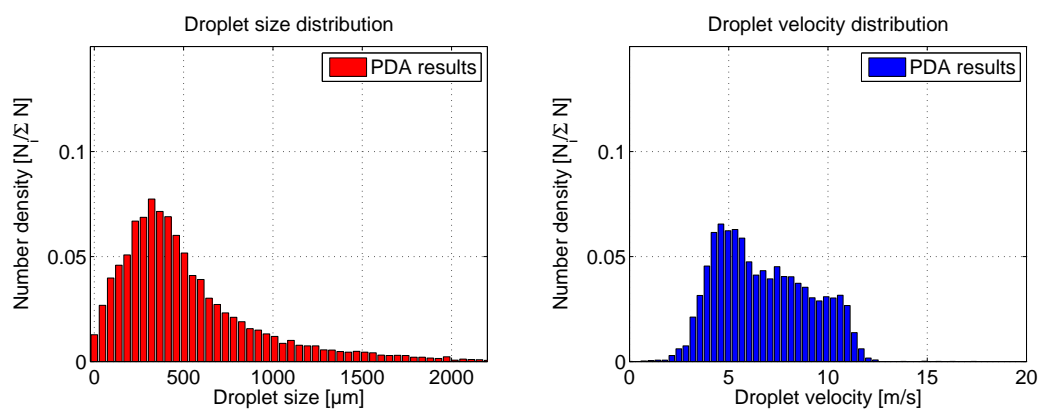
FIGURE 6.8: Spray droplet size and velocity distribution measured by means of PDA; exemplarily for 15 m/s at measurement point $x = 0.2$, $y = 0$, $z = 0.005$ m

The mean values of the histograms are used again to obtain an overview of the spatial distribution of droplet size and velocity (see Fig. 6.9). These results are useful for model validation and comparison. As expected, the droplet size and velocity decrease

with decreasing distance to the wall. For a better orientation, the wall is located close below $z = -0.02$ m. The presence of many small droplets, generated from spray-wall-interaction, reduces the mean diameter. The change of the mean droplet x-velocity is even more significant. It is decreased from formerly 10 $\mathrm{m/s}$ down to 5 $\mathrm{m/s}$.

FIGURE 6.9: Spatial mean droplet diameter and velocity distribution measured by means of PDA; exemplarily for 15 $\mathrm{m/s}$ at the $x = 0.2$ m-plane

Beside inlet and validation values, the spray properties have been analyzed at selected positions along streamwise profiles near the surface of the inclined plate. The aim is to obtain information concerning splashing of primary droplets on the film. From the profiles given in Fig. 6.10 one can see that the mean diameter decreases with increasing wind tunnel velocity. This is clearly an effect of increased impact velocities of the primary droplets, leading to more and smaller secondary droplets. The mean diameter decreases also as a whole with decreasing distance from the wall. However, this trend is not as obvious as the velocity dependency. Nevertheless, it is logical that close to the wall more secondary droplets can be observed. For the same reason, the diameter decreases toward the rear end of the plate (from left to right, with a plate length ≈ 200 mm). The lowest mean diameter is always found at the end of the curves, while close to the front end of the plate the highest mean diameter values are observed.

In addition, the spreading of the mean values is reduced, when increasing wind tunnel velocity (compare top and bottom figure). It should be kept in mind, that these mean values are used as being representative for the whole droplet size distribution found at each measurement point. More details of the full distributions can be found in the experimental data base.
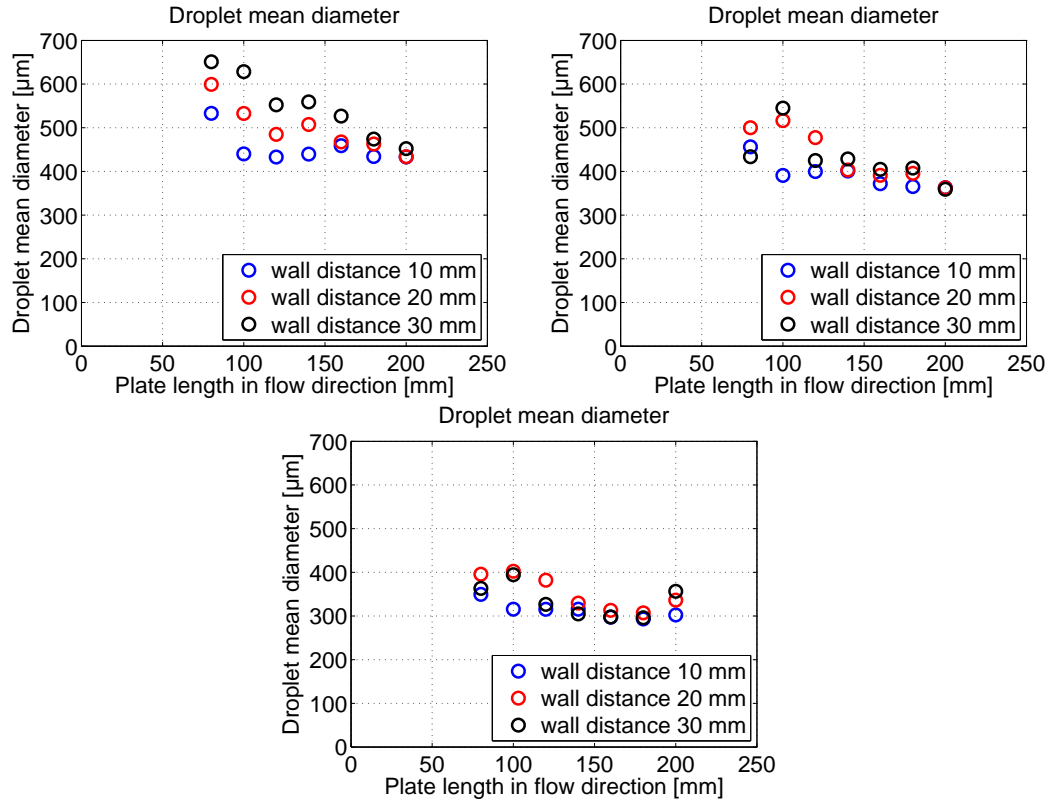
FIGURE 6.10: Droplet mean diameter profiles measured by means of PDA for wind tunnel velocities of 15 (top left), 20 (top right) and 25 $^{m}/_{s}$ (bottom) at the $y = 0$ m-profile

6.2 Experimental Results: Configuration K2 (Rear View Mirror)

After presenting the experimental results for the windshield configuration, the results for the rear view mirror are presented in the following. At first, the air flow properties measured by means of LDV (Section 4.4) are described. The mirror geometry prohibits measurements in a part of the wind tunnel cross-section. This area is encircled with a black line in what follows, indicating approximately the surface line of the geometry. Obviously, it is not the surface of the mirror housing itself, but of the connecting plate to which the mirror is mounted to (compare with Fig. 4.6 in Section 4.4). The area blocked by the connecting plate increases with increasing x-coordinate.

The results for the air flow velocity are presented exemplarily for a wind tunnel velocity of 15 $^{m}/_{s}$. Further results are shown in Appendix D.

Characteristics of the continuous gas phase

The cross-sectional inlet x-velocity distribution is presented in Fig. 6.11. Globally, the flow velocity is distributed homogeneously in the cross-sectional area. Small disturbances can be observed in the wake of the injection system, showing the shape of two horizontally connected circles. Here the axial mean velocity is slightly reduced, otherwise the mean flow velocity coincides almost perfectly with the wind tunnel velocity.
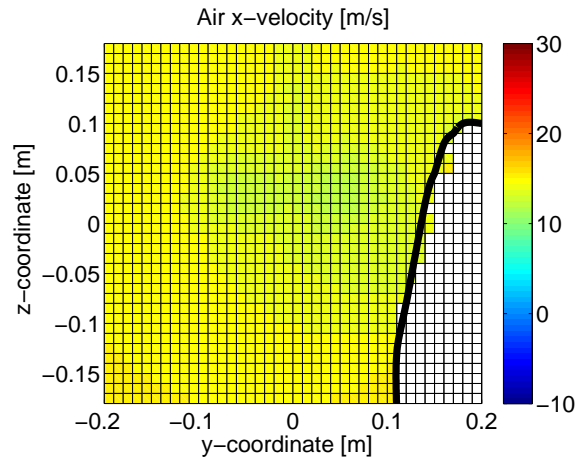
FIGURE 6.11: Cross-sectional x-velocity distribution measured by means of LDV; exemplarily for 15 $^m/_s$ at the $x = 0$ m-plane
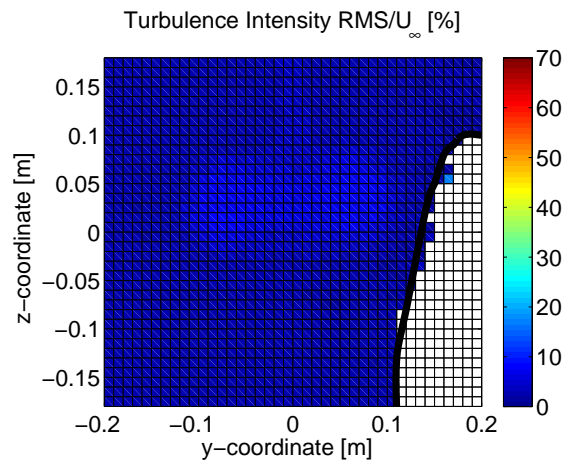
FIGURE 6.12: Cross-sectional turbulence intensity distribution measured by means of LDV; exemplarily for 15 $^m/_s$ at the $x = 0$ m-plane

The turbulence intensity is visualized in Fig. 6.12. The turbulence intensity is again distributed homogeneously across the inlet cross-section. Only in the wake of the injection system, the turbulence intensity values are slightly increased. The behavior is similar for all wind tunnel velocities.

Fig. 6.13 shows the results for the cross-sectional outflow x-velocity. The velocity distribution reflects the shape of the mirror housing. Around the geometry, the velocity is
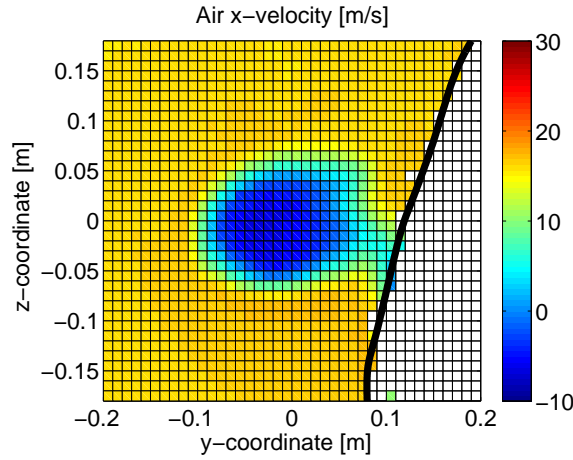
FIGURE 6.13: Cross-sectional x-velocity distribution measured by means of LDV; exemplarily for 15 m/s at the $x = 0.325$ m-plane
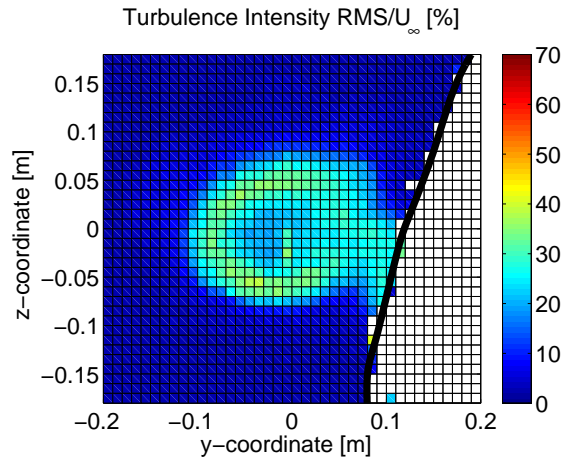
FIGURE 6.14: Cross-sectional turbulence intensity distribution measured by means of LDV; exemplarily for 15 m/s at the $x = 0.325$ m-plane

increased compared to the inlet velocity. Moreover, back flow occurs in the wake of the mirror with mean x-velocities up to $\bar{u}_x = -10$ m/s. The area without data grows with increasing x-coordinate, as already stated. It is due to the fact, that the mounting plate extends towards the rear end, mimicking the real vehicle surface.

The turbulence is strongly enhanced in the wake of the mirror (see Fig. 6.14). A ring-shaped area of high turbulence intensity represents the high fluctuation velocities of the detaching flow. Far from the mirror surface, the turbulence intensity decreases to the level observed at the inlet, well below 10 %. Identical tendencies are found for the other wind tunnel velocity configurations (see Appendix D).

Characteristics of the dispersed liquid phase

In addition to the air flow properties, the spray properties have been investigated. In the following corresponding results are presented.

At first, the local droplet size and velocity distributions are shown for a selected point at the inlet cross-section (see Fig. 6.15). Similarly to the windshield configuration, moments
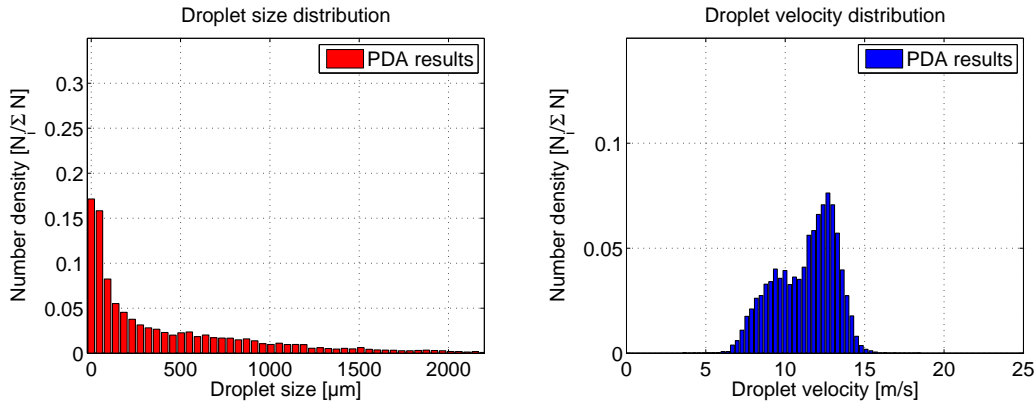
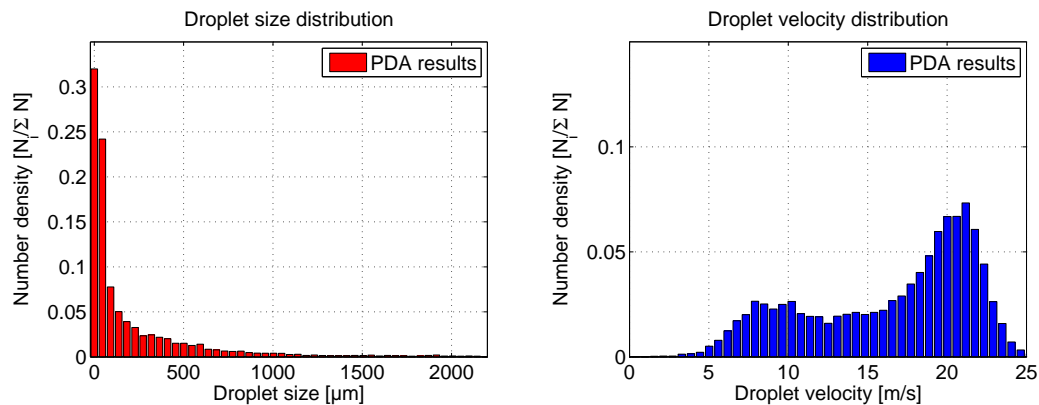FIGURE 6.15: Spray droplet size and velocity distribution measured by means of PDA; exemplarily for 15 m/s at measurement point $x = 0$, $y = 0$, $z = 0.005$ m

of the distributions are used to describe the results for the size and velocity properties of the spray in the mirror configuration. The 0th-moment is always $m_0 = 10000$, since a constant number of samples was acquired at each measurement point. Therefore, it is not presented any further. The remaining moments of the size distribution at the point in front of the mirror (inlet-position) are $m_1 = 4.0164 \cdot 10^6$ μm, $m_2 = 3.9123 \cdot 10^9$ μm² and $m_3 = 5.0579 \cdot 10^{12}$ μm³. Correspondingly, the mean and Sauter mean diameters are $d_{10} = 401.6$ μm and $d_{32} = 1292.8$ μm. Throughout, these three moments are higher than those for the size distribution at the inlet position in the windshield configuration. This may be due to the lower blockage ratio associated with the mirror geometry, resulting in a less disturbed atomization.

The velocity distribution has a bimodal shape, but this cannot be seen from the moments. They are $m_1 = 1.1252 \cdot 10^5$ m/s, $m_2 = 1.3024 \cdot 10^6$ m²/s² and $m_3 = 1.5441 \cdot 10^7$ m³/s³. A resulting mean velocity of $v_{10} = 11.2$ m/s, represents the higher axial velocity associated with the lower blockage ratio of the mirror geometry. An overview of the inlet results is given in Fig. 6.16 in terms of spatially distributed mean values. As expected, the spatial distribution of the droplet mean diameters corresponds to the cone shape of the spray head. Small droplets are located in the center of the spray cone with mean diameters around 450 μm. The diameter values increase with increasing distance from the center, up to values around 800 μm at the edges of the measurement grid. However, there is a deviation between the spatial diameter distribution for the windshield (see Fig. 6.7)
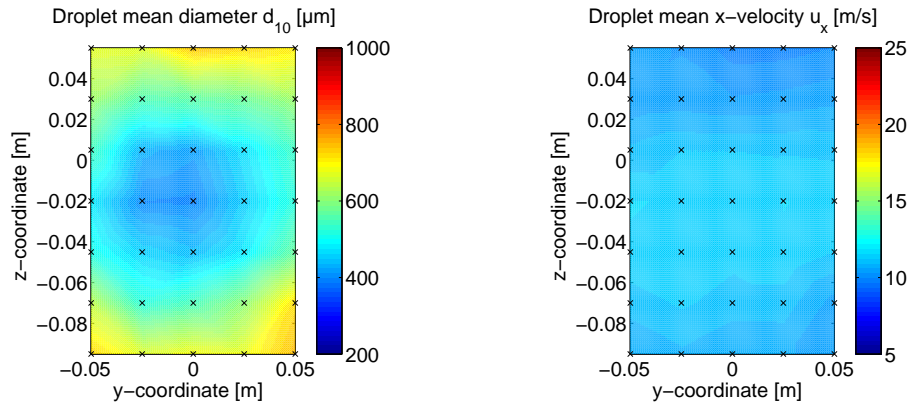
FIGURE 6.16: Spatial mean droplet diameter and velocity distribution measured by means of PDA; exemplarily for 15 m/s at the $x = 0$ m-plane

and the mirror configuration. This is due to the very high blockage ratio found for the windshield geometry, which degenerates the spray cone shape. In addition, the droplet mean velocities are measured simultaneously. They show slightly decreasing droplet velocities from the center to the edge of the spray cone. These are typical findings for a spray cone. Further results are summarized in Appendix D for the inlet cross-section at different wind tunnel velocities.

Furthermore, the spray properties have been investigated behind the mirror geometry to validate the simulations. Therefore, the same number of measurement points as for the inlet is investigated to obtain size and velocity distributions. The results are presented in Fig. 6.17 for a selected measurement point. Obviously, these size and

FIGURE 6.17: Spray droplet size and velocity distribution measured by means of PDA; exemplarily for 15 m/s at measurement point $x = 0.4$, $y = 0$, $z = 0.005$ m

velocity distributions show a high deviation from former results. The spray properties are governed by the strong fluctuations within the wake of the mirror geometry. A large number of very small droplets is visible.

All droplets in the lower diameter classes are most likely issued from spray-wall interaction. These secondary droplets are small enough to follow the flow accurately, such that

they may reach the wake with enhanced turbulence and increased velocity fluctuations. Primary droplets with diameters of $d \geq 1000$ μm are almost excluded from this region. Once again, the moments of the size distribution are given: $m_1 = 2.0020 \cdot 10^6$ μm, $m_2 = 1.5826 \cdot 10^9$ μm^2 and $m_3 = 1.9556 \cdot 10^{12}$ μm^3.

The significant number of small secondary droplets is also visible from the statistical values $d_{10} = 200.2$ μm and $d_{32} = 1235.7$ μm.

Furthermore, the droplet velocity distribution shows a broad spread of the velocity values. Two peaks can be observed at either side of the histogram. Accordingly, the shape is more like an arch, which represents the effect of droplets with different origins. The corresponding moments of the velocity distribution and the mean velocity are $m_1 = 1.6482 \cdot 10^5$ m/s, $m_2 = 2.9887 \cdot 10^6$ m^2/s^2, $m_3 = 5.7363 \cdot 10^7$ m^3/s^3 and $v_{10} = 16.5$ m/s. A diameter-velocity plot is a more appropriate way to show the correlation between droplet size and velocity (see Fig. 6.18).

Especially, when dealing with highly complex flows a diameter-velocity plot may yield a better insight. For instance, Brenn et al. [19] investigated the collision behavior of bubbles in bubble column using diameter and velocity information obtained with PDA. This shows that the method is useful for correlating experimental data and gain additional information.

Several regimes can be clearly distinguished in the present case. Further data are gathered in the project data base.
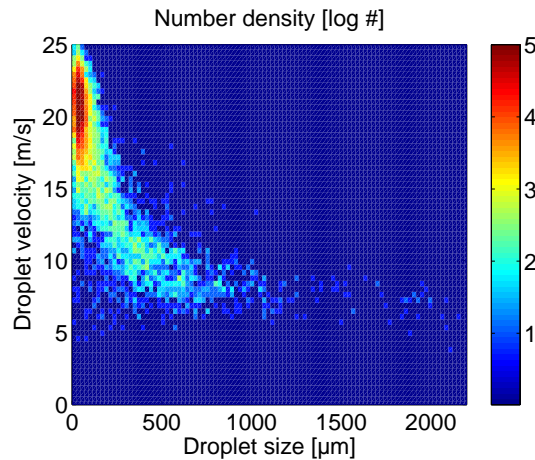
FIGURE 6.18: Droplet size-velocity correlation at the measurement point $x = 0.4$, $y = 0$, $z = 0.005$ m

Once again, the large amount of very small droplets is obvious within the sample. Their origin is the splashing of primary droplets. Obviously, the smallest droplets have the highest velocities, which can be derived from correlating the diameters and associated

velocities. This is also the combination that is most likely to occur. The velocity decreases with increasing droplet diameter in a tail-like manner (Fig. 6.18).

The spatial distribution of mean values is given in Fig. 6.19. Indeed, the droplet properties are clearly affected by the flow around the mirror geometry, which can be verified from the spatial velocity distribution. It shows almost the shape of the mirror housing with low droplet velocities in the wake. Additional results are presented in Appendix D for different wind tunnel velocities. In contrast, the spatial diameter distribution does
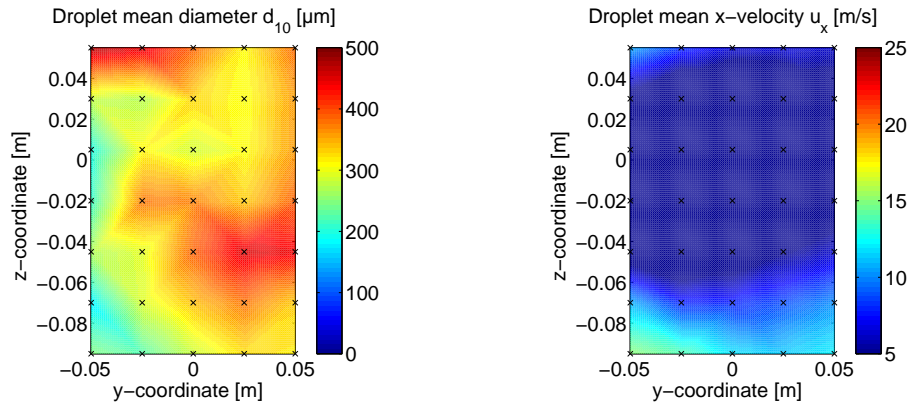
FIGURE 6.19: Spatial mean droplet diameter and velocity distribution measured by means of PDA; exemplarily for 15 $^{\mathrm{m}}\!/\!_{\mathrm{s}}$ at the $x = 0.4$ m-plane

not show any clear shape. Increased droplet diameters can be observed at the right side of each contour plot. This is the side where the mirror is mounted to the connecting plate. The increased diameter values may be because of liquid film break-up, with large droplets detaching from the mirror surface. Additionally, primary droplets may flow through the gap between the mirror and the connecting plate. Therefore, they can be a reason for increased mean diameter values as well.

Further data have been acquired following profiles around the mirror surface at the front side of the geometry. The procedure has been described in more detail in Section 4.4. Exemplary results are presented in Fig. 6.20 in terms of size and velocity distribution as well as size-velocity correlation (Fig. 6.21). They have been obtained at the measurement point 1 ($x = 0.215$, $y = 0$, $z = -0.075$ m) of the curved profile grid. Both, the size and the velocity distribution yield several peaks and cannot be represented with a simple distribution function. The distribution of diameter and velocity is strongly affected by the spray-wall interaction. Therefore, the spray consists of primary and secondary droplets (from splashing) with different pathways at this point. There are also droplets originating from film break-up with their respective size and velocity properties. Moments of the distributions are available, independent from how complex a distribution function is. The moments for the size distribution are $m_1 = 3.1646 \cdot 10^6$ µm, $m_2 =$
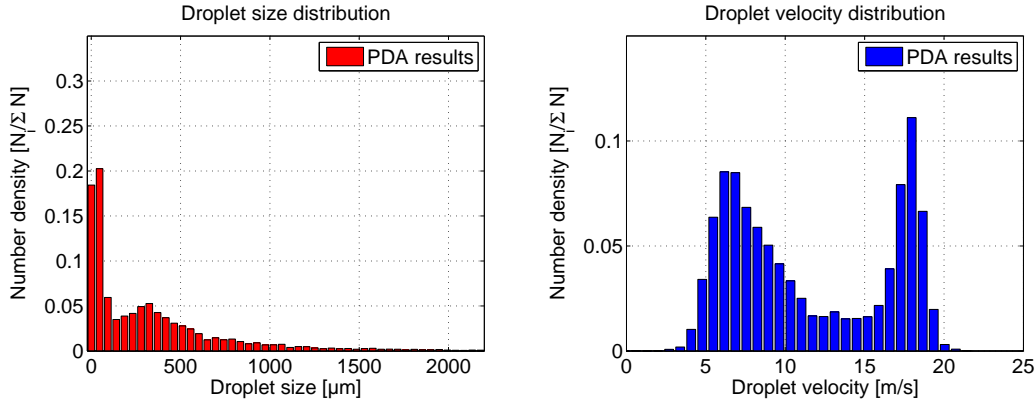
FIGURE 6.20: Spray droplet size and velocity distribution measured by means of PDA; exemplarily for 15 m/s at the measurement point $x = 0.215$, $y = 0$, $z = -0.075$ m

$2.5166 \cdot 10^9$ μm^2 and $m_3 = 2.9019 \cdot 10^{12}$ μm^3 in this case. They result in statistical diameters of $d_{10} = 316.5$ μm and $d_{32} = 1153.1$ μm.

Additionally, the moments of the velocity distribution have been computed. They are: $m_1 = 1.1534 \cdot 10^5$ m/s, $m_2 = 1.5849 \cdot 10^6$ m^2/s^2 and $m_3 = 2.4412 \cdot 10^7$ m^3/s^3 and yield a mean velocity of $v_{10} = 11.5$ m/s. However, this value is of no significance, since there are only a few droplets with this very velocity within the sample. An attempt has been made to
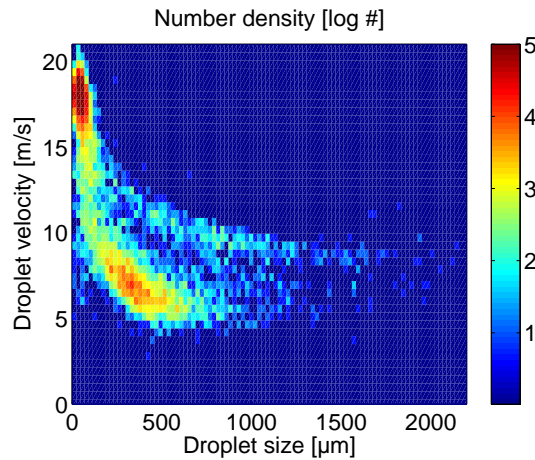
FIGURE 6.21: Droplet size-velocity correlation at measurement point $x = 0.215$, $y = 0$, $z = -0.075$ m

separate the droplets according to their origin, using the size-velocity correlation (see Fig. 6.21). The correlation evolves as a tail from a region with high number density. Two characteristics can be observed for the tail. At first, there is an accumulation of values in the region between $200 - 600$ μm and $5 - 10$ m/s. This accumulation is related to the second (right) peak in the size distribution, and to the left peak in the velocity distribution (Fig. 6.20).

Secondly, a small separation of the tail can be observed, which divides it into an upper and a lower velocity part. This characteristic can be found for other measurement locations, too. Occasionally, a complete separation occurs and two individual regimes are detectable. Full results are included in the data base.

The droplet mean diameter and velocity are plotted as function of the observation angle of the measurement grid in Fig. 6.22 and 6.23, in order to analyze their spatial evolution. The observation angle is the angle in counter-clockwise direction around the mirror housing in the x-y-plane of the wind tunnel. Obviously, the mean diameter increases
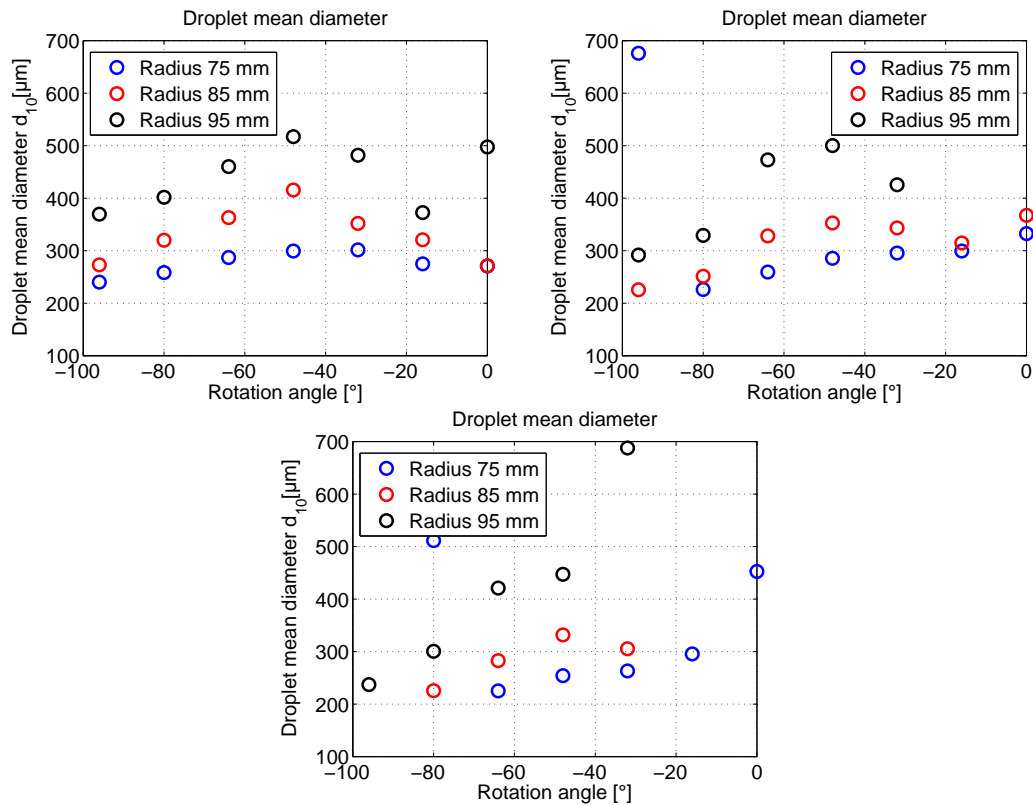
FIGURE 6.22: Droplet mean diameter profiles measured by means of PDA for 15 $^\text{m}/\text{s}$ and at a channel depth of $y = -0.025$ (top left), $y = 0$ (top right) and $y = 0.025$ m (bottom)

with increasing distance to the wall (blue to black curves). Maximum diameter values are detected at around $-48°$ for all radial profiles at all velocities (see also Appendix D). The missing data points are due to the measurement grid, which is adapted to the shape of a quarter circle. This shape slightly deviates from the real contour of the mirror. All measurement points without values are listed in Table 4.3 in Section 4.3.

In addition, the droplet mean velocity is acquired (Fig 6.23). It shows some unusual behavior. The droplet x-velocity decreases with decreasing rotation angle toward negative values (from right to left), which is logical since there is a stagnation point at the front side of the mirror. Generally, the mean velocities are maximum for the largest radius
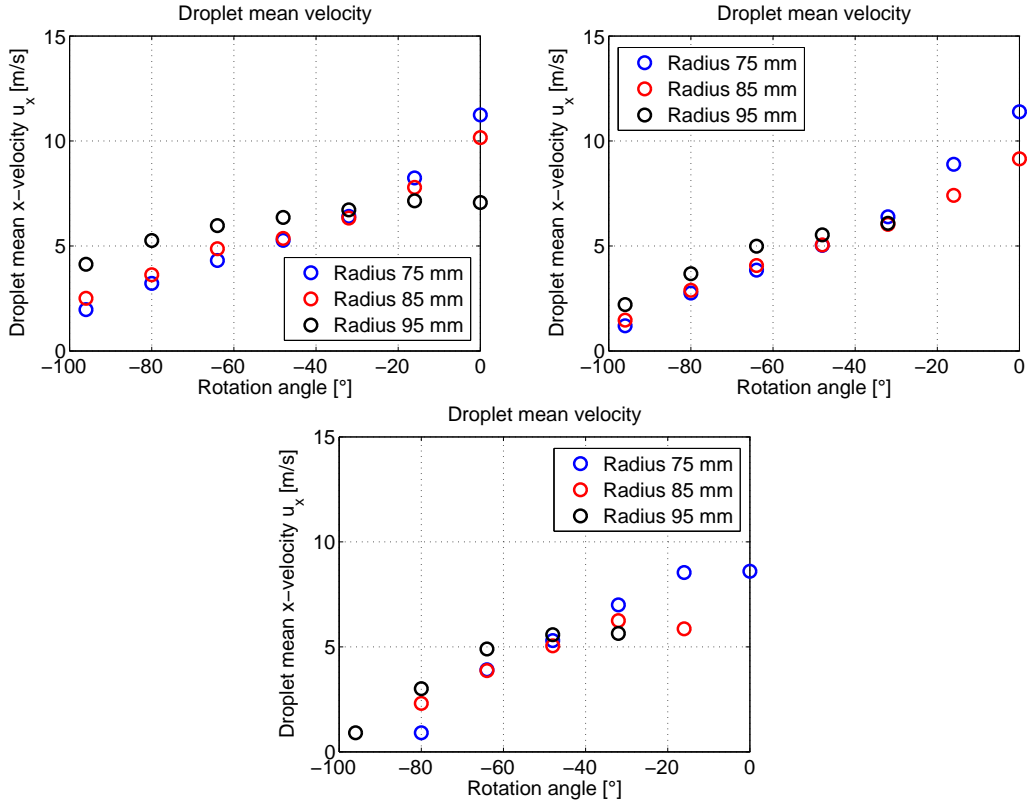
FIGURE 6.23: Droplet mean x-velocity profiles measured by means of PDA for 15 m/s and at a channel depth of $y = -0.025$ (top left), $y = 0$ (top right) and $y = 0.025$ m (bottom)

and minimum for the smallest radius. These tendencies are inverted at a rotation angle of $-32°$. An intersection point of the three data lines can be found for all cases. This behavior can be explained by the droplet paths. They enter the region where the air flow velocity decreases as consequence of the wall friction. Such a flow behavior has been discussed earlier in Section 5.2.2.3, where Figure 5.5 shows the mean velocity of the air flow along different profiles. Comparing the numerical configuration with the experiments, one can associate the profile P1 (simulation) with the rotation angle of zero (experiment). This can be done for each profile, ending with P7, which is associated with a rotation angle of $-96°$.

The droplet velocities can be interpreted more accurately, when the air velocity is known. It is assumed here that the droplets respond rapidly to the velocity changes of the air flow. The connection between air and droplet velocity is described by the equation of motion (Eq. 3.38). The profiles P4 to P7 (i.e. angles $-48°$ to $-96°$) are characterized by continuously increasing dimensionless velocity u^+ with increasing dimensionless wall distance y^+. Similarly, the corresponding experiments show continuously increasing droplet velocities with increasing wall distance. At P3 (equivalent to angle $-32°$), an almost constant mean velocity profile can be observed for $y^+ \geq 50$. This behavior

is shown by the droplets too, which have almost the same velocities for different wall distance values. The velocity profiles P1 and P2 (associated to angles $0°$ and $-16°$) first increase to a maximum value (at $y^+ \approx 100$) and then decrease with increasing wall distance. Consequently, the droplets are expected to have higher velocities when they are closer to the wall, which is confirmed by the corresponding experiments.

In conclusion, the flow behavior of the droplets in the vicinity of the mirror surface can be explained, if the numerical results for aerodynamics are considered. Therefore, the measured droplet motion is in agreement with the simulations.

6.3   Experimental Results: Film Thickness Measurements

After presenting the experimental results for the measurements carried out in the wind tunnel facility, the results for the film thickness measurements are presented in the following. Some of these results have been already published in Hagemeier et al. [52].

Results for Open Channel Flow

The first film measurements have been carried out to validate the film thickness measurement technique. Therefore, an open-channel flow configuration is investigated at three different Re numbers, as described before (see Section 4.5). An instantaneous result is shown for the lowest Re number in Fig. 6.24. The highest film thickness values are found in the middle of the plate, as expected. The corresponding value decreases towards the left and right boundaries. The visible line in the upper third of the image is due to a scratch on the acrylic glass plate, but does not perturb the measurements due to the full wetting of the plate.

The vertical lines in the contour plots always correspond to the location of the profiles selected for the profile plots (see for example Fig. 6.24, right). The influence of inlet and outlet conditions is visible in the profile plots of Fig. 6.24. There (near 0 and 60 mm), the local film thickness values decrease slightly, but not as much as on the left and right side of the plate. This is caused by the small scales of the model compared to the image size that is used in the tests, as mentioned earlier in Section 4.5.3. In order to validate the developed measurement technique, the obtained results are compared with the values deduced from theoretical considerations of Zhou et al. [166]. The film thickness has been averaged in space and time for this comparison. As shown in Fig. 6.25, an excellent agreement is obtained between the measured and the predicted film thickness values, with a deviation of less than 3 % for the worst case.
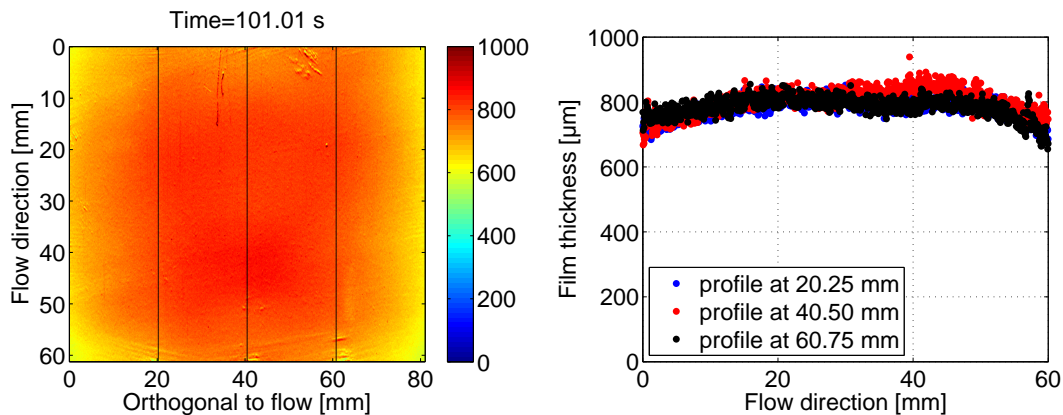
FIGURE 6.24: Result for open-channel flow at Re=525, showing instantaneous film thickness (left, in μm) and selected streamwise film thickness profiles (right, in μm)
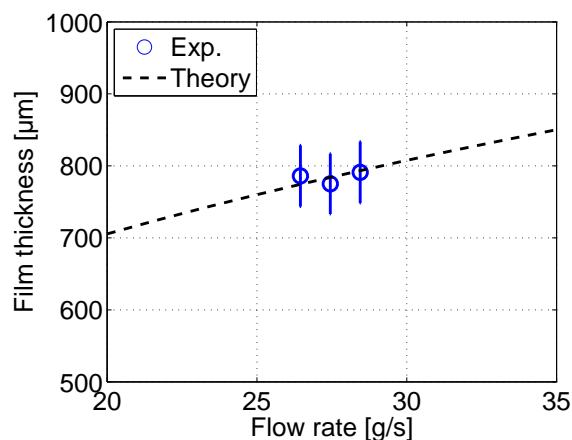

FIGURE 6.25: Comparison of experimental results and theoretical estimation for open film flow at Re=525, 545 and 565

In order to increase the complexity of this configuration, a cylindrical obstacle is placed in the flow. This investigation has been carried out only at a single Reynolds number of 565. Here, a horseshoe vortex structure appears clearly around the cylinder, which is a classical phenomenon for flows around obstacles mounted onto walls [98] (see Fig. 6.26). This vortical structure is characterized by an increase of the film thickness by a factor of almost two. Simultaneously, the film thickness is decreased to both sides of this wave.

The flow structures close to the cylinder walls, in particular the interference patterns are extremely well resolved by the developed measurement procedure. However, reflections from the LEDs are visible at a few isolated spots around the cylinder. These reflections are particularly visible for the center profile at 40.5 mm in the profile plots of Fig. 6.26. They lead to signal saturation at around 12 mm in flow direction. The other spurious peaks observed along the centerline profile are associated to the interference patterns, as mentioned before.
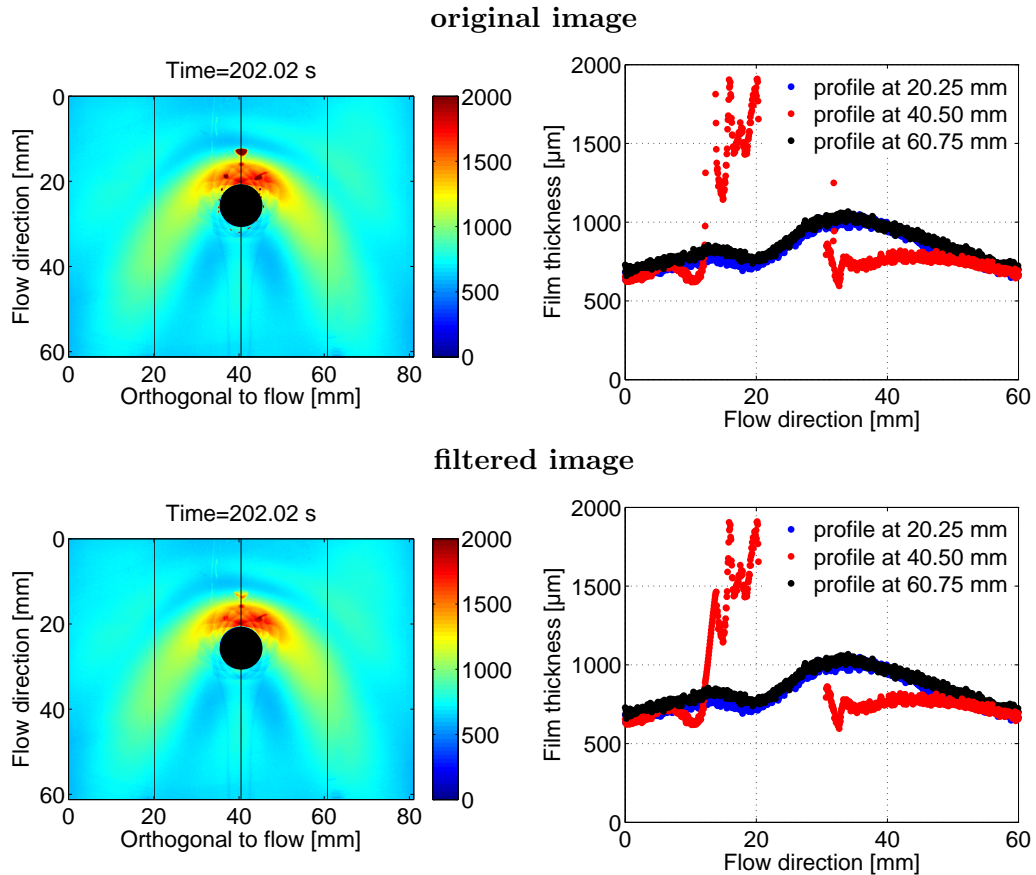
FIGURE 6.26: Results for open-channel flow around a cylindrical obstacle at Re=565, showing instantaneous film thickness (left, in µm) and selected streamwise film thickness profiles (right, in µm)

A digital filtering has been applied to reduce efficiently the image noise due to such effects. It works only on the concerned areas, which are recognized and segmented by computing the magnitude of the image gradient and prescribing a maximum threshold. Finally, the areas identified in this way are filled out with interpolated data from surrounding pixel values. The result can be seen in the bottom image pair of Fig. 6.26. This process improves considerably the images in a spatially adaptive manner, without modifying the rest of the signal. It has been applied systematically for all other cases described in what follows.

Results for Sliding Droplets and Rivulet

Images obtained from experiments with sliding droplets and rivulets are presented in Fig. 6.27 and Fig. 6.28 for two different time steps. The first image (left) depicts the instantaneous film thickness value, while the second plot (right) shows selected film thickness profiles in streamwise direction. To clarify the directions, all contour plots contain the streamwise direction as vertical direction (y-axis), while the transversal axis

is included as horizontal direction (x-axis). The profile plots include only the streamwise direction on the x-axis.
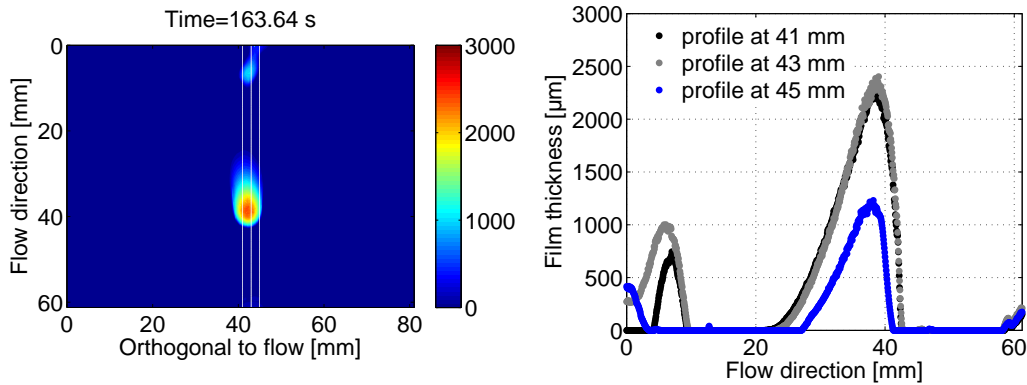

FIGURE 6.27: Results for sliding droplets (cannula II, inclination 15°), showing instantaneous film thickness (left, in µm) and selected streamwise film thickness profiles (right, in µm)

As discussed previously, the liquid flow starts after an accumulation of a sufficient number of droplets in each configuration. This can be seen in Fig. 6.27, left. The large droplet agglomerate in the middle of the image is already sliding down the plate, while the upper one is still at rest, accumulating more droplets until reaching the minimum mass leading to motion.
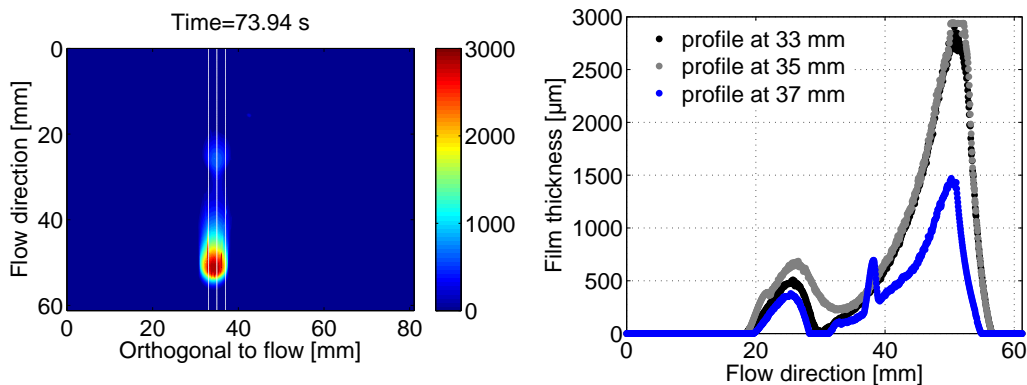
FIGURE 6.28: Results for rivulet flow (cannula II, inclination 19°), showing instantaneous film thickness (left, in µm) and selected streamwise profiles (right, in µm)

Figure 6.28 shows results obtained for a rivulet formed by merging droplets. Generally, the merging process has two effects. At first, it increases the film thickness above the maximum value found for a single droplet package, as a comparison of profiles in Figs. 6.27 and 6.28 reveals. Additionally, it accelerates the liquid stream, as expected from theoretical velocity estimation of laminar films by means of Nusselt's solution [112]. It is even possible to visualize changes of surface shape due to instabilities, when capturing images of long rivulets. For instance, see the liquid constriction at $y \approx 30$ mm in Fig. 6.28.

Besides the droplet height, the sliding velocity and wetting properties of the droplet are interesting. All these information can be evaluated from the film thickness gradient. The film thickness gradient along the profile in flow direction can be obtained during the post-processing. It is associated with the dynamic contact angle. At the droplet front (advancing side), the gradient is found to be significantly higher. The values correspond to the advancing contact angle. In contrast, smaller values can be observed at the back of the droplet (receding side) which is related to the receding contact angle. These properties are directly visible in Figs. 6.27 and 6.28 (right).

The velocity results are visualized in the images of Fig. 6.29 and Fig. 6.30. One film thickness profile is plotted along the main droplet track for each time step. A velocity distribution is created by evaluating this matrix (as explained in Section 4.5.3), including acceleration and deceleration of individual droplets. For example, one can observe two peaks in the velocity distribution of Fig. 6.29 (right image). The desired information is the velocity peak at 2.5 mm/s and the distribution around it. It is related to the sliding motion of the droplets. In contrast, the peak at zero mm/s corresponds to the stagnating liquid mass, where the film thickness remains constant in time.

Besides, a small fraction of negative velocities is visible. These negative values are not artifacts. Instead, they capture local upstreaming liquid mass which is associated with the droplet impingement after release from the cannula. If the impingement spot is set outside the FOV, these negative values disappear (see for instance Fig. 6.30).
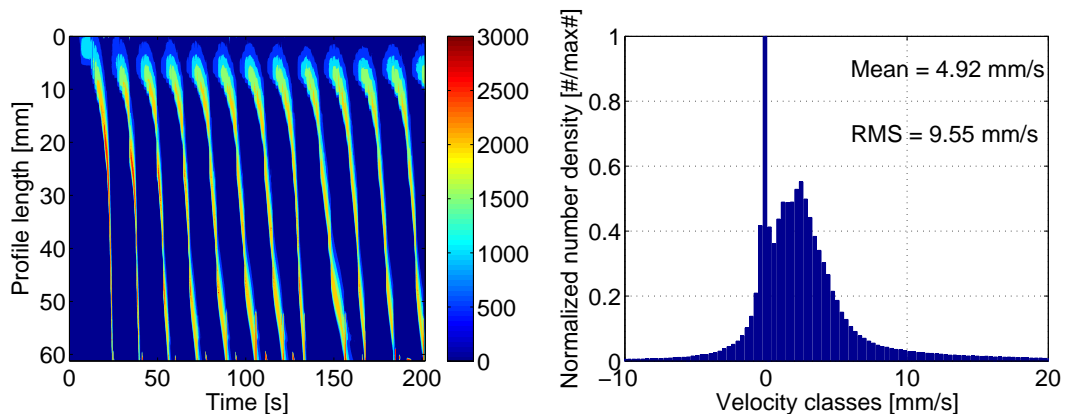

FIGURE 6.29: Temporal film thickness profiles (left, in μm) and deduced velocity histogram (right, velocity in mm/s) for cannula II, inclination 15°

The useful information concerning droplet motion is contained in the positive values of the velocity histogram. Hence, the computation of mean and rms values is limited to the positive quadrant. The results (mean velocity and rms value) are summarized in Table 6.1. The configuration with the smallest inclination angle is excluded from the velocity estimation, since a sliding motion could not be realized (values indicated with *n.v.* in Table 6.1). Indeed, a clear trend can be observed. The sliding velocity and
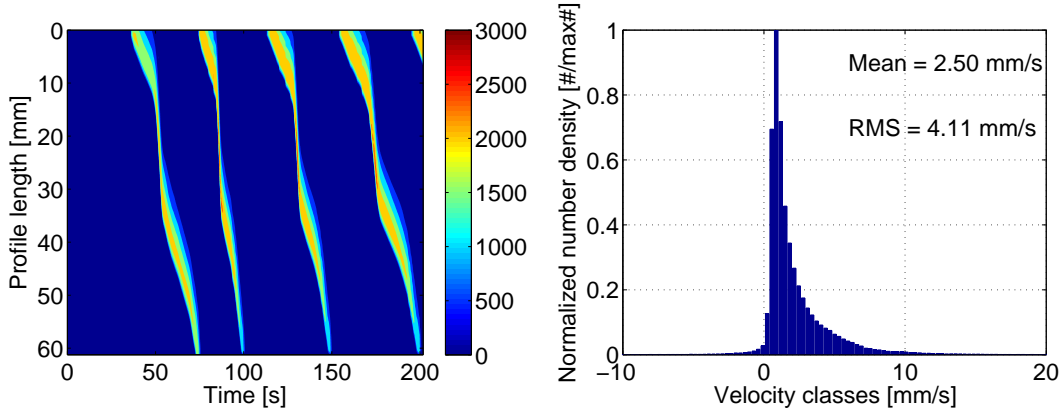
FIGURE 6.30: Temporal film thickness profiles (left, in µm) and deduced velocity histogram (right, velocity in mm/s) for cannula I, inclination 15°

TABLE 6.1: Mean velocity and rms of the sliding droplets and rivulets (in mm/s).

Inclination angle [deg]	cannula I 2.16 mm	cannula II 2.86 mm	cannula III 3.3 mm
5	n.v.	n.v.	n.v.
15	2.50 ± 4.11	4.92 ± 9.55	4.79 ± 11.86
19.5	2.89 ± 5.21	5.85 ± 11.03	6.16 ± 12.57

velocity variation (rms) increase with increasing inclination angle. Droplets lead to a broader range of velocity values, if they are captured during the acceleration process. Consequently, the rms values are higher. The vector plot in Fig. 6.31 shows the sliding velocities of isolated rivulets and single droplets as function of time. Each vector represents the velocity obtained from two consecutive images and is plotted according to the current time and the associated streamwise location. For a better visualization, the tracks of three isolated droplets have been selected and plotted. The start position has been set to a unique value in streamwise direction of 55 mm.

In the upper diagram, the velocity plot shows the experimental results for three different inclination angles, for an exemplary time frame for cannula II. The velocity increases with increasing inclination angle, which agrees completely with the expectations. As mentioned before, it is difficult to obtain clear information for the smallest plate inclination (black color), where many vectors are directed counter current. However, a continuous sliding motion can be obtained sometimes (here after 33 seconds), but only at very low velocity.

The lower image in Fig. 6.31 illustrates the velocity for the three cannulas used in the experiments, at a fixed plate inclination of 15°. The tracks do not differ as much as in the case of different inclination angles. Nevertheless, they show specific behavior. An almost linear track can be observed for the rivulet associated to the largest impingement
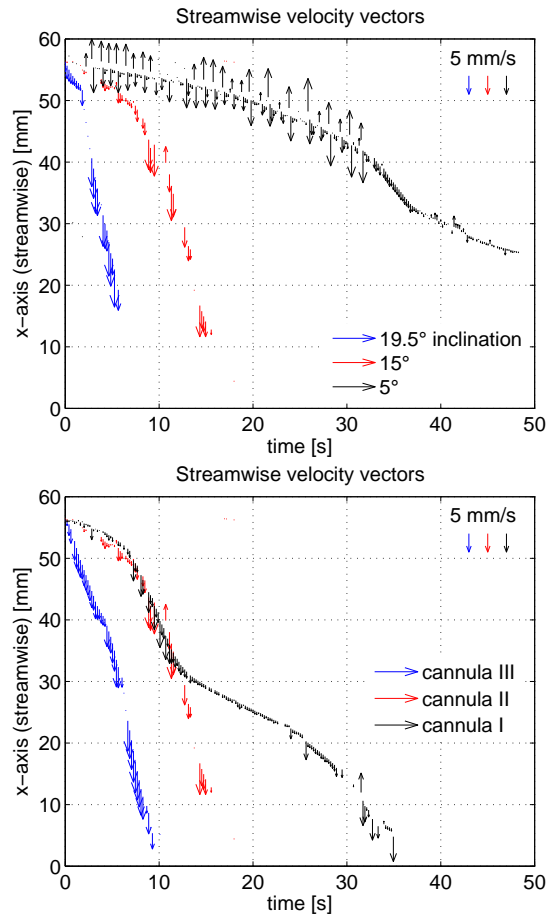
FIGURE 6.31: Sliding (streamwise) velocity vectors of isolated rivulets and droplets (reference vectors of 5 mm/s located in the upper right corner). The upper figure corresponds to cannula II, the lower figure to a plate inclination of 15°.

mass load (cannula III). On the contrary, the set in of the sliding motion is delayed for a decreased mass load. Moreover, the motion itself oscillates (increasing velocities followed by decreasing velocities) for the smallest mass load. The region around 55 mm in streamwise direction is related to the location of the droplet impact. Droplets at the highest inclination or with the largest mass load (cannula III) leave this area first, as can be seen from Fig. 6.31. Therefore, they faster become independent from subsequent droplet impacts. At very small inclination angles, the droplet spread is very large, such that more than half of the droplet track is affected by further droplet impacts. Consequently, the streamwise velocity is strongly influenced.

Each droplet stream shows a systematic temporal behavior. At first, the streamwise droplet velocity is low near the impingement location. Subsequently, they accelerate to a maximum speed which they retain until leaving the FOV. Deceleration and acceleration phases often alternate (Fig. 6.31) for very small mass loads.

The transversal velocity is also important to fully describe the rivulet motion. The corresponding results are shown as vector plots in Fig. 6.32. Similar to the vector plots
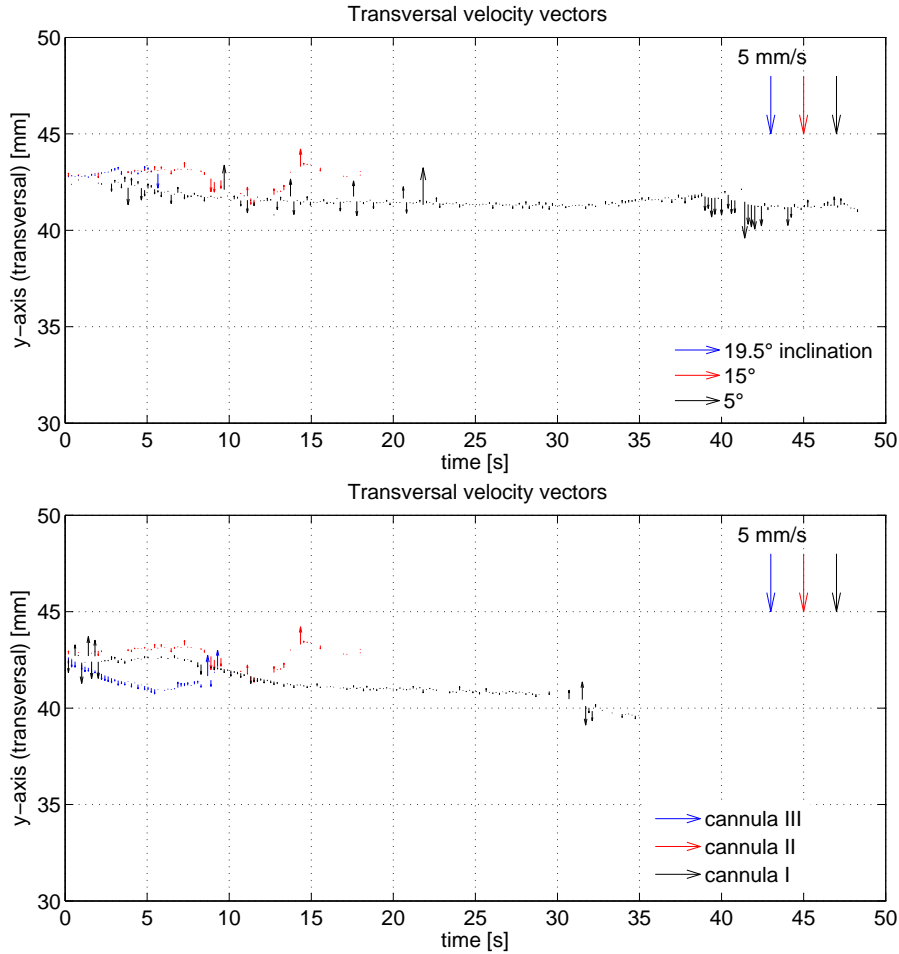
FIGURE 6.32: Transversal velocity of rivulets and droplets (reference vectors of 5 $^{mm}/_s$ located in the upper right corner). The upper figure corresponds to cannula II, the lower figure to a plate inclination of 15°.

of the streamwise velocity, the start position of the tracks has been shifted to a unique value of 43 mm. This makes it easier to compare the individual tracks. Basically, the transversal velocity component is very small compared to the streamwise component, in particular for large inclination angles (see upper plot in Fig 6.32). The transversal velocity remains almost constant (see lower plot in Fig. 6.32) for different mass loads. Obviously, the plots differ in their length, which is a consequence of the different streamwise velocities. The residence time of a rivulet in the FOV increases with decreasing inclination angle. Furthermore, it increases with decreasing mass load.

Small oscillating velocities can be observed around a mean value, when taking a closer look at Fig 6.32. Indeed, this type of rivulet motion (which is called meandering) is well known and discussed in the literature [34]. Meandering rivulet motion can be observed, if the plate inclination is small. A reduced mass load promotes meandering flow behavior. The droplets and rivulets follow a straighter path, when a stronger driving force leads

to a higher streamwise velocity. In contrast, the direction of the transversal velocity changes much more for smaller streamwise velocities.
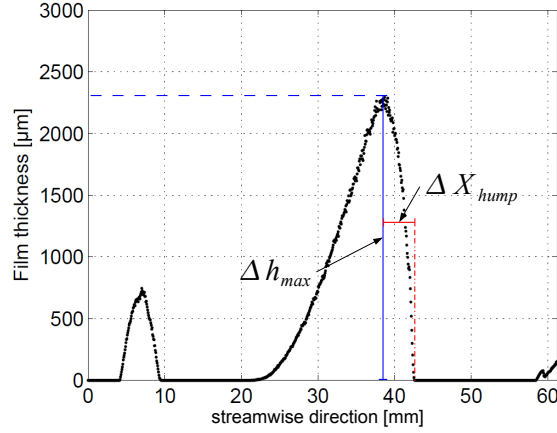

FIGURE 6.33: Definition of the important gradient quantities at advancing side, Δh_{max} and ΔX_{hump}

The spatial resolution of the presented method is lower than that of alternative techniques like shadowgraphy [156]. Nevertheless, it is possible to quantify the wetting behavior including apparent contact angles, also known as rivulet front angles [75]. Most interesting is the film thickness gradient at the advancing side of the droplets or rivulets. Accordingly, the quantities Δh_{max} and ΔX_{hump} are necessary, as defined exemplarily in Fig. 6.33 for cannula II. The ratio $\Delta h_{max}/\Delta X_{hump}$ of sliding droplets on each image is evaluated in flow direction, in order to obtain a quantitative result for the dynamic contact angle. It is plotted as function of the local film thickness (Fig. 6.34, left). It is assumed that the dynamic contact angle remains below 90°, otherwise it would lead to $\Delta X_{hump} \rightarrow 0$. This has to be kept in mind for further interpretation of the results. The slope of the correlation between film thickness and the ratio of $\Delta h_{max}/\Delta X_{hump}$ increases roughly linearly when increasing the inclination angle of the plate (see Fig. 6.34, right). A similar behavior is observed for instance by Johnson et al. [75] for other fluids. In principle, this slope corresponds to a global value of the dynamic contact angle.

In order to capture the wetting behavior the dynamic contact angle θ_D is plotted as function of the Capillary number (Ca), which is defined in Eq. (2.1), including the contact line velocity v, the dynamic viscosity μ and the surface tension σ. The correlation between Ca number and the dynamic contact angle has been deduced from the Voinov relation

$$\theta_D = \theta_e + c_T \, \mathrm{Ca}^{\frac{1}{3}}, \tag{6.3}$$

as explained in Šikalo et al. [156] and Winkels et al. [163]. Therefore, the experimental results can be fitted, using a root function. The best fit is obtained for the fitting parameters $c_T = 66.14$ and $\theta_e = 68.87°$, involving simultaneously all three plate inclinations.
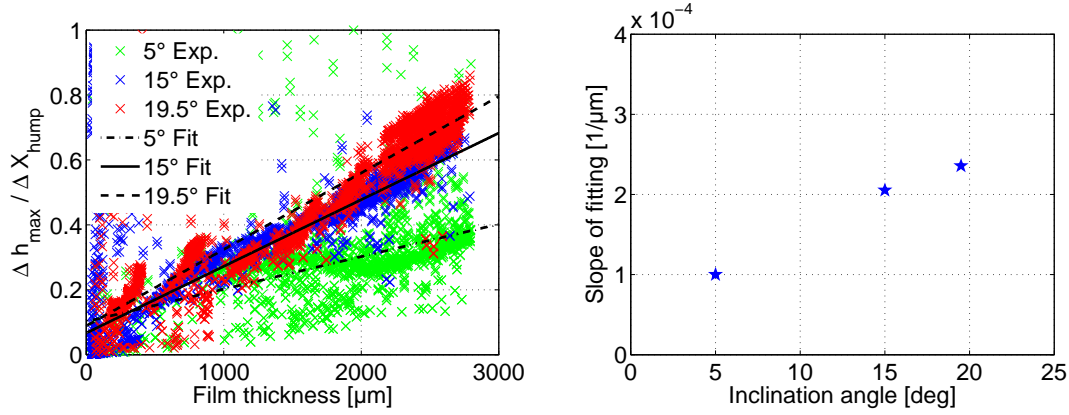
FIGURE 6.34: Ratio $\Delta h_{max}/\Delta X_{hump}$ over the film thickness for different plate incli-
nations fitted with a linear function (left), and resulting slope (right)

The quality of the fit is given by the r^2 coefficient. It takes a value of $r^2 = 0.78$, which
proves the reasonability of the fitting function. Usually, the Ca number is built with the
contact line velocity. Instead, the rivulet tip velocity is used in the present case. It can
be used for this purpose, as reported by Johnson et al. [75]. The intersection point with
the y-axis corresponds to the static contact angle, which has been reported to be around
70° [37], for the employed material combination (water on acrylic glass). Preliminary
experiments confirm this value, as discussed in Section 2.2. Using the shadowgraphy
technique with a spatial resolution of 2.6 μm/pixel, the static contact angle has been ob-
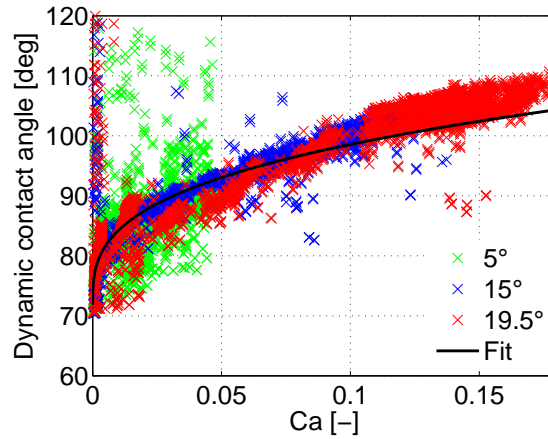served in the range of $60° - 70°$. Finally, the dynamic contact angle can be plotted as

FIGURE 6.35: Dynamic contact angle as a function of the Ca number

function of the Ca number (Fig 6.35), following:

$$\theta_D = 68.87 + 66.14 \, \mathrm{Ca}^{\frac{1}{3}} \tag{6.4}$$

The tendencies and quantities deduced from the experimental measurements are logical
and fully agree with theoretical expectations. A large scatter can be observed for the

smallest plate inclination. It indicates again the difficulty of obtaining a continuous sliding motion.

In conclusion, this new film measurement technique yields information concerning film flow properties (also of single droplets and rivulets) with high spatial and temporal resolution. The simplicity of the method and the low financial effort attributed to the illumiation technique are clear advantages of this new technique. However, an application in the wind tunnel environment or to complex geometries such as the mirror geometry is still not possible. Restrictions are made by safety requirement, primarily coming in to play with the fluorescent dye. Often, these chemicals are toxic and consequently, should not be atomized and distributed.

Nevertheless, there are some interesting results. Specific details can be revealed concerning wetting properties, which are worth to investigate further. The contact angle results can be used directly to improve the film model in order to predict surface wetting with higher accuracy. The contact line velocity is also associated with surface wetting. It was assumed equal to the sliding velocity of single droplets. In reality this is more complex, since the contact line does not move with a unique velocity everywhere. These details are generally interesting for all kinds of free surface flows involving contact line motion. They will be subject to future research.

6.4   Numerical Results

The main purpose of the numerical work has been to improve and to test the resulting film model. All details concerning the model improvements have been given in Section 3.2.3. Now, the film simulation results are presented for the rear view mirror geometry. The preliminary results for the windshield configuration have been reported earlier in Hagemeier et al. [53]. Both, the original and the improved film model have been used to predict the film flow. In particular, the film thickness and the film break-up in terms of mass release rate are evaluated. The simulation results are compared with experimental data obtained by colleagues from the ISM Braunschweig.

6.4.1   Configuration K2 (Rear View Mirror)

The numerical results for the rear view mirror are shown here, starting with the film thickness results. They were obtained from simulations using the original and the improved film model. The results are shown for quasi-steady state conditions, which are reached after approximately 1.5 s, as discussed earlier in Section 5.2.4. Globally, the

difference in film expansion and thickness values are small (see Fig. 6.36). The mirror housing is wetted almost completely. Small rivulets can be observed near the mounting plate for the improved film model. Once more, this is a sign of active wetting limitation, where the film tends to expand into separate streams. More differences can be found
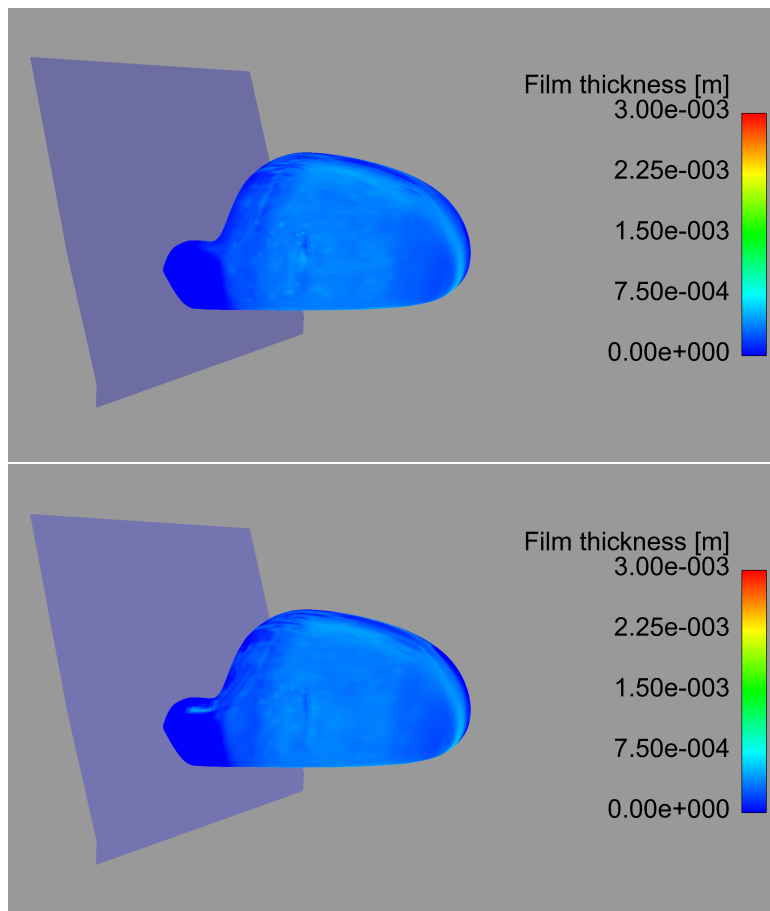

FIGURE 6.36: Compared results of original (top) and improved (bottom) film model for film thickness, exemplary results at 15 $^m/_s$ air flow velocity

when changing the point of view. Figure 6.37 shows the film flow beneath the mirror housing. The film covers the complete area with the original film model. Large values of film thickness can be observed almost everywhere. In fact, the locations to the front part of the lower side correspond to a local minimum of wall shear stress, as can be seen in Figure 6.38. As expected, the film is now restricted to the front area of the mirror housing, when using the improved film model. The boundary between wet and dry surfaces follows the minimum shear stress curve (see Fig. 6.38). Therefore, the film expansion is inhibited along this line using the improved formulation.

The liquid accumulates along this line until the film break-up criterion is fulfilled and droplets are released. Figure 6.39 shows film break-up at different locations for the two modeling approaches. The upper part of the mirror is not visualized, because no release is encountered there.
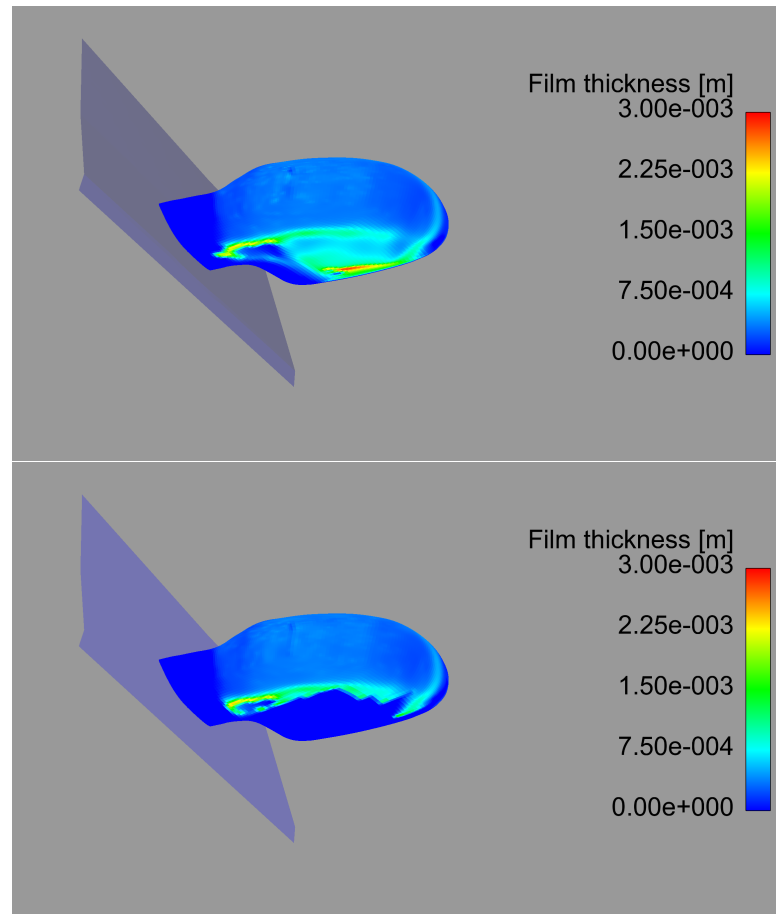
FIGURE 6.37: Compared results of original (top) and improved (bottom) film model for film thickness, exemplary results at 15 ᵐ/s air flow velocity
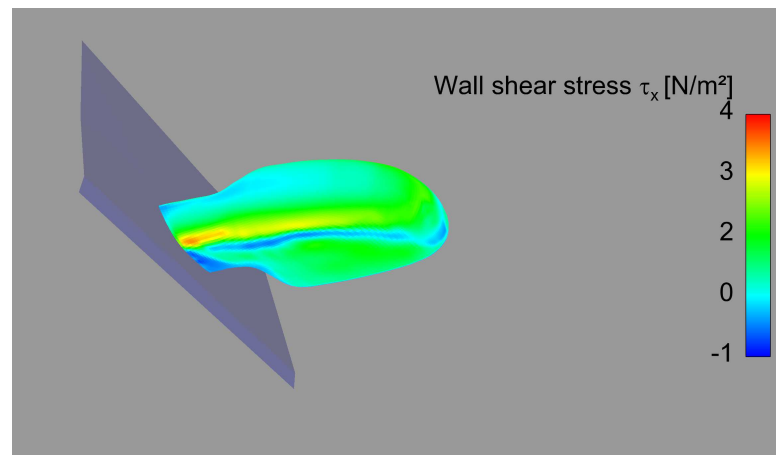

FIGURE 6.38: Shear stress x-component, exemplary results at 15 ᵐ/s air flow velocity

It is a matter of fact that the film break-up is strongly affected by the film flow behavior. Hence, the accumulation of liquid along the aforementioned line and local peaks in film thickness play an important role for locating the break-up spots.

In case of the original film model, the film breaks up exactly at the positions where
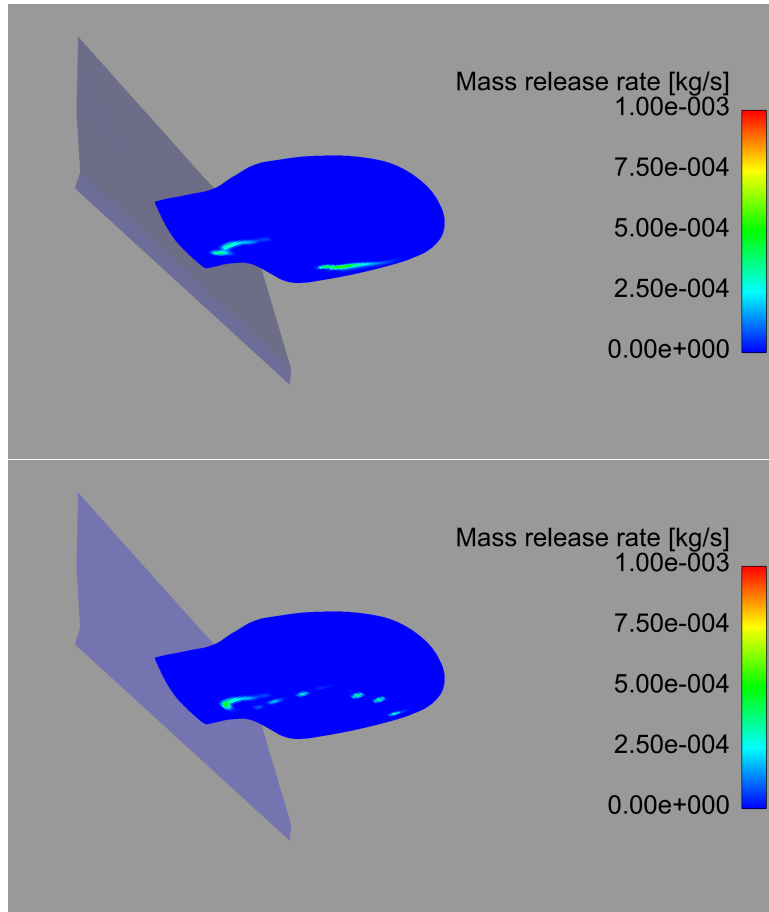
FIGURE 6.39: Compared results of original (top) and improved (bottom) film model for release rate associated to film break-up, exemplary results at 15 ^{m}/$_s$ air flow velocity

the film thickness peaks are located. The position near the mounting plate may be a reasonable prediction, since it is in the area of high film thickness and high shear stress. On the contrary, the break-up spot near the trailing edge of the mirror housing is at least questionable. The mass release rate is there in the same order of magnitude as found for the windshield configuration.

In the improved model, the film break-up is related to high shear stress and high film thickness. Several break-up spots are located along the line of high shear stress (see Fig. 6.38) which is in direct correlation to the area where the liquid accumulates. The mass release rate is almost the same as in case of the original film model. Maximum release rates of 7.11 10^{-4} ^{kg}/$_s$ and 6.61 10^{-4} ^{kg}/$_s$ are predicted by the original and improved film model, respectively. These values correspond to droplet release rates of 50 ^{droplets}/$_s$ and 47 ^{droplets}/$_s$.

In conclusion, there are small but noticeable differences in the predictions of the film break-up between the two film models for the rear view mirror geometry. Globally, almost identical release rates have been predicted. One break-up location is identical, the

other one completely different. Since the release location will decide if and where secondary droplets might impact the drivers window, these small differences might indeed be highly relevant for practical purpose.

Unfortunately, it is not possible to compare the predicted release rates with direct measurements. The numerical results are nevertheless evaluated later on, based on an indirect comparison.

Comparisons with experiments

Similar to the windshield configuration, the rear view mirror has been investigated experimentally by the project partner from ISM Braunschweig. They obtained data concerning the film thickness on the mirror housing. Consequently, the predicted film thickness values can be compared with experimental results. The experiments have been conducted at 4 different locations, shown with color lines in Fig. 6.40. A new measurement technique, described by Brinkmann [20], has been applied to quantify the film thickness on curved surfaces. This is an extremely challenging task and still leads to very high measurement uncertainties. The mean film thickness and the standard deviation are reported for each measurement location. Detailed information concerning the experiments are given in Brinkmann [20].
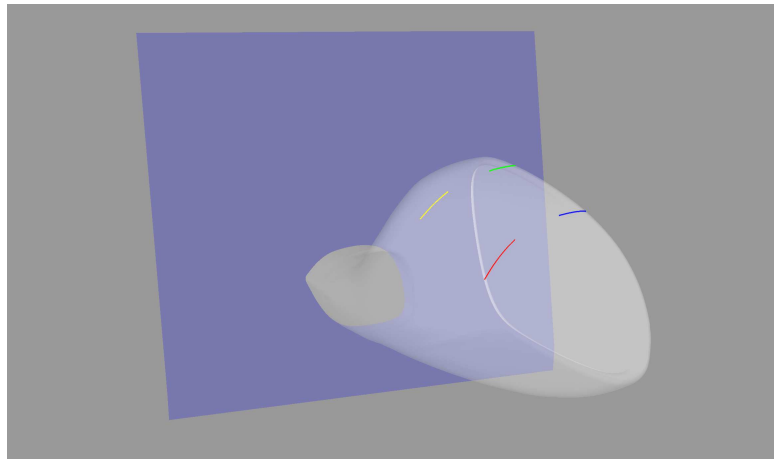

FIGURE 6.40: Measurement locations investigated at ISM Braunschweig (color lines)

Figure 6.40 shows the 4 measurement locations as colored lines. The yellow and the green lines correspond to the inner side, which is located 35 mm from the centerline towards the mounting plate. These measurement locations can be distinguished by their angular position, such that the yellow curve is associated with an angle around $45°$, while the green curve corresponds to an angle around $90°$.

The outer position is located 35 mm from the centerline towards the mirror tip. In agreement with the inner configuration, the red and blue curves are located at angles around 45° and 90°, respectively. The numerical results have been averaged for the respective area, to obtain mean values and standard deviations for the film thickness.
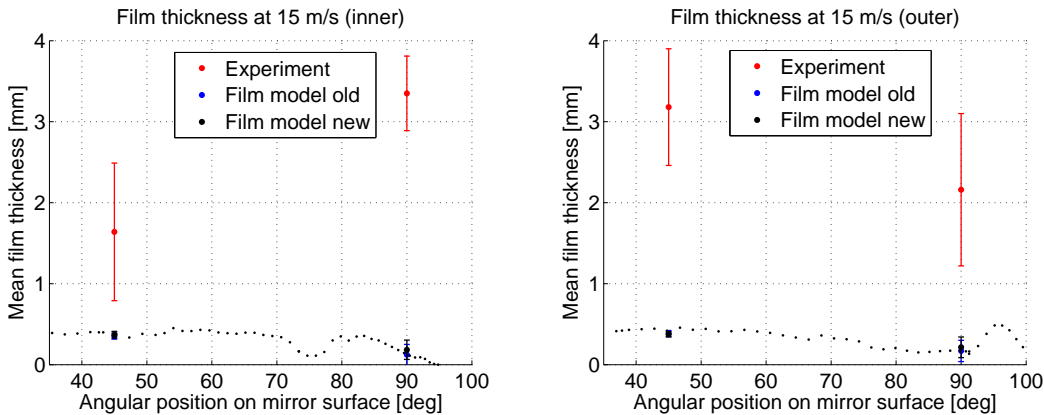

FIGURE 6.41: Comparison of experimental and numerical results for the film thickness at 15 m/s air flow velocity. The dotted lines show the film thickness obtained with the improved film model.

Comparing the experimental and numerical results for the film thickness (see Figure 6.41) major differences can again be observed. Generally, the predicted film thickness values (up to 500 μm) are quite large but still far below the values obtained from the measurements (several mm). The differences are even worse than in case of the windshield configuration, due to increased film thickness values measured in the experiments. The predicted film thickness values are even outside the range of measurement uncertainty for the case at 15 m/s air flow velocity.

The experiments show an increase of the film thickness from 45° to 90° at the inner side. In contrast, a decrease can be observed from 45° to 90° at the outer side.

In contrast, the numerical results show identical trends for the inner and the outer side. The film thickness decreases slightly from 45° to 90° for the case of 15 m/s air flow velocity. This trend is in better qualitative agreement with visual observations reported in Brinkmann and Hagemeier [22]. An air flow velocity of 15 m/s was found to be too low, to drive the liquid film upward an inclined plate (inclination of 28.5°). Therefore, it seems unlikely that the film flows up the mirror housing easily. It remains as an open question whether experimental or numerical results are closer to reality. At least for this special case, the experimental results are surprising and further tests are recommended.

Similar to the windshield configuration, the original and the improved film model yield almost the same results for the film thickness and the standard deviation. Accordingly, the original film model has not been considered further in these comparisons.
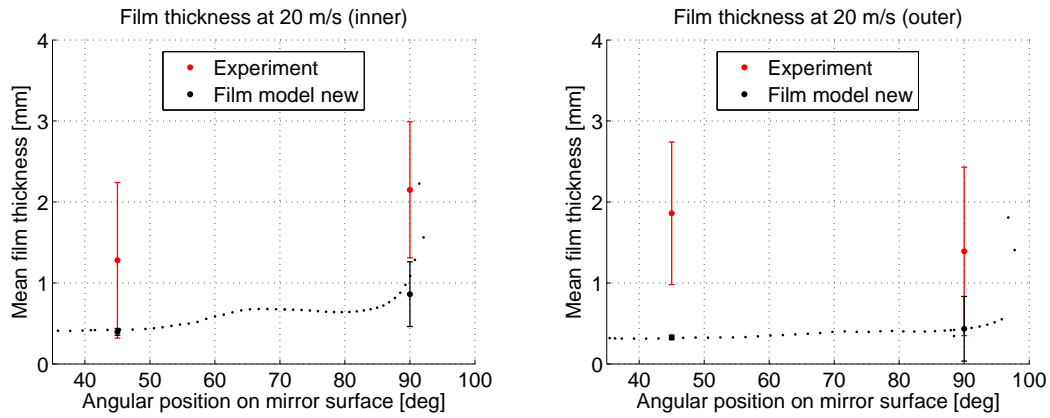
FIGURE 6.42: Comparison of experimental and numerical results for the film thickness at 20 m/s air flow velocity. The dotted lines show the film thickness obtained with the improved film model.
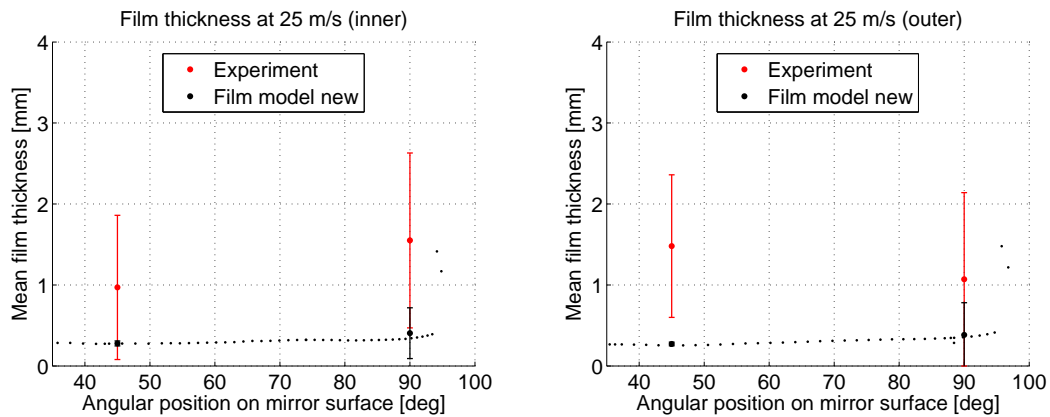

FIGURE 6.43: Comparison of experimental and numerical results for the film thickness at 25 m/s air flow velocity. The dotted lines show the film thickness obtained with the improved film model.

The experimental results are compared with numerical results obtained from the improved film model for the other cases, at 20 and 25 m/s air flow velocity (Figs. 6.42 and 6.43). They show slightly reduced film thickness values compared to the case discussed before.

Nevertheless, the trends remain different concerning the measurements for the inner and the outer side. Now, the predicted film thickness always increases from 45° to 90°. This trend is reasonable, since the driving shear stress increases with increasing air flow velocity. Occasionally, the predicted film thickness values fall within the range of measurement uncertainty.

As mentioned before, a comparison of experiments and simulations concerning the film break-up fails due to the lack of direct measurement data. Therefore, an attempt is now made to evaluate the film model and its break-up law indirectly. This means that additional data are used, in particular data describing the dispersed liquid phase. It is easy

to compare the dispersed phase properties, since they are available from the experiments (PDA measurement) as well as the simulations (lagrangian particle simulation).

Generally, film break-up leads to dispersed droplets with different velocities. The droplets are initialized by considering the air flow and the film flow conditions at the release point. Consequently, the correlation of droplet diameter and velocity is an indirect measure for the quality of the film break-up simulation.
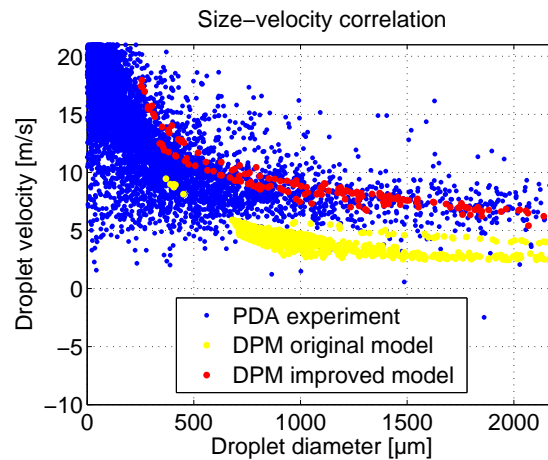

FIGURE 6.44: Comparison of experimental and numerical results for diameter-velocity correlation, exemplary for $x = 0.4$ m-plane at 15 $^\mathrm{m}/_\mathrm{s}$ air flow velocity

Figure 6.44 shows the comparison of experimental and numerical results for the diameter-velocity correlation. The experimental data have been obtained at an air flow velocity of 15 $^\mathrm{m}/_\mathrm{s}$ for the $x = 0.4$ m-plane, which corresponds to a position in the wake of the mirror. The numerical results (simulated droplet properties, red and yellow points) are limited to droplets originated by film break-up. The results obtained with the improved model are in fair agreement with the measurement results (blue points). In contrast, the original model predicts secondary droplets that are in majority too large and too slow. Almost constant velocity values can be observed for droplets with diameters ranging from 750 to 2200 μm.

Therefore, the film simulation results using the improved model appear to be more reliable concerning the predicted break-up conditions. All properties of the secondary droplets are governed by the film conditions. Both the initial size and the release position dictate where a certain droplet will go during the particle tracking simulation. Due to the fact that identical break-up models are employed in the original and improved version, the break-up properties are dictated by the simulated film conditions. Hence, the improved model predicts more realistic film flow behavior compared to the original model.

6.5   Conclusions

The improved film model works numerically fine. The qualitative comparisons of the original and the improved models show reasonable changes when using the improved model. Especially, the wetting limitation alters the film flow and break-up behavior and the predictions appear more realistic. However, the validation of the improved film model is not yet finished. Further quantitative comparisons of simulation results with different experimental results are needed. The available experimental results (only film thickness) are limited, sometimes surprising, and the associated measurement uncertainty is very large. The desired validation data should include several film quantities. In particular highly accurate values for the film thickness, velocity and break-up rates would considerably improve such comparisons. Additional experimental work is encouraged and planed for the future, for example using the recently developed fluorescence imaging technique described in Section 4.5. It is applicable to measure 2D film thickness values and possibly film surface velocity for planar geometries, as for example the windshield. However, such measurements are still complex and connected to high safety requirements (toxic fluorescence dyes). Therefore, they could not be carried out up to now.

The improved film model has been indirectly evaluated, using information concerning the dispersed liquid phase behind the mirror. It appears, that the model predicts secondary droplets in a realistic range of the diameter-velocity correlation. The range of predicted data fits very well to the right part of the diameter-velocity correlation measured with PDA. It seems now that this part, which is separated from most of the PDA samples for upstream measurement positions (compare Fig. 6.21) is related to secondary droplets released from the film.

6.6   Data Base

All obtained results have been gathered within a data base containing experimental and numerical work. It is built in a Wiki style format and includes all experimental raw data that have been shown and presented in this chapter. Additionally, the user can find specific information concerning the measurement techniques and facility. As second important part of the work, the source code files of the different film model versions have been stored in the data base as well. Four different models are stored there, representing the original model version and three improvement steps. They are described in details in the corresponding part of the data base. Therefore, the user can easily follow the single changes.

All publications, peer-reviewed journal papers as well as conference contributions are stored in a separate part of the data base.

Due to confidentiality the access to the data base is restricted to Volkswagen AG Wolfsburg.

Chapter 7

Conclusions and Outlook

7.1 Conclusions

An extensive literature survey revealed many issues associated to practical vehicle soiling investigations, as applied in the automobile industry and in many scientific projects. Details of this review are published in Hagemeier et al. [54]. Different film models are recommended as a function of the specific application. Furthermore, the main unresolved issues associated to vehicle soiling are discussed within the review. As a matter of fact, the exact quantitative prediction of the soiling pattern is still an open question, in particular when film break-up is included. The present study contributes usefully to this topic on the basis of experimental and numerical investigations.

The experimental work includes the characterization of the multiphase flow conditions in the wind tunnel. Two geometrical configurations have been investigated. The K1 configuration considers the flow around a generic windshield, while the K2 configuration is that of a realistic rear view mirror geometry. Using laser optical measurement techniques (LDV, PDA and PIV), the velocity of both the gas and droplet phases, together with the droplet size have been characterized. The results provide new and interesting information concerning vehicle soiling processes. For instance, the wind tunnel experiments reveal details of the continuous gas and dispersed droplet phases. The flow fields for both geometrical configurations are described by the mean velocity and the turbulence intensity of the gas phase. Furthermore, vector plots describe the 2D velocity field around the windshield. All values are available for use in numerical studies, for setting boundary conditions or for validation purposes.

Mean values for droplet diameter and velocity are available from the PDA measurements. Moreover, there are detailed information concerning the local probability density

functions of both variables. In near-wall regions, a complex shape can be observed for the local size-velocity pdf. Additionally, the size-velocity correlations are derived, which describe the droplet behavior even better. Secondary droplets can be identified by examining size-velocity correlations. This analysis confirms a complex spray-wall interaction behavior. Further insight is provided by relating the experimental results to the numerical findings. For instance, PDA observations show unexpected droplet deceleration with increasing distance from the mirror surface. This droplet behavior becomes logical, when considering information from aerodynamic simulations. The predicted air velocity reveals unusual trends induced by the mirror shape, which explain the experimental findings.

Vehicle soiling is generally evaluated in terms of liquid film quantities. Therefore, film thickness measurements have also been conducted. A film thickness measurement technique was developed, based on fluorescence imaging. A two-dimensional film flow (open channel flow) was investigated and the experimental results were employed to validate the film model. The measurement technique has been further applied to investigate sliding droplets and rivulets. These experiments proved that contact angles and surface tension forces have significant effects on liquid film flow dynamics. Sliding droplets and rivulets are common patterns in vehicle soiling due to rain. These results are highly relevant, in particular to improve the film model. The experimental work was published in Hagemeier et al. [52] together with supplementary flow visualization.

In parallel with the experiments, CFD studies have been carried out for a rear view mirror configuration. The flow field is computed by employing a simple RANS approach. A fair agreement is observed for the mean velocity values when compared with the experimental results. An even better agreement is probably impossible with a RANS approach. Using a high-resolution approach (SAS, DES, LES) would improve the predictions. A correct prediction of wall shear stress values is ensured by grid refinement in the boundary layer region. The wall shear stress is the most decisive parameter for the film flow simulation, which is derived from the CFD simulations.

A central objective of the work was to improve a simple film model. The model of Anderson and Coughlan [8] was chosen as starting point. The first improvement relies on correlations from the literature. In particular, the contributions of Mundo et al. [109], O'Rourke and Amsden [118], Penn et al. [122] and Foucart and Blain [46] have been used to extend the model formulation. In particular, complex spray-wall interaction, wetting limitation and an alternative break-up model have been implemented as new submodels.

Subsequently, the liquid film flow was simulated for the rear view mirror configuration. Both the original film model of Anderson and Coughlan [8] and the improved version

developed during this study have been used for the numerical investigations. Finally, applying the two film models show slightly differing results (qualitatively and quantitatively) for the film expansion, film thickness and break-up.

The numerical results are further compared with the experimental findings of Brinkmann [20]. The comparison for the mean film thickness is limited to 2×2 points for the mirror configuration. No satisfactory agreement is observed between experimental and numerical results. However, a clear conclusion can not be drawn from these findings yet due to the limited number of simulations and validation points and to the large experimental uncertainty.

An attempt has been made to indirectly evaluate the film flow prediction. This is done by comparing the experimental (PDA) and numerical (Lagrangian particle tracking) results for the size-velocity correlation. Here good agreement is observed when using the improved model.

Some more conclusions can be drawn from a practical point of view, such as concerning the applicability of the model within a real development process. First, the film model is already included in the Fluent CFD software as a UDF. It is a useful tool, though still at a development level. Further steps are therefore necessary, in particular with respect to code optimization and operator convenience. An issue is that this UDF runs only on a single core. Consequently, there is a strong restriction to small grids, as discussed already during this study. Secondly, even if there are diffrences between the results from the original and the improved model, a final model validation is pending due to still insufficient quantitative comparisons between experimental and numerical results. Qualitatively, the improved film model performance is good, which means that it is at least applicable for preliminary studies and rough estimations.

In conclusion, the film model shows high potential for predicting the film flow behavior in a simple and fast way. Further improvements of the simulation quality are possible, if reliable experiments deliver suitable validation data, in particular highly accurate film thickness values and break-up rates.

7.2   Outlook

As mentioned in the conclusions, the model improvements are based on correlations from the literature. If further work leads to new results and different correlations, it is quite easy to change the implemented model equations for specific submodels, such as wetting or break-up. The existence of different break-up models leading to highly differing consequences is an issue with high impact for further soiling simulations. A

sensitivity analysis of the models in combination with new experiments can deliver the basis for an improved break-up model.

With respect to continuously increasing computer power, it is also possible to include more detailed and complex models. Some of these complex models already exist, although they have not yet been applied to vehicle soiling simulation. Moreover, the combination of different model approaches within hybrid models might be promising.

The improved film model presented in this study may also be subject to further adaptation. When including heat or concentration fluxes and complex material properties, the model could be used in process engineering applications.

Concerning the experiments, it is noteworthy that it is still a very difficult task to measure the film thickness and velocity with high spatial and temporal resolution on curved geometries. Complex calibration procedures often limit the application of a certain method to special geometries. New and improved measurement techniques for film characterization are required for many applications. The presented method, based on fluorescence imaging is very promising, especially when involving the high potential of rapidly improving LED technique.

Appendix A

Film Model Journal

iter   time/iter

Elapsed Time since Film Initialised : 988.058(ms)

Rate of water-liquid-dpm Droplet Collection
+--------------+----------------------+----------------------+
| | Mass Flux | Enthalpy Flux |
+--------------+----------------------+----------------------+
| on Wall 3 | 0.0398167 (kg/s) | 0 (W) |
+--------------+----------------------+----------------------+
| Total | 0.0398167 (kg/s) | 0 (W) |
+--------------+----------------------+----------------------+

Initialising Edges on Threads: 3 Done.

 First Iteration of 1 in New Timestep.

 Timestep for Steady Film Flow calcs = 0.670529(ms)

 Last Iteration in Timestep.
 Film will be Updated at End.

Resetting DPM film release sources... Done.

Setting new DPM film release sources... Done.

   Rate of Build Up of the Film
+--------------+----------------------+
| | Mass |
+--------------+----------------------+
| Build Up | -0.0269571 (kg/s) |
+--------------+----------------------+

Rate of water-liquid Leaving Domain in Film
+--------------+----------------------+
| | Mass Flux Out |
+--------------+----------------------+
| Film Edges | -0.0103905 (kg/s) |
+--------------+----------------------+

+--------------+----------------------+
|Depth Limiting | -0.0167295 (kg/s) |
+--------------+----------------------+

Freeing Edges on Threads: 3 Done.

Injecting from random...
DPM film source under-relaxation = 1

Randomly moving particle injections on surface 0 of random...
 80 particles created on injection point surface 0.
Done.

Injecting from film-release...
Film release injection has 1125 particles ,

Freeing particles on film-release...
Done.
number tracked = 1205, escaped = 361, aborted = 0, trapped = 0, evaporated = 0, incomplete = 0

Updating Film over timestep of 0.000670529 (s)...
 Film Depth limited to 0.500 (mm) on 143 faces.
 Water Removed at 0.0167295 (kg/s).
Done.

Elapsed Time since Film Initialised : 988.728(ms)

FIGURE A.1: Output journal for typical film modeling time step

Appendix B

Measurement Technique Settings

TABLE B.1: LDV settings, laser and transmitting optic parameters.

Parameter	Setting
Laser	Coherent E70
Power output overall (W)	2
Power/Beam (mW)	180
User interface	1
High voltage activation	1
Anode current warning level (µA)	90
Data collection mode	0
Duty-cycle	100
Dead-time	0.0001
Calibration mode	0
40 MHz frequency shift	1
Variable frequency shift	1
Variable shift frequency	4e+007
Max. samples	5 000
Max. acquisition time (s)	2 000
Coincidence method	1
Coincidence window	1e-005
Scope display	1
Scope zoom	400
Scope trigger channel	-1
Center velocity (Hz)	2.34e+006
Velocity span (Hz)	3.75e+006
Record length mode	1
Minimum record length	64
Maximum record length	256
Sensitivity (V)	1200
Signal gain	26
Burst detector SNR level	0
Anode current limit (µA)	1 500
Level validation ratio	4
Sensitivity (channel 2) (V)	1 200
Balance high voltage (channel 2)	0
Sensitivity (channel 3) (V)	1 600
Balance high voltage (channel 3)	0
Wavelength (nm)	514.5
Focal length (mm)	600
Beam diameter (mm)	1.3
Expander ratio	2.97
Beam spacing (mm)	18.5
Frequency shift (Hz)	4e+007
Number of fringes	18
Fringe spacing (µm)	5.624
Beam half-angle (deg)	2.622
Probe volume - dx (mm)	0.1019
Probe volume - dy (mm)	0.1018
Probe volume - dz (mm)	2.226

TABLE B.2: PDA settings, receiving optic parameters.

| Parameter	Setting
Receiver type	Fiber PDA
Scattering angle (deg)	160
Receiver focal length (mm)	800
Receiver expander ratio	1
Fringe direction	Positive
Scattering mode	2nd Order Refraction
Aperture mask	Mask C
Phase ratio validation	30
Eff. scattering mode	2nd Order Refraction
Eff. scattering angle (deg)	160
Phase factor P12	0.5781
Phase factor P13	0.1246
Max. diameter (μm)	2087
Relative refractive index	1.334
Eff. spatial filter width	0.64
Critical angle (deg)	82.88
Brewster angle (deg)	73.71
Rainbow angle (deg)	138.1

Appendix C

Windshield Configuration
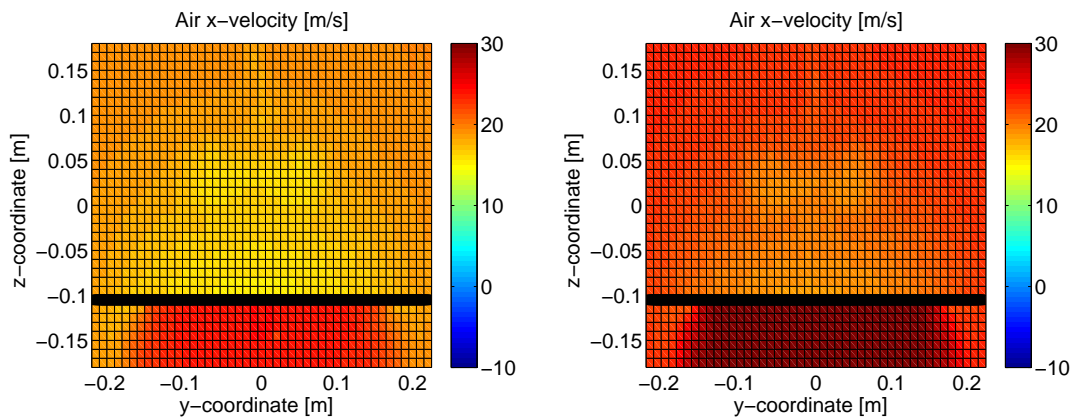
FIGURE C.1: Cross-sectional x-velocity distribution measured by means of LDV for wind tunnel velocities of $u_\infty = 20$ m/s (top) and $u_\infty = 25$ m/s (bottom) in the x0-plane.
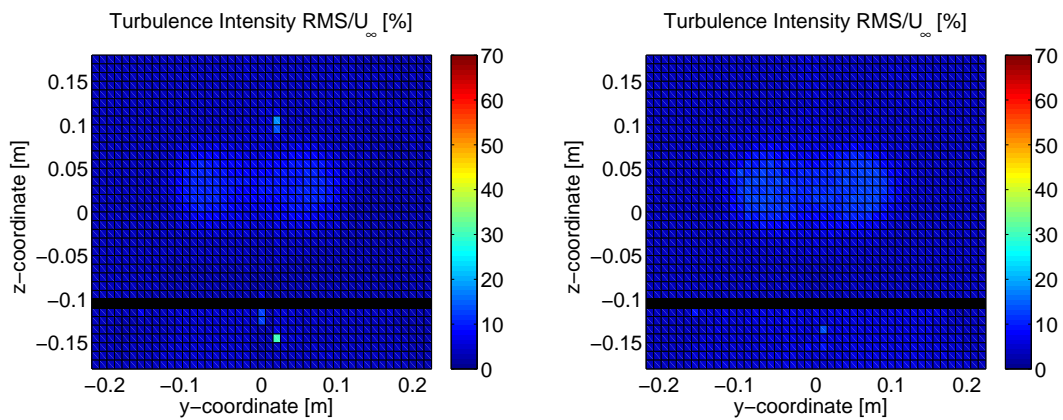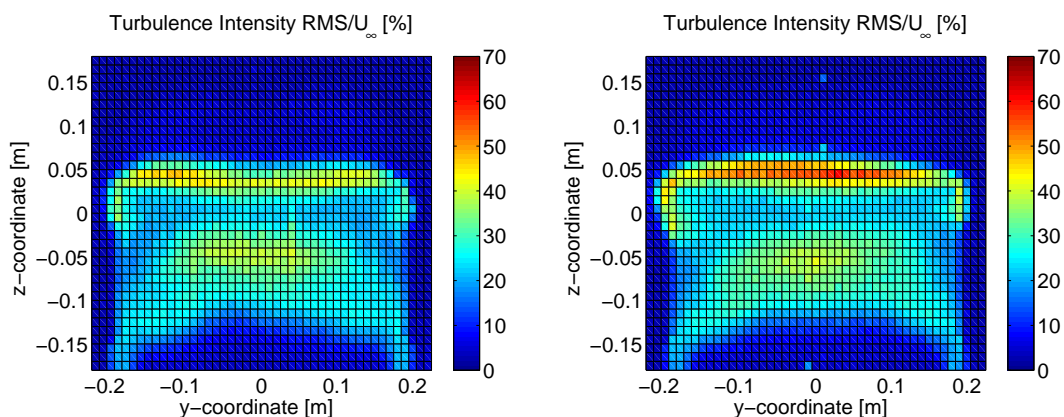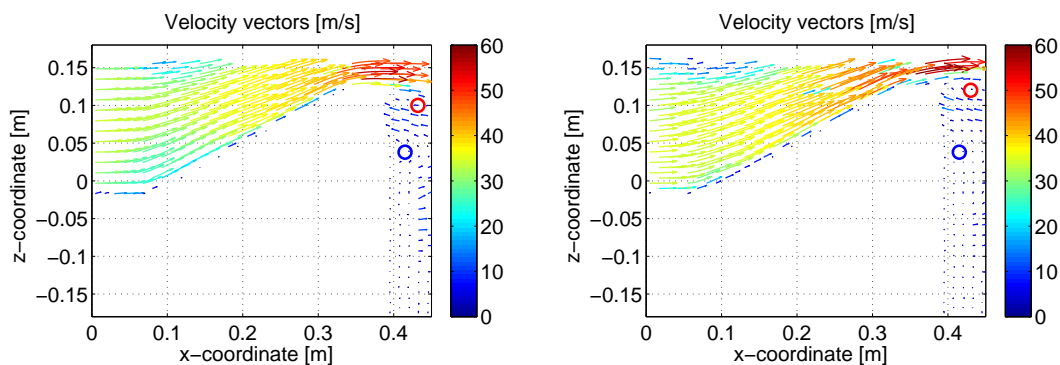

FIGURE C.2: Cross-sectional turbulence intensity distribution measured by means of LDV for wind tunnel velocities of $u_\infty = 20$ m/s (top) and $u_\infty = 25$ m/s (bottom) in the x0-plane.
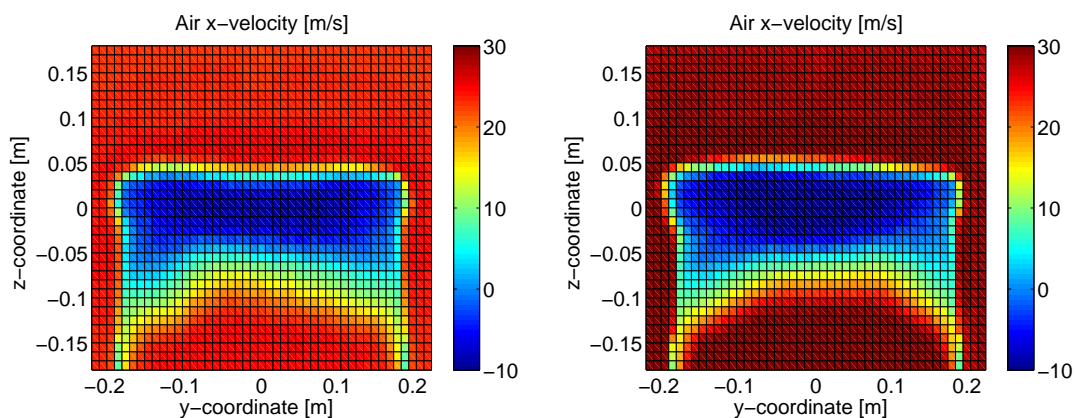
FIGURE C.3: Cross-sectional x-velocity distribution measured by means of LDV for wind tunnel velocities of $u_\infty = 20$ m/s (top) and $u_\infty = 25$ m/s (bottom) in the x400-plane.

FIGURE C.4: Cross-sectional turbulence intensity distribution measured by means of LDV for wind tunnel velocities of $u_\infty = 20$ m/s (top) and $u_\infty = 25$ m/s (bottom) in the x400-plane.

FIGURE C.5: Average air velocity measured by PIV for wind tunnel velocities of $u_\infty = 20$ m/s (top) and $u_\infty = 25$ m/s (bottom) in the y0-plane. The red circles mark the centers of clockwise rotating vortices, the blue ones mark the centers of counterclockwise rotating vortices.
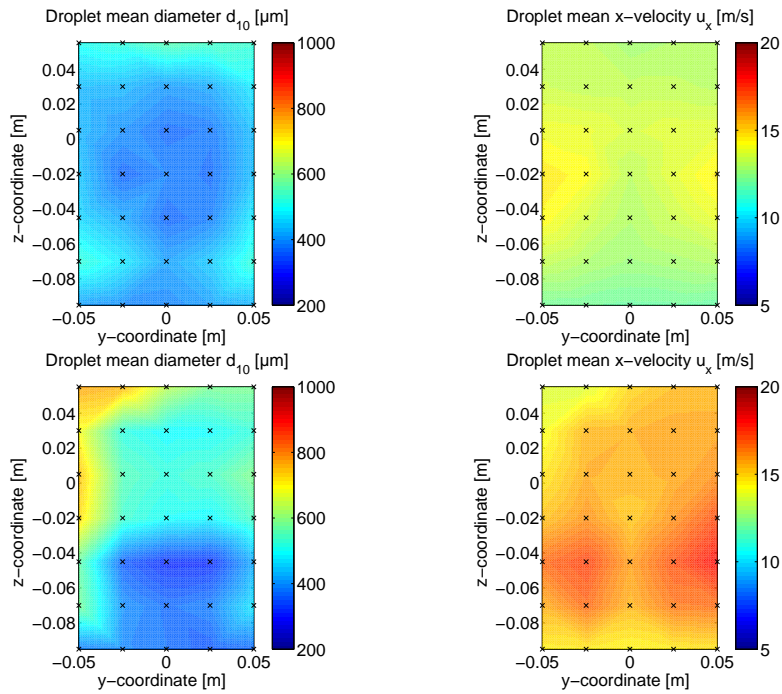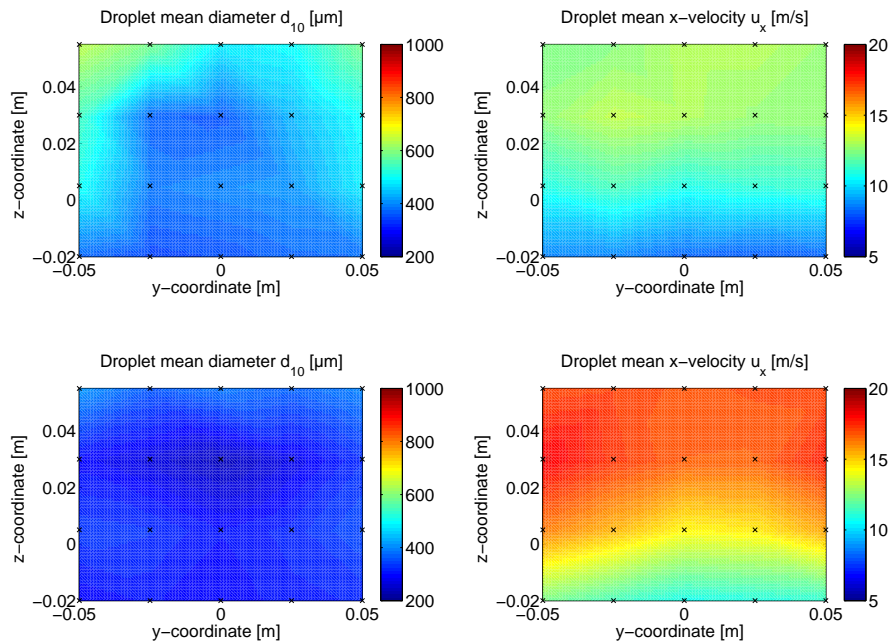
FIGURE C.6: Spatial mean droplet diameter and velocity distribution measured by means of PDA for wind tunnel velocities of $u_\infty = 20$ m/s (top) and $u_\infty = 25$ m/s (bottom) in the x0-plane.

FIGURE C.7: Spatial mean droplet diameter and velocity distribution measured by means of PDA for wind tunnel velocities of $u_\infty = 20$ m/s (top) and $u_\infty = 25$ m/s (bottom) in the x200-plane.

Appendix D
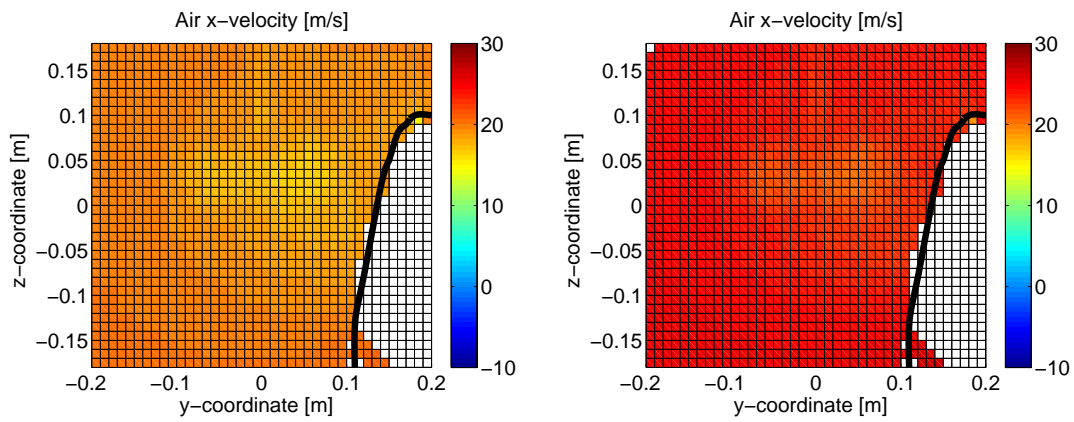
Rear View Mirror Configuration

FIGURE D.1: Cross-sectional x-velocity distribution measured by means of LDV for wind tunnel velocities of $u_\infty = 20$ m/s (top) and $u_\infty = 25$ m/s (bottom) in the x0-plane.
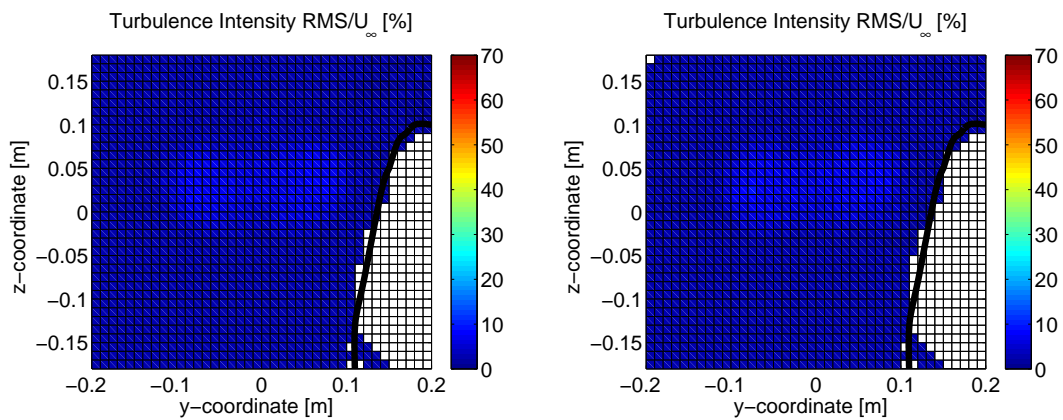

FIGURE D.2: Cross-sectional turbulence intensity distribution measured by means of LDV for wind tunnel velocities of $u_\infty = 20$ m/s (top) and $u_\infty = 25$ m/s (bottom) in the x0-plane.
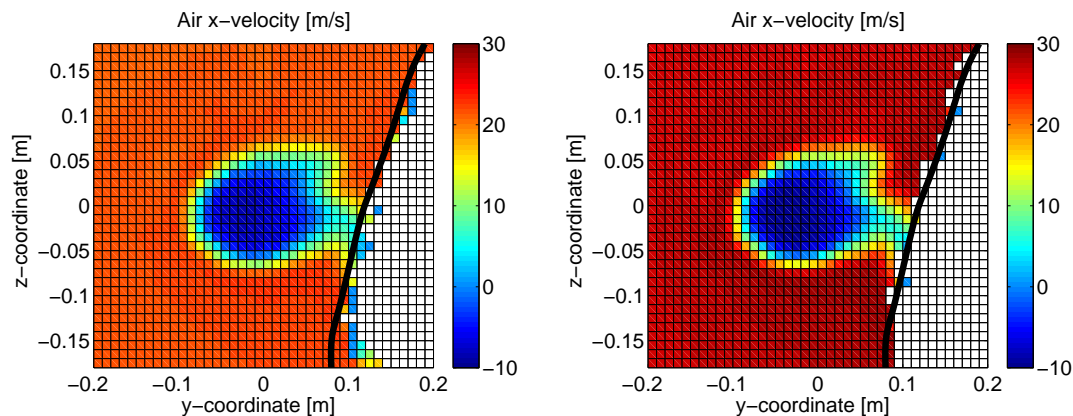
FIGURE D.3: Cross-sectional x-velocity distribution measured by means of LDV for wind tunnel velocities of $u_\infty = 20$ m/s (top) and $u_\infty = 25$ m/s (bottom) in the x325-plane.
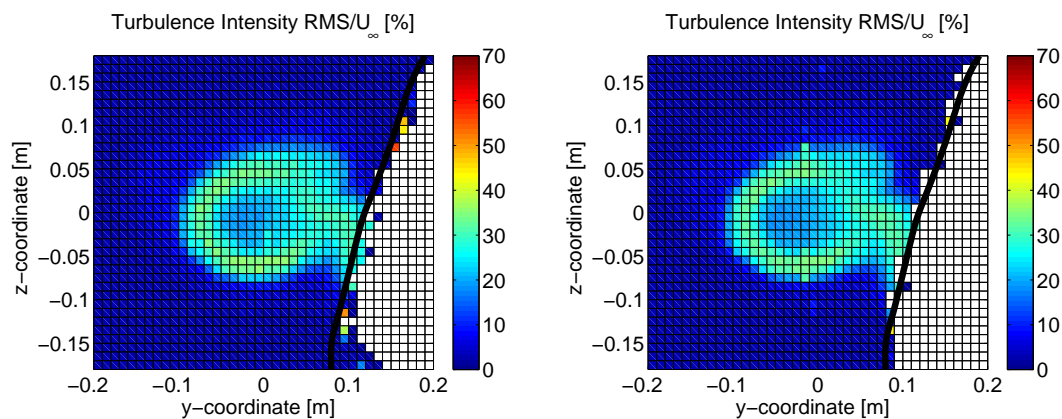

FIGURE D.4: Cross-sectional turbulence intensity distribution measured by means of LDV for wind tunnel velocities of $u_\infty = 20$ m/s (top) and $u_\infty = 25$ m/s (bottom) in the x325-plane.

FIGURE D.5: Spatial mean droplet diameter and velocity distribution measured by means of PDA for wind tunnel velocities of $u_\infty = 20$ m/s (top) and $u_\infty = 25$ m/s (bottom) in the x0-plane.
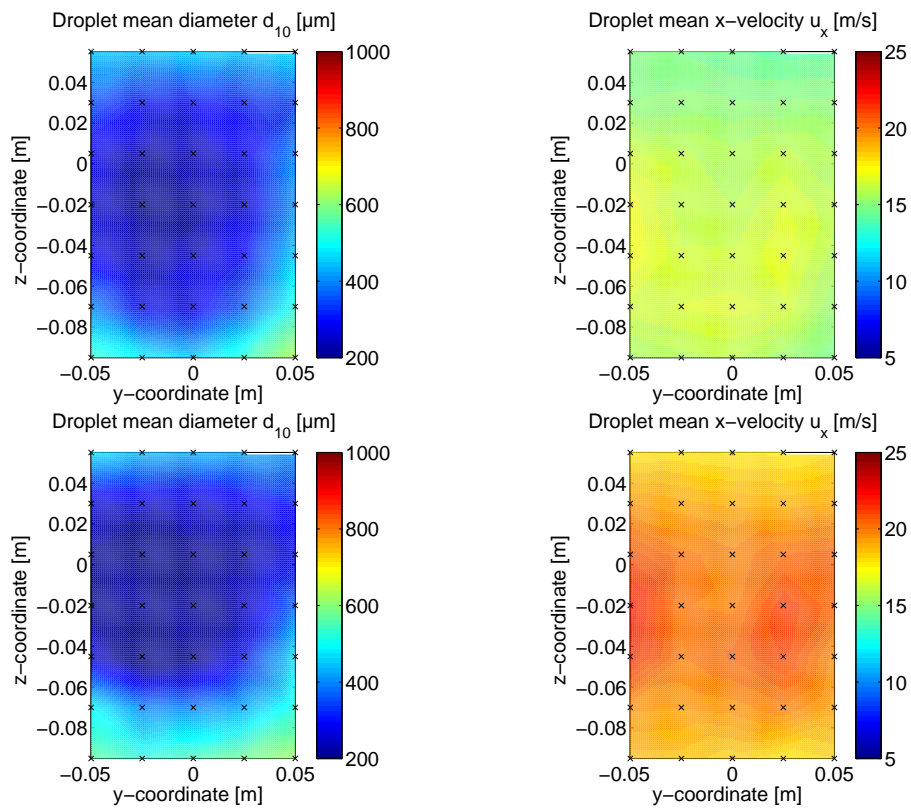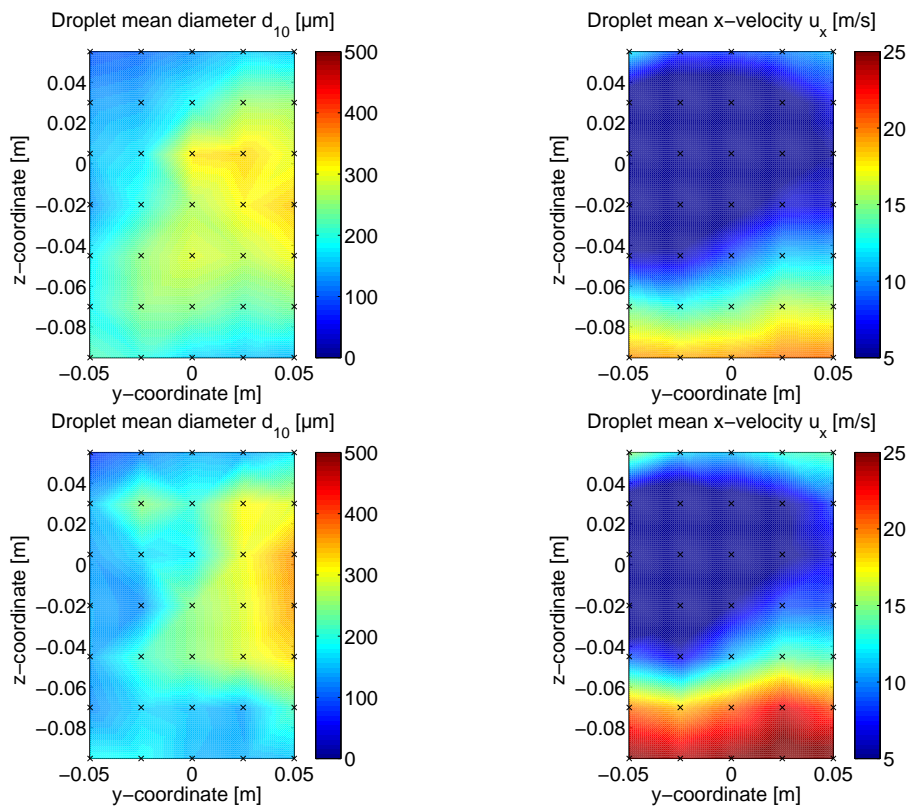
FIGURE D.6: Spatial mean droplet diameter and velocity distribution measured by means of PDA for wind tunnel velocities of $u_\infty = 20$ m/s (top) and $u_\infty = 25$ m/s (bottom) in the x400-plane.
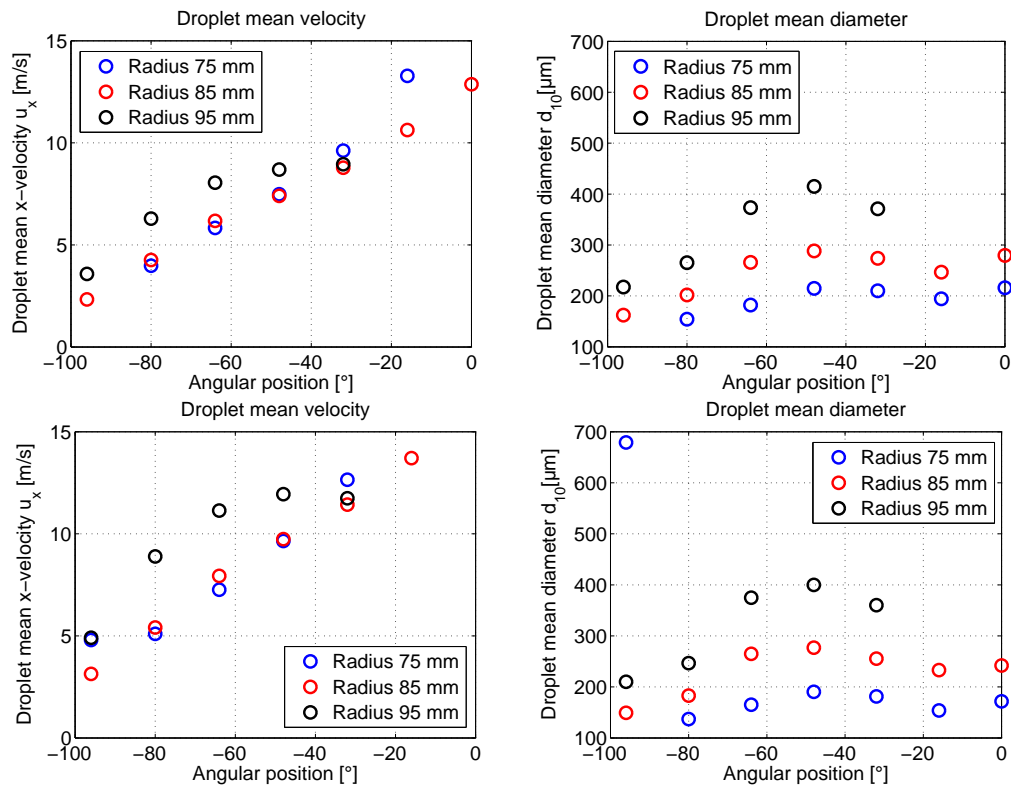
FIGURE D.7: PDA results for droplet x-velocity u_x (left) and droplet mean diameter d_{10} (right) for wind tunnel velocities of $u_\infty = 20$ m/s (top) and $u_\infty = 25$ m/s (bottom) along the y0-profile.

FIGURE D.8: PDA results for droplet x-velocity u_x (left) and droplet mean diameter d_{10} (right) for wind tunnel velocities of $u_\infty = 20$ m/s (top) and $u_\infty = 25$ m/s (bottom) along the y25-profile.

FIGURE D.9: PDA results for droplet x-velocity u_x (left) and droplet mean diameter d_{10} (right) for wind tunnel velocities of $u_\infty = 20$ m/s (top) and $u_\infty = 25$ m/s (bottom) along the y-25-profile.
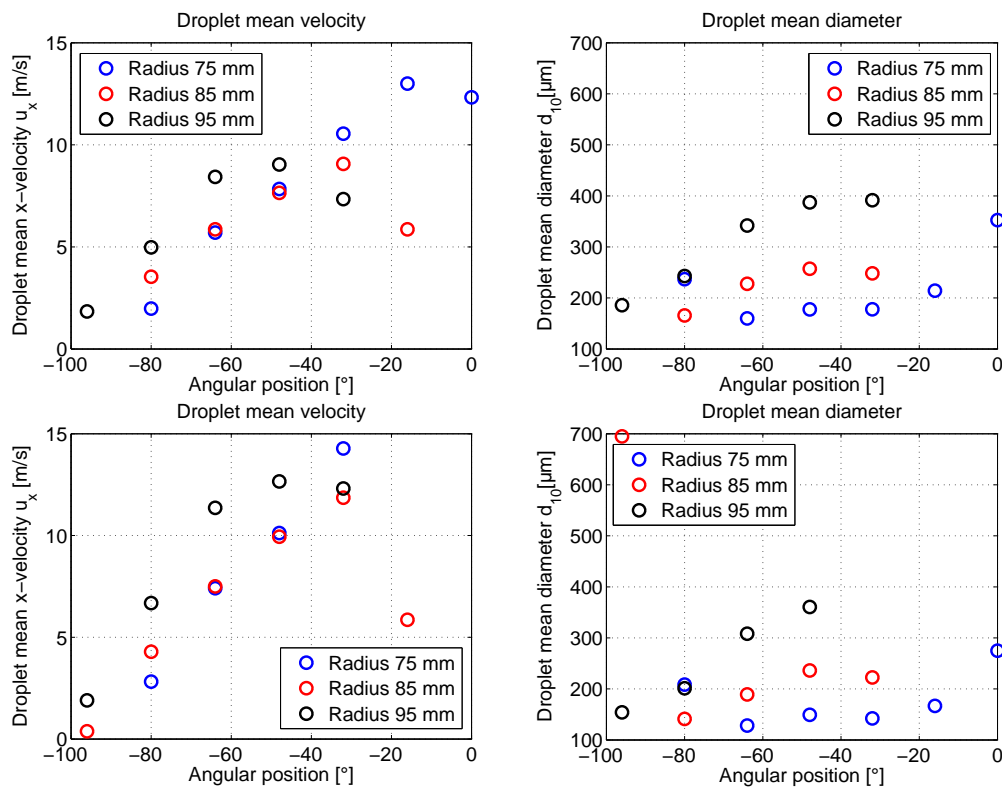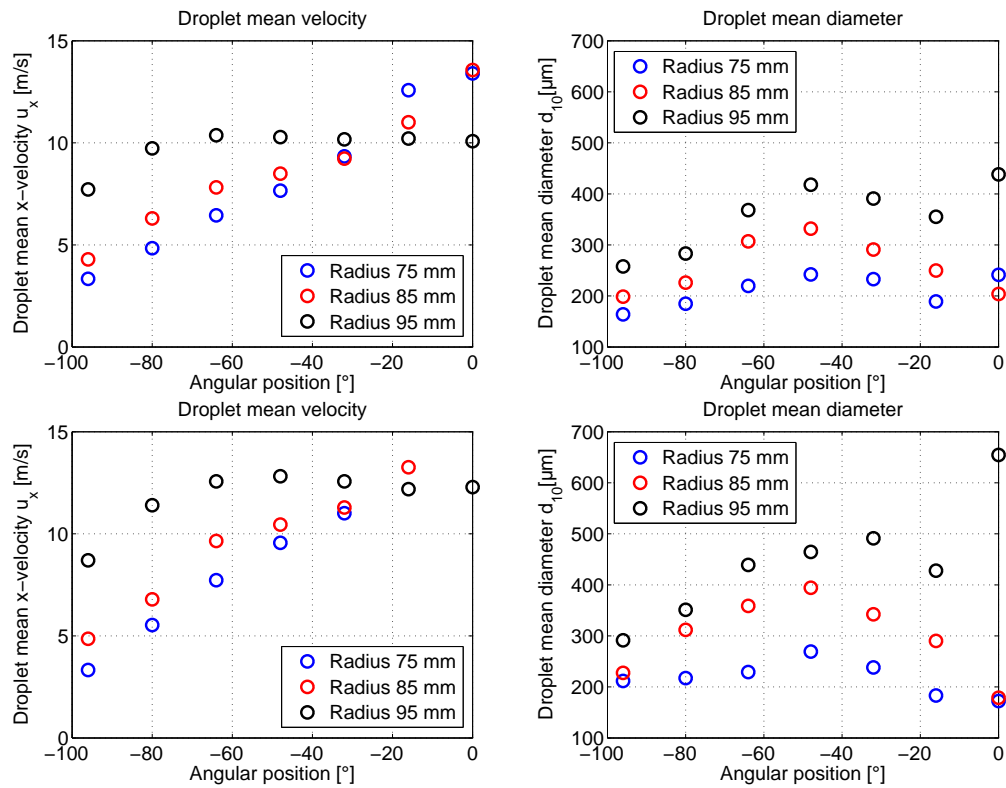
Bibliography

[1] Adomeit, P., Renz, U., 2000. Hydrodynamics of three-dimensional waves in laminar falling films. International Journal of Multiphase Flow 26 (7), 1183–1208.

[2] Aguinaga, S., Borée, J., Simonin, O., Bouchet, J.-P., Herbert, V., 2008. Droplets dispersion and deposition measurements in an axisymmetric sudden expansion flow. In: 14th Int Symp on Application of Laser Techniques to Fluid Mechanics, Lisbon, Portugal.

[3] Aguinaga, S., Bouchet, J.-P., 2009. Quantitative assessment by UV fluorescence of rain water flow on vehicle body in Jules Verne Climatic Wind tunnel. In: 7th FKFS Conference "Progress in Vehicle Aerodynamics and Thermal Management", Stuttgart, Germany.

[4] Al-Sibai, F., 2004. Experimentelle Untersuchung der Strömungscharakteristik und des Wärmeübergangs bei welligen Rieselfilmen. Ph.D. thesis, Fakultät für Maschinenwesen, RWTH Aachen.

[5] Alekseenko, S., Antipin, V., Guzanov, V., Kharlamov, S., Markovich, D., 2005. Three-dimensional solitary waves on falling liquid film at low Reynolds numbers. Physics of Fluids 17 (12), 121704.

[6] Alekseenko, S., Nakoryakov, V., Pokusaev, B., 1994. Wave Flow of Liquid Films. Begell House, ISBN 1567800 0215.

[7] Amsden, A., O'Rourke, P., Butler, T., 1989. KIVA-II: A Computer Program for Chemically Reactive Flows with Sprays. Tech. rep., Los Alamos National Laboratory report, LA-11560-MS.

[8] Anderson, A., Coughlan, B., 2006. Liquid film flows over solid surfaces. In: 6th MIRA International Vehicle Aerodynamics Conference. pp. 368–379.

[9] Ausner, I., 2006. Experimentelle Untersuchungen mehrphasiger Filmströmungen. Ph.D. thesis, Fakultät III - Prozesswissenschaften, Technische Universität Berlin.

[10] Bai, C., Gosman, A., 1996. Mathematical modeling of wall films formed by impinging sprays. In: Society of Automotive Engineers, SAE Paper Nr. 960626.

[11] Bannister, M., 2000. Drag and dirt deposition mechanisms of external rear view mirrors and techniques used for optimization. In: SAE World Congress, Detroit, Technical Paper Series Nr. 2000-01-0486. pp. 97–114.

[12] Björtin, A., 2008. Computational modeling of liquid film creation and flow on vehicle surfaces. Master's thesis, Department of Applied Mechanics, Division of Fluid Dynamics, Chalmers University of Technology, Gothenburg.

[13] Bordás, R., Hagemeier, T., Thévenin, D., 2010. Experimental investigation of droplet-droplet interactions. In: ILASS2010, 23rd Annual Conference on Liquid Atomization and Spray Systems, Brno, Czech Republic. ISBN 978-80-7399-997-1, pp. 198.1–198.6.

[14] Bordás, R., Hagemeier, T., Thévenin, D., Wunderlich, B., 2006. LDV-Signale beinhalten mehr Informationen als nur die Geschwindigkeit. In: Lasermethoden in der Strömungsmesstechnik, GALA. pp. 23/1–23/7.

[15] Borg, A., Vevang, R., 2004. On the development of a wind tunnel method for the prediction of exterior contamination (Correlation and calibration with on road conditions). In: 5th International Vehicle Aerodynamics Conference, Warwick.

[16] Borg, A., Vevang, R., 2006. On the prediction of exterior contamination with numerical simulation (Simple Lagrangian particle tracking methods with and without wall film model). In: 6th MIRA International Vehicle Aerodynamics Conference. pp. 380–388.

[17] Bouchet, J.-P., Delpech, P., Palier, P., 2004. Wind tunnel simulation of road vehicle in driving rain of variable intensity. In: 5th International Vehicle Aerodynamics Conference, Warwick.

[18] Brauer, H., 1971. Grundlagen der Einphasen- und Mehrphasenströmungen. Sauerländer, Aarau.

[19] Brenn, G., Braeske, H., Durst, F., 2002. Investigation of the unsteady two-phase fliw with small bubbles in a model bubble column using phase-doppler anemometry. Chemical Engineering Science 57, 5143–5159.

[20] Brinkmann, B., 2011. Abschlussbericht Verschmutzungsprojekt. Tech. rep., Internal Report to Volkswagen AG Wolfsburg.

[21] Brinkmann, B., Hagemeier, T., 2008. Review der Versuche zum Sprayaufprall am generischen Windschutzscheibenmodell im Zweiphasen-Windkanal Magdeburg. Tech. rep., Internal Report to Volkswagen AG Wolfsburg.

[22] Brinkmann, B., Hagemeier, T., 2008. Review der Vorversuche zum Sprayaufprall auf eine ebene Platte im Zweiphasen-Windkanal Magdeburg. Tech. rep., Internal Report to Volkswagen AG Wolfsburg.

[23] Brinkmann, B., Möller, T., 2009. Dickenbestimmung eines schubspannungs-getriebenen Wandfilmes auf einer geneigten ebenen Platte mittels Laser-lichtschnitt. In: 17. GALA-Fachtagung, Erlangen, Deutschland. ISBN 978-3-9805613-5-8.

[24] Campos, F., Mendonca, F., Weston, S., Islam, M., 2006. Vehicle soiling simulation. In: 6th MIRA International Vehicle Aerodynamics Conference. pp. 358–367.

[25] Campos, F., Mendonca, F., Weston, S., Islam, M., 2007. CFD Simulation of Vehicle Soiling. In: NAFEMS World Congress, Vancouver.

[26] Chandrasekhar, S., 1961. Hydrodynamic and Hydromagnetic Stability. Courier Dover Publications.

[27] Chinnov, E., Kharlamov, S., Saprykina, A., Zhukovskaya, O., 2007. Measuring deformations of the heated liquid film by the fluorescence method. Thermophys. Aeromech. 14, 241–246.

[28] Coghe, A., Brunello, G., Cossali, G., Marengo, M., 1999. Single drop splash on thin film: Measurements of crown characteristics. In: 15th Conference on Liquid Atomization and Spray Systems ILASS-Europe, Toulouse.

[29] Cossali, G. E., Coghe, A., Marengo, M., 1997. The impact of a single drop on a wetted solid surface. Experiments in Fluids 22, 463–472.

[30] Cramblitt, B., Gilfrin, P., Jun. 2011. Harpoon used in Audi Vehicle Soiling Study @online.
URL http://www.sharc.co.uk/html/case_audi.htm

[31] Craster, R., Matar, O., 2009. Dynamics and stability of thin liquid films. Reviews of Modern Physics 81, 1131–1198.

[32] Crowe, C., 2006. Multiphase Flow Handbook. CRC Press.

[33] Crowe, C., Sommerfeld, M., Tsuji, Y., 1998. Multiphase flows with droplets and particles. CRC Press.

[34] Culkin, J., Davis, S., 1984. Meandering of Water Rivulets. AlChE Journal 30, 263–267.

[35] Dantec Dynamics, Aug. 2011. Particle dynamics analysis, measurement principles of PDA @online.
URL http://www.dantecdynamics.com/Default.aspx?ID=1058

[36] de Gennes, P., Brochard-Wyart, F., Quéré, D., 2003. Capillarity and Wetting Phenomena: Drops, Bubbles, Pearls, Waves. Springer.

[37] Dhiman, R., Chandra, S., 2009. Rupture of thin films formed during droplet impact. Proceedings of Royal Society A 466 (2116), 1229–1245.

[38] Dietz, A., 2010. Numerical simulation with particle transport to compute self- and third party soiling of motor vehicles. In: 5th OpenFOAM Workshop, Gothenburg, Sweden.

[39] Diez, J., Kondic, L., 2002. Computing Three-Dimensional Thin Film Flows Including Contact Lines. Journal of Computational Physics 183, 274–306.

[40] Durst, F., Melling, A., Whitelaw, J., 1987. Theorie und Praxis der Laser-Doppler-Anemometrie. Braun Verlag.

[41] Durst, F., Zaré, M., 1975. Laser Doppler measurements in two-phase flows. In: Proceedings of LDA Symposium, Copenhagen. pp. 403–429.

[42] Elghobashi, S., 1994. On Predicting Particle-Laden Turbulent Flows. Applied Scientific Research 52, 309–329.

[43] Erpul, G., Gabriels, D., Janssens, D., 1998. Assessing the drop size distribution of simulated rainfall in a wind tunnel. Soil and Tillage Research 45, 455–463.

[44] Faeth, G., Hsiang, L.-P., Wu, P.-K., 1995. Structure and breakup properties of sprays. International Journal of Multiphase Flow 21, 99–127.

[45] Ferziger, J., Perić, M., 2008. Numerische Strömungsmechanik. Springer Verlag, Berlin, Heidelberg.

[46] Foucart, H., Blain, E., 2005. Water-flow simulation on vehicle panels by taking into account the calculated aerodynamic field. In: Commercial Vehicle Engineering Congress and Exhibition, Chicago, Technical Paper Series Nr. 2005-01-3572.

[47] Foucart, H., Habchi, C., Le Coz, J., Baritaud, T., 1998. Development of a three dimensional model of wall fuel liquid film for internal combustion engines. In: SAE International Congress and Exhibition, Warrendale, Technical Paper Series Nr. 980133.

[48] Gaylard, A., Duncan, B., 2011. Simulation of Rear Glass and Body Side Vehicle Soiling by Road Sprays. In: Society of Automotive Engineers, SAE Paper Nr. 2011-01-0173.

[49] Ghani, S., Aroussi, A., Rice, E., 2001. Simulation of road vehicle natural environment in a climate wind tunnel. Simulation Practice and Theory 8, 359–375.

[50] Greszik, D., Yang, H., Dreier, T., Schulz, C., 2011. Measurement of water film thickness by laser-induced fluorescence and Raman imaging. Applied Physics B 102, 123–132.

[51] Hagemeier, T., Bordás, R., Bencs, P., Wunderlich, B., Thévenin, D., 2008. Determination of droplet size and velocity distributions in a two-phase wind tunnel. In: Prenel, J. P. and Bailly, Y. (Ed.), 13th International Symposium on Flow Visualization, Nice, France. pp. 094/1–094/10.

[52] Hagemeier, T., Hartmann, M., Kühle, M., Thévenin, D., Zähringer, K., 2012. Experimental characterization of thin films, droplets and rivulets using LED fluorescence. Experiments in Fluids 52 (2), 361–374.

[53] Hagemeier, T., Hartmann, M., Thévenin, D., 2010. Improved Eulerian Model for Liquid Films. In: 7th International Conference on Multiphase Flow, ICMF, Tampa, USA. pp. 1–9.

[54] Hagemeier, T., Hartmann, M., Thévenin, D., 2011. Practice in Vehicle Soiling Investigation: a Review. International Journal of Multiphase Flow 37 (8), 860–875.

[55] Hagemeier, T., Thévenin, D., 2010. Interaction of droplets and liquid films. In: Proceedings of the 12th Workshop on Two-Phase Flow Predictions, Halle (Saale) Germany. pp. 1–11.

[56] Haines, P., Luers, J., 1983. Aerodynamic Penalties of Heavy Rain on Landing Aircraft. Journal of Aircraft 20, 111–119.

[57] Hartley, D., Murgatroyd, W., 1964. Criteria for the break-up of thin liquid layers flowing isothermally over solid surfaces. International Journal of Heat and Mass Transfer 7 (9), 1003 – 1015.

[58] Hessel, V., Renken, A., Schouten, J., (Eds.), J. Y., 2009. Micro Process Engineering: A Comprehensive Handbook, Band 1. Wiley-VCH Verlag GmbH Co. KGaA, Weinheim.

[59] Hessenkemper, J., 2011. Die Aerodynamik des PKW Rückspiegel unter Berücksichtigung von Aspekten der Fahrzeugverschmutzung. Bachelor's Thesis LSS-B02/10, Lehrstuhl für Strömungsmechanik und Strömungstechnik, Univ. of Magdeburg "Otto von Guericke".

[60] Hidrovo, C., Hart, D., 2001. Emission reabsorption laser induced fluorescence (ER-LIF) film thickness measurement. Measurement Science and Technology 12, 467–477.

[61] Höfer, P., 2004. Wind tunnel studies on extrinsic pollution at Daimler Chrysler AG. Tech. rep., Technische Mitteilungen, Haus der Technik e.V.

[62] Hoffmann, R., 1975. A study of the advancing interface. I. interface shape in liquid-gas systems. Journal of Colloid Interface Science 50 (2), 228–241.

[63] Hommel, M., 2006. Parallelisierte Simulationsprozesse für virtuelles Prototyping in der Automobilindustrie. Ph.D. thesis, Fakultät Elektrotechnik und Informationstechnik, Technischen Universität 'Carolo Wilhelmina', Braunschweig.

[64] Horvat, K., 2006. Computational modelling of spray impingement accounting for the wall film formation. Ph.D. thesis, Fachbereich Maschinenbau, Technische Universität Darmstadt.

[65] Hsiang, L.-P., Faeth, G., 1992. Near-Limit Drop Deformation and Seconday Breakup. International Journal of Multiphase Flow 18 (5), 635–652.

[66] Hucho, W., Sovran, G., 1993. Aerodynamics of Road Vehicles. Annual Review of Fluid Mechanics 25 (1), 485–537.

[67] Hucho, W.-H., Ahmed, S., 2005. Aerodynamik des Automobils. Vieweg+Teubner Verlag ISBN 3-528-03959-0, 5. Auflage.

[68] Inagaki, H., Saito, A., Murakami, M., Konomi, T., 1995. Development of Two-Dimensional Oil Film Thickness Distribution Measuring System. SAE Paper 952346, 59–67.

[69] Ishigai, S., Nakanisi, S., Koizumi, T., Oyabu, Z., 1972. Hydrodynamics and heat transfer of vertical falling liquid films (Part 1, classification of flow regimes). Japan Society of Mechanical Engineers Bulletin 15, 594–602.

[70] Islam, M., 2004. Advanced Topics in the Simulation of External Vehicle Flows at Audi. In: STAR-CD Conference, London.

[71] Islam, M., Decker, F., de Villiers, E., Jackson, A., Gines, J., Grahs, T., Gitt-Gehrke, A., Comas i Font, J., 2009. Application of Detached-Eddy Simulation for

Automotive Aerodynamics Development. In: Society of Automotive Engineers, SAE-Paper Nr. 2009-01-0333. pp. 209–221.

[72] Jiang, T., Oh, S., Slattery, J., 1979. Correlation for dynamic contact angle. Journal of Colloid Interface Science 69 (1), 74–77.

[73] JIS-D-0203, 1994. Method of moisture, rain and spray test for automobile parts.

[74] Johnson, M., Schluter, R., Bankoff, S., 1997. Fluorescent imaging system for global measurement of liquid film thickness and dynamic contact angle in free surface flows. Review of Scientific Instruments 11, 4097–4102.

[75] Johnson, M., Schluter, R., Miksis, M., Bankoff, S., 1999. Experimental study of rivulet formation on an inclined plate by fluorescent imaging. Journal of Fluid Mechanics 394, 339–354.

[76] Josserand, C., Zaleski, S., 2003. Droplet splashing on a thin liquid film. Physics of Fluids 15, 1650–1657.

[77] Kalantari, D., Tropea, C., 1997. Spray impact onto flat and rigid walls: Empirical characterization and modelling. International Journal of Multiphase Flow 23 (4), 749–763.

[78] Kamitani, K., Teranishi, T., 2003. Development of Water-Repellent Glass Improved Water-Sliding Property and Durability. Journal of Sol-Gel Science and Technology 26, 823–825.

[79] Karbon, K., Longman, S., 1998. Automobile Exterior Water Flow Analysis using CFD and Wind Tunnel Visualization. In: Society of Automotive Engineers, SAE-SP 1361, Paper Nr. 980035.

[80] Kohse-Höinghaus, K., Jeffries, J., 2002. Applied Combustion Diagnostics. Taylor & Francis.

[81] Kondic, L., 2003. Instabilities in Gravity Driven Flow of Thin Fluid Films. SIAM Review 45, 95–115.

[82] Kruse, N., Chen, K.-H., 2007. Exterior Water Management Using a Custom Euler-Lagrange Simulation Approach. In: SAE World Congress, Detroit, Technical Paper Series Nr. 2007-01-0101.

[83] Kuhlman, J., Gray, D., Kreitzer, P., 2011. Progress in Modelling of Spray Cooling. In: ILASS-24th European Conference on Liquid Atomization and Spray Systems.

[84] Kuthada, T., Widdecke, N., Wiedemann, J., 2004. Advanced Investigation Methods on Vehicle Soiling. In: 5th International Vehicle Aerodynamics Conference, Warwick.

[85] Lafuente, J., 2007. Experimental studies of water management on a flat plate and simplified rear view mirror. Master's thesis, Division of Fluid Dynamics, Department of Applied Mechanics, Chalmers University of Technology, Gothenburg.

[86] Langrish, T., Kota, K., 2007. Assessing the Deposition of a Water Spray on a Plate in a Simple Box Configuration Using Computational Fluid Dynamics (CFD). Chemical Product and Process Modeling 2 (3), 1–33.

[87] Lefebvre, A., 1989. Atomization and Sprays. CRC Press, Taylor and Francis.

[88] Lehnhäuser, T., 2007. Method Evaluation for Soiling Simulation using Computational Fluid Dynamics. Tech. rep., Internal Report to Volkswagen AG Wolfsburg.

[89] Lehwald, A., Thévenin, D., Zähringer, K., 2010. Quantifying macro-mixing and micro-mixing in a static mixer using two-tracer laser-induced fluorescence. Experiments in Fluids 48, 823–836.

[90] Lel, V., Al-Sibai, F., Leefken, A., Renz, U., 2005. Local thickness and wave velocity measurement of wavy films with chromatic confocal imaging method and a fluorescence intensity technique. Experiments in Fluids 39, 856–864.

[91] Liu, J., Paul, J., Gollub, J., 1993. Measurement of the primary instabilities of film flows. Journal of Fluid Mechanics 250, 69–101.

[92] Luers, J., Haines, P., 1983. Heavy Rain Influence on Airplane Accidents. Journal of Aircraft 20, 187–191.

[93] Mack, G., 2009. Eine neue Methodik zur modellbasierten Bestimmung dynamischer Betriebslasten im mechatronischen Fahrwerkentwicklungsprozess. Ph.D. thesis, Fachbereich Maschinenbau, Universität Karlsruhe.

[94] Macklin, W., Metaxas, G., 1976. Splashing of drops on liquid layers. Journal of Applied Physics 47, 3963–3970.

[95] Malamataris, N., Vlachogiannis, M., Bontozoglou, V., 2002. Solitary waves on inclined films: Flow structure and binary interactions. Physics of Fluids 14, 1082–1094.

[96] Manser, M., 2003. Evaluation of Splash and Spray Suppression Devices. Tech. rep., AAA Foundation for Traffic Safety.

[97] Marchioli, C., Picciotto, M., Soldati, A., 2007. Influence of gravity and lift on particle velocity statistics and transfer rates in turbulent vertical channel flow. International Journal of Multiphase Flow 33, 227–251.

[98] Martinuzzi, R., Tropea, C., 1993. The flow around surface-mounted, prismatic obstacles placed in a fully developed channel flow. Journal of Fluids Engineering 115, 85–92.

[99] Maskell, E., 1963. A Theory of the Blockage Effects on Bluff Bodies and Stalled Wings in a Closed Wind Tunnel. Tech. rep., Reports and Memoranda No. 3400, Ministry of Aviation.

[100] Matysiak, A., 2007. Euler-Lagrange Verfahren zur Simulation tropfenbeladener Strömung in einem Verdichtergitter. Ph.D. thesis, Fachbereich Maschinenbau, Helmut-Schmidt-Universität, Hamburg.

[101] Ménard, T., Tanguy, S., Berlemont, A., 2007. Coupling level set/VOF/ghost fluid methods: Validation and application to 3D simulation of the primary break-up of a liquid jet. Interantional Journal of Multiphase Flow 33, 510–524.

[102] Menter, F., 1993. Zonal two equation k-ω turbulence models for aerodynamic flows. Tech. rep., AIAA Paper 1993-2906.

[103] Meredith, K., 2010. Thin liquid film modeling in OpenFOAM. In: 5th OpenFOAM Workshop, Gothenburg, Sweden.

[104] Moran, K., Inumaru, J., Kawaji, M., 2002. Instantaneous hydrodynamics of a laminar wavy liquid film. International Journal of Multiphase Flow 28 (5), 731 – 755.

[105] Morud, J., 2007. Dilute gas-liquid flows with liquid films on walls. Progress in Computational Fluid Dynamics 7, 170–175.

[106] Mouza, A., Vlachos, N., Paras, S., Karabelas, A., 2000. Measurement of liquid film thickness using a laser light absorption method. Experiments in Fluids 28, 355–359.

[107] Mühlbauer, M., 2009. Modelling wall interactions of a high-pressure, hollow cone spray. Ph.D. thesis, Fachbereich Maschinenbau, Technische Universität Darmstadt.

[108] Mundo, C., Sommerfeld, M., Tropea, C., 1994. Experimental studies of the deposition and splashing of small liquid droplets impinging on a flat surface. In: ICLASS, Rouen, France. pp. 1–18.

[109] Mundo, C., Sommerfeld, M., Tropea, C., 1995. Droplet-wall collisions: Experimental studies of the deformation and breakup process. International Journal of Multiphase Flow 21, 151–173.

[110] Murase, H., Nanishi, K., Kogure, H., Fujibayashi, T., Tamura, K., Haruta, N., 1994. Interactions between heterogeneous surfaces of polymers and water. Journal of Applied Polymer Science 54, 2051–2062.

[111] Murgatroyd, W., 1965. The Role of Shear and Form Forces in Stability of a Dry Patch on Two-phase Film Flow. International Journal of Heat and Mass Transfer 8, 297–301.

[112] Nusselt, W., 1916. Die Oberflächenkondensation des Wasserdampfes. VDI-Zeitschrift 60, 541.

[113] Nylander, P., 2008. CFD modeling of water ingestion in air intake system. Master's thesis, Department of Applied Physics and Mechanical Engineering, Division of Fluid Mechanics, Lulea University of Technology.

[114] O'Brien, S., Schwartz, L., 2006. Theory and modeling of thin film flows. Encyclopedia of Surface and Colloid Science, 5283–5297.

[115] Okawa, T., Shiraishi, T., Mori, T., 2006. Production of secondary drops during the single water drop impact onto a plane water surface. Experiments in Fluids 41, 965–974.

[116] Okawa, T., Shiraishi, T., Mori, T., 2008. Effect of impingement angle on the outcome of single water drop impact onto a plane water surface. Experiments in Fluids 44, 331–339.

[117] Orno, A., Davis, S., Bankhoff, S., 1997. Long-scale evolution of thin liquid films. Reviews of Modern Physics 69, 931–980.

[118] O'Rourke, P., Amsden, A., 1996. A Particle Numerical Model for Wall Film Dynamics in Port-injected Engines. In: Society of Automotive Engineers, SAE Paper Nr. 961961.

[119] O'Rourke, P., Amsden, A., 2000. A Spray/Wall Interaction Submodel for KIVA-3 Wall Film Model. In: Society of Automotive Engineers, SAE Paper Nr. 2000-01-0271.

[120] Ostrach, S., Koestel, A., 1965. Film Instabilities in Two-Phase Flows. AIChE Journal 11, 294–303.

[121] Paschkewitz, J., 2006. Simulation of spray dispersion in a simplified heavy vehicle wake. Tech. rep., Energy and Environment Directorate, Lawrence Livermore National Laboratory, CA, 94551.

[122] Penn, D. G., de Bertodano, M. L., Lykoudis, P. S., Beus, S. G., 2001. Dry patch stability of shear driven liquid films. Journal of Fluids Engineering 123 (4), 857–862.

[123] Piatek, R., Hentschel, W., 1989. Strömungssichtbarmachung in der aerodynamischen Entwicklung von Kraftfahrzeugen. In: Tagung: Sichtbarmachung technischer Strömungsvorgänge, Haus der Technik e.V., Essen.

[124] Pilch, M., Erdman, C., 1987. Use of breakup time data and velocity history data to predict the maximum size of stable fragments for acceleration-induced breakup of a liquid drop. International Journal of Multiphase Flow 13, 741–757.

[125] Pilkington, G., 1990. Splash and Spray: Surface Characteristics of Roadways. International Research and Technologies ASTM STP 1031, 528–541.

[126] Pope, S., 2000. Turbulent Flows. Cambridge University Press.

[127] Potthoff, J., 1974. Untersuchung der Verschmutzung von Kraftfahrzeugen im Windkanal. In: VDI-Jahrestagung Fahrzeugverschmutzung, Duesseldorf.

[128] Prosperetti, A., Tryggvason, G., 2007. Computational Methods for Multiphase Flow. Cambridge University Press.

[129] Raffel, M., Willert, C., Kompenhans, J., 1998. Particle Image Velocimetry. Springer.

[130] Rein, M., 1993. Phenomena of liquid droplet impact on solid and liquid surface. Fluid Dynamics Research 12 (2), 61–93.

[131] Roettger, S., Schulz, M., Bartelheimer, W., Ertl, T., 2001. Automotive Soiling Simulation Based on Massive Particle Tracking. In: EG/IEEE TCIVG Symposium on Visualization, VisSym. pp. 309–317.

[132] Roisman, I., Horvat, K., Tropea, C., 2006. Spray impact: Rim transverse instability initiation fingering and splash, and description of secondary spray. Physics of Fluids 18 (10), 102104/1–102104/19.

[133] Saber, H., El-Genk, M., 2004. On the breakup of a thin liquid film subject to interfacial shear. Journal of Fluid Mechanics 500, 113133.

[134] SAE-J2245, 2002. Recommended Practice for Splash and Spray Evaluation.

[135] Samenfink, W., Elsässer, A., Dullenkopf, K., Wittig, S., 1999. Droplet interaction with shear-driven liquid films: analysis of deposition and secondary droplet characteristics. International Journal on Heat and Fluid Flow 20, 462–469.

[136] Schiller, L., Naumann, Z., 1935. A drag coefficient correlation. Z. Ver. Deutsch. Ing. 77, 318.

[137] Schlichting, H., 1951. Grenzschicht-Theorie. Verlag G. Braun.

[138] Schubring, D., Ashwood, A., Shedd, T., Hurlburt, E., 2010. Planar laser-induced fluorescence (PLIF) measurements of liquid film thickness in annular flow. Part I: Methods and data. International Journal of Multiphase Flow 36 (10), 815 – 824.

[139] Schubring, D., Shedd, T., Hurlburt, E., 2010. Planar laser-induced fluorescence (PLIF) measurements of liquid film thickness in annular flow. Part II: Analysis and comparison to models. International Journal of Multiphase Flow 36 (10), 825 – 835.

[140] Sivakumar, D., Tropea, C., 2002. Splashing impact of a spray onto a liquid film. Physics of Fluids, Letters 14 (12), L85–L88.

[141] Sommerfeld, M., Wachem, B., Oliemans, R., 2008. Best Practice Guidelines for Computational Fluid Dynamics of Dispersed Multiphase Flows. ERCOFTAC, ISBN 978-91-633-3564-8.

[142] Spruss, I., Kuthada, T., Wiedemann, J., Cyr, S., Duncan, B., 2011. Spray pattern of a free rotating wheel: CFD simulation and validation. In: Progress in vehicle aerodynamics and thermal management: proceedings of the 8th FKFS Conference.

[143] Stanton, D., Rutland, C., 1998. Multi-dimensional modeling of heat and mass transfer of fuel films resulting from impinging sprays. In: Society of Automotive Engineers, SAE Paper Nr. 980132.

[144] Szeri, A., Snyder, V., 2006. Convective inertia effects in wall-bounded thin film flows. Meccanica 41 (5), 473–482.

[145] Thompson, B., Marrochello, M., 1999. Rivulet Formation in Surface-Water Flow on an Airfoil in Rain. Journal of Aircraft 37, 45–49.

[146] Tivert, T., 2009. Computational study of rivulets using Volume of Fluid. Licentiate Thesis, Department of Applied Mechanics, Division of Fluid Dynamics, Chalmers University of Technology, Gothenburg.

[147] Tivert, T., Borg, A., Marimon, J., Davidson, L., 2007. Wind-driven rivulet over an edge with break-up. In: 6th International Conference on Multiphase Flow, ICMF, Leipzig, Germany.

[148] Tivert, T., Davidson, L., 2010. Experimental study of water transport on a generic mirror. In: 7th International Conference on Multiphase Flow, ICMF, Tampa, USA.

[149] Tropea, C., Yarin, A., Foss, J., 2007. Handbook of Experimental Fluid Mechanics. Springer Verlag.

[150] Tuković, Ž., Jasak, H., 2009. Simulation of thin liquid film flow using OpenFOAM finite area method. In: 4th OpenFOAM Workshop, Montreal, Canada.

[151] Urban, J., 2009. Numerische Untersuchung und Modellierung von Tropfen-Wand-Interaktionen. Ph.D. thesis, Institute of Aerospace Thermodynamics, University Stuttgart.

[152] Urban, J., Weigand, B., Roth, N., Eyselein, M., Trackl, K., Tatschl, R., Raulot, A., 2007. Modeling of Droplet Wall Interaction. In: 6th International Conference on Multiphase Flow, ICMF, Leipzig, Germany.

[153] Urban, J., Weigand, B., Roth, N., Trackl, K., Eyselein, M., Raulot, A., Tatschl, R., 2006. Fortschritte bei der Simulation von Wasserabscheidungsvorgängen in Wasserkästen von Automobilen. In: Spray 2006, Lampoldshausen, Germany.

[154] Valentine, J., Decker, R., 1995. Tracking of Raindrops in Flow over an Airfoil. Journal of Aircraft 32, 100–105.

[155] Vander Wal, R., Berger, G., Mozes, S., 2006. Droplets splashing upon films of the same fluid of various depths. Experiments in Fluids 40, 33–52.

[156] Šikalo, Š., Wilhelm, H.-D., Roisman, I., Jakirlić, S., Tropea, C., 2005. Dynamic contact angle of spreading droplets: Experiments and simulations. Physics of Fluids 17, 1–13.

[157] Wang, A.-B., Chen, C.-C., 2000. Splashing impact of a single drop onto very thin liquid films. Physics of Fluids 12 (9), 2155–2158.

[158] Wang, Q., Squires, K., Chen, M., McLaughlin, J., 1997. On the role of the lift force in turbulence simulations of particle deposition. International Journal of Multiphase Flow 23 (4), 749–763.

[159] Watkins, S., 2009. Spray from Commercial Vehicles: A Method of Evaluation and Results from Road Tests. In: Browand, F., McCallen, R., Ross, J. (Eds.), The Aerodynamics of Heavy Vehicles II: Trucks, Buses, and Trains. Vol. 41 of Lecture Notes in Applied and Computational Mechanics. Springer Berlin / Heidelberg, pp. 387–402.

[160] Weiss, C., 2005. The liquid deposition fraction of sprays impinging vertical walls and flowing films. International Journal of Multiphase Flow 31, 115–140.

[161] Widdecke, N., Kuthada, T., Wiedemann, J., 2001. Moderne Verfahrensweisen zur Untersuchung der Fahrzeugverschmutzung. In: Operative und Strategische Ziele der Fahrzeugdynamik, Haus der Technik, München.

[162] Wilcox, D., 2006. Turbulence Modeling for CFD. DCW Industries.

[163] Winkels, K., Peters, I., Evangelista, F., Riepen, M., Daerr, A., Limat, L., Snoeijer, J., 2011. Receding contact lines: From sliding drops to immersion lithography. The European Physical Journal Special Topics 192, 195–205.

[164] Yarin, A., 2006. Drop impact dynamics: splashing, spreading, receding, bouncing. Annual Review of Fluid Mechanics 38, 159–192.

[165] Yoshida, M., Yamatani, A., China, H., 1998. Prediction of dirt contamination on vehicle body surface. JSAE Review 19, 257–262.

[166] Zhou, D., Gambaryan-Roisman, T., Stephan, P., 2009. Measurement of water falling film thickness to flat plate using confocal chromatic sensing technique. Experimental Thermal and Fluid Science 33 (2), 273 – 283.

[167] Zivkov, V., 2004. Experimentelle und numerische Untersuchung der aerodynamischen Kraftfahrzeugeigenverschmutzung. Ph.D. thesis, Fakultät für Maschinenbau, Technische Universität Karlsruhe.

Thomas Hagemeier

PERSONAL DATA   Date of birth: 21/07/1981

Place of birth: Neubrandenburg

Citizenship: German

Marital status: Single

RESEARCH INTERESTS

Experimental und numerical investigation of multiphase flows in the fields of process engineering and automobile development.

WORK EXPERIENCE

02/2011 - present

University of Magdeburg "Otto von Guericke", Germany

RESEARCH AND TEACHING ASSISTANT "Investigation of multiphase flows, in particular liquid films, sprays and bubble columns".

EDUCATION

09/2007 - 01/2011

University of Magdeburg "Otto von Guericke", Germany

PH.D. STUDENT at the Lab of Fluid Dynamics and Technical Flow

THESIS TOPIC: "Experimental and numerical investigation of vehicle soiling processes", project funding by Volkswagen AG Wolfsburg.

Defended on 6th of December 2012, magna cum laude

10/2001 - 08/2007

University of Magdeburg, "Otto von Guericke", Germany

DIPLOMA DEGREE in Process Engineering, 2007

THESIS TOPIC: "Experimentelle Simulationsmodelle für komplexe Strömungen auf Basis der Ähnlichkeitstheorie"

TEACHING EXPERIENCE

04/2008 - present

Lab of Fluid Dynamics and Technical Flow

Fluid Mechanics, seminar: Fundamentals of fluid mechanics, conservation laws, pressure loss in pipe flows, Navier-Stokes equations, fundamentals of isotropic compressible flows

Measurement Technology, supervision of laboratory: Constant Temperature Anemometry

Supervision of various B.Sc./M.Sc theses: mostly concerned with optical measurements of fluid dynamic properties in the two-phase wind tunnel

List of publications

JOURNAL
PUBLICATIONS

Hagemeier, T., Bordás, R., Zähringer, K., Thévenin, D. Stereoscopic fluorescence analysis of droplets creeping down a tilted plate. submitted to *Experiments in Fluids*

Hagemeier, T., Hartmann, M., Kühle, M., Thévenin, D., Zähringer, K. Experimental characterization of thin films, droplets and rivulets using LED fluorescence. *Experiments in Fluids* 52(2), (2012) 361-374.

Bordás, R., Hagemeier, T., Wunderlich, B. and Thévenin, D. Droplet collisions and interaction with the turbulent flow within a two-phase wind tunnel. *Physics of Fluids* 23(8), (2011) 085105/1-085105/11.

Hagemeier, T., Hartmann, M. and Thévenin, D., Practice of vehicle soiling investigations: a review. *International Journal of Multiphase Flow* 37(8), (2011) 860-875.

PROCEEDINGS
AND
CONFERENCE
PUBLICATIONS

Hagemeier, T., Thévenin, D. and Zähringer, K.: Stereoscopic fluorescence analysis of films, droplets and rivulets. In: 16th International Symposium on Applications of Laser Techniques to Fluid Mechanics, Lisbon, Portugal, Paper 282, 1-8, 2012.

Bordás, R., Hagemeier, T. and Thévenin, D.: Experimental quantification of droplet collision rates in turbulent sprays. In: *7th International Symposium on Turbulence and Shear Flow Phenomena*, Ottawa, Canada, 4B5P1/4B5P-5, 2011.

Bordás, R., Hagemeier, T. and Thévenin, D.: Experimental investigation of droplet-droplet interactions. In: *ILASS2010, 23rd Annual Conference on Liquid Atomization and Spray Systems*, Brno, Czech Republic, 198.1-6, 2010.

Hagemeier, T., Hartmann, M. and Thévenin, D.: Improvement of Eulerian model for liquid films. In: *7th International Conference on Multiphase Flow*, Tampa, Florida, 1-9, 2010.

Hagemeier, T. and Thévenin, D.: Interaction of droplets and liquid films. In: *12th Workshop on Two-Phase Flow Predictions*, (Sommerfeld, M., Ed.), Halle-Merseburg, Germany, 1-11, 2010.

Hagemeier, T., Bordás, R. and Janiga, G.: Numerical modeling of aerodynamics around a half cylinder. In: *microCAD'08 International Scientific Conference*, (Lehoczky, L., and Kalmár, L., Eds.), Miskolc, Hungary, ISBN 978-963-661-816-2, 9-14, 2008.

Hagemeier, T., Bordás, R., Bencs, P., Wunderlich, B. and Thévenin, D.: Determination of droplet size and velocity distributions in a two-phase wind tunnel. In: *13th International Symposium on Flow Visualization*, (Prenel, J.P. and Bailly, Y., Eds.), Nice, France, 094/1-10, 2008.

Bordás, R., Hagemeier, T., Thévenin, D. and Wunderlich, B.: LDV-Signale beinhalten mehr Informationen als nur die Geschwindigkeit. In: *Lasermethoden in der Strömungsmesstechnik*, (Dopheide, D., Müller, H., Strunck, V., Ruck, B. and Leder, A., Eds.), Braunschweig, Germany, GALA , ISBN 3-9805613-3-X, 23/1-23/7, 2006.